THE UNIVERSITY *of* EDINBURGH

A High Resolution Reanalysis of Wind Speeds over the British Isles for Wind Energy Integration

Sam Hawkins

A thesis submitted for the degree of Doctor of Philosophy.
The University of Edinburgh.
July 9, 2012

Abstract

The UK has highly ambitious targets for wind development, particularly offshore, where over 30GW of capacity is proposed for development. Integrating such a large amount of variable generation presents enormous challenges. Answering key questions depends on a detailed understanding of the wind resource and its temporal and spatial variability. However, sources of wind speed data, particularly offshore, are relatively sparse: satellite data has low temporal resolution; weather buoys and met stations have low spatial resolution; while the observations from ships and platforms are affected by the structures themselves.

This work uses a state-of-the art mesoscale atmospheric model to produce a new high-resolution wind speed dataset over the British Isles and surrounding waters. This covers the whole region at a resolution of 3km for a period of eleven consecutive years, from 2000 to 2010 inclusive, and is thought to be the first high resolution re-analysis to represent a true historic time series, rather than a statistically averaged climatology. The results are validated against observations from met stations, weather buoys, offshore platforms and satellite-derived wind speeds, and model bias is reduced offshore using satellite derived wind speeds.

The ability of the dataset to predict power outputs from current wind farms is demonstrated, and the expected patterns of power outputs from future onshore and offshore wind farms are predicted. Patterns of wind production are compared to patterns of electricity demand to provide the first conclusive combined assessment of the ability of future onshore and offshore wind generation meet electricity demand and contribute to secure energy supplies.

Declaration of originality

I hereby declare that the research recorded in this thesis and the thesis itself was composed and originated entirely by myself in the School of Engineering at The University of Edinburgh.

The analysis in §8.4.2 was done in collaboration with Dan Eager and has been published in [Hawkins et al., 2011].

Sam Hawkins

Acknowledgements

Many thanks to everyone who made this possible. Thanks to my supervisor Professor Gareth Harrison for all of your support and guidance, helpful and sometimes even legible comments: without your help this would not have been possible. Many thanks to the help desk team at HECToR, who made my life a lot easier. Also thanks to everyone involved in designing, building, maintaining and supporting WRF, it really is a fantastic community tool. Thanks to Scottish Power Renewables, Community Windpower, Shell UK, the Irish Marine Institute, Met Éireann and the UK Met Office for providing data.

Thanks to all my great office mates and friends Niall, Lucy, Laura, Aby, Richard and Dougal, I hope I see more of you outside of King's Buildings. Thanks to all my other IES colleagues for lunch, banter, coffee, cakes, and, far too occasionally, beer. Let's redress that balance.

Thanks as ever to my parents for their ongoing support, no matter what I do or where my career takes me. You'll be pleased to know I got there in the end.

Finally, and most importantly, thanks to Katie for your love and support throughout the whole process. There is no question I could not have achieved this without you. There were some tough times, but you always stuck with me, and even, in the midst of it all, agreed to marry me.

Contents

List of figures

List of tables

Abbreviations

agl	Above ground level
amsl	Above mean sea level
AVHRR	Advanced Very High Resolution Radiometer
BADC	British Atmospheric Data Centre
CFD	Computational Fluid Dynamics
CDF	Cumulative Distribution Function
ECMWF	European Centre for Medium Range Weather Forecasting
EQNW	Equivalent Neutral Wind
FDDA	Four Dimensional Data Assimilation
GCM	General Circulation Model
GFS	Global Forecast System
GTS	Global Telecommunication System
GRIB	Gridded binary
GWL	Großwetterlage
HECToR	High End Computing Terrascale Resource
IQR	Inter-quartile range
LES	Large Eddy Simulation
MIDAS	Met Office Integrated Data Archive System
NAO	North Atlantic Oscillation
MODIS	Moderate-Resolution Imaging Spectroradiometer
MOS	Model Output Statistics
MOST	Monin-Obhukov similarity theory
MPI	Message Passing Interface
NETA	New Electricity Trading Arrangements
NCAR	National Center for Atmospheric Research
NCEP	National Center for Environmental Prediction
NWP	Numerical Weather Prediction
PBL	Planetary Boundary Layer
PDF	Probability Density Function

p.u.	per unit
QQ	Quantile-quantile
SQL	Structured Query Language
SAR	Synthetic Aperture Radar
SST	Sea Surface Temperature
std	Standard deviation
TKE	Turbulent Kinetic Energy
UKMO	UK Met Office
UM	Unified Model
USGS	US Geological Survey
WAsP	Wind Atlas Analysis and Application Program
WRF	Weather Research and Forecast Model

Symbols

Symbol	Meaning	Units
α_c	Charnock parameter	-
A	Turbine swept area	m^2
c	Weibull location parameter	ms^{-1}
C_p	Turbine power coefficient	-
g	Acceleration due to gravity	ms^{-2}
Γ_d	Dry adiabatic lapse rate	K/m
Γ_w	Moist adiabatic lapse rate	K/m
Γ_e	Environmental lapse rate	K/m
k	Weibull shape parameter	-
κ	von Karmann constant	-
L	Obhukov length	m
LF	Load factor	-
P	Power	W
ρ	Air density	kg m^{-3}
Ri_b	Bulk-richardson number	-
T	Temperature	K
T_v	Virtual temperature	K
θ	Potential temperature	K
τ	Reynold's stress	Pa
U	Wind speed	ms^{-1}
u	West-east wind velocity component	ms^{-1}
u_*	Friction velocity	ms^{-1}
v	South-north velocity component	ms^{-1}
w	Vertical velocity component	ms^{-1}
ζ	Dimensionless stability parameter	-

Chapter 1
Introduction

"You don't need a weather man to know which way the wind blows"
Bob Dylan - *Subterranean Homesick Blues*

1.1 Background

Concern over climate change and security of energy supply has lead many countries to look to renewable resources as a future source of energy. In March 2007, a binding EU-wide target was agreed to source 20% of the EU's total energy demand from renewable sources by 2020. Member states were required to set targets consistent with these; the UK has target of supplying 15% of primary energy demand from renewables by 2020, which will require around 30% of electricity to be generated from renewable sources [DECC, 2009]. Furthermore, the UK's Climate Change Act [UKGOV, 2008] requires a mandatory cut of at least 80% in the UK's carbon emissions by 2050, which implies an increasing proportion of renewable or other low-carbon electricity beyond 2020.

Wind is currently the fastest growing source of renewable electricity in the UK, and it is widely expected to contribute most to the renewable energy targets [DECC, 2009]. In particular, the UK has ambitious plans for offshore wind, with more than 30GW of potential projects earmarked for development [National Grid, 2008]. Harnessing this amount of renewable energy presents an enormous opportunity for society, but also an enormous engineering challenge.

Wind speeds are variable across a wide range of spatial and temporal time-scales, and relatively small changes in wind speed lead to large changes in power generated. Since wind generation is not dispatchable in the same way as conventional fossil fuel generation, harnessing wind generation on a very large scale potentially requires fundamental aspects of the power system to be redesigned. A great deal of research is ongoing to investigate how this can be best achieved, this is perhaps one of the most important engineering questions faced today.

Key to exploring and overcoming the challenges is a detailed understanding of the physical resource, both the average conditions which determine how much energy is available, and also the spatial and temporal variability which govern when and where it is available. Together these dictate what kind of conventional and new approaches are needed to integrate wind generation into a secure and reliable energy system.

Despite the extent of the challenge and the range of research in this field, detailed data on the wind resource is not readily available to researchers. Traditional meteorological observations onshore are taken at 10m above ground level (agl), are strongly affected by local terrain, and are not necessarily available in the areas of interest for wind generation. Offshore, observations are relatively sparse and are often taken just a few metres above sea level. Data collected by private developers is commercially sensitive, and is not made publicly available.

As a consequence, research, and policy making based on it, is often hampered by a lack of high quality data spanning a sufficiently long period. Research effort is frequently duplicated trying to obtain data before any other important questions can be answered. There is a long, and often heated, debate e.g. [Gross and Heptonstall, 2008, Oswald et al., 2008] as to whether the variability of wind is a 'show stopper', that is, too difficult or costly to be harnessed by society. However, critical arguments are made or dismissed on the basis of a selective time period, or only using observed wind speeds onshore. Since much of the planned development in the UK is offshore, there is an urgent need to examine this question using a dataset which is robust, reliable, and long enough to give sufficient confidence in the results. Within the wind industry, many stakeholders are independently pursuing their own, often very costly assessments, involving modelling and measurement campaigns. However without any framework for coordination, they have no incentive to share the results and consequently the overall process is very inefficient.

This project attempts to address this issue by building a model of the UK's onshore and offshore wind resources with high spatial and temporal resolution, to be provided as publicly available dataset to support future research in this area. It also attempts to answer some of the key questions regarding variability in a robust way. The future adequacy, security and reliability of the energy system upon which we all depend demands that we have a openly accessible dataset with which we can at least begin to address some of the key questions in more detail than is currently possible.

1.2 Objectives and scope

The main aim of the project is to model, in a scientifically robust way, the UK's wind resource with high spatial and temporal resolution. The objective is to produce a well-validated dataset which can be used to answer key questions with a good degree of confidence. This dataset must:

- be a realistic representation of the average onshore and offshore wind conditions;
- capture spatial and temporal variability across a range of scales; and
- be physically based, so that relations between wind speed, temperature and other meteorological variables are preserved.

The hypothesis proposed is that using advanced meteorological model can deliver new insight into the UK's wind energy resource, and the potential to intrate this on a large scale.

1.3 Contribution to knowledge

This work represents the first publicly available high-resolution reanalysis of wind speeds around the UK for a period longer than ten years. It is the first study to use a complete record of satellite scatterometer winds to correct model bias over the whole offshore region. It contains the first publicly available assessment of the wind speed distributions at hub height at all of the UK's proposed offshore wind farms, and is the first study to analyse the likely power production at offshore wind farms based on a dataset longer than ten years. It also is the first study to match the output from onshore and offshore wind farms to co-incident patterns of electricity demand, and to assess the impact large scale wind integration will have on hourly patterns of electricity demand.

1.4 Thesis outline

The thesis is split into chapters as follows:

Chapter 1 Is this introduction.

Chapter 2 reviews some background material relevant to mesoscale atmospheric modelling to provide context for the rest of the work.

Chapter 3 Gives a review of mesoscale models and their use in relation to wind energy, and selects a model to used as the main tool for this work.

Chapter 4 Describes the available observations, selects a case study period, compares a number of model configurations over the case study period, and selects a final model configuration to use for main modelling phase.

Chapter 5 Describes the main modelling phase and presents a detailed verification against observations.

Chapter 6 Reviews satellite data sources, develops and applie a methodology for removing model bias offshore.

Chapter 7 Describes and verifies the conversion of wind speeds into power outputs of windfarms, and compares simulated results to published figures.

Chapter 8 Analyses the dataset in terms of the implications for wind energy integration, predicting average outputs from future offshore farms, and showing the spatio-temporal patterns across the study domain.

Chapter 9 Summarises the results of the analysis and presents conclusions for wind integration.

Appendix A Presents maps of the average wind resource, broken down by month of the year.

Appendix B Gives the full specification of the model configuration and output variables.

Appendix C Presents comparison plots against individual in-situ observation stations.

Chapter 2
Background

2.1 Introduction

Wind speeds measured close to the surface of the Earth show variation across a range of spatial and temporal scales. Turbulent gusts cause fluctuations over the course of a few seconds, while wind speeds change hour-to-hour and day-to-day as weather systems pass over the country, and season-to-season as the global circulation changes.

Spatially, wind speeds show well defined global and regional patterns, with the UK among the windiest places on Earth, and the highest regional wind speeds found in the northwest of Scotland. Wind speeds also show spatial variations on smaller scales: wind flow is influenced by terrain, local roughness changes, and local temperature gradients.

The aim of this research is to produce a model of wind speeds over the UK which,

- covers the whole UK and offshore region;
- is spatially and temporally coherent;
- is temporally coherent with patterns of energy demand;
- covers a long enough period to capture important weather episodes; and
- has a spatial resolution high enough to give realistic wind speeds at wind farm sites.

These requirements strongly suggest a physical, rather than a statistical model. Although it is possible to produce and summarise the wind climate via statistical models, it is more difficult to produce a multivariate model that allows wind speeds to be matched to coincident variables such as temperature or electricity demand. Furthermore, a physical model representing true historic time periods is much easier to validate against independent observations.

Given a preference to use a physically-based model, this section now briefly reviews the physical systems governing the atmosphere. A very basic description is given of the scales of

the atmosphere and the modelling approaches used at each scale. This is to give a background and context to the modelling approach used in this work, so that the strengths and limitations can be discussed. It is not intended to be an overview of atmospheric dynamics. The information is drawn from a number of textbooks and papers on the subject namely [Dutton, 1976, Holton, 2004, Martin, 2006, Petersen et al., 1998, Stull, 1988, Warner, 2011], and those facts which are generally regarded as common knowledge are not referenced.

2.2 The Atmosphere

The atmosphere is a thin layer of gases surrounding the Earth. It rapidly thins with height, and although there is no clear boundary, beyond 100km is usually considered to be outer space. The primary cause of all the weather we experience is the uneven heating of a fluid on a rotating sphere. This gives rise to a vast array of features at every scale from dust devils a few meters across, to high level jets which encircle the globe. Features of the atmosphere are often categorised according to their scale, Table 2.1.

Scale	Length scale	Time scale	Example features	Modelling approach
Planetary	6000 km	days to months	Hadley cells Jet stream Rossby waves	General Circulation Model (GCM)
Synoptic	2000 km	days to weeks	Pressure systems Frontal systems	GCM & Mesoscale
Meso	100 km	hours to days	Sea breezes Low-level jets Gap winds	Mesoscale
Sub-meso	10 km	minutes to hours	Thunderstorms Dust devils	Mesoscale & Large Eddy Simulations (LES)
Micro	2m	seconds	Small eddies Tip vortices	Computational Fluid Dynamics (CFD)

Table 2.1: Scales of the atmosphere, adapted from [Donald Ahrens, 2008, Holton, 2004]

2.2.1 The troposphere

The lowest layer of the atmosphere, the troposphere, extends only to 10-20km above the surface yet accounts for around 80% of the mass of the atmosphere [Pidwirny and Jones, 2010]. It is this thin layer is most important for weather and climate, and it is a tiny fraction of the energy contained in this layer which is harnessed for wind generation.

The troposphere is largely transparent to incoming short wave solar radiation, and is mainly heated by convection and radiation from the ground. Apart from the air immediately above the surface, or where water vapour is condensing, processes in the troposphere are close to adiabatic. Due to this convective heating, the troposphere is relatively well-mixed vertically, with declining temperature with height. This is in marked contrast to the stratosphere above, where increasing temperature with height inhibits vertical mixing, leading to the highly stratified structure which gives it its name.

The boundary between the troposphere and the stratosphere is the tropopause. Stratospheric processes and stratosphere-troposphere interaction are also important drivers of weather systems and global circulation [Butchart et al., 2011], and most atmospheric models place their upper boundary somewhere in the stratosphere, typically at a pressure of 50hPa or less.

2.2.2 General circulation

The flow in the lower atmosphere shows distinct global patterns, referred to as the general circulation, and described in any meteorology text e.g. [Holton, 2004, Martin, 2006]. A very brief and simplified overview is that differential heating between the tropics and the polar regions gives rise to large convective cells, which transport warm air poleward from the equator. Areas where warm air rises in these cells lead to zones of generally low surface pressure with frequent rainfall; areas where air is sinking correspond to zones of high pressure and low rainfall. Since the Earth is a rotating reference frame, the poleward moving air in these cells is acted on by an apparent force, the Coriolis force, which gives rise to the bands of easterly and westerly winds, shown in Figure 2.1. Additionally, the distribution of land and ocean produce semi-permanent continental pressure systems such as the Siberian high, an area of cold, dense, dry air which forms over much of northern Eurasia, and the Icelandic low, a region of low pressure in the Atlantic ocean.

The UK lies roughly at the polar front, the boundary of two convection cells, where warm air from the tropics meets colder polar air. The temperature difference between these air masses causes a pressure gradient at height, which leads to the jet stream. The course of the jet stream meanders and changes, perturbed by a succession of planetary-scale westward moving *Rossby waves*, and is influenced by continental and synoptic pressure systems. The position of the polar front and the jet stream is a major influence of the weather at mid latitudes.

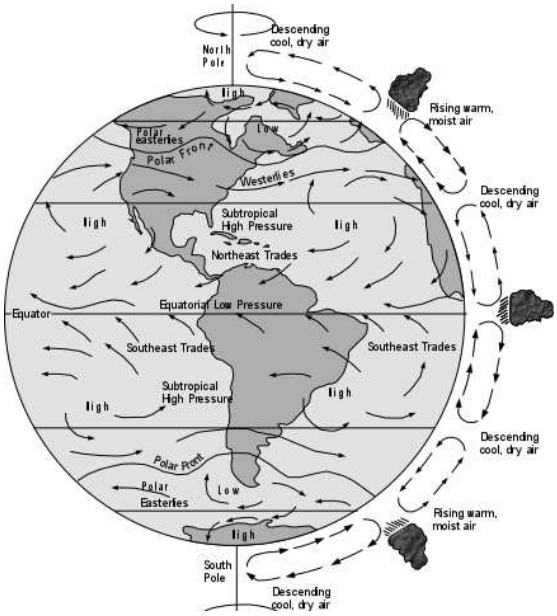

Figure 2.1: General circulation. Public domain image from `http://rst.gsfc.nasa.gov/Sect14/Sect14_1c.html`

The dominant weather feature at these latitudes is the mid-latitude cyclone or depression. Initial instabilities or waves in the polar front cause cold air to be pulled southward and warm air northward around a deepening area of surface low pressure known as a depression. The fronts circle the depression, and the system begins to dissipate when the cold front catches and occludes the warm front. The location of the jet stream and the frequent passage of depressions across the UK is the major reason for the high wind speeds.

Conversely, conditions which alter the usual position of the jet stream and the path of depressions across the UK, such as ‘blocking high’ patterns, can lead to much lower wind speeds than average. Thus, depending on the prevailing conditions, individual months, years, and decades can show a significant amount of variation from the average.

2.2.3 Turbulence and the spectral gap

Observations of the surface wind field show a *spectral gap*, Figure 2.2. That is, a clear separation is observed between slower synoptic scale processes and faster turbulent processes. In the equations which describe atmospheric motion, this allows a convenient separation into explicitly resolved mean fields and parameterised turbulent processes. *Reynold’s averaging* is the technique of decomposing variables into slowly varying average fields and rapidly varying,

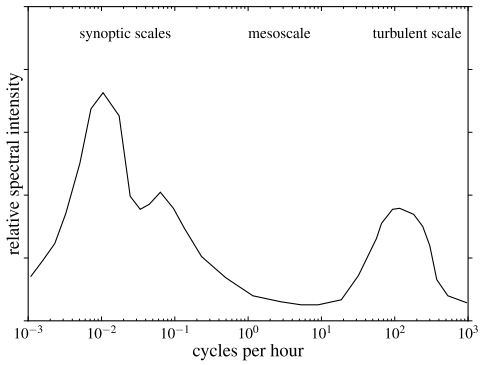

Figure 2.2: Schematic representation of the observed spectral gap in the surface wind. After [Stull, 1988]

zero-mean turbulent fields:

$$\phi = \bar{\phi} + \phi' \tag{2.1}$$

Where ϕ is any of the atmospheric variables: wind speed, temperature etc. By definition, the mean $\bar{\phi'} = 0$. The over-bar on the average terms is usually omitted.

Turbulence is often quantified as a *turbulence intensity*, I. This is the standard deviation of horizontal wind speed over a sampling window, normalised by the mean wind speed over the sampling window [Petersen et al., 1998]:

$$I = \frac{\sigma_u}{\bar{U}} \tag{2.2}$$

For neutral conditions over flat terrain, turbulence intensity might be around 8% over the open sea, 13% over flat grassland, and 20% or more over complex or rough terrain [Petersen et al., 1998]. Turbulence intensity is sensitive to the sample rate and averaging window used; generally the aim is to ensure the mean wind speed corresponds to the left of the spectral gap, while I gives a measure of the fluctuations on time scales to the right of the spectral gap. Hence, sampling every minute or less, and averaging over 10 minutes to one hour is common.

2.3 Atmospheric modelling

Atmospheric modelling grew out of the desire to predict the weather. The idea that this could be achieved by numerically integrating a set of equations dates back over one hundred years [Lorenz, 2006], but was only made possible with advent of the computer. Since then the need for more accurate weather forecasting as well as the desire to understand the global climate has lead to an enormous development of numerical models with an enormous number of applications. Lorenz [2006] gives a review of the history and development of atmospheric models and numerical weather forecasting.

2.3.1 Primitive equations

The basis for all atmospheric models is a set of *primitive equations* imposing conservation of mass, momentum, and energy on the motion of the atmosphere, related by the equation of state. The primitive equations are simplified through various assumptions, for example molecular viscosity is neglected since this is negligible at large scales. In addition, since the transport and transformation of water is so important to weather and climate, equations describing the continuity of moisture are introduced. The development of the primitive equations is covered in any fluid mechanics text e.g. [Douglas et al., 2005].

Although most climate and Numerical Weather Prediction (NWP) models are based on a very similar set of primitive equations [Warner, 2011], they can differ significantly in the simplifying assumptions made e.g. whether or not they are coupled to an ocean model, how the equations are cast, the vertical and horizontal coordinates used, and the numerical schemes used to integrate them.

The primitive equations are a set of non-linear partial differential equations which cannot be solved analytically, and are integrated numerically instead. They govern atmospheric motion at all scales from the global down to local turbulence. However, it is infeasible to resolve all scales of turbulent motion in a global model and different classes of model have evolved to suit each scale, which make different sets of simplifications to suit the scale of the domain.

2.3.2 Global

General Circulation Models (GCMs), are the primary tool for understanding global weather systems in the long term, and are used extensively in climate change research. They recreate many of the features of the global atmosphere very well, and are often coupled to models of ocean circulation and biological systems to give a more complete understanding of the biosphere. A large advantage of a global model is that since they represent the whole globe, there is no need to specify lateral boundary conditions. This enables weather forecasts to be run for several days or weeks, and climate forecasts to be run indefinitely.

However, GCMs are computationally intense due to their very large domain, and resolution is limited even on the most powerful supercomputers. GCMs tend to be spectral models, with an equivalent grid spacing of around 0.5° or more, and are therefore unable to resolve many local features of the wind climate. However, higher resolution GCMs are being deployed, including mesoscale-resolving global models [Shen et al., 2006], and there an increasing convergence between GCMs and mesoscale models.

2.3.3 Mesoscale

Mesoscale models are a class of atmospheric model designed to study weather phenomena smaller than synoptic scale but larger than microscale [Mass and Kuo, 1998]. Typically they are used to study regions of the order of tens to hundreds of kilometers, and are used over a much shorter timescale than GCMs: predicting weather conditions a few days ahead, rather than climate forecasts over decades. They solve an expanded set of equations compared to GCMs, and are usually non-hydrostatic since many of the features of interest, e.g. convective storms, require vertical motion to be a prognostic variable. They usually have more detailed schemes to represent cloud processes, surface exchanges, and turbulent fluxes in the the Planetary Boundary Layer (PBL).

Although they have been an important part of weather forecasting for at least twenty years [Mass and Kuo, 1998], it is only in the last decade that computing power and the availability of global gridded datasets for boundary conditions has enabled their use outside of a few national centres. A review of mesoscale models in relation to wind energy is given in Section 3.2.

2.3.4 Sub-meso scale

Mesoscale models are run over a wide range of grid spacings, sometimes below 1km. However, at scales much below this, the models begin to resolve some of the largest turbulent eddies, and may need a different approach to separate resolved and unresolved turbulence.

Large Eddy Simulation (LES) models are the term given to this class or application of a model, where the largest of the energy carrying turbulent eddies are resolved explicitly. LES models may give a more realistic profile through the PBL since they explicitly model turbulent eddies, rather than rely on semi-empirical parameterisation schemes. They also capture turbulent fluctuations on short timescales. However, the resolution is too high to allow simulation of large domains, and it is more difficult to cleanly separate resolved and unresolved turbulence.

2.3.5 Microscale

Microscale models of wind flow can be broadly split into two categories: linear and non-linear.

Non-linear microscale models fall in the domain of Computational Fluid Dynamics (CFD), which are based on the full Navier-Stokes equations. The term Computational Fluid Dynamics comes from engineering, and has come to mean models applicable at this particular scale, even though all atmospheric modelling involves computation of fluid dynamics.

There are a large array of CFD models depending on what simplifications are made to the primitive equations, how space and time are discretised, whether Reynold's averaging is used, and what numerical methods are applied to integrate the equations. Typically CFD models are used to study the detailed interaction of fluid with other objects, e.g. the flow past a turbine blade, or the wake caused by a single turbine, and have a grid mesh on the order of centimetres. As a result, most CFD models are too computationally intense to be used across large domains, although there is an overlap between CFD and mesoscale models, and recently there have been some models developed specifically with wind power analysis in mind see e.g. [Castro et al., 2003, Undheim, 2005].

Linear flow models, such as the widely used Wind Atlas and Application Program (WAsP) [Troen et al., 2008], largely developed out of a need to resolve the effects of microscale features (small hills, obstacles, changes in roughness, etc) on the average flow, in a manner which did not require the intense computation of a CFD model. Typically they model a steady state,

incompressible flow using linearised equations to conserve mass and momentum. The big advantage is computational speed, which allows them to be run over much larger domains than non-linear models. The disadvantage is the linearised equations are a simplification which cannot represent complex flow, such as flow separation and re-circulation in the lee of steep hills [Bowen and Mortensen, 1996, 2004].

2.4 Nesting and downscaling

Downscaling is the method of relating the output of large, coarse resolution models to smaller scale, higher resolution ones. There are two main approaches: direct nesting and statistical dynamical downscaling.

Statistical dynamical downscaling begins from the assumption that the large scale weather system for a particular area can be characterised by a limited number of different weather types or episodes. The first step is to define these episodes and to calculate how often they occur. This is usually done by analysing multi-year time series output from a GCM. Higher resolution regional models are then run to determine the local wind conditions during that type of episode. Then, based on the frequency of each episode, the overall wind conditions can be derived statistically.

The first use of downscaling to assess wind conditions was published by Wippermann and Gross [1981], while Heimann [1986] used the approach to derive a two dimensional array of wind roses describing a region. Frey-Buness et al. [1995] was the first to use the method in conjunction with the output of GCMs in order to study the effects of predicted warming in the Alpine region. The method was also applied by Mengelkamp [1997], and further refined by Fuentes [1998]. Fuentes and Heimann [2000] gives more details on the development and application of this approach.

The advantage of statistical downscaling is that it reduces the amount of modelling required to arrive at long-term statistics describing the wind climate. The accuracy of such an approach depends on the accuracy of both the larger model and the smaller regional model. Accuracy is limited by the representation of weather by a finite number of episodes which may miss the tails of the wind speed distribution and miss extreme but important events e.g. very high winds or exceptionally calm periods.

The other approach, becoming more common with increasing computing power, is to directly nest models within each other, for example, using a GCM to drive a mesoscale model, or using a mesoscale model to drive a CFD model or microscale flow model.

2.5 Scale selection

Returning to the criteria listed in the introduction to this chapter, the aim is to produce a dataset which can realistically represent wind speeds over the UK and offshore for a period of ten years or more, but has high enough resolution to capture important features of the wind climate such as the interaction with terrain and coastal processes.

Based on these criteria and the discussion above, the most relevant scales are the synoptic down to the mesoscale. It would be unnecessary to run a global model simply to look at the UK, when global reanalysis datasets already exist, and it would be infeasible to run a microscale model over a domain this large. Therefore the most appropriate approach is to use a mesoscale model on a regional domain covering the UK and surrounding waters.

This choice means that only the steady terms of Eq. 2.1 will be resolved, that is, wind speed changes on the timescales of several minutes to hours, not higher frequency turbulent fluctuations on timescales of seconds. Although higher frequency turbulent fluctuations are important considerations for wind energy, impacting on power system stability, mechanical loading, power quality and many other areas, they are outside the scope of this work.

However, the net effect of turbulence is very important on the wind speed profile close to the surface. Since the hub-heights of wind turbines are up to 100m, boundary-layer processes are very important for accurately modelling wind speeds at this height. To give some background to later discussions, the following sections briefly introduce planetary boundary layer theories, and how they are dealt with in atmospheric models.

2.6 Planetary boundary layer

The Planetary Boundary Layer (PBL) is defined by Stull [1988] as

> "the part of the troposphere that is directly influenced by the presence of the

> Earth's surface, and responds to surface forcings with a time scale of about an hour or less."

The defining characteristic of the PBL is the presence of turbulence. The no-slip condition at the surface means that whenever the wind blows, a wind shear exists driving mechanical turbulence, while the heating of the ground surface by solar radiation causes convective turbulence. The result is a well-mixed layer where potential temperature and humidity are almost constant with height.

By contrast, in the *free atmosphere* above, the flow is rarely turbulent, vertical mixing is much less, and there is a clearly defined vertical profile of potential temperature and humidity.

In the PBL, turbulent eddies cause vertical mixing of momentum, temperature and other variables. As discussed previously it is infeasible to resolve these turbulent eddies explicitly in synoptic or mesoscale models. In the free atmosphere, the turbulent terms are small in relation to mean flow and can be ignored. However in the PBL their influence on the mean flow must approximated through a parameterisation scheme.

The vertical mixing of horizontal momentum, the momentum flux, can be described by an equivalent shear stress known as the *Reynold's stress*, τ_r. The magnitude of Reynold's stress due to the vertical (z) transport of horizontal (x) momentum is given by Stull [1988]:

$$\tau_{xz} = -\rho(\overline{u'w'}) \tag{2.3}$$

where u' and w' are the horizontal and vertical fluctuations associated with turbulent motion, and ρ is air density. The total vertical flux of horizontal momentum is then given by:

$$|\tau_r| = \left[\tau_{xz}^2 + \tau_{yz}^2\right]^{1/2} \tag{2.4}$$

The magnitude of the Reynold's stress is an important scaling variable for surface wind speeds, and is usually expressed as a velocity scale, the friction velocity, u_*, defined by the size Reynold's stress vector [Stull, 1988].

$$u_*^2 = \frac{|\tau_r|}{\rho} \tag{2.5}$$

Although it is usually assumed that τ_r is parallel to the mean wind vector, this may not hold in complex terrain [Weber, 1999]. The friction velocity can be expressed as:

$$u_*^2 = \sqrt{\overline{u'w'}^2 + \overline{v'w'}^2} \tag{2.6}$$

Boundary layer theories are usually based on *mixing length* arguments. Turbulent eddies are treated as 'units' which travel an average mixing length, l, before imparting their momentum to the mean flow, analogous to the mean free path in the kinetic theory of gases. The mean wind profile for a homogeneous and stationary flow can then be related to the momentum flux by:

$$\frac{\partial u}{\partial z} = \frac{u_*}{\kappa l} \tag{2.7}$$

where κ is the Von Karmann constant, an empirical constant usually taken to be 0.4 [Andreas et al., 2006]. The challenge is to find expressions for a length scale, which may depend on the depth of the boundary layer, height above the surface, atmospheric stability and other factors.

2.6.1 Closure schemes

Eq. 2.6 contains double correlation, or second moment, terms, $\overline{u'w'}$ and $\overline{v'w'}$. The inclusion of turbulent terms means there are more variables than prognostic equations, and additional relations are needed to close the equation set. If prognostic equations are developed for the second moment terms, they are found to contain third moment terms e.g. $\overline{u'u'w'}$, and so on. This is the *closure problem* [Stull, 1988, Warner, 2011]. Additional, diagnostic equations are needed to close the set of equations, and the assumptions on which these are based are called closure assumptions. Closure schemes are usually categorised by their order [Warner, 2011]: if the second moment terms are parameterised in terms of the mean variables, the scheme is a first order closure scheme. If the third moment terms are parameterised in terms of the second and first, the scheme is second order. The order of a closure scheme is given by the highest-order prognostic equations retained. However in some closure schemes, some of the higher order terms may be parameterised and others predicted. In this case the order of the closure scheme may be given a non-integer order e.g. 2.5 [Warner, 2011]. For example, the simplest simple first-order closure is:

$$u'w' = -K\frac{\partial u}{\partial z} \tag{2.8}$$

Where K is known as the eddy viscosity coefficient, or the exchange coefficient, and this type of closure is known as K-theory [Brown, 1981]. Higher order closure schemes will have a more complex expression for Eq. 2.8.

The other aspect of a closure scheme is whether only adjacent grid points in the vertical are used, known as *local closure*, or whether grid points further away in the vertical are considered, a *non-local closure*. Physically, a local closure scheme assumes that turbulent eddies have a vertical length scale comparable to the models vertical spacing, so that mixing only occurs between adjacent levels, while in non-local closure schemes, vertical mixing can occur between non-adjacent vertical levels.

2.6.2 Atmospheric stability

Atmospheric stability describes whether an air parcel will continue to rise or return when displaced vertically. This is governed by the *lapse rate*, the rate of change of temperature with height.

The dry adiabatic lapse rate, Γ_d, is the rate of change of temperature that a dry air parcel would experience if it rose adiabatically through an atmosphere in hydrostatic equilibrium [AMS, 2000]. The moist adiabatic lapse rate, Γ_w is the rate of change of temperature a saturated parcel of air would experience, accounting for the latent heat of condensation [AMS, 2000]. The actual lapse rate, or environmental lapse rate, Γ_e, is simply the observed temperature change with height. This varies day to day around an average value of -6.5K/km [Martin, 2006].

A dry parcel of air displaced upward will experience a lower pressure, expand and cool. If $\Gamma_e < \Gamma_d$, the parcel will be cooler and denser than its new surroundings and will sink. The atmosphere is said to be absolutely stable, and vertical motion is damped. If $\Gamma_e = \Gamma_d$, there will be no net buoyancy force, the parcel will remain at its new height. The atmosphere is said to be neutral: vertical mixing occurs, but free convection does not develop. If $\Gamma_e > \Gamma_d$, a rising parcel of air will be warmer than its surroundings and will continue to rise, and the atmosphere is said to be absolutely unstable. Free convection will develop leading to rapid vertical mixing, which tends to bring the atmosphere back towards neutral.

If the air contains water vapour, and $\Gamma_e > \Gamma_w$, then the parcel will rise and cool at the rate of Γ_d, until it reaches the dew point and clouds begin to form. In general, it will continue to rise until all of the moisture has condensed, and its stability is thereafter determined by the environmental lapse rate above this level.

In an unstable (convective) boundary layer, convection dominates turbulence creation, and the PBL can grow to a depth of several kilometres. This is typical in tropical and mid-latitudes during the daytime, but can also occur when cold air advects over a warm surface, such as offshore winds when the sea is warmer than the land.

In a stable boundary layer, vertical motions are damped and any turbulence is driven by the wind shear between the free atmosphere and the surface. A stable boundary layer is typical at night when the ground surface is cooling, or when warm air is advected over a cold surface. An inversion often separates the stable layer from the atmosphere above, and the flow above the stable layer can become decoupled-coupled from the surface, such as with the formation of low level jets [Smedman et al., 1996].

Stability was first classified by Pasquill [1974] according to insolation and wind speed; Pasquill stability classes are shown in Table 2.2.

Stability class	Typical occurrence conditions
Stable	Low wind speeds, nocturnal, or warm air advecting over colder surface
Slightly stable	
Neutral	High winds and overcast skies
Slightly unstable	
Unstable	High insolation, or cold air advecting over a warm surface

Table 2.2: Pasquill stability classes

There are variety of more objective approaches to determining stability, see e.g. Golder [1972]. A commonly used approach used the Obhukhov length, L, defined as [AMS, 2000]:

$$L = -\frac{u_*^3 T_v}{g\kappa\overline{w'\theta_v'}} \tag{2.9}$$

where, T_v, is virtual temperature, and $\overline{w'\theta_v'}$ is the flux of virtual potential temperature at the surface. L can be interpreted as a length scale describing the height below which shear production dominates over buoyant production of turbulence [AMS, 2000]. It is often combined with the height above the surface z as a *dimensionless stability parameter*:

$$\zeta = \frac{z}{L} \tag{2.10}$$

A number of slightly different mappings between L or ζ and stability class exist in the literature e.g. [Gryning et al., 2007, Hsu, 1992, Peña et al., 2008, Yague et al., 2006]. The approach used here is taken from Gryning et al. [2007] and summarised in Table 2.3. Figure 2.3 shows a schematic representation of these stability class boundaries in relation to ζ and L.

Obukhov length interval (m)					Stability class
10	$\leq$	L	$\leq$	50	Very stable
50	$\leq$	L	$\leq$	200	Stable
200	$\leq$	L	$\leq$	500	Near stable
		$\|L\|$	$\geq$	500	Neutral
-500	$\leq$	L	$\leq$	-200	Near unstable
-200	$\leq$	L	$\leq$	-100	Unstable
-100	$\leq$	L	$\leq$	-50	Very unstable

Table 2.3: Stability class boundaries from [Gryning et al., 2007]

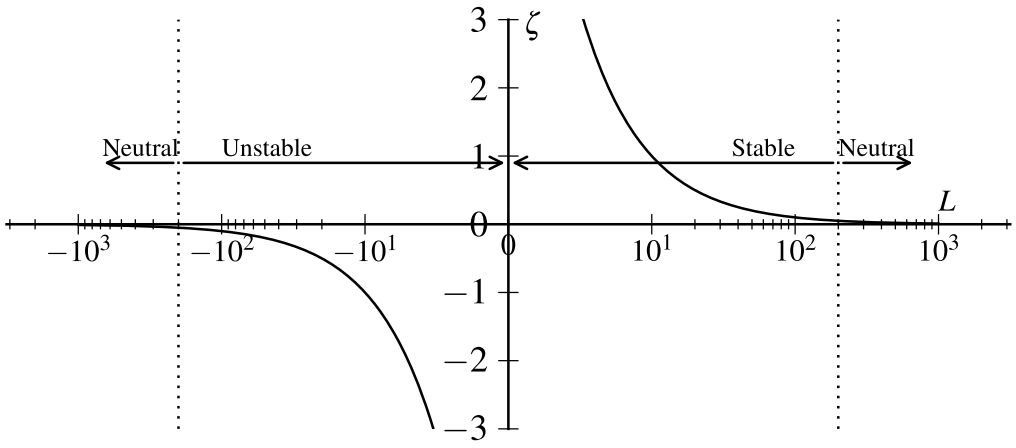

Figure 2.3: Schematic representation of stability classes according to Obhukhov length L, and ζ for $z = 10m$. x-axis is shown with a log scale

2.6.3 The surface layer profile

The lowest part of the PBL is known as the *surface layer*, typically defined as the region where fluxes vary by less than 10% of their magnitude with height [Stull, 1988], and is often assumed to be about 10% of the PBL height. Surface drag means wind speeds in the surface layer are typically much lower than geostrophic speed.

Monin and Obukhov [1954] developed a theory describing the wind speed profile in the surface layer, known now as Monin-Obhukov Similarity Theory (MOST). MOST is based on the assumption that the momentum flux in the surface layer, u_* is approximately constant with height, so that local fluxes at a height z can be taken as equal to the surface flux [Gryning et al., 2007, Peña et al., 2008]:

$$u_* = u_{*0} \tag{2.11}$$

The mixing length in the surface layer, l_{SL} is assumed to be a function only of the height above the surface, z, and the atmospheric stability:

$$l_{SL} = \frac{z}{\phi_m(\zeta)} \tag{2.12}$$

Where ϕ_m is known as a *stability correction function*. Various formulations of ϕ_m exist based on field experiments, see e.g. [Dyer, 1974, Garratt and Pielke, 1989, Hogstrom, 1988], though most find a power-law dependence [Peña et al., 2008]:

$$\phi_m = \begin{cases} \left(1 - a\frac{z}{L}\right)^p & \text{unstable} \\ 1 & \text{neutral} \\ \left(1 + b\frac{z}{L}\right) & \text{stable} \end{cases} \tag{2.13}$$

For unstable conditions, there is reasonable consensus that $p = -1/4$ and $a = 16$, see e.g. Garratt and Pielke [1989] for a review. For weakly stable conditions, a range of values are reported for b, from 4.6 to 9.4 [Garratt and Pielke, 1989, Yague et al., 2006], and other other functional forms or various extensions have been proposed to account for strongly stable conditions [Beljaars and Holtslag, 1991, Hicks, 1976, Sharan, 2009].

Combining equations 2.7 and 2.12:

$$\frac{\partial u}{\partial z} = \frac{u_* \phi_m}{\kappa z} \tag{2.14}$$

The height at which the wind profile is equal to zero is known as the roughness length, z_0, and is described further §2.6.4. Integrating from z_0 to a height z, gives the surface wind profile:

$$u = \frac{u_*}{\kappa}\left[ln\left(\frac{z}{z_0}\right) - \Psi_m\left(\frac{z}{L}\right)\right] \tag{2.15}$$

where Ψ_m is the integrated stability correction function, which is related to Φ_m by [Garratt and Pielke, 1989]:

$$\Psi_m = \int (1 - \phi_m(\zeta))d(ln(\zeta)) \tag{2.16}$$

In neutral conditions $\psi_m = 0$ and 2.15 reduces to:

$$u = \frac{u_*}{\kappa} ln\left(\frac{z}{z_0}\right) \tag{2.17}$$

This is often known as the adiabatic wind profile, or just the logarithmic wind profile, since the wind speed varies with the natural log of height. It is widely used within the wind industry, as the atmosphere is neutral on average, and therefore it is often a good approximation to the surface layer profile.

To account for atmospheric stability, Eq. 2.13 must be integrated. Under (weakly) stable conditions, Eq. 2.13 can be integrated to [Panofsky and Dutton, 1984]:

$$\psi_m(\zeta) = -b\zeta \tag{2.18}$$

where b has the same uncertainty described previously. In unstable conditions, the integrated form of Eq. 2.13 depends on the value of the constants, but the form most often found in the literature is [Paulson, 1970]:

$$\psi_m(\zeta) = ln\left[\left(\frac{1+x^2}{2}\right)\left(\frac{(1+x)^2}{2}\right)\right] - 2tan^{-1}x + \frac{\pi}{2} \tag{2.19}$$

where

$$x = (1 - 16\zeta)^{1/4}$$

The particular forms of the stability correction functions (Eq 2.18-2.19) are often collectively

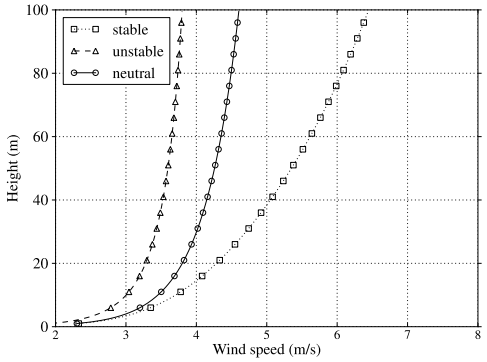

Figure 2.4: Surface layer wind profiles under different stability classes.

known as the Businger-Dyer formulations after [Businger, 1988, Businger et al., 1971, Dyer, 1974, Skibin and Businger, 1985].

MOST is only valid at sufficient height that the surface can be regarded as homogeneous with a single roughness length. As most atmospheric models have their lowest level around 20m or so, and may diagnose wind speed at 10m, this is not a problem over relatively smooth surfaces such as grassland or lows crops. However, over rough terrain such as forestry or cities, this layer will be in the *roughness sub-layer*, where the effects of individual roughness elements are significant, and MOST may not be valid Hsu et al. [2009].

2.6.4 Roughness length

The roughness length is the height at which the logarithmic profile observed in the surface layer tends to zero. If observations are available at multiple heights in the surface layer, then the wind profile can be determined and the local roughness length estimated directly. Alternatively it can be estimated from observations at one height using gust information [Manwell et al., 2002a].

Roughness length is found to be related to the typical lengths of obstacles or vegetation. Davenport [1960] first classified roughness lengths according to land use, and the classification has been subsequently updated [Davenport et al., 2000, Wieringa, 1993, Wieringa et al., 2001]. Table 2.4 gives some typical values. However, over non-homogeneous or very rough surfaces, there is large uncertainty when assigning a single roughness length.

Roughness length is the main determinant of momentum flux in the surface layer, and the sole determinant in neutral conditions [Beljaars and Holtslag, 1991]. It is source of inaccuracy

Class	Terrain Description	z_0 m
Sea	Open sea or lake	0.0002
Smooth	Featureless land surface i.e. sand, snow.	0.005
Open	Level country with low vegetation i.e. grass	0.03
Roughly open	Cultivated area with high crops	0.25
Rough	Low, densely planted vegetation. Trees and occasional buildings	0.5
Very rough	Forests, small towns and suburbs	1.0
Skimming	City centres, large forests.	> 2

Table 2.4: Davenport roughness categories [Wieringa et al., 2001].

for atmospheric models, as scaling theories assume a homogeneous surface. An effective roughness length for an entire grid cell must be estimated, which in reality will cover inhomogeneities in land use. In addition, and sub-grid scale terrain features exert form drag, and this must also be accounted for in roughness length [Beljaars and Holtslag, 1991].

2.6.5 Offshore and coastal boundary layer

Much of boundary layer theory has been developed based on experiments over land. It is only relatively recently, in particularl with interest in offshore wind generation, that more attention has been paid to offshore and coastal boundary layers. At the coast, the sharp change in characteristics between the sea and land breaks any assumptions of horizontal homogeneity, and the sharp change in roughness and temperature causes internal boundary layers to grow [Mortensen et al., 1990, USNRC, 1992].

USNRC [1992] recommended a complete re-examination of boundary layer processes in the coastal zone including " surface and boundary layer scaling theories, higher order moment relationships throughout the PBL, and the relative importance of turbulent vs coherent motions", and Peña et al. [2008] states our understanding of the processes in the marine boundary layer is "particularly immature".

Most atmospheric models derive surface fluxes using empirical stability correction functions developed over land. In addition, the sea surface roughness is usually assumed only to depend on the instantaneous surface momentum flux, and the effect of humidity flux on stability is usually ignored, despite its significance offshore [Barthelmie et al., 2009].

However, Vickers and Mahrt [2006] note that despite many of these assumptions not holding in the coastal layer, there is often no viable alternative, and mesoscale and other atmospheric

models remain a useful tool, and are able to recreate many features of the marine and coastal boundary layer. This is underscored by their growing use, e.g. for offshore wind resource assessment.

Sea surface roughness

In general, the sea surface is much more aerodynamically smooth than land. However, the surface roughness is not static, but depends on wave conditions. This must be represented in atmospheric models, and is particularly important in coupled atmosphere-ocean models where the momentum flux is a major driver of ocean currents, and hence a large influence on weather and climate. Wind flow over the ocean is often modelled as two regimes: a 'smooth' regime where the main driver of surface exchange is the viscous sub-layer, and a 'rough' regime where the effect of waves dominate [Janjic, 1994].

Charnock [1955] first proposed that surface roughness due to waves depends on the surface stress and the restoring force:

$$z_0 = \frac{\alpha_c u_*^2}{g} \tag{2.20}$$

where α_c is an empirically derived constant. α is often taken to be 0.018 in the open ocean [Hersbach, 2011], however, it has long been known that a single value of α cannot describe all the experimental data [Drennan et al., 2005]. A wide range of values between 8×10^{-3} and 6×10^{-2} are found in the literature [Peña and Gryning, 2008].

This spread has been explained by various modifications to the basic Charnock equation to account for wave fetch [Lange et al., 2001], wave age and steepness [Drennan et al., 2005, Lange et al., 2004]. However, there is still no consensus, and several recent studies approaches have proposed fundamental re-examinations of the basic relationships [Foreman and Emeis, 2010, Vickers and Mahrt, 2010]. For example, Vickers and Mahrt [2010] found roughness lengths much smaller than formulations commonly used in atmospheric models, based on several recent sets of observation from mid-latitude coastal regions. They found no evidence for a smooth flow regime and proposed an empirical relation for surface roughness very different to a Charnock formulation.

Without detailed information about the wave state, and without any consensus on the relation between roughness and wave state, assuming a constant $\alpha_c = 0.018$ is currently the only

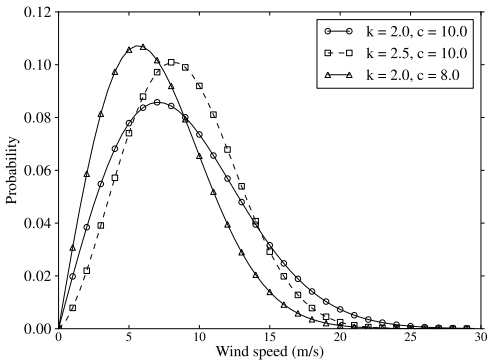

Figure 2.5: Examples of Weibull distributions with different parameters

feasible approach for most models.

2.7 Wind speed distributions

The observed distribution of surface wind speeds at a particular location is often found to be a two-parameter Weibull distribution [Manwell et al., 2002a]. The Weibull probability density function $f(x)$ and cumulative distribution function $F(x)$ are given by:

$$f(x) = \frac{k}{c}\left(\frac{x}{c}\right)^{k-1} exp\left[-\left(\frac{x}{c}\right)^{k}\right] \tag{2.21}$$

$$F(x) = 1 - exp\left[-\left(\frac{x}{c}\right)^{k}\right] \tag{2.22}$$

where k is a dimensionless shape parameter and c is the location parameter with the same units as x. k determines how 'peaked' the distribution is. For a given mean wind speed, a higher value of k implies less distribution around the mean speed. Figure 2.5 shows the effect of different parameters on the distributions shape.

There are a number of different ways of fitting Weibull parameters to observed data [Manwell et al., 2002a], with maximum likelihood generally thought to be the most robust [Chang, 2010]. The maximum likelihood method is used throughout this work.

2.8 Chapter review

This chapter introduced some background material on the atmosphere, and the separation of atmospheric process by scale. It briefly reviewed the classes of atmospheric model by their target scale, and selected mesoscale modelling as the technique to use for this work. The importance of boundary layer processes was highlighted, and a brief discussion of PBL theories was presented to give some context to future discussions. Some of the inherent challenges of the marine and coastal boundary layer were highlighted. Finally, the Weibull distribution commonly used to describe wind speed distributions was presented.

The next chapter reviews available mesoscale models in more detail, and will refer to the theories outlined here.

Chapter 3
Modelling approach

3.1 Introduction

The previous chapter gave some theoretical background, and justified the use of a mesoscale model as the primary tool for this work. This chapter presents a review of alternative mesoscale models, to explain the choice of the Weather Research and Forecast (WRF) model for this work. WRF is then explained in more detail, and the strengths and limitations are discussed.

3.2 Comparison of alternative models

There are a wide range of mesoscale atmospheric models used in operational forecasting, research, and within industry. Many of them share similar features, though there are significant differences between models. This section briefly reviews some of the available models, before selecting one to be used in this research. A summary of some of these models is also given in [Giebel et al., 2002].

3.2.1 WAsP

The Wind Analysis and Siting Programme (WAsP) is developed by Risø National Laboratory [Troen et al., 2008]. While it is not a dynamic atmospheric model, it is so widely used within industry it has become something of a *de facto* standard, and warrants a brief review here.

WAsP is primarily observation driven: it takes an observed wind speed distribution together with a description of the orography, roughness and obstacles surrounding an observation point, and derives a generalised 'cleaned' wind climate adjusted to a standard height and roughness. This cleaned wind climate can then be used to downscale to a different site in the general vicinity.

This approach can be accurate [Bowen and Mortensen, 1996], provided (i) the reference site and prediction site are subject to the same overall weather regime, (ii) the prevailing weather

Measurement Issues	Insufficient masts to give good spatial resolution Mast measurements typically at 10m agl, and strongly influenced by local orography, roughness, and obstacles No guarantee of data quality Measurements may be effected by the mast configuration Instrument configuration or surroundings may change Sparse observations offshore
Model Issues	Only produces statistical distributions Requires detailed orography and roughness, but cannot handle large maps Assumes a neutral boundary layer Predictions only valid for locations subject to the same prevailing wind climate Manually time consuming for large areas Not well parallelised

Table 3.1: Difficulties using WAsP analysis over wide areas

conditions are close to being neutrally stable, (iii) the reference wind data are reliable, (iv) the surrounding terrain of both sites is sufficiently gentle and smooth to ensure mostly attached flows and (v) the topographical model inputs are adequate and reliable [Bowen and Mortensen, 2004, Frank et al., 2001].

However, this type of approach faces a number of difficulties, summarised in Table 3.1. The major limitation is that, since it is driven by observations, the predicted site must be subject to the same weather conditions as the observations. This limits the distance over which WAsP can be used, as there are a large number of features such as low-level jets, sea breezes, katabatic winds, etc, which may be significantly different between the observed and predicted site. Furthermore, WAsP assumes a neutral boundary layer, which may be a reasonable assumption when dealing with average distributions, but could lead to large errors during specific periods.

WAsP was designed to allow transformation of wind speed distributions: it is not a dynamical model which can be used to produce time-series. In light of this, and the limitations described above, it is clear it is not well suited to this type of study. That said, Boehme and Wallace [2008] showed that WAsP can be used with surface observations to provide a reanalysis on a national scale, using it to model hourly wind speeds across the whole of Scotland.

3.2.2 MC2

The Mesoscale Compressible Community (MC2) model [Benoit et al., 1997] is a fully compressible, non-hydrostatic mesoscale model developed by a number of academic groups in Canada. It uses a semi-langrangian, semi-implicit integration scheme with time splitting in

order to efficiently integrate acoustic and meteorological modes. The vertical coordinate is a terrain-following pressure-based (σ) coordinate. It has been used for air-quality modelling in complex terrain [Niewiadomski et al., 1999], and for weather forecasting over the entire Alps region [Benoit et al., 2002], although this revealed a spurious sensitivity to orographic forcing, traced to a numerical inconsistency, later fixed [Girard et al., 2005].

MC2 been used to study wind resources across Canada [Glazer and Yu, 2005] driven by NCEP/NCAR reanalysis data and using statistical dynamical downscaling to derive wind climate, with WAsP used to account for small scale terrain features. MC2 has also been used to study offshore and coastal wind climates, with Beaucage et al. [2007] comparing the wind field from MC2 to Synthetic Aperture Radar (SAR) and scatterometer wind speeds from satellites.

MC2 has been combined with the micro-scale model MS-Micro in a commercial package called the Wind Energy Simulating Toolkit (WEST) [Pinard et al., 2005], which it is claimed gives good results. However, the cost of a license is $ 10 000, and ongoing community support appears to be limited. The most recent training programme listed is from 2005 [RPN, 2011].

3.2.3 Eta

The Eta model [Black, 1994, Janjic, 1994, 1996] was mainly developed by the National Center for Environmental Prediction (NCEP). It has been running operationally since 1993, and still runs today [NCAR, 2011]. It was the first model to use the 'step-mountain' vertical coordinate [Mesinger et al., 1988], where mountains are represented in grid-boxes with vertical sides. This reduces errors in the calculation of the pressure-gradient force, and allows it to model well orographic effects, such as blocking and channelling. It uses an explicit integration scheme in the horizontal and an implicit scheme in the vertical.

Eta has been widely used for weather forecasting. It has also recently been used to model the output from wind farms in complex terrain [Lazić et al., 2010]. However, the use of the step-mountain coordinate can make it difficult to model PBL processes over elevated terrain, and can lead to waves forming at step changes in height [Gallus, 2000].

3.2.4 SKIRON

The SKIRON forecasting system was developed at the University of Athens [Kallos, 1997, Kallos et al., 1998, Papadopoulos et al., 2001]. The dynamical core is based on the NCEP Eta model, with modifications and improvements in the parameterisation of various processes such as atmospheric radiation and surface processes. In particular, it is able to model the mobilisation and transport of dust, and the subsequent impact on incoming and outgoing radiation [Kallos and Nickovic, 2001].

It is run operationally at the University of Athens, and has been used to forecast wind energy production using a Kalman filter to further improve the raw model output [Louka et al., 2008]. SKIRON is freely avalilable on request, and documentation is available from the Atmospheric Modeling and Weather Forecasting Group, at the University of Athens.

3.2.5 KAMM

The Karlsruhe Atmospheric Mesoscale Model [Adrian and Fiedler, 1991] is a three dimensional, non-hydrostatic atmospheric mesoscale model, which has been implemented for parallel processing [Adrian, 1999]. It uses a terrain-following pressure-based vertical coordinate.

KAMM was used widely for a time to produce wind atlases in combination with WAsP where the output from KAMM at scales of a few km is used to drive WAsP using a statistical dynamical downscaling approach. This technique has been used to derive wind atlases in a number of countries including Denmark, Ireland, Portugal, and Chile [Frank et al., 2001, Kalthoff et al., 2002]. However, it appears the model must be run as a steady-state model for a range of geostrophic wind speeds and inflow directions [Giebel et al., 2002], rather than a time-series model. Up-to-date documentation on the model is lacking, and it does not appear to be under active development.

3.2.6 MM5

The Fifth Generation Mesoscale Model (MM5) is the most recent in the ‘MM’ series of NWP models developed by Pennsylvania State University and NCA. It is a fully compressible non-hydrostatic mesoscale model, which uses a terrain-following, pressure-based vertical

coordinate.

Research began on these models in the early 1970s [Anthes and Warner, 1978], and they are now widely used in academic research. MM5 has been used extensively in numerical weather prediction, air quality, and hydrological studies e.g. [Mass and Kuo, 1998], both regionally and locally. For example Yim et al. [2007] coupled MM5 with the mass-conserving microscale CALMET model and high resolution terrain and land-use data to produce the hourly wind field at 100m resolution. Jimenez and Tambke [2007] used MM5 to model offshore wind speeds, comparing the predictions from offshore observations and WAsP simulations. However, the development of MM5 is frozen, as it is largely being replaced by the Weather Research and Forecasting Model (WRF).

3.2.7 WRF

The Weather Research and Forecasting modelling system is the most recently developed mesoscale model, produced mainly by National Center for Atmospheric Research (NCAR) with collaboration from the National Oceanic and Atmospheric Administration (NOAA), the National Centers for Environmental Prediction (NCEP) and the Forecast Systems Laboratory (FSL), the Air Force Weather Agency (AFWA), the Naval Research Laboratory (NRL), Oklahoma University, and the Federal Aviation Administration (FAA).

At its core, WRF is a fully compressible non-hydrostatic mesoscale model, which uses an explicit time-split integration scheme, with different time-steps for meteorological acoustic modes. It actually support two dynamical solvers: the Advanced Research WRF (ARW) [Klemp et al., 2008b] developed and maintained by NCAR, and the Non-hydrostatic Mesoscale Model (NMM) [NCEP, 2008], developed by NCEP and mainly used for operational forecasting. The model architecture is described in more detail in a further section. It owes a significant amount to MM5, though WRF has been entirely re-written to be a flexible, portable model, efficient in a massively parallel computing environment with advanced data assimilation techniques.

The success of WRF has largely come from its design as a community model, with dedicated support and training provided by NCAR, and the encouragement of user contribution to physics and other parameterisation packages. It has been widely adopted among academic groups due to its relative ease of use and flexibility, coupled with advanced data assimilation capabilities.

It is also used in industry, forming the basis of a number of commercial modelling packages.

WRF is run operationally for North America at both NCAR and NCEP, and also at a wide number of academic institutions (see [WRF, 2011]), including an operational run in the UK by the National Centre for Atmospheric Science (NCAS).

It has been used in academic studies to numerous to catalogue here; these include as a regional climate model [Bukovsky and Karoly, 2009], combined with WAsP for wind energy assessment [Berge and Bredesen, 2007], for modelling large scale grid integration [Brower, 2010, Ploski, 2007, Potter et al., 2008], as an LES model to examine the detailed flow around wind farms [Liu et al., 2011], to study the impact of Low-Level Jets (LLJs) on wind power [Storm, 2008], to study the marine boundary layer [Berge et al., 2009, Sood and Suselj, 2006]. A search on the Science Direct database lists 240 papers using WRF in 2011 alone.

3.2.8 COAMPS

The Coupled Ocean/Atmosphere Mesoscale Prediction System (COAMPS) [NRL, 2003] is used and developed by the US Navy for short term numerical weather prediction. As the name suggests, it can be run in coupled mode with an ocean model, and the atmospheric model solves the compressible, non-hydrostatic equations using an explicit time-split integration scheme. The vertical coordinate is a terrain-following sigma coordinate. The model includes a 3D data assimilation package, which allows the assimilation of ocean observations. As such, COAMPS is well suited to ocean-atmosphere studies and long-range forecasts, and is reasonably widely used in this field e.g. [Doyle et al., 2009, Kong, 2002]. There is support and training provided for COAMPS, although the user base is smaller than WRF or MM5. However, for a reanalysis, using a coupled ocean model may not be necessary when observed SST datasets can be used as the lower boundary of a non-coupled model.

3.2.9 RAMS

The Regional Atmospheric Modeling System (RAMS) is a flexible mesoscale model developed at Colorado State University [Cotton et al., 2003, Tremback and Walko, 2005], largely by Dr. William Cotton and Roger Pielke. RAMS supports two-way and moveable nests for the tracking features such as hurricanes [Tremback and Walko, 2005]. RAMS uses a terrain-following sigma coordinate in the vertical, and uses time-split explicit integration

scheme similar to WRF and MM5.

RAMS has been used in studies too numerous to list here. These include for operational NWP, for example at the University of Athens [2011] for regional climate studies [Liston and Pielke, 2000], for air quality modelling [Chandrasekar et al., 2003, Pilinis et al., 1994], and to study mesoscale features such as LLJs [Liu et al., 2006], and katabatic flow and mountain waves [Poulos et al., 2007]. Since there is no lower limit to the domain size or the mesh cell size of the grid, high resolution studies have used RAMS to study microscale phenomena such the turbulent flow over buildings [Cermak et al., 1995], and the flow over vegetated hills [Paiva et al., 2009].

The code is freely available and RAMS has a reasonable user base with an active forum. However the most recent user workshop appears to have been in 2006, and there are no regular training courses.

3.2.10 HIRLAM/HARMONIE

The High Resolution Limited Area Model (HIRLAM) is a synoptic scale model developed by a broad collaboration of European meteorological institutions. In began development in the 1980s and continues to undergo extensive development and improvement. A ‘reference system’ is maintained by the European Centre for Medium Range Weather Forecasting (ECMWF). The reference model is hydrostatic, and uses a semi-implicit, semi-lagrangian integration scheme, and a hybrid vertical coordinate based on the Eta model. It supports sophisticated data assimilation [Driesnaar, 2011].

HIRLAM is used extensively for operational forecasting, including in Ireland [Hamilton, 2008] and Denmark [Petersen et al., 2005]. It is used widely for academic studies - the web page lists several hundred journal papers in recent years [Meteo France, 2012]. For example, it has been used for air quality studies [Rantamaki et al., 2005], and was perhaps one of the first NWP models to be used for power forecasting for wind farms [Landberg, 1999]. It has a wide and active user base.

In recent years, the members of HIRLAM have focused on the development of a mesoscale non-hydrostatic model in cooperation with the ALADIN consortium, leading to the development of the Hirlam Aladin Research on Mesoscale Operational NWP In Europe (HARMONIE).

	Global	North Atlantic	UK
Approximate resolution	40 km	12 km	4 km
Grid points	640 x 481	600 x 360	288 x 360
Vertical levels	50	38	38
Forecast length	144 hrs	48 hrs	36 hrs

Table 3.2: Standard configurations of the Met Office Unified Model [UKMO, 2008]

The source codes are available for academic use, however support for users external to the development consortium is very limited.

3.2.11 UK Met Office Unified Model

The suite of oceanic and atmospheric numerical models developed and operated by the UK Met Office are known as the Unified Model (UM) [UKMO, 2008]. It can be configured for different domains and resolutions, and can be run in atmosphere-only, ocean-only, or in coupled mode, enabling it to be used both for weather forecasting and global climate modelling. For forecasting, the models are usually run in one of the standard configurations outlined in Table 3.2.

At its core, the UM is a fully-compressible, non-hydrostatic model, which uses a semi-implicit, semi-lagrangian integration scheme. It has advanced data assimilation capabilities, and is well parallelised. The source code is available for academic research, but only once a proposal has been accepted by the UKMO. However the UM has limited support for external users. In addition, the UKMO have a commercial product, the virtual met mast, aimed at the wind industry. This sells archived UM output at the cost of several thousand pounds per grid cell, which conflicts with one of the aims of this work which is to make similar data freely available.

3.3 Choice of model

The previous sections have briefly reviews some of the main candidate mesoscale models which could be used to create a high resolution wind speed reanalysis. The review is neither particularly wide nor deep; to review every available model in detail would be an enormous task. The aim is to provide enough information to make a (semi) informed decision about which model to take forward as the basis for this work.

Many of the models have similar technical capabilities, solve similar equations, and have been well validated over many years. In light of this, many of the important criteria relate to the practicality of using a particular model, for example whether the code would be easy to obtain, and whether support is available from other users. A set of criteria were drawn up to allow comparison of the models available, this is shown in Table 3.3. Most criteria are self-explanatory: 'validation' refers to whether the model has been validated by numerous studies against observations; 'documentation' refers to whether online guides exist explaining how to install and use the model; 'maintained' relates to whether the model appears to be currently maintained; and 'interfaces' relates to whether tools exists to facilitate running the model and working with the outputs.

The judgements were made entirely subjectively, on the basis of the available documentation, the existence of user-forums and help desks, and the numbers of references to the model in recent academic publications.

Model	Capabilities	Data assimilation	Validation	Availability	Parallelisation	Documentation	Support	User community	Maintained	Interfaces
MC2	good	good	ok	good	good	good	ok	ok	ok	ok
Eta	good	good	good	good	good	good	ok	ok	good	ok
SKIRON	good	good	good	good	good	good	ok	good	good	good
KAMM	ok	poor	poor	good	good	poor	poor	poor	poor	poor
MM5	good	good	good	good	good	good	good	ok	poor	good
WRF	good	good	good	good	good	good	good	good	good	good
COAMPS	good	good	good	good	good	ok	ok	poor	good	ok
RAMS	good	good	good	good	good	good	ok	good	good	good
HIRLAM	good	good	good	good	good	ok	poor	good	good	good
UM	good	good	good	poor	good	ok	poor	ok	good	ok

Table 3.3: Comparison of mesoscale models

It can be seen that most of the models were deemed to have good, well validated capabilities. The deciding factors were mainly how available the code was and the user support. On the basis of these criteria, the final choice was between WRF and RAMS. Both are technically very advanced, openly available and widely used.

The final decision was taken to use WRF, based on the better user support provided through a dedicated helpdesk and forums, and regular (bi-annual at least) training courses. WRF is also used with the University of Edinburgh to model pollutant transport [Vieno, 2005]. Given this decision, the following section briefly describes the main features of WRF.

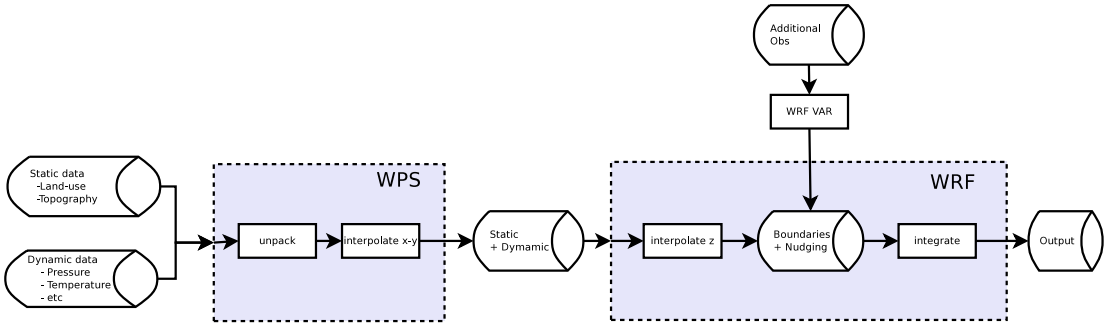

Figure 3.1: Schematic overview of WRF-ARW model

3.4 Description of WRF

The WRF-ARW model has already been introduced and in §3.2.7 . This section describes the architecture in slightly more detail, based mainly on Klemp et al. [2008b] and NCAR [2008]. However, only a brief overview of the main features is given here. The dynamics and physics are not presented in detail, as repeating them here would simply be a exercise in copying a pasting. Some things are best left to the experts.

3.4.1 Model components

WRF consists of two main components, the dynamic model itself, and the WRF Pre-processing System (WPS). These are shown conceptually in Figure 3.1.

The task of WPS is to interpolate static and dynamic data horizontally onto whatever projection is chosen for the computational grid. Static data consists of topography and land-use, while dynamic data consists of the meteorological data needed for initial and boundary conditions. Dynamic data is accepted in gridded binary (grib) format, which allows most global forecast and reanalysis datasets to be used as input. Static data is accepted in a simple binary format. If custom static data is used, this must be first converted to this binary format.

3.4.2 Vertical coordinate

WRF uses a terrain-following coordinate based on hydrostatic pressure. It is given the symbol η (although it is not the step-mountain coordinate used in the Eta model), defined as:

$$\eta_z = \frac{p_z - p_{ht}}{p_{hs} - p_{ht}} \tag{3.1}$$

where p_z, p_{ht}, and p_{hs} are the hydrostatic pressures at height z, at the model top, and at the model surface respectively. Since the hydrostatic pressure is the dry mass of a column, η_z gives the fraction of mass above z compared to the total column mass. The upper boundary is a gravity-wave absorbing layer using a technique by Klemp et al. [2008a].

3.4.3 Governing equations

WRF solves the Euler equations in flux form, which ensures they are mass-conservative with an explicit integration scheme. The governing equations are listed in [Klemp et al., 2008b]. Variables are defined as perturbations from a hydrostaticly balanced reference state to reduce truncation errors. The prognostic variables are the velocity components u and v, vertical velocity w, perturbation potential temperature, perturbation geopotential, and the perturbation surface pressure of dry air [Klemp et al., 2008b]. There may be prognostic equations for other variables such as turbulent kinetic energy (TKE), water vapour mixing ratio and others, depending on the various physics and parameterisation schemes used.

3.4.4 Numerical integration scheme

An explicit integration scheme with a split timestep is used, with acoustic modes are integrated over a smaller timestep to preserve model stability, allowing a longer timestep to be used overall. The meteorological modes are integrated with a third order Runge-Kutta integration scheme. This arrangement makes for an efficient model, as relatively long timesteps can be used and remain numerically stable.

3.4.5 Horizontal coordinate

Variables are defined on a C-staggered horizontal grid [Klemp et al., 2008b]. This means scalars are defined at the centre of grid cells, while vectors defined at the boundaries of the cells.

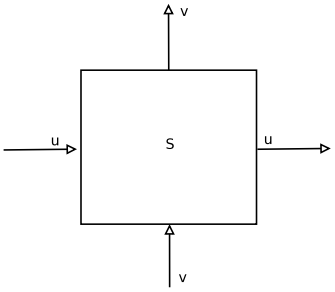

Figure 3.2: C-staggering in the horizontal direction. Vertical velocities are similarly staggered, and defined on the lower and upper faces of the grid cube.

3.4.6 PBL and surface schemes

PBL schemes exist to allow the effect of sub-grid scale boundary layer processes - turbulent mixing - to be reflected in the model. It is worth noting that although the schemes are known as PBL schemes, they actually handle vertical mixing throughout the atmosphere, including above the PBL. It is also worth mentioning that, over water, the surface roughness z_0 and friction velocity u_* both depend on each other, and therefore must be solved iteratively.

The surface layer scheme computes the parameters needed to calculate fluxes of heat, moisture and momentum between lowest model level and the surface. These fluxes then provide the lower boundaries for the PBL scheme. The parameters passed from the surface scheme to the PBL are the friction velocities and exchange coefficients for heat, moisture and momentum. The ground surface scheme governs the exchange of moisture between soil layers and, provides inputs into the surface scheme. Usually only certain combinations of surface, ground surface and PBL schemes can be used together.

WRF supports a number of PBL and surface schemes. The two generally recommended for use with WRF (Dudhia, personal communication), are the Mellor-Yamanda-Janjic (MYJ) scheme [Janjic, 2002], and the Yonsei State University (YSU) [Hong et al., 2006].

The MYJ scheme is a local, 2.5 order Turbulent Kinetic Energy (TKE) scheme. A diagnostic relationship is used to determine the mixing length. A prognostic equation for the production or

dissipation of TKE is then used to update the TKE at each timestep. Since it is a local scheme, the prognostic equation for TKE production is based only local gradients.

In WRF the MYJ PBL scheme must be coupled to a surface layer scheme inherited from the Eta model [Janjic, 1996], which uses the Businger-Dyer forms of the stability correction functions (see §2.6.3). Over water, exchange coefficients are calculated from the viscous sub-layer, except for momentum in rough sea conditions which is prescribed by a Charnock relation.

The YSU PBL scheme [Hong et al., 2006] is a development of the Medium Range Forecast (MRF) scheme which became widely used in MM5. YSU is a non-local scheme which first diagnoses the PBL height, and then constraints the eddy diffusion coefficient, K, to a prescribed profile through the PBL. It is non-local as it contains a correction to the local gradient which incorporates the effect of large-scale eddies to the total flux [Hong et al., 2006].

In WRF, the YSU scheme must be coupled to the surface layer scheme inherited from MM5 (see [Bianco, 2008]). In this scheme there are four stability regimes and associated correction functions following [Zhang and Anthes, 1982]. Over water, surface roughness is estimated by a Charnock relation, and exchanges calculated using the same stability correction functions used over land.

It is also worth noting that the surface and PBL schemes typically impose limits on some of the variables to prevent spuriously high values. For example in the YSU surface scheme, the bulk Richardson number is constrained to be < 0.2 [Bianco, 2008]

3.4.7 Static data

Land use

By default WRF uses a land-use dataset referred to in the documentation as the US Geological Survey (USGS) dataset. Land use categories from this are used to designate various parameters such as surface roughness and leaf-area index for determining evapotranspiration rates. Despite its importance, metadata on the exact source of this 'USGS' dataset is severely lacking. Sertel and Robock [2010] indicates the source is the land cover dataset of the International Geosphere Biosphere Programme (IGBG) [Loveland et al., 2000]. This was produced from unsupervised classification of 1km resolution Advanced Very High Resolution Radiometer (AVHRR) images dating from 1992 and 1993. As such, the USGS dataset is generally considered outdated [Sertel

and Robock, 2010].

The alternative dataset which is readily available for use in WRF is the land-use derived from Moderate Resolution Imaging Spectroradiometer (MODIS) images Justice et al. [2002]. This is generally thought to be more up to date and more accurate, though not without problems [Giri et al., 2005]. For this to be used in WRF requires the NOAH land-surface scheme [Ek et al., 2003].

It is possible to use other land-use datasets in WRF. For example it may be beneficial to use the CORINE dataset [European Environment Agency, 2000] for European land use, which is thought to be more accurate [Neumann et al., 2007] However, there is no consensus on how land-use categories map to each other, and various assumptions would have to made on the roughness lengths and leaf-area, on top of the practical difficulty of converting this into the binary format required for WPS.

Terrain elevation

The default source of terrain elevation comes from the Shuttle Radar Topography Mission (SRTM) data [Farr et al., 2007]. It is available by default in WRF at resolutions of up to 30 arc-second resolution, which equates to around 500m resolution at the latitude of the UK. Since SRTM data is generally known to be very accurate, and since terrain input into models is usually smoothed to reduce noise, the SRTM data is adequate, and there is no need for higher resolution terrain data, unless modelling down to a very high resolution.

3.4.8 Analysis nudging

Nudging is a method of directing a model toward a a particular solution. When a mesoscale model is driven by a global reanalysis, it is possible for the mesoscale model to diverge from the larger global analysis. For example, a storm may follow a different track within the high resolution model compared to the analysis. Analysis nudging is a way of keeping the mesoscale model ‘on track’ with a larger set of global observations.

WRF implements analysis nudging through Newtonian relaxation [Klemp et al., 2008b]. Each grid point is nudged toward a value which is time-interpolated from the analysis, by introducing a nudging term for horizontal winds, potential temperature and water vapour. The nudging

terms are not physical and represent fake sources or sinks for conserved variables.

It is usually not recommended to use nudging within the PBL, particularly with temperature [Dudhia, 2010, Zhang et al., 2001], as the PBL scheme within the model ought to give a more realistic representation of the temperature profile than an interpolation from an analysis.

3.4.9 Data assimilation

WRF supports a range of data assimilation options including observational (Newtonian) nudging, three-dimensional and four-dimensional variational assimilation (3DVAR and 4DVAR), and also an Ensemble Kalman Filter (EnKF) through an external package.

However, doing additional data assimilation at a regional level is no mean feat. Any datasets of sufficient quality and coverage will already have been assimilated into the global model, after the application of sophisticated quality controls developed over several decades. Assimilating data from specific point sources, of unknown quality, is very likely to degrade the performance overall.

Perhaps the only candidate data source which might be assimilated is sea-surface winds from satellite scatterometers, described in more detail in Chapter 6. Although these are already ingested into global models, there is some indication that they are under-utilised compared to traditional in-situ measurements [Chelton et al., 2006]. However, the computational costs and complexity of doing this well, coupled with the difficulty of treating the coastal zone where satellite winds become contaminated, meant this option was deemed too difficult to attempt.

3.4.10 Parallel environment

WRF supports MPI and OpenMP parallelism. The model domain is decomposed into tiles, which can be further decomposed into patches. Tiles are assigned to MPI tasks with their own memory space which communicate via message passing; patches within a tile are assigned to OpenMP threads. Domain decomposition provides a limit on scaling performance of WRF, as at some point tiles within a domain become too small to fully utilise individual CPUs, and the latency of message passing degrades performance.

3.5 Chapter review

The previous chapter outlined the context for the work, and described the decision to use a mesoscale atmospheric model to create a high resolution dataset of wind speeds of the UK and surrounding waters.

This chapter briefly reviewed available mesoscale models in terms of their capabilities and ease of use. On the basis of this review, the WRF model was selected. This model was then described in more detail, outlining the model structure, the datasets available, and the parameterisation schemes supported. The capabilities for data assimilation were also touched on, and the decision not to use additional data assimilation explained.

This chapter provides the definitions and background for the following chapter, which describes the use of a case study simulation to test different model configurations against observations.

Chapter 4
Observations and Model Configuration

4.1 Introduction

There are a large number of different options to consider when running an atmospheric model such as WRF, for example, the layout and resolution of model domains, the number and spacing of vertical levels, how observations are used to constrain the model, and how a variety of sub-grid scale processes and land-model interactions are represented.

The model configuration has to be chosen carefully. However, computational expense makes it impractical to evaluate all possible model permutations. Conversely, it would be unwise to commit to a very large simulation without having done some testing and verification first; this obviously requires a set of observations to verify against.

For these reasons, a week-long case study was simulated to allow different model configurations to be tested and compared to observations. This chapter describes some practical constraints encountered during this phase of work, the observations used for verification, the model options which were held constant throughout the case study model runs, the model options which were varied, the error statistics used for verification, the case study chosen, and the comparative performance of different model configurations. The final model configuration is then selected to be carried forward into the main simulation stage.

4.2 Computing platform and practical constraints

Producing a reanalysis dataset which covers ten years or more at a reasonable resolution is a computationally demanding task only feasible using a parallel computing environment. Initial testing revealed very quickly that the local computing cluster, which despite its 128 cores, was insufficient for this task. This was mainly due to the use of standard shared ethernet as the interconnect with relatively high-latency. Under these conditions, WRF cannot be effectively

parallelised since the network latency quickly becomes a bottleneck, and performance actually deteriorates when run on a large number of cores.

Therefore an application was made for an account on the High-End Computing Terascale Resource (HECToR). HECToR is a world-class high performance computing facility to support UK based research institutions [UKRC, 2011], which at the time had around 10 000 cores, subsequently upgraded to around 90 000.

There is a defined process for securing an account, and a hierarchy of classes which allow for different allocations. At this model configuration phase, an application was submitted under the Class 2a mechanism, designed to support pump-priming and exploratory research, and to allow new users access to a high-performance computing environment. Under this mechanism 200 000 Allocation Units (AU) were granted for the testing and configuration of WRF. One AU is equivalent to a 1 GFlop (floating point operations per second) processor running for one hour. For comparison, a typical modern desktop CPU might be rated at 30-40 GFlops, therefore 200 000 AU is roughly equivalent to 5000 hours on a single CPU.

This allocation had to be used within a fixed timescale; in addition the configuration had to be completed reasonably quickly in order to apply for a larger allocation. Therefore the number of test cases and extent of configuration was limited by practical constraints on the time and resource available. This meant that all permutations could not be tested, and also that some observation were not available during this phase.

4.3 Parallel performance

With an account established on HECToR, a test domain covering the whole of the UK at 3km was established to test the parallel performance of WRF and estimate the computational requirement of later stages. Performance was measured by the number of integration steps performed per wallclock (i.e. real) hour..

WRF was compiled using the Portland Group Compilers (PGI), with only Message Passing Interface (MPI) parallelisation. Testing showed no performance gains using hybrid (MPI + OpenMP). The scaling performance is shown in Figure 4.1. Scaling is almost linear at core counts below 150, and begins to diminish above two hundred, although reasonable scaling is still seen up to 512 cores. A much larger model domain would be needed to see continued

performance gains beyond 512 cores, otherwise the individual tiles and patches become too small to make efficient use of the processors.

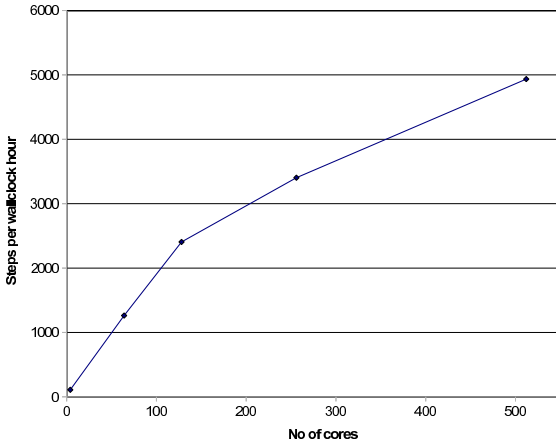

Figure 4.1: Parallel performance on HECToR. Number of integration steps per wallclock hour vs core count

4.4 Observations

This section details the observations which were used throughout the course of the study. Some of the observations were not publicly available and required (in some cases lengthy) negotiations before they could be used. Others were publicly available but required some effort to obtain and process. This meant that not all datasets were available during the configuration phase. They are described here for completeness and consistency, so that the descriptions are all contained within one section. At the end of this section, Table 4.5 summarises which datasets were available during the configuration phase.

4.4.1 Anemometers

Many of the observations come from cup anemometers. A typical modern cup anemometer states an accuracy of $\pm 2\%$ [Manwell et al., 2002a, p72]. However, when deployed the accuracy depends on many factors including turbulence intensity and the inclination of the mean flow [Pedersen, 2003]. As turbulence increases, cup anemometers tend to record a higher signal due to the inertia of the cups, termed 'overspeeding' [Kristensen, 1998]. Additionally there may be flow distortion caused by the mast. Therefore it is difficult to specify the exact measurement error of a deployed anemometer, and the stated accuracy is likely to be a lower bound on the

actual error when deployed.

All cup anemometers have a minimum speed needed to overcome the inertia of the cup, which for some older anemometers may be as high as six knots ($3\ \mathrm{ms}^{-1}$). In addition, a malfunctioning anemometer may report a zero wind speed, which may not be flagged as an error. This means that calms are much more common in observed data than would be expected.

4.4.2 Meteorological stations

The UK has a large network of meteorological stations (hereby referred to as met stations) observing synoptic and climatic variables. A database of historic measurements is maintained as the Met Office Integrated Data Archive System (MIDAS) [BADC, 2006]. This contains surface observations as far back as the digital record extends, as well as radiosonde measurements and some marine observations.

UK met stations are organised into networks to suit different end-users. The basic network types are synoptic, climate, wind, and rainfall. One station can report observations to multiple networks, and may have a different identifier within each network. Within MIDAS, stations are identified uniquely by their *src_id*. Observations to a particular network take the form of a standard *message*, reported using a standard *message type*.

The synoptic network is designed for real-time exchange of information to support weather forecasting. There are 225 stations reporting to the synoptic network in the UK, with a guaranteed spacing of less than 50 km [UKMO, 2010]. Observations reported to the synoptic network are encoded in the international SYNOP message format. Wind speed is reported as a 10-minute average and the UK uses a non-standard observation period of HH-20 to HH-10 i.e. a wind speed reported at 0500 GMT will represent the average between 0440-0450 GMT.

Most stations in the synoptic network, plus some additional stations, also report hourly-average wind speeds in the Hourly Climate Message (HCM) format[1]. Hourly averages cover the period HH-70 to HH-10 [UKMO, 2010, Section 5.5]. Speed and direction are averaged separately, and maximum gusts are calculated from 3-second averages of speed. Table 4.1 summarises the variables and precision recorded.

Hourly-averaged wind speeds for the 11 years 2000-2010 were downloaded and stored locally

[1] Automatic weather stations use the AWSHRLY format

in a relational SQL database. MIDAS data is quality checked by the Met Office before being archived and erroneous records are flagged; only records flagged as clean were used in this study. Missing data averaged 5% of the total number of observations.

Data from Irish met stations was obtained from Met Éireann. The data was very similar in nature to the UK data: hourly averaged wind speeds and direction mainly from cup anemometers at 10m agl.

Variable	Units and precision
Mean hourly wind direction	10 degree bins
Mean hourly wind speed	1 knot bins
Direction of maximum gust	10 degree bins
Speed of maximum gust	1 knot bins
Time of maximum gust	Nearest minute
10 cm soil temperature	0.1°C
Global irradiation	W hr/m^2

Table 4.1: Variables reported in the HCM and AWSHRLY message type

Instrumentation

A met station is a collection of measuring instruments at a particular site. Wind speeds are measured by an anemometer with a 'standard exposure' meant to be equivalent to 10m above open terrain. The MIDAS user guide [UKMO, 2010] states:

> "The standard exposure is over level, open terrain at a height of 10m above the ground. Open terrain is defined as an area where the distance between the anemometer and any obstruction is at least 10 times the height of that obstruction. If standard exposure is unobtainable the anemometer may be installed at a height greater than 10m. Whether or not such an adjustment is made, all anemometers are allocated an 'effective height' which is defined as the height above open, level terrain in the vicinity at which mean wind speeds would be the same as those actually recorded by the anemometer. Various methods have been devised for the calculation of effective height. At stations where the effective height differs substantially from the actual height, corrections are applied to the 10-minute wind speed reported in the SYNOP message. No corrections are applied to any gusts measurements or to any hourly mean wind speeds. "

Figure 4.2: Bealach na Ba met station: the anemometer mast is on the right. Picture taken by the author.

Problems with met station observations

The main problem with met station observations is that they are taken at 10m agl, and are therefore influenced by surrounding obstacles and local orography. Although masts are meant to have a standard exposure, this is not exact and may vary with direction. Figure 4.2 shows one particularly extreme example: the Bealach na Ba met station in mountainous terrain in Scotland. The mast itself is clearly well below 10m agl and in the lee of a building which will distort the flow substantially. The surrounding terrain is very complex: the station is perched above the steep headwall of a valley which leads from the sea.

Another issue is that instrumentation varies between stations and over time. Older and heavier cup anemometers had slow response and high start-up speed. In particular the Munro MK4 had a start-up speed of 6 knots, and was in common usage. A programme to replace these with lighter anemometers was started in the 1990s, but it is unclear from the record when this occurred at a particular station, or whether any are still in use today. A high start-up speed would show up as a large frequency of zero speeds, which is found in many met station records. Wind speeds are only recorded as an integer number of knots and histograms for some met stations show regular spikes and troughs, suggesting a bias in binning method, Figure 4.3.

Another problem is inaccurate location information: Boehme [2006] found the latitude and longitude recorded in the MIDAS database to be inaccurate, and corrected the locations for 21 selected stations in Scotland based on OS maps. The UK Met Office has since updated the

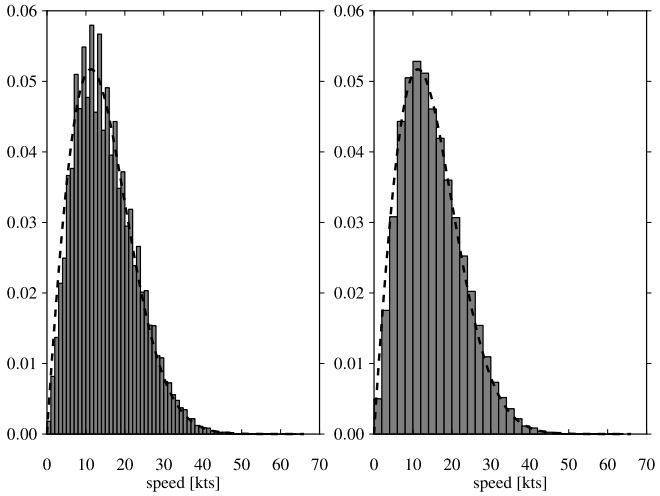

Figure 4.3: Example of the binning problem: observed hourly wind speeds and fitted Weibull parameters at Lerwick, 2005. Original one-knot bins (left) and two-knot bins (right)

coordinates of the met stations, and these updated locations were used in this study.

Boehme [2006] also rated the exposure of each met station in order to select only the exposed stations. However, selecting met stations by this method for verification would risk excluding stations in complex terrain, and could lead to an unrealistic assessment of model performance. Therefore, no attempts were made to choose 'better' met stations, or weight some observations over others.

Despite these problems, the density and historical record of surface met stations means they offer a very comprehensive way of verifying onshore surface wind speeds.

4.4.3 Wind farm masts

Wind farms typically require at least a year of observations to secure finance, and typically will continue to monitor wind speeds over their operation, although this data is usually commercially sensitive. Scottish Power Renewables (SPR) kindly provided pre-construction data for three sites, and Community Wind Power provided data for three sites, summarised in Table 4.2. This data is covered under a non-discosure agreement and the mast locations or raw time-series are not revealed.

These masts are important for a number of reasons. First, they are at sites characteristic of actual wind farms, which is not always the case with met stations. Second, they are independent and do

Label	Location	Terrain	Period	Instrument heights	Farm status at time
S1	England	Flat	Mar 2003 - Mar 2004	10m, 50m	Pre-construction
S2	Scotland	Moderate	Nov 2003 - Dec 2004	20m, 30m, 40m	Pre-construction
S3	Scotland	Complex + Forestry	Jun 2001 - Nov-2004	20m,30m,40m	Pre-construction
C1	Scotland	Moderate + Forestry	Jan 2007 - Jan 2010	30m	Operational
C2	Western Isles	Moderate	Jun 2005 - Mar 2007	30m, 40m, 50m	Operational
C3	Scotland	Moderate	Jan 2010 - Jan 2011	80m	Operational

Table 4.2: Windfarm met masts used for verification. 'S' mast data provided by Scottish Power Renewables Ltd, 'C' mast data provided by Community Wind.

not report to central meteorological organisations, and hence have not been assimilated into any reanalysis datasets. Third, mast heights are significantly higher than met station observations, up to 80m in the case of mast C3.

However, the measurements are still subject to flow distortions caused by the mast and the local orography. In the case of the masts at operational farms, there may be major wake effects due to the wind farm. Masts are usually located in the prevailing upwind direction, in order to sample the free-flow, but will be in the park wake from some directions. Also, the wind speeds are provided as raw-data, and extensive quality-control and data cleaning is usually applied to the raw wind speeds before being used commercially (Scottish Power, personal communication).

4.4.4 Buoys

The Met Office has a series of buoys, and the Irish Marine Institute has a network of six buoys, five of which were inside the model domain. Buoy locations are shown in Figure 4.5. The deployment dates of the Irish buoys are summarised in Table 4.3. M4 was moved in May 2007, so has been labelled M4a before the move, and M4b after.

Buoy	Deployed
M1	Nov 2000
M2	April 2001
M3	July 2002
M4a	April 2004
M4b	May 2007
M5	Oct 2004

Table 4.3: Deployment dates of Irish Marine Institute Buoys

All of the buoys used here record wind speed primarily via a cup anemometer, with a typical accuracy of around $\pm$2kn below 40kn and $\pm$1.5% above 40kn [Turton, 2009]. Some Met Office buoys are being re-equipped with dual cup and sonic anemometers [Turton, 2009]. Out of the

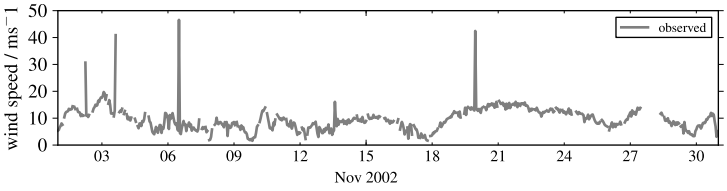

Figure 4.4: Raw buoy data showing frequent missing data and sharp spikes. The spikes were removed with a simple quality control algorithm

water the buoys are 6m high, so for verification it was assumed the anemometer was at 4m when afloat.

Missing data is relatively common, both individual missing hours and longer periods. For example, the K7 buoy was lost on 27th of October 2000 and replaced in September 2001. Buoys need frequent maintenance, and the time to failure for the anemometer may be as little as six-months [Turton and Pethica, 2010]. Before failure, quality may degrade substantially over time, and salt ingress into the oil slows the anemometer [Turton and Pethica, 2010].

Given the low height, in moderate seas they will be in the direct influence of roughness elements (waves), and surface-law scaling may not necessarily apply [Large et al., 1995]. Also, buoys are thought to be affected by wave sheltering [Gilhousen, 2006]. However, averaging over an hour should reduce the effect of swell on the readings, although flow separation in very high waves may still be a problem [Ingleby, 2010].

UK buoy data was supplied before any quality control had been applied, and showed occasional spurious spikes of winds speeds $> 40\text{ms}^{-1}$, Figure 4.4. These spikes were obvious as single-hour spikes, not matched by neighbouring readings. For that reason, a simple quality control algorithm was applied: any wind speeds which were above 30ms^{-1}were cross-checked against the nearest neighbouring buoy or met-station. If the wind speed there was less than 10ms^{-1}, the spike was flagged as erroneous. This successfully eliminated the small number < 300 of erroneous observations.

4.4.5 Lightships

The Met Office operate a number of lightships. These are small moored ships which act as lighthouses and automatic weather stations; these are dedicated vessels, distinct from voluntary observing ships. Ship winds are known to be higher than buoy winds, even after the height of

the anemometer has been accounted for [Gilhousen, 2006], which may be due a combination of the sheltering of buoys in high waves and acceleration of the flow by the ship. Yelland et al. [2002] found significant de-acceleration or acceleration of the flow can occur depending on the position of the anemometer on the ship and the wind direction.

4.4.6 Oil Platforms

Shell kindly provided data from the Auk Alpha, Lemana A, and Nelson A oil platforms, Figure 4.5, for the month of January 2005. The exact instrumentation on the platforms varies although they are all cup anemometers similar to those used at onshore met stations. The instruments are at heights above mean sea level of 100m, 78m and 110m respectively. Wind speeds are reported as 10-minute averages, and are further averaged to hourly values for verification.

The largest problem with platform observations is the platform's influence on the flow. The platforms are large, bluff bodies in an otherwise open sea. The effects are complex, site and direction specific, and would require detailed flow modelling to correct [Högström et al., 2008]. Therefore, oil platform winds are not used in the calculation of error statistics, but they are used to check the time series of wind speeds and the timing of major features appears sensible.

4.4.7 Radar profilers

UKMO have a number of radar profilers which can measure wind speed at multiple heights through the troposphere. The main purpose is to observe high-level wind speeds, and typically the minimum observation height is 100m or more, which makes them less useful for surface verification. Some of the profilers are mobile and occasionally move location; the locations, heights, and time periods covered are summarised in Table 4.4.

4.4.8 Satellites

There are a number of satellite-derived sources of wind speed data over oceans, see e.g. [JPL, 2010, Nielsen et al., 2004], and satellite data have been used in a number of resource assessment studies e.g. [Capps and Zender, 2010, Christiansen et al., 2006, Hasager et al., 2002, Kim et al., 2010]. However, it is a relatively new discipline and the uncertainties in the methods are not

Name	Heights (km)			Dates	
	Min	Max	Step (m)	From	Until
Cambourne	0.3	8.0	60	1998	Present
South Uist (915 MHz)	0.2	8.0	100	2003	2004
South Uist (64 MHz)	1.0	13.0	400	2004	Present
Dunkeswell	0.1	7.9	100	1999	Present
Wattisham	0.2	8.2	100	2001	Present
Isle of Man	0.3	8.0	60	2005	2008
Aberystwyth	0.3	8.0	60	1999	2002

Table 4.4: Summary of radar profiler data held by UKMO

fully quantified [Barthelmie and Pryor, 2003]. Although satellite data was not be obtained until after the configuration phase, it is used extensively in later chapters, so is described here for completeness.

The source which offers the longest contigous record of ocean winds comes from the remote sensing of microwave backscatter from centimetre-scale capillary waves, which allows wind speed and direction to be estimated. Dedicated active sensing scatterometers for wind speed and direction have been carried on a number of satellites since the early 1990s, notably NSCAT, QuickSCAT, and ASCAT [JPL, 2010]. Together, QuickSCAT and ASCAT provide an almost continuous record over the study period, and for that reason were used for this study.

There are other satellite sources of wind speeds, such as the European Remote Sensing satellites (ERS-1 and ERS-2), TOPEX/Poseidon and others. JPL [2010] gives an excellent review of satellite data sources. However, working with multiple satellite datasets at different spatial and temporal resolutions, with different accuracies, masked at various distances from the coast, presents significant practical difficulties, without necessarily adding extra detail. The Cross-Calibrated Multi-Platform Ocean Surface Wind Velocity Product (CCMP) dataset [JPL, 2010] would have been ideal to use, except that it is masked very conservatively near the coast, sometimes up to 100km from the coast, making it unsuitable in its current form.

Therefore, only scattermeter winds from QuickSCAT and ASCAT were used, as these offered the best coverage, resolution, and proximity to the coast. Since scatterometer winds are used, the equivalent neutral wind is now introduced, before the sources are described in more detail.

Equivalent neutral wind

Scatterometers measure backscatter from capillary waves, which are assumed to be in equilibrium with the surface stress, τ. The surface stress is then converted into an Equivalent Neutral Wind (EQNW), U_n, usually at 10m above the surface [Liu et al., 1996]. This represents the wind speed which would exist at that height if the atmosphere were neutral. $U_n < U$ in stable conditions, and $U_n > U$ in unstable conditions.

There are a number of algorithms to derive actual wind speed from EQNW [Liu et al., 1996, Winterfeldt et al., 2010]. Generally these require air temperature, sea temperature and humidity, although humidity can be assumed with minor consequence [Babin and Thompson, 2000]. However, many authors [Chelton et al., 2006, Kara, 2008, Sampe and Xie, 2007, Winterfeldt et al., 2010] note that the difference between the neutral wind and the actual wind at 10m is relatively small. For example, Kara [2008] found the difference between monthly-averaged stability-dependent and neutral winds was 0.2ms^{-1}, while the difference in hourly values was at most 0.5ms^{-1}. Sampe and Xie [2007] found that for high winds, the difference due to stability was around 0.2ms^{-1}.

It light of this, it was decided to use the EQNW directly, since attempting to correct it based on air and sea temperature, which may themselves have errors, is just as likely degrade rather than improve the quality of the wind speeds.

Quickscat

The SeaWinds scatterometer was launched on the QuickSAT mission satellite in 1999, as a 'quick recovery' following the early failure of the NSCAT satellite. It provided data from 1999 until until 2009 and is probably the longest and highest resolution single satellite record of surface winds over the period in question.

In mid-latitudes it provides observations twice per day, on the ascending and descending path. Accuracy is estimated as 0.75 ms^{-1}in the along- wind component and about 1.5 ms^{-1}in the crosswind component [Chelton et al., 2006], and it has been shown to have little or no bias when compared to in-situ observations [Wallcraft et al., 2009, Winterfeldt et al., 2010]. QuickSCAT retrievals are known to be contaminated by heavy rain (this is flagged), although accurate assessment is still possible provided winds are relatively strong, and Chelton et al. [2006] suggests the extent of rain contamination has been over-estimated.

Satellite data is available on a number of processing 'levels'. Level 1 data represents the raw data i.e. scatterometer returns. Level 2 represents one stage of post-processing: for QuickSCAT this consists of wind speeds and directions on the original 12.5km swaths corresponding to the ascents and descents of the satellite. Level 3 data represents globally gridded data on a regular spatial grid.

Working with Level 2 data is difficult, since it is not on a regular spatial grid, and therefore Level 3 data was used here. The Institut Français de recherche pour l'exploitation de la mer (Ifremer) produce a globally gridded dataset on a 0.5°grid [Ifremer, 2002]. Average wind fields are derived from discrete observations by an objective kriging technique [Ifremer, 2002]. The advantage of this dataset over others is that wind speeds are not explicitly masked near the coast, allowing users to define their own mask based on sensible values of the wind speeds (scatterometer readings over land produce wind speeds of > 60 ms^{-1}). This allows a much closer mask to be used compared to other Level 3 datasets, which are typically masked within 20 or 30km of the coast. In March 2011 a coastal dataset from QuickSCAT winds was released which gets within 5km of the coast [Vanhoff et al., 2009]; this is only available for the eastern coast of the US.

ASCAT

The Advanced Scatterometer (ASCAT) is carried on board the European Space Agency's MetOp satellite, launched in 2007. It has lower horizontal resolution than QuickSCAT, with an effective resolution of 25km rather than 12.5km grid. The stated accuracy of the 10m wind speed is 0.5ms^{-1}bias, and 2ms^{-1}Route-Mean-Square Difference (RMSD), and it has been found to compare very well to buoy and QuickSCAT data, particularly within the range 3-20ms^{-1}[Bentamy et al., 2008].

Ifremer provide a globally gridded dataset derived from ASCAT at 0.25°resolution. This uses ECMWF analysis data to derive the real ocean wind (rather than the EQNW), and also for temporal interpolation so that so that a more accurate daily average can be assessed from the two passes of the satellite [Bentamy and Fillon, 2011].

4.4.9 Summary of observations

This section has outlined all of the observational data used in the course of this study. Many of the observational datasets described were not available during the configuration phase of this work, but are described here for completeness. Table 4.5 summarises the datasets used in each stage, and the locations of all the in-situ observations are shown in Figure 4.5.

Class	Type	Source	Number	Period	Available during configuration
In-situ	UK met stations	UK Met Office	200	11 years	yes
	Irish met stations	Met Éireann	22	11 years	no
	Wind farm masts	Scottish Power Renewables	3	$\sim$ 2 years	no
	Wind farm masts	Community Wind Scotland	3	$\sim$ 2 years	no
	UK buoys	UK Met Office	4	11 years	no
	Irish buoys	Irish Marine Institute	5	$\sim$ 4 years	yes
	Lightships	UK Met Office	4	11 years	no
	Oil Platforms	Shell UK	3	1 month	yes
Remote sensing	Radar profilers	UK Met Office	6	$\sim$ 10 years	no
	QuickSCAT satellite	Ifremer	-	9 years	no
	ASCAT satellite	Ifremer	-	2 years	no

Table 4.5: Summary of observations available during and after the configuration phase

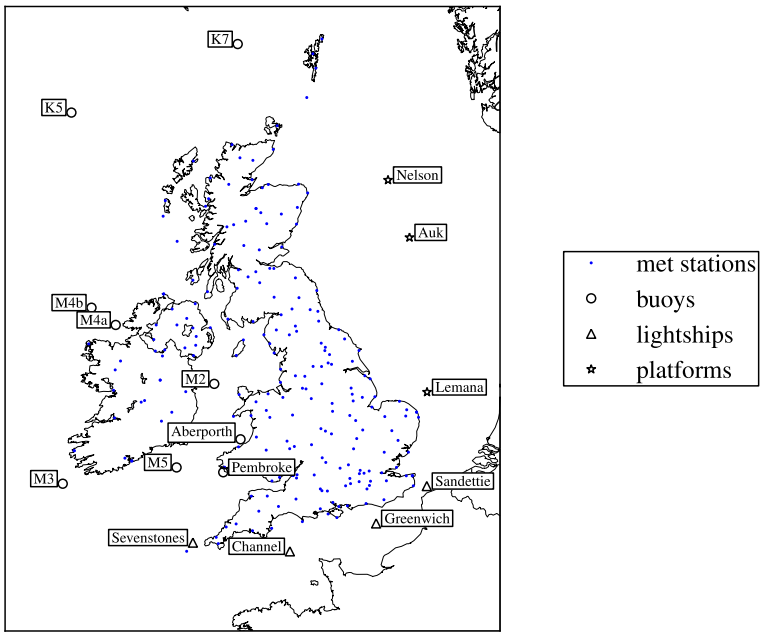

Figure 4.5: Locations of in-situ observations

4.5 Options held constant

Certain aspects of the model configuration were dictated by the available computational resource, storage requirements, and other practicalities. This section describes the options which were defined in advance and not varied between model runs.

4.5.1 Domain and horizontal resolution

One of the most influential choices is model resolution, since this determines the scale of features which can be explicitly represented, and also influences the choice of parameterisation schemes. An important aim is to ensure a clear separation of grid-scale processes, which are modelled explicitly, and sub-grid process which must be parametrised.

For a given domain size, the number of grid points in the horizontal dimension increases with $1/(\Delta x)^2$, where Δx is the horizontal grid spacing. In addition, the time-step must be decreased with Δx to maintain numerical stability. Therefore the number of grid points per vertical level increases as $1/(\Delta x)^3$. If n_v is the number of vertical levels, the total computational requirement is $O(n_v/(\Delta x)^3)$, and hence the resolution quickly becomes a limiting factor even on the most powerful computers.

Additionally, to perform high-resolution simulations, it is generally recommended to use a series of nested domains of increasing resolution. This ensures a smooth transition from the relatively coarse boundary conditions to the high resolution inner domain, and limits the impact of noise from the boundaries. The horizontal resolution of the child domain must be smaller than the parent by an integer factor, and a nest factor of 3 or 5 is often recommended [NCAR, 2008].

With a requirement for a dataset spanning the whole UK and surrounding waters for a period of at least 10 years, initial simulations showed that 3km was the highest resolution feasible in the inner domain. At this resolution, with a minimal set of output variables (listed in Appendix B), each day of raw output required 30GB of storage space, and one month of simulations could be completed in 12 hours using 512 processors.

The model domains used are shown in Figure 4.6. A Lambert conformal conic projection is used, which is well suited to mid-latitudes [NCAR, 2008] and is also well supported by most post-processing and visualisation tools. The projection is defined by a central meridian of 5°W

and one standard parallel at 54°N.

A nest factor of 3 is used, with the outer domain at 27km which is approximately a factor of three less than a resolution of 1° typically found in global reanalysis datasets.

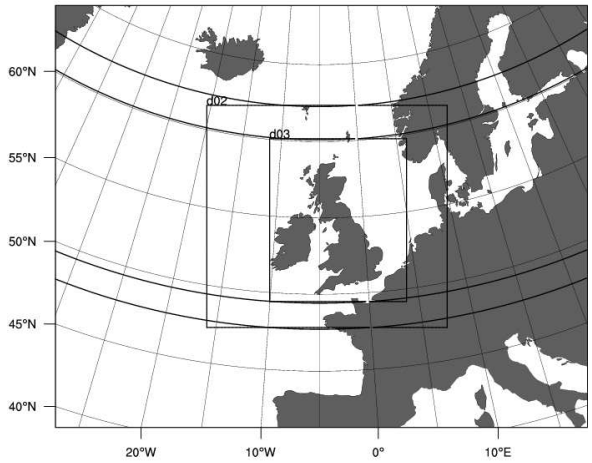

Figure 4.6: The model domains at 27km, 9km and 3km resolution.

4.5.2 Vertical levels

The number of vertical levels was set at 28. Although this may be on the low side, it has worked well in previous studies [Vieno, 2005], and was a tradeoff to allow a higher horizontal resolution. Although the total number of vertical levels was fixed, the spacing was varied to position more η levels close to the surface, as it was thought this may improve predictions of the wind profile close to the ground, and also limit any errors introduced when interpolating from η to height levels.

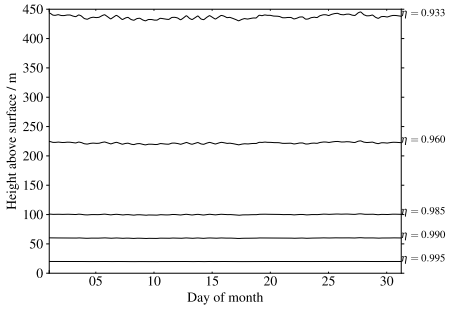

Figure 4.7: Typical heights above the surface of η levels over one month.

Figure 4.7 shows the typical height above mean sea level of the increased spacing. This is illustrative for a point over the sea for one day in January; as described in §3.4.2, η levels are pressure-based and terrain-following so vary with time and terrain height. However the variation in height of the lowest three levels is relatively small, and was $< 1\%$.

4.5.3 Microphysics and cumulus schemes

Since the primary focus of this study is wind speeds rather than precipitation, different microphysics and cumulus schemes were not compared. However, precipitation and cloud fraction outputs may be useful for future work, such as for examining solar and hydro resource, so it is still preferable to use sensible schemes for these. Additionally, the choice of scheme may have implications for wind speed, for example by removing atmospheric instabilities through enhanced convective mixing.

Following guidance in NCAR [2008], a Kain-Fritsch cumulus scheme [Kain, 2004] was used in the outer two domains, though not in the inner 3km domain, which may be at (just) high enough resolution not to require a scheme. A five-class microphysics scheme [Hong et al., 2004] is used, a simple downward shortwave radiation scheme [Dudhia, 1989], and the Rapid Radiative Transfer Model [Mlawer et al., 1997] for long-wave radiation were used throughout. These and all other options are specified in Appendix B.

4.5.4 Time resolution of output

To maintain numerical stability, an integration time-step, Δt, in seconds, of roughly $6\Delta x$, in km, is recommended [NCAR, 2008]. With an inner resolution of 3km, this means $\Delta t \approx 18s$. To ensure the output fits into a whole number of minutes, a timestep of 15s was used in the inner domain, achieved using a timestep of 135s in the other domain.

It is infeasible to store the output every 15 seconds. First, writing so frequently to disk would severely slow down the simulation; second it would require far too much storage (many hundreds of Terabytes); third since WRF solves the Reynold's averaged equations, even at high frequency the output only represents the evolution of steady wind component, not turbulent fluctuations, so storing output more frequently does not necessarily add more information. Figure 4.8 shows a comparison between WRF output archived at ten-minute and one-hour intervals over the course of a meteorologically active day. Although the 10-minute output

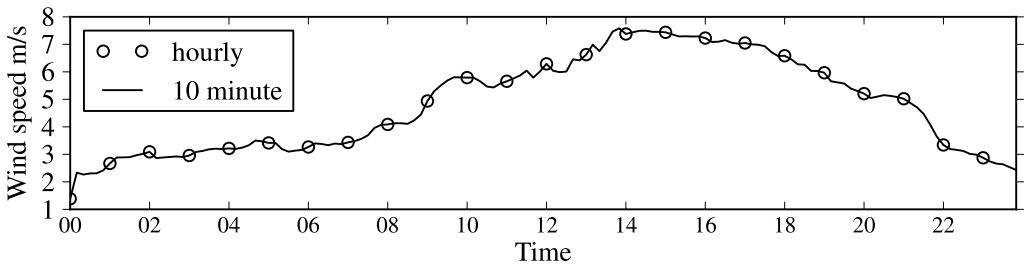

Figure 4.8: Output from WRF at 10m and 1h intervals over the course of one day. The 1h output reveals little more detail than the 10m

shows some more variation, very little information is added to the hourly output, while the storage requirement is increased six-fold. Therefore the final output was stored at one-hour resolution.

4.5.5 Boundary conditions

Boundary conditions are taken from the NCEP/NCAR Final Analysis (FNL) dataset [NCEP, 2010]. These are archived analyses at 00z, 06z, 12z and 18z from the NCEP Global Forecast System (GFS) see e.g. Werth and Garrett [2010], on the operational grid '003', at approximately 1° resolution.

This dataset is similar in nature to the NCEP/NCAR reanalysis [Kalnay et al., 1996], but at higher resolution and more recent, although with no guarantee that the modelling system is fixed throughout the analysis period. The GFS assimilates data from all validated sources reporting to the Global Telecommunications System (GTS). This includes global radiosonde data, surface observations and satellite data [Kalnay et al., 1996].

The advantage of using the operational analysis rather than a re-analysis is the increased resolution, the more recent time coverage, and the most recent model configuration, using the most assimilated data. The disadvantage is that the configuration is not fixed over the period, so that the quality of data may change over time, with potential step-changes in variables as configuration is changed. According to Werth and Garrett [2010], the most significant change in the GFS over the period in question was the update in resolution, from T254 (around 50km) to T382 (around 35km) on 30 May 2005. However, improvements are only made after significant testing and verification, and so small improvements are more likely than large step changes.

It was also hoped to use data from ECMWF, such as the ERA-Interim reanalysis [Uppala et al., 2005] for comparison. However, there were several practical difficulties getting WRF to run correctly with ECMWF data. Furthermore, at the time, the copyright agreement was much more restrictive than GFS, making it questionable whether a dataset heavily derived from the ECMWF data could be made freely available. Since it was planned to make the outputs of this study freely available, this provided the main reason to use NCEP GFS data.

4.6 Verification process

4.6.1 Interpolation to height

Model winds are given on η levels, and additionally the diagnostic 10m wind. For this analysis, the 10m wind was regarded as if it were simply an extra model level below the first η level. For verification at surface met stations, the 10m wind can be used directly. For all other heights, wind speeds were interpolated from the closest model level logarithmically in height. Given the decreased spacing of model η levels near the surface, the vertical interpolation distance was typically very small, no more than a few metres.

4.6.2 Comparing grid cells to point measurements

Variables in WRF represent time-averaged and volume averaged flows - steady state components of the Reynold's averaged flow through a grid cell. The boundary of the lowest grid cell is an area-average of terrain height. These factors present two sets of difficulties when comparing model output against point measurements.

The first set are the intrinsic difficulties in comparing point-based measurements to volume-averaged model solutions. Point measurements will include contributions from turbulent eddies at a variety of spatial and temporal scales, and could be highly influenced by local topography or obstacles.

The second set of difficulties relate to extrapolating from model levels to heights above the surface. Model terrain height is averaged to the grid resolution, in this case 3km. This means the actual met station will be above or below the modelled terrain, and may even be above the first few model levels, Figure 4.9.

Accounting for this is neither straightforward nor obvious. For example, for point X it may be argued that the second or third model level may be more representative of the wind speed than the lowest model level, which is 'below' the real terrain. However, the second or third level still does not account for the shape of the hill and its influence on the low-level flow, nor the proximity and roughness of the ground. Also, it implies that the wind speed at Y should be reduced by some factor to represent the valley. Howard and Clark [2007] proposed a method for correcting this based on the linear flow theories of Jackson and Hunt [1975], but their approach is not yet well verified, and relies on being able to characterise features by a length scale, an approach which is difficult to generalise across the whole model domain. Given this uncertainty, for this analysis the observation stations are regarded as if they sit on the model terrain, i.e. at X' and Y'.

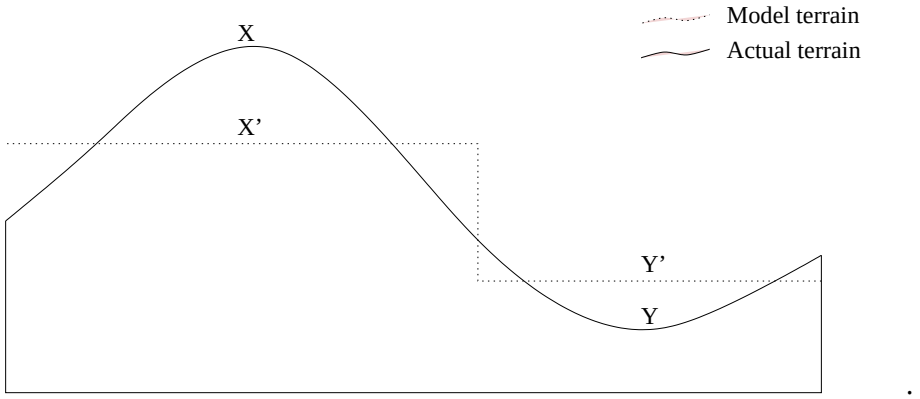

Figure 4.9: Observation stations at X and Y having positions in the model terrain at X' and Y'.

4.6.3 Self verification

The GFS model assimilates observational data from multiple sources, including surface wind speed from SYNOP stations [Kalnay et al., 1996]. There is therefore some degree of self verification when comparing model output to met station observations. This is not a problem in itself, after all, the purpose is to create a dataset which matches observations. The danger is that the model performs well *only* near observation sites, and that any verification therefore gives an overly optimistic picture of performance.

The standard approach of partitioning met stations into a training and verification set cannot be used here, since the data assimilation has already been done. However, the main use of the analysis is as initial conditions (on all domains), and boundary conditions every six hours (on the outermost domain). If the model can recreate hourly wind speeds at observations points

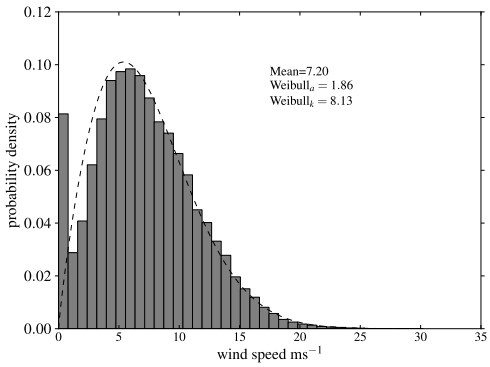

Figure 4.10: Observed wind speed at Sella Ness, an exposed station in Shetland. Zero wind speeds in observed data appear as a large spike in the frequency distribution. The size of the spike and the exposure of the met station suggests this is due to missing data not properly flagged, rather than low wind speeds below the start-up speed of the anemometer

across the whole domain (i.e. well away from the boundaries) over several days (i.e. well away from the initial conditions), then this is a good indicator that the predictions are correct due to a realistic representation of the physical flow, rather than simply an effect of being constrained by observations. Therefore, verification against met stations is still a useful exercise, and is an approach commonly taken many similar studies.

4.6.4 Zero wind speeds

Zero-wind speeds are common in observational data, either because the wind speed is below the start up speed of the anemometer, which might be considered a genuine calm, or because the anemometer is malfunctioning or stuck and error is not flagged, which would be considered a ‘spurious calm’. Spurious calms are easily visible in the wind speed distribution as a spike at zero, as shown in Figure 4.10. Spurious calms affect error statistics, particularly R^2 which is not robust to outliers. For that reason, all zero wind speeds are ignored in the calculation of the error statistics.

4.6.5 Error statistics

Error statistics used here are the Mean Bias Error (MBE) also called Bias (B), Root Mean Square Difference (RMSD) and a coefficient of determination R^2. If e_i is the difference

between an individual prediction, p_i, and observation o_i:

$$e_i = p_i - o_i \tag{4.1}$$

then standard error statistics can be defined:

$$\mathrm{B} = \frac{1}{n}\sum_{i=1}^{n} e_i = \bar{p} - \bar{o} \tag{4.2}$$

$$\mathrm{RMSD} = \sqrt{\frac{1}{n}\sum_{i=1}^{n} {e_i}^2} \tag{4.3}$$

$$R = \frac{\sum_{i=1}^{n}(o_i - \bar{o})(p_i - \bar{p})}{\sigma_o \sigma_p} \tag{4.4}$$

where σ_o and σ_p are the observed and predicted standard deviations.

Bias is a simple indicator of whether the simulation over or under-predicts wind speeds. RMSD is a measure of the overall error, with the property that positive and negative errors do not cancel. RMSD also depends on the distribution of errors, with larger errors contributing most. It is possible for a forecast to have zero bias, but be wrong at every location. RMSD is therefore a good complementary measure to B. The coefficient of determination, R^2, is a measure of degree of the linear relationship between the observed and predicted data. R^2 is a useful statistic in the presence of systematic errors since it indicates goodness of fit independent of systematic errors.

However, R^2 not robust and is heavily influenced by outliers [Legates and McCabe, 1999]. Zero wind speeds have been eliminated as a source of outliers in the observed data. However, unrealistically low wind speeds can also be caused by stuck anemometers, or for other reasons which are much more difficult to identify. Also, since R^2 is not robust, it is heavily influenced by phase errors. The following section briefly shows how the measures are affected by errors of different types.

4.6.6 Types of error

In relation to modelling, there is often a distinction between systematic errors in the average value of variables, often termed bias or level errors, and errors in the patterns of variables.

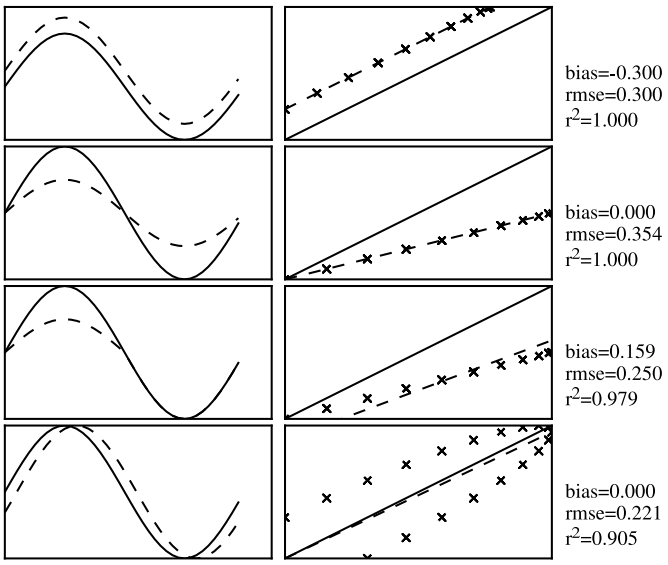

Figure 4.11: Schematic error types and effects on error statistics. Systematic errors (top) don't affect correlation. Amplitude errors, 2nd and 3rd, may affect both bias and correlation depending on whether they are symmetric. Phase errors (bottom) primarily affect correlation. The x-axis can be interpreted as time or space

Different types of pattern error affect error statistic in different ways, shown schematically in Figure 4.11. In relation to the wind speed dataset, different types of error have different implications. A systematic error could lead to wrong conclusions about the overall energy yield or profitability of a wind farm. However systematic errors are the easiest to correct using post-processing.

Phase or timing errors of a few hours could affect conclusions about how wind speed and electrical demand are related, but are not important from an overall energy production point of view. However, even small phase error can have very large impact on correlation statistics. For example, Kok et al. [2008] notes that high resolution models are often double-penalised in their assessment of performance, since although they may resolve smaller features than coarser models and hence provide more information,they may misplace or mis-time these features, leading to higher error statistics. This demonstrates the need for multiple statistics when comparing model performance, as there is no single measure which can adequately describe a model fit.

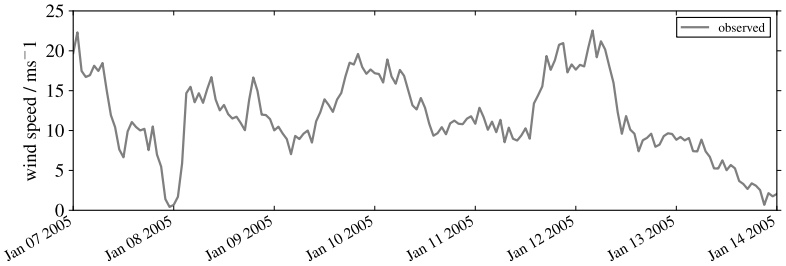

Figure 4.12: Observed wind speeds at Blackford Hill, Edinburgh over the case study period

4.7 Description of case study

The week of 7th-15th January 2005 is used as a case study. This was an active week with two very deep depressions crossing the north of the UK, causing some damage. Observed wind speeds at Blackford Hill met station (Edinburgh) are shown in Figure 4.12. Detailed description of the meteorological conditions associated with these events is described in [Hisscott, 2007], and the evolution of synoptic conditions in the GFS model are shown in Figure 4.13. This week shows a wide range of variability, from periods of relative calm, to periods where wind speeds exceed the typical cut-out speeds of turbines; the ability to recreate such patterns accurately is therefore very important.

It would have been preferable to also include a case study where synoptic forcing was not so strong, and thermal effects were more significant. However, during this phase of the project, time and computational constraints did not permit this.

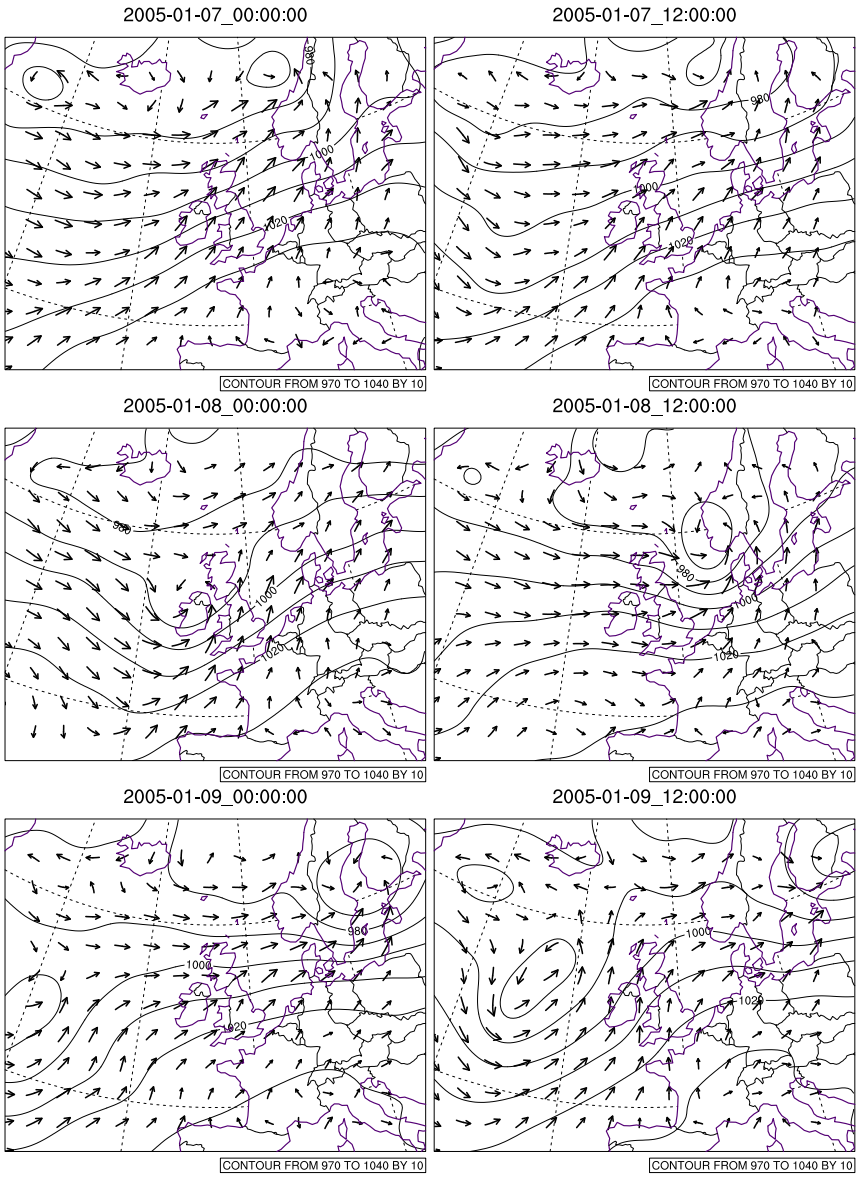

Figure 4.13: Evolution of synoptic conditions over the first few days of the case study period. This was a week of generally westerly flow with frequent formation and passage of depressions, with an occasional ridge of high pressure. Surface pressure and 10m wind speed are shown from GFS final analysis.

4.8 Comparison of model configurations

4.8.1 Baseline

The baseline configuration is summarised in Table 4.6.

	Domain		
	d01	d02	d03
Resolution (km)	27	9	3
Grid cells west-east	145	196	331
Grid cells south-north	115	181	391
Vertical levels	27	27	27
Timestep (s)	135	45	15
Feedback	-	Yes	Yes
SST update	No	No	No
Vegetation fraction update	Yes	Yes	Yes
PBL scheme	YSU[a]	YSU	YSU
Analyses nudging	No	No	No
Nudging in PBL	No	No	No
Cumulus scheme	Kain-Fritsch[b]	Kain-Fritsch	None
Boundary conditions	NCEP GFS final analysis $1^\circ \times 1^\circ$		
Land use dataset	USGS		
Surface layer physics	Monin-Obhukov [Janjic, 1996]		
Ground surface scheme	Noah Land Surface Model [Chen and Dudhia, 2000]		
Microphysics	WSM 5 class [Hong et al., 2004]		
LW physics	Rapid Radiative Transfer Model [Mlawer et al., 1997]		
SW Physics	Simple downward [Dudhia, 1989]		
Diffusion	2nd order on model levels		
Eddy diffusion coefficient	Smagorinksy first-order closure		

[a] YSU [Hong et al., 2006]
[b] [Kain, 2004]

Table 4.6: Baseline configuration

4.8.2 Alternatives

Land use options tested were the default USGS and the MODIS dataset (see §3.4.7). PBL options tested were the YSU and MYJ schemes, (see §3.4.6). Different permutations of configurations of analysis nudging were tested, both in upper levels and within the PBL, and default and increased spacing of η levels were tested.

Table 4.7 describes the alternative configurations studies and presents the overall error statistics against the in-situ observations,, while Figure 4.14 presents the distribution of B between observation sites.

The baseline configuration [1] gave relatively high bias and low correlation. The distribution

Label	Land use	Eta spacing[a]	PBL[b]	Analysis nudging[c]				Error statistics		
				d1	d2	d3	PBL	B (ms^{-1})	RMSD (ms^{-1})	R^2
[1]	USGS	d	YSU	—	—	—	—	2.11	3.61	0.69
[2]	USGS	d	YSU	tqu	tqu	tqu	—	2.35	3.56	0.76
[3]	Modis	d	YSU	tqu	tqu	tqu	—	1.62	3.14	0.77
[4]	Modis	d	MYJ	tqu	tqu	tqu	—	1.44	2.89	0.78
[5]	Modis	d	MYJ	tqu	tqu	—	—	1.41	3.06	0.73
[6]	Modis	d	MYJ	tqu	tqu	tqu	tqu	0.79	2.84	0.77
[7]	Modis	d	MYJ	tqu	tqu	tqu	–u	1.34	2.84	0.73
[8]	Modis	i	MYJ	tqu	tqu	tqu	tqu	0.63	3.01	0.74
[9]	Modis	i	MYJ	tqu	tqu	tqu	–u	1.34	2.84	0.81

[a] d=default spacing, i=increased spacing close to the ground
[b] YSU=Yonsei state university, MYJ=Mellor Yamanda and Janjic
[c] t=temperature, q=water vapour mixing ratio, u=wind speeds.

Table 4.7: Comparison of error statistics for configurations tested

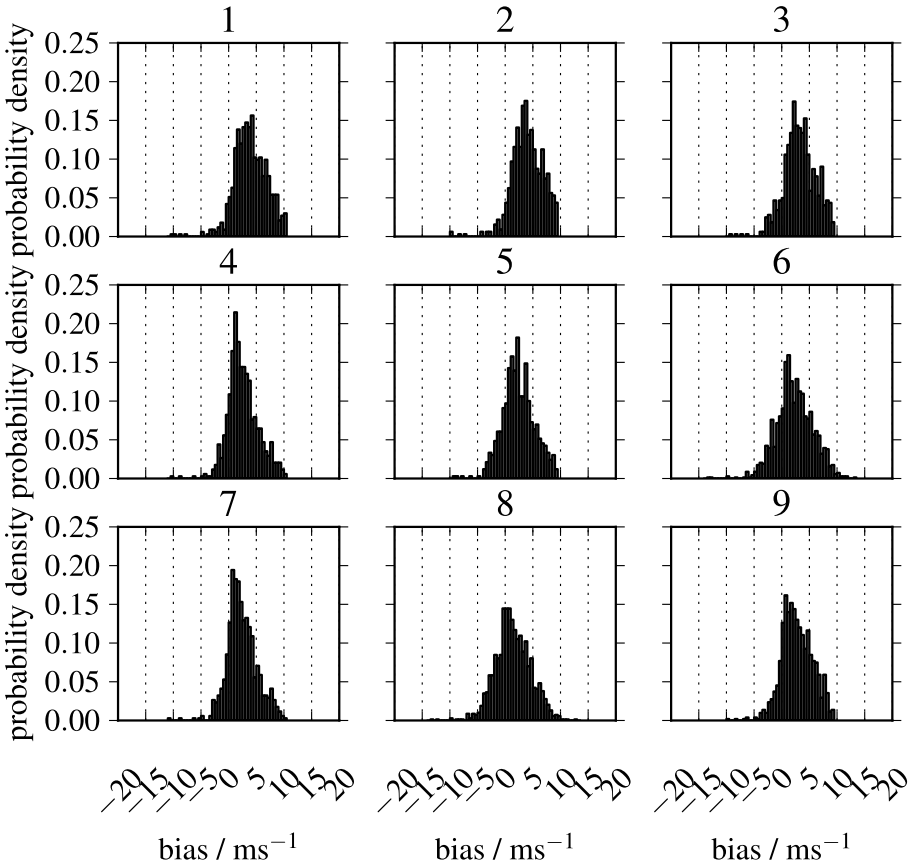

Figure 4.14: Error distributions at met stations for alternative model runs. Plot numbers refer to labels in Table 4.7

of errors can be seen to be skewed towards the high end, showing wind speeds are consistently over-predicted at most sites.

Using analyses nudging, [2], substantially improves the correlation (R^2=0.76) although does not significantly change B or RMSD. An explanation might be that nudging helps to correct phase errors, which can which have a large impact on R^2.

Using the MODIS land use dataset [3] gives a small improvement in B and RMSD, with little effect R^2. A possible explanation is a more realistic roughness values around observation sites, but a high wind-speed bias still exists.

Using the MYJ PBL scheme [4], instead of the YSU [3], appears to give a reasonable improvement in B and RMSD, although the reasons for this were not investigated in detail, as no vertical profiles of wind speed, temperature or other variables were available at this stage.

The configurations [4-7] use different approaches for analysis nudging. Turning analysis nudging off completely in the inner domain, [5] compared with [4], reduces R^2 slightly, from 0.78 to 0.73. Nudging within the PBL, [6] compared with [4], significantly reduces B to 0.79 ms$^-1$. Nudging u, but not t and q within the PBL, [7], causes the B to increase again.

Increasing the vertical resolution close to the ground, [8] compared to [6], decreases the B from 0.79 ms^{-1} to 0.63 ms^{-1}, although with a slight reduction in correlation. This also gives a reasonably symmetric distribution of errors.

Finally [9], using increased vertical resolution close to the ground, coupled with no-nudging of t or q in the PBL gives the highest correlation of all configurations tested $R^2 = 0.81$, although with a reasonably high bias of 1.34 ms^{-1}.

From these comparisons, no single configuration appears a clear winner, although there are significant improvements over the baseline. Given the end use is to assess the contribution that wind energy may make, it is prudent to weight B more heavily than other statistics, to avoid systematically over-stating the energy available from wind. For that reason, configuration [8] was selected for the full simulation runs, as this gives the lowest overall bias, yet reasonable correlation and RMSD.

One consistent result among the comparisons is a high wind speed seen at onshore surface stations. It seems that analysis nudging corrects this systematic high bias somewhat. However,

this may be by providing an artificial sink for momentum which should more properly get removed by other processes.

A recent analysis [Mass and Ovens, 2011] suggests that WRF exhibits a high wind speed bias over land due to the exclusion of sub-grid orographic drag in the formulation of roughness lengths. By formulating roughness length including these effects, they were able to significantly reduce the high wind speed bias in low-level winds. However, their adapted PBL scheme is not yet available in WRF. In the absence of this, it seems that analysis nudging may be providing an artificial sink of momentum which should be removed by turbulent processes.

A number of recent studies have evaluated different PBL schemes and other options in WRF [Hu et al., 2010, Jin et al., 2010], although these were not available at the time of this analysis. However the findings are generally inconclusive, with different PBL schemes having different strengths and weaknesses, and no single scheme found to be decidedly better. Furthermore, results from different regions of the world may not be applicable, and each configuration may have its own particular strengths and weaknesses depending on the application.

4.9 Choice of configuration

Configuration [8] was used for the full simulations. This is summarised in Table 4.8, and the complete set of options, as defined by the *namelist.input* file is included in Appendix B.

4.10 Chapter summary

This chapter describes how WRF was configured and verified against observations, before committing to a long reanalysis. The practical limitations regarding the availability and timing of the computing resource were described, which limited the number of permutations which could be tested and the length of the case study used. All the observational datasets used for verification, both in this chapter and in later chapters are described. The options which were held constant during this and later stages were outlined.

The verification process was then described, including the technique for comparing model output to point observations with a discussion of some of inherent challenges. A number of error statistics were defined, and it was demonstrated how they are affected by different error

	Domain		
	d01	d02	d03
Resolution (km)	27	9	3
Grid cells west-east	145	196	331
Grid cells south-north	115	181	391
Vertical levels	27	27	27
Timestep (s)	135	45	15
Feedback	-	Yes	Yes
SST update	Yes	Yes	Yes
Vegetation fraction update	Yes	Yes	Yes
PBL scheme	MYJ[a]	MYJ	MYJ
Analyses nudging	tqu[b]	tqu	tqu
Nudging in PBL	tqu	tqu	tqu
Cumulus scheme	Kain-Fritsch[c]	Kain-Fritsch	None
Simulation block	One month + 1 day spin up		
Boundary conditions	NCEP GFS final analysis $1^\circ \times 1^\circ$		
Land use dataset	MODIS[d]		
Surface layer physics	Modified Monin-Obhukov[e]		
Ground surface scheme	Noah Land Surface Model[f]		
Microphysics	WSM 5 class[g]		
LW physics	Rapid Radiative Transfer Model[h]		
SW Physics	Simple downard[i]		
Diffusion	2nd order on model levels		
Eddy diffusion coefficient	Smagorinksy first-order closure		

[a] [Janjic, 2002, Mellor and Yamada, 1982]
[b] t=temperature, q=water vapour mixing ratio, u=wind speeds
[c] [Kain, 2004]
[d] [Friedl, 2002]
[e] [Janjic, 1996]
[f] [Chen and Dudhia, 2000]
[g] [Hong et al., 2004]
[h] [Mlawer et al., 1997]
[i] [Dudhia, 1989]

Table 4.8: Final configuration of WRF used for all future simulation runs

types. Then, a week-long case study represented a meteorologically active week was chosen and outlined, and a series of model runs were made using different model configurations. Aggregate error statistics were calculated for each of the model runs, and were used to compare different configurations. On the basis of this comparison, the final configuration was chosen and defined; this is now taken forward to the main simulation phase.

Chapter 5
Simulation and Verification

5.1 Introduction

The previous chapter described a week long case study used to test different model configurations and select a configuration to use during main simulation phase.

This chapter now describes the simulation process used to create the reanalysis. Then, the complete reanalysis dataset is verified against available observations. Long-term averages and spatial and temporal patterns are compared to observations, and the nature of model errors are explored. A systematic low bias in offshore wind speeds is identified, which is then corrected in the following chapter.

5.2 Simulation process

For the main simulation phase an application was made via the Class 1B 'direct access' mechanism for an extended allocation on HECToR. The application was successful, and 6M AU were granted, roughly equivalent to 200 000 hours, or 23 years of processing time on a single CPU, to be used within six months of the allocation.

Simulation was performed in blocks of one calendar month, allowing one day for model spin-up. Using a simulation block of one month enables mesoscale features to develop and persist in the model, and avoids frequent re-initialisation. However, it also runs the risk of biases and errors compounding over time, for example, a low precipitation bias could lead to soil levels becoming too dry, which would re-enforce this bias. For that reason one month was deemed to be a good compromise to allow features to develop and persist, but prevents long-term drift. Additionally, using 512 processors, one month could be simulated within a single 12-hour job, which is the time-limit for single jobs on HECToR.

A reduced set of output variables were written to disk, detailed in Appendix B, and only the inner domain output files were kept, resulting in a raw output file size of 30GB per day. Storage

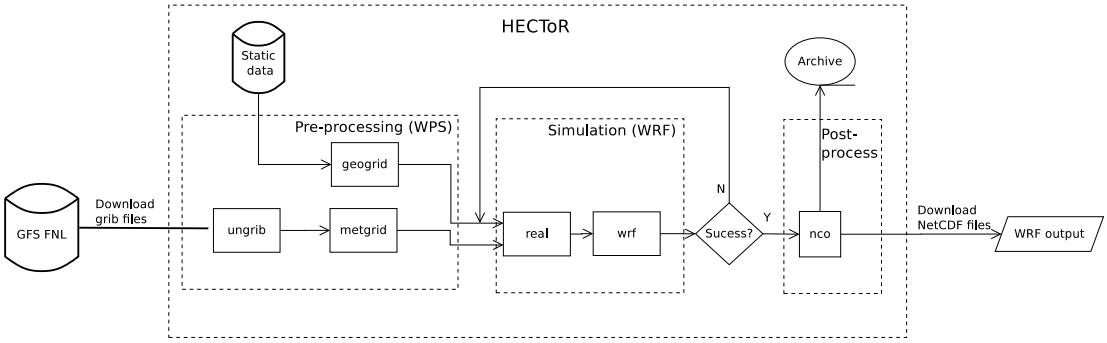

Figure 5.1: Schematic of the simulation process.

limitations meant that only one month at a time could be simulated. After completion, output files were processed using the NetCDF operators[1] (NCO) to remove all but the lowest five η levels, reducing the file size to just over 1GB per day. This meant variables were only retained in about the lowest 500m or so of the atmosphere, and a significant amount of information was disregarded. However, this was the only way to ensure the final dataset was a manageable size.

Each month required around 12-hours to simulate, plus several hours pre-processing and post-processing. The process was automated via a series of scripts, although manual intervention was frequently required, for example, to restart runs which had been interrupted by hardware failures. Additionally, during the six-month access window, the hardware on HECToR was upgraded from quad-core to 12-core, meaning system closures were fairly regular, and the system was split between two architectures which required re-compilation of various codes. Ten years of simulations were completed within the 6-month allowance, and an extension granted to compensate hardware disruption allowed another year to be simulated, giving an 11-year reanalysis.

Figure 5.1 shows a schematic of the process. Detailed information on the software components which collectively make up WRF are given in the user manual [NCAR, 2008], and are only briefly described here. GFS final analyses are downloaded directly to HECToR in gridded binary (GRIB) format one month at a time. These are unpacked (ungrib.exe) and interpolated (metgrid.exe) to the model domain using the WRF pre-processing software. Static data e.g. land-use and topography, are stored on HECToR and interpolated to the model domain only once (geogrid.exe). The meteorological data and static data are combined and vertically

[1] http://nco.sourceforge.net/

interpolated (real.exe) to produce initial conditions, boundary conditions and analysis nudging files. Finally the WRF solver (wrf.exe) is run to produce the simulation and write the output. If the simulation completed successfully, the the NCO tools are invoked to reduce the number of vertical levels and the resulting files are then transferred to a machine in Edinburgh, and also to the tape archive facility provided by HECToR. If simulation failed, the reason for the failure is investigated (usually a hardware failure, or a storage quota exceedance) and the simulation re-started from the nearest (weekly) restart point. Once a month of simulation files has been transferred from the working filespace, the process begins again for the next months simulation.

Table B.2 in Appendix B gives details of the output variables retained in the final output.

The final dataset consists of around 5 terabytes (TB) of NetCDF files, stored as one file per simulated day. Working with this volume of raw data is very slow, and makes analysis difficult. To facilitate analysis, time series are extracted at points of interest and stored in a relational SQL database. The gridded files are retained and used for the production of resource maps and for continuous spatial analysis; this dual data strategy is illustrated in Figure 5.2.

Eleven-year time series were extracted from the raw data file at all points of interest, namely the locations of observation stations and the locations of current and future wind farms. These time series were then stored in a relational database which allowed for detailed validation against observations, and for easy conversion to power output time series.

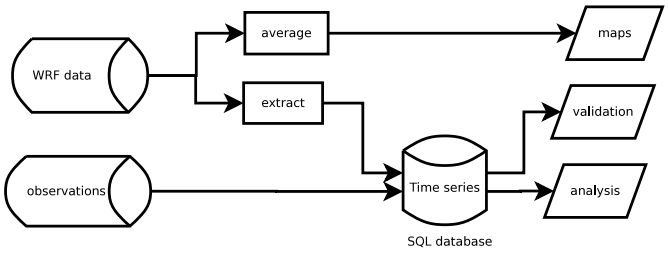

Figure 5.2: Data strategy involved the averaging of gridded data and the extraction of time series for analysis

5.3 Verification process

This section shows the results of verification of the whole dataset against observations described earlier in §4.4. The figures and statistics presented here summarise the performance across multiple observation sites; verification against specific individual sites are presented in

Appendix C.

In addition to the statistics described in §4.8.2, a number of visual tools were used to aid verification, which allow for more detailed insight into the nature of model errors.

5.3.1 Taylor and target diagrams

Taylor diagrams [Taylor et al., 2000] are based on centered statistics and summarise how well a model captures patterns in observations. Continuing the notation defined in §4.6.5, the centered RMSD is defined as:

$$RMSD' = \left\{ \frac{1}{N} \sum_{i=1}^{N} [(p_i - \bar{p}) - (o_i - \bar{o})]^2 \right\}^{1/2} \tag{5.1}$$

which can be decomposed into amplitude and correlation terms [Murphy, 1988]:

$$RMSD'^2 = {\sigma_p}^2 + {\sigma_o}^2 - 2R \cdot \sigma_p \sigma_o \tag{5.2}$$

Eq. 5.2 has the same form as the cosine rule, and Taylor diagrams are plotted in polar coordinates, (a, θ), where:

$$a = \sigma_* = \frac{\sigma_p}{\sigma_o} \tag{5.3}$$

$$\theta = cos^{-1}(R) \tag{5.4}$$

This makes RMSD′ proportional to the distance from the reference point $(1, 0)$. Points with higher correlation lie closer to the x-axis, and points which capture the observed standard deviating well lie closer to the contour $\sigma_* = 1$. Since Taylor diagrams are based on centred statistics, they do not say anything about absolute bias, and should be interpreted alongside an indications of bias. To facilitate this, data on the Taylor diagrams presented here are shown coloured by B. An example is shown in Figure 5.3.

Target diagrams [Jolliff et al., 2009] show centered statistics and bias on the same diagram. The

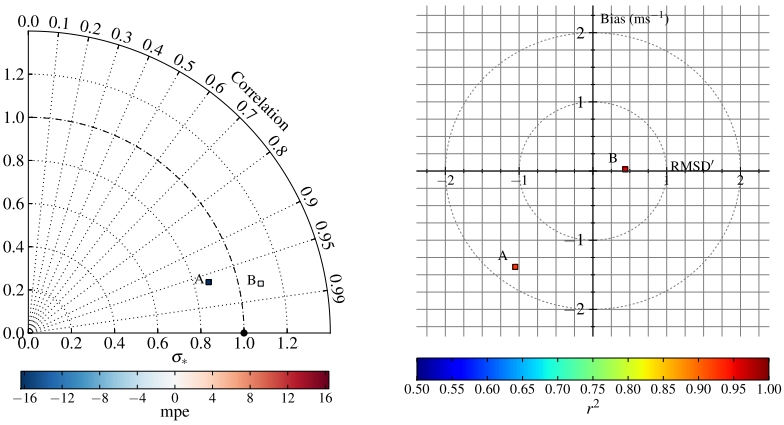

(a) Taylor diagram

(b) Target diagram

Figure 5.3: Example Taylor and target diagrams. Taylor diagrams show how well a model captures patterns in observations; target diagrams show how much of the total RMSD is due to bias. Points A and B have similar correlation, but A has a systematic bias. Point A underestimates σ, and B overestimates σ.

total RMSD is related to RMSD′ and the bias by [Murphy, 1988]:

$$RMSD^2 = B^2 + RMSD'^2 \tag{5.5}$$

A target diagram plots RMSD′ on the x-axis and B on the y-axis: the x-axis indicates how much of the RMSD explained by pattern error, and the y-axis indicates how much is explained by systematic error. The distance to the origin gives the total RMSD. Furthermore, although RMSD′ is, by definition, positive, the whole axis can be used by assigning it the sign of $\sigma_p - \sigma_o$ [Jolliff et al., 2009]. Therefore, whether a point is left or right of the y-axis indicates whether the model variance is larger or smaller than the observed. Since target diagrams contain no information about correlation, points on the diagrams have been coloured according to R^2. An example is shown in Figure 5.3.

5.3.2 QQ plots

Quantile-quantile (QQ) plots are a way of comparing two distributions. Quantiles from an observed set of data are plotted against quantiles of another, either observed or theoretical, distribution. Figure 5.4 shows a comparison of two Weibull distributions. $S2$ is a linearly scaled version of $S1$, which manifests itself in the QQ plot as a steeper, but constant gradient.

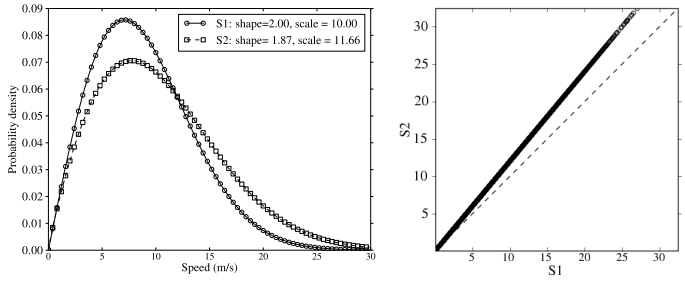

(a) (b)

Figure 5.4: (a) Distributions $S1$ and $S2$, where $S2 = 1.2 \times S1$. (b) Resulting QQ plot.

5.4 General agreement

Table 5.1 presents overall error statistics by class of in-situ observation, computed by pooling all observations within that category. It shows a small positive bias at met stations and windfarm masts, and a reasonably large negative bias at offshore, particularly at lightships where B=-1.35ms^{-1}. WRF consistently under-predicts the observed standard deviation. This is evident on the Taylor and target diagrams, Figure 5.5. The centered statistics show better performance offshore, but systematic bias at buoys and lightships is evident.

category	n	obs mean ms^{-1}	wrf mean ms^{-1}	obs σ ms^{-1}	wrf σ ms^{-1}	B ms^{-1}	RMSD ms^{-1}	R^2
Met station	222	5.00	5.15	3.34	2.85	0.15	2.03	0.64
Mast	6	7.66	7.93	4.14	3.81	0.27	2.27	0.71
Buoy	9	7.30	6.48	3.63	3.24	-0.82	2.02	0.74
Lightship	4	8.48	7.13	4.31	3.60	-1.35	2.30	0.82

Table 5.1: Summary of error statistics by in-situ observation type

The wind speed distributions and resulting QQ plots are shown in Figure 5.7. For onshore met stations, the model output is very good, representing the observed distribution very well across the range of wind speeds.

For onshore windfarm masts, the agreement is also very good, but begins to deviate towards the tail of the distribution, showing that WRF does not represent peak wind speeds well. In terms of the overall energy from wind this is not important, since wind speeds in this range will be in the constant region of the power curve. However, it suggests against using the dataset to explicitly investigate peak wind speeds e.g. when assessing the frequency of high-wind cut-outs or for assessing structural design loads.

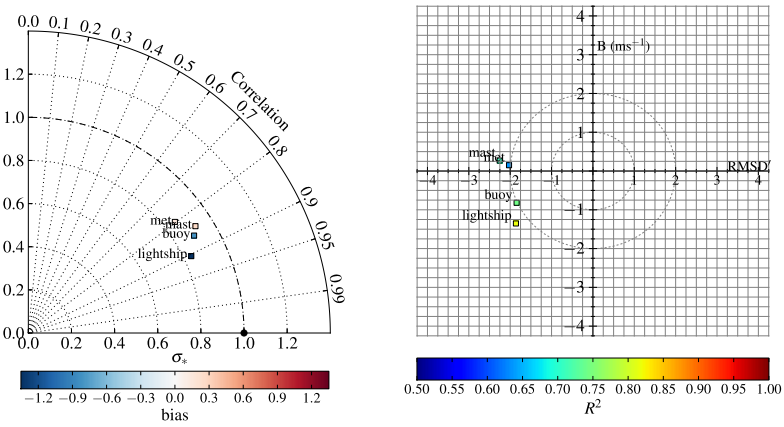

(a) Taylor diagram

(b) Target diagram

Figure 5.5: Taylor and target diagrams by observation category

For buoys and lightships the distributions confirm a systematic negative bias, evident in a steeper gradient on the QQ plot, which is most evident at lightships. This also shows the bias not entirely due to the failure to represent peak wind speeds, but is present across a wider range of speeds. However, the linear nature of the QQ plot shows that, aside from the systematic error, the underlying form of the distribution is very good. This is also confirmed by the high correlation seen at buoys and lightships, which shows that the patterns of wind speed are captured very well.

Finally, the error in the average hourly speed is calculated across all onshore and offshore observations, and the distribution of this is shown in Figure 5.8. Again, onshore wind speeds can be seen to be unbiased overall,with a almost zero-centered and symmetric distribution. The offshore speeds are consistently too low, with a distribution shifted to the left, and symmetric about the mean.

In each case, the errors are not quite Normally distributed. Given the large number of observations, confidence intervals can be estimated directly from the percentiles, are summarised in Table 5.2.

5.5 Spatial agreement

Figures 5.9 show the spatial distribution of error statistics against in-situ observations. There are a range of values, though there is no noticeable geographic trend i.e. the performance does

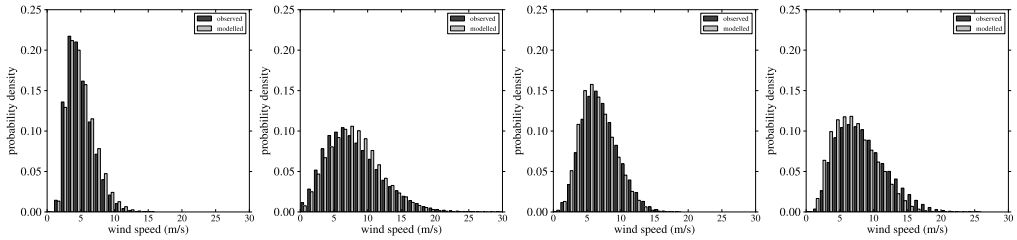

(a) Met station (b) Masts (c) Buoys (d) Lightships

Figure 5.6: Histograms of observed and simulated wind speed by category of observation

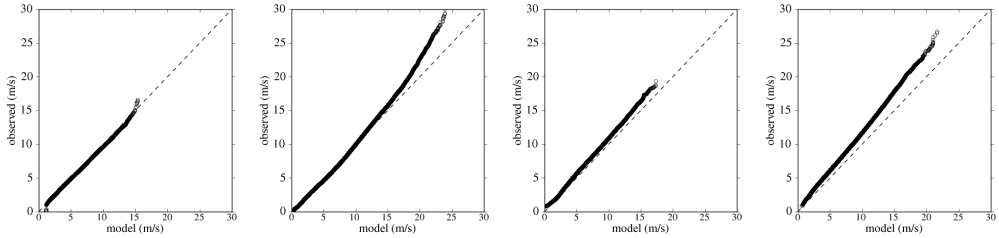

(a) Met station (b) Masts (c) Buoys (d) Lightships

Figure 5.7: QQ plots by observation category

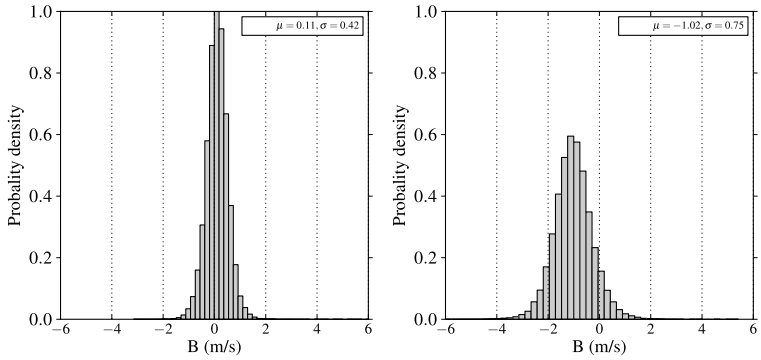

(a) Onshore error distribution (b) Offshore error distribution

Figure 5.8: Distribution of hourly bias against all onshore and offshore in-situ observations.

	Onshore ms^{-1}	Offshore ms^{-1}
B	0.11	-1.02
80% CI	$\pm$0.51	$\pm$0.91
90% CI	$\pm$0.68	$\pm$1.21
95% CI	$\pm$0.85	$\pm$1.50

Table 5.2: Confidence intervals on B by comparison with in-situ observations

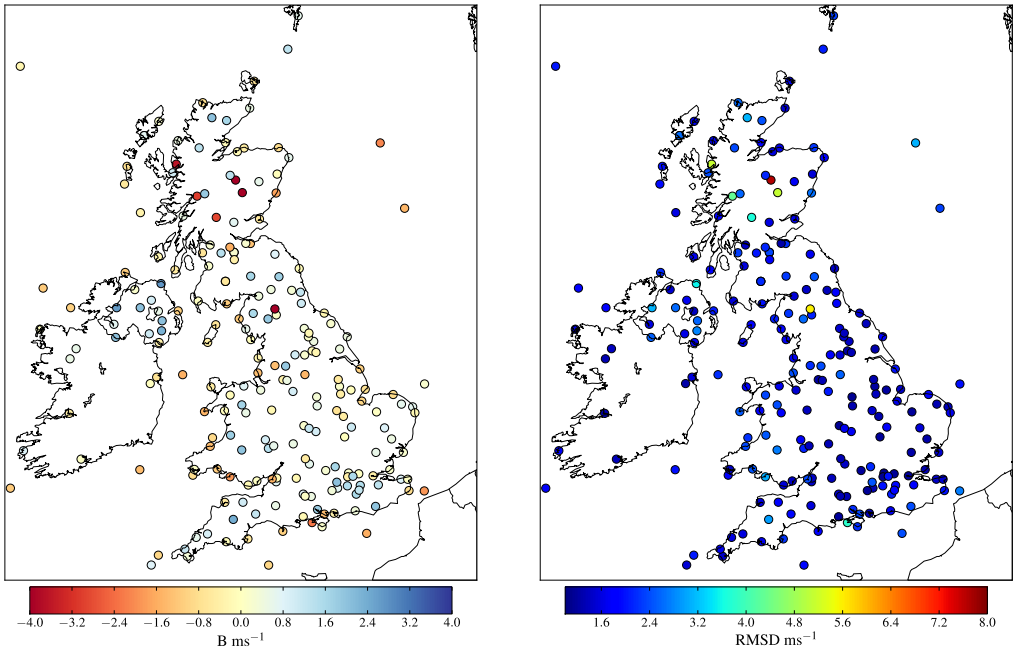

Figure 5.9: Geographic distribution of B and RMSD

not depend on latitude or longitude.

Figure 5.10 shows the distribution of B across in-situ observation points. It can be seen that the vast majority of stations have $-2.0 < B < 2.0$, with a few outliers with very high error statistics. These outliers in terms of error statistics are investigated later.

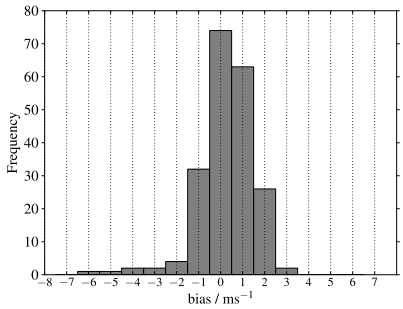

Figure 5.10: Distribution of average bias at individual met stations

5.6 Temporal agreement

This section examines the extent to which model winds recreate temporal patterns on a number of temporal scales.

5.6.1 Time series

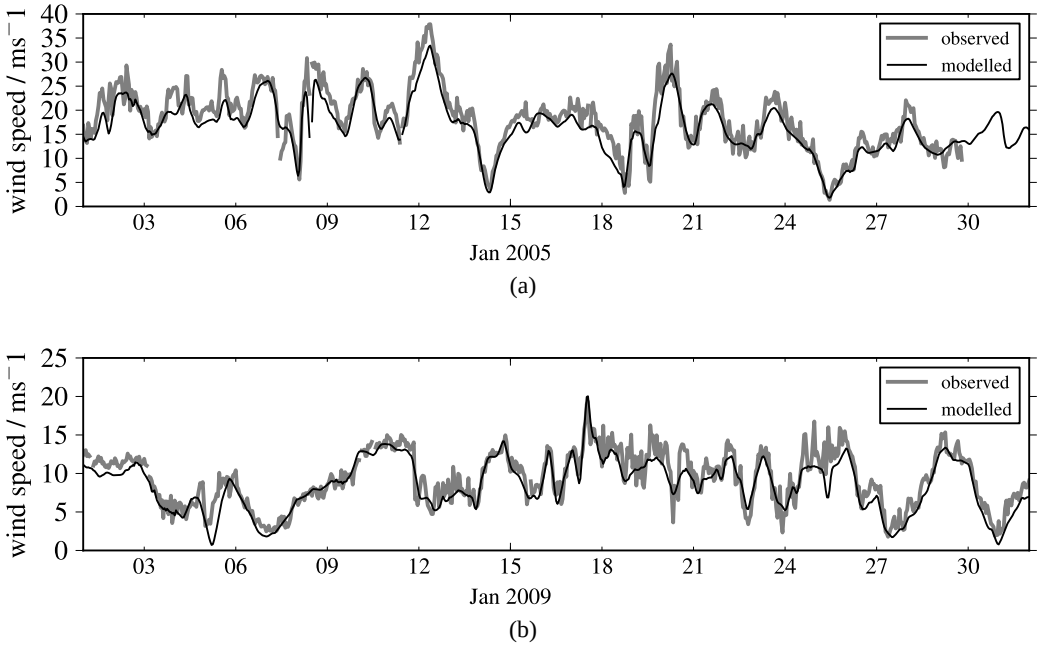

Figure 5.11: Simulated and observed wind speed at for one month at (a) Nelson A oil platform and (b) M3 buoy

Time series plots show the model wind match observed patterns very well: Figure 5.11 gives an example of the typical match between observed and simulated wind speeds. The observed wind speeds show some higher-frequency variation than model speeds, but the main patterns are captured very well. There are too many such plots to include, so the following sections examine the temporal match in average wind speeds across temporal scales.

5.6.2 Diurnal

Figure 5.12 shows observed and simulated wind speeds by hour of the day across all observation types. Wind speeds are presented as anomalies from mean, so that systematic errors are excluded.

At met stations the modelled diurnal pattern is very close to the observed, and has the correct amplitude and shape. It appears to lead the observed pattern by around one hour, suggesting the growth of the daytime boundary layer is slightly too fast, and its decay too rapid. At wind farms masts, the diurnal amplitude is slightly underpredicted. It is worth noting that the observed diurnal pattern seen at wind farms masts is much smaller than the pattern seen at met

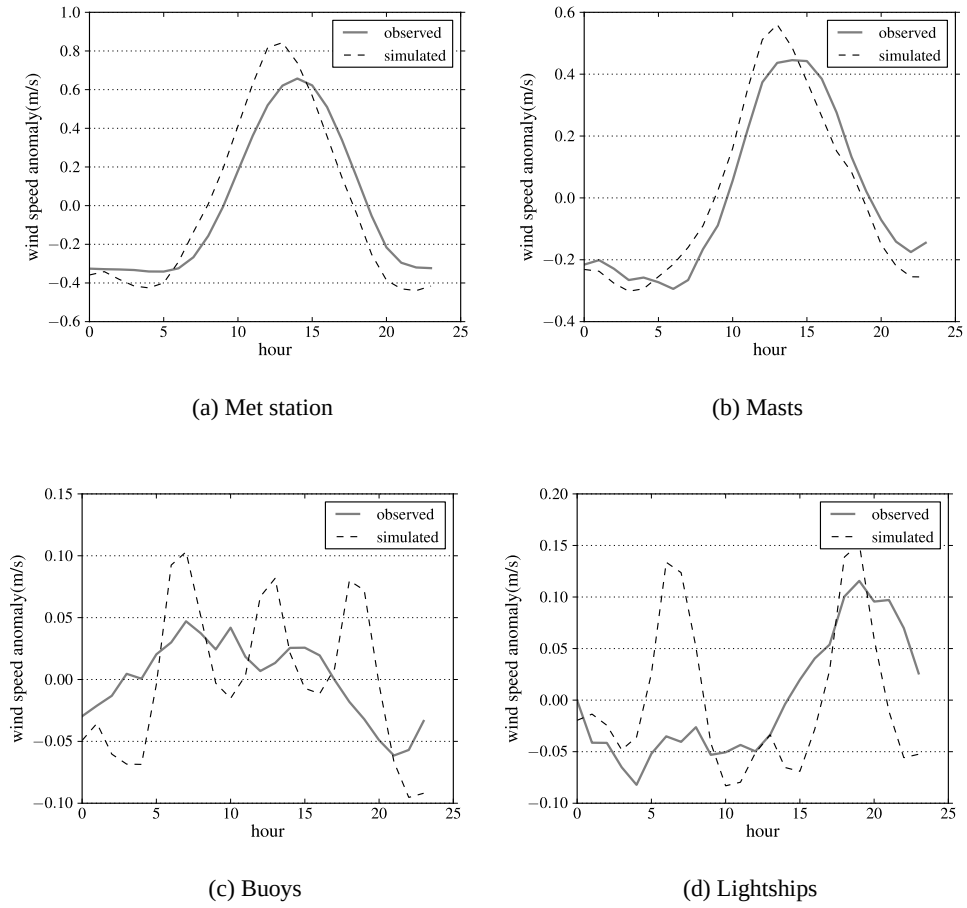

(a) Met station

(b) Masts

(c) Buoys

(d) Lightships

Figure 5.12: Observed and modelled average diurnal variation at in-situ observations.

stations, which are at 10m agl.

Offshore, diurnal variation would be expected to be less, and both the observations and simulations reflect this, with any departures from the mean only around 0.1ms^{-1}. At lightships, both the observations and simulations show a pattern possibly characteristic of a weak sea breeze, although the amplitude of this pattern is larger in the simulations. At buoys, the simulated pattern has three distinct peaks, which may be a superposition of different diurnal patterns seen in onshore and offshore flows. A three-peak pattern is faintly present in the observation. The amplitude of all of these patterns is very small. It is worth noting that Lapworth [2005] also found a diurnal pattern at lightships which was not characteristic of a sea breeze or orographic induced jets.

Overall, this analysis suggests the model captures diurnal variations very well, with only minor

differences compared to observations. It would be interesting to look in more detail at coastal thermal circulations, but this is left for future work.

5.6.3 Seasonal

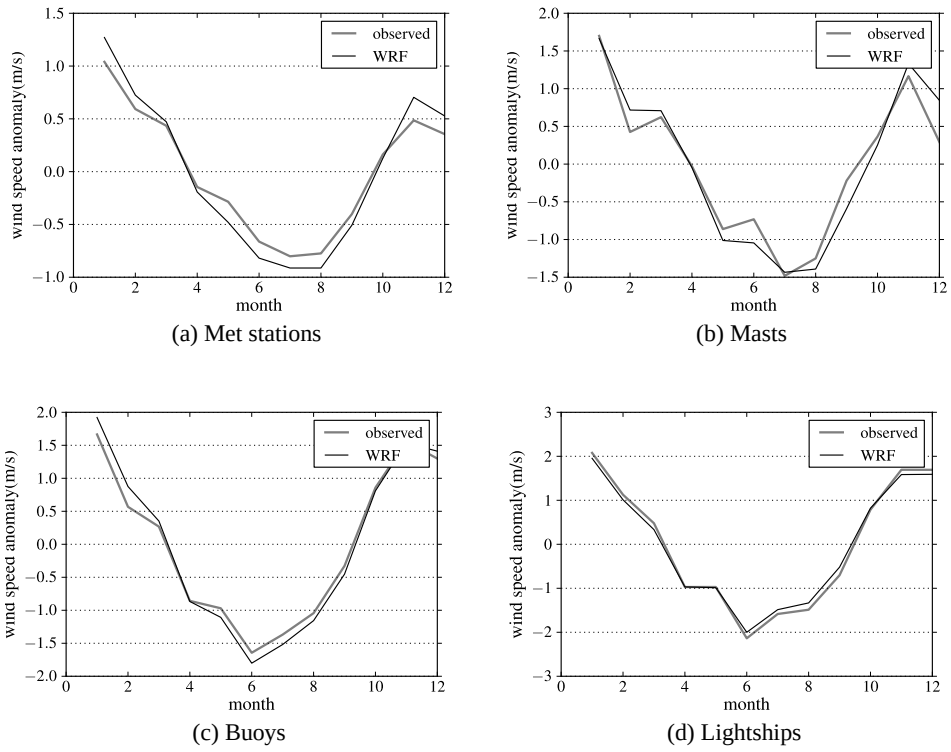

(a) Met stations (b) Masts

(c) Buoys (d) Lightships

Figure 5.13: Observed and modelled variation in monthly wind speeds

Figure 5.13 shows observed and simulated wind speeds by month of the year. The seasonal pattern matches observations very well in all cases, with highest wind speeds in January, and lowest between June and August, and with seasonal variation slightly larger offshore.

5.6.4 Inter-annual

Figure 5.14 shows wind speed anomalies over 2000-2010 across all the in-situ observations which had observations spanning the whole period. Separate plots per category are not presented, since many sources do not span the whole period, or have periods of missing data in certain years. The model capture the inter-annual variations well. There are only minor differences, which may have a physical cause, but equally could relate to changes in the number

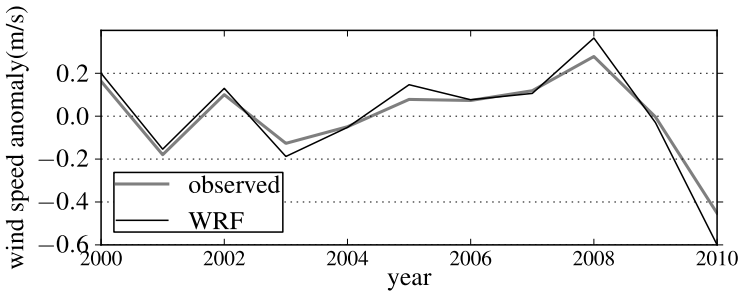

Figure 5.14: Observed and simulated annual wind speed anomalies over the period 2000 - 2010.

of sources included in the observational record.

Of note is the unusually low wind speeds in 2010. These were caused by a strong blocking high pattern over northern Europe, evident in a negative winter North Atlantic Oscillation (NAO) index, perhaps the lowest on record. These variations in the large-scale circulation are very significant in terms of power production [Brayshaw et al., 2011].

5.7 Vertical profiles

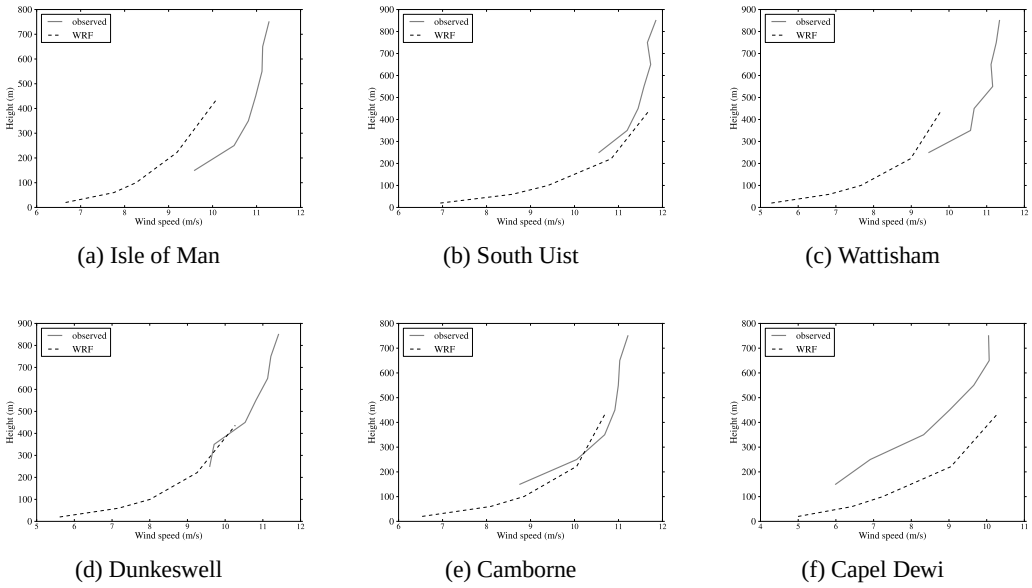

(a) Isle of Man (b) South Uist (c) Wattisham

(d) Dunkeswell (e) Camborne (f) Capel Dewi

Figure 5.15: Comparison of vertical profiles from WRF and radar profilers. The agreement in the overlapping region is reasonably good aside from the Isle of Man and Capel Dewi, where the shape is reasonable but the profile shows a systematic displacement

Substantial effort was made to obtain data from offshore masts with anemometers at multiple heights. However, due to the very high cost of the masts and the commercial sensitivity of the results, detailed observations of offshore profiles were not available. The only datasets available with vertical profiles are the UKMO radar profilers described in §4.4.7.

Most of the UKMO radar profilers begin reading at 200m agl or more. Since only the lowest five η levels are retained in the WRF output, this gives limited overlap, and doesn't allow comparison at typical hub heights. The radar profilers are at least 1km inland, with the exception of the Isle of Man and South Uist. The Isle of Man profiler is on the east coast with prevailing winds coming over land; only South Uist is likely to be representative of an offshore profile.

Raw profiler data was obtained from the BADC, and then bin-averaged using 50m bins to derive vertical profiles at each site. Figure 5.15 compares average vertical profiles derived from radar observations to WRF simulations over the same period.

A promising feature of the comparison is that, in the overlapping region, the profile shapes

appear to agree very well. At the Isle of Mann and Capel Dewi there is a systematic displacement of the profile. This suggests that any systematic errors detected at low levels might be reasonably constant with height, and any corrections determined at surface level may be applicable up to typical hub-heights.

5.8 Investigation of errors

The verification so far has shown that average wind speeds agree well onshore, although there is a low bias offshore. It has also shown that the spatial and temporal patterns are captured very well. This section investigates potential causes of errors, so that a better understanding of the model performance can be gained, and so that some insight might be gained as to how to tackle the systematic bias offshore.

5.8.1 Terrain

Figure 5.10 shows the majority of stations have -2ms^{-1}< B <2ms^{-1}, with a few outliers with a large negative bias. On inspection, the stations with $B < -3$ms^{-1}are those situated on mountain tops, listed in Table 5.3.

Station	Elevation m	B ms^{-1}	RMSD ms^{-1}	R^2
Cairngorm Summit	1245	-6.24	7.68	0.68
Great Dun Fell	847	-4.68	5.57	0.74
Cairnwell	933	-3.94	5.10	0.72
Bealach na Ba	773	-3.63	5.15	0.63
Aonach Mor	1130	-3.02	4.28	0.58
Glen Ogle	564	-2.88	3.69	0.62

Table 5.3: Outlier met stations were those situated on mountain tops. Elevation given is the station elevation, not the model terrain.

Terrain has the largest influence on local wind speed, and mesoscale model at 3km resolution will not represent complex terrain very well. To explore this a measure of terrain complexity was computed using higher resolution SRTM4 terrain data [Farr et al., 2007]. SRTM4 data at approximately 90-metre resolution was used to compute Δh, the terrain height range within each 3km model cell, based on the 90m DEM data. Figure 5.16 shows the range of B and R^2 if the stations are partitioned by Δ_h, using the definitions:

- smooth: $\Delta_h \leq 50m$;
- complex: $50 < \Delta_h \leq 100m$; and
- extreme: $\Delta_h > 100m$

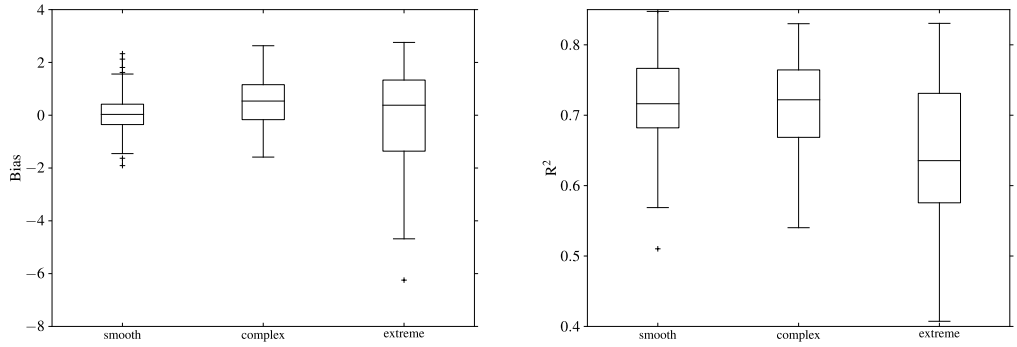

Figure 5.16: Distribution of B and R^2 for met stations in smooth, complex and extreme terrain. Whiskers denote 1.5 times the inter-quartile range.

It is evident that performance degrades in complex terrain. This is not surprising since five grid points are needed to accurately capture a terrain feature, although simply shaped hills can be represented with less. It may be possible to correct for terrain using one of the numerous 'rules of thumb' e.g. [Lemelin et al., 1988, Lubitz and White, 2007]. These are formulated based on wind tunnel experiments and field trials, in particular the Askervein field trial [Castro et al., 2003]. Typically terrain is classified as distinct features such as a ridge or a hill, which can represented by a characteristic length and height, used to determine a speed-up factor. For example, Howard and Clark [2007] develop and apply a simple terrain correction for NWP forecasts based on the linear flow theories of Jackson and Hunt [1975]. However, this approach would be difficult to generalise across the whole country, and difficult to automate.

A better way to account for the local terrain would be to nest a higher resolution linear or non-linear flow model, see e.g. Ayotte [2008] for a review of these techniques. However, even with a higher resolution model the flow in complex terrain is difficult to model, particularly where there is flow detachment and recirculation and this remains a challenge for many models e.g. [Bitsuamlak et al., 2004, Castro et al., 2003, Undheim, 2005]. Since the purpose here is a national-scale assessment, it was not thought necessary to adopt this kind of microscale approach across the whole model domain for the purposes of improving point predictions. Such an approach can be performed as necessary if the data is to be used for micro-siting.

Additionally, the output from WRF is the steady flow through a 3km grid cell, which in some cases may be a better indicator of the average wind conditions across a whole wind farm site than a highly-resolved prediction at a single point. Therefore it was not thought necessary to apply considerable effort to resolve fine-scale features, at least not until the power outputs from windfarms had been verified.

Furthermore, although wind farms are found in reasonably complex terrain, they are unlikely to be sited in terrain classified here as extreme, partly due to physical reasons of increased turbulence and construction difficulties, but mainly as these areas correspond to mountain ranges which, in the UK, mostly have environmental designations that prevent windfarm development.

5.8.2 Roughness length

Although performance against windfarm masts was generally very good, systematic biases were found at a some of the windfarm masts sites. This can be seen in a raw time series plot for the mast S1, shown in Figure 5.17.

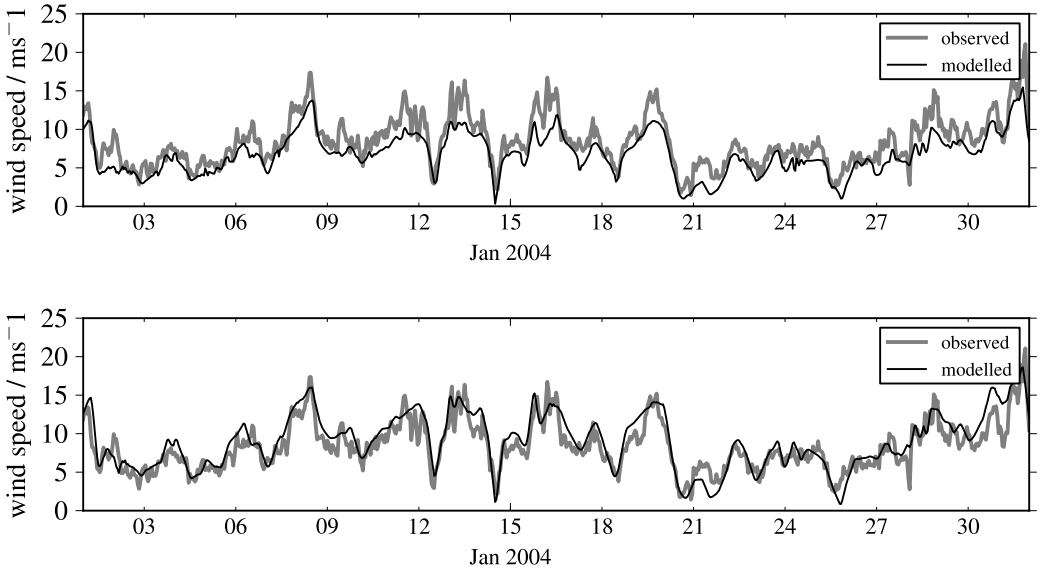

Figure 5.17: Influence of roughness length on simulated wind speed mast S1. Top: wind speeds are interpolated from the closest model level using the original roughness length. Bottom: wind speeds are interpolated from a higher model level ($\approx$ 100m) using the revised roughness length. This can be seen to remove much of the systematic error.

Mast	Figures	z_0	B	RMSD	R^2
C1	default	0.21	-2.52	3.50	0.77
C1	revised	0.05	-1.78	2.90	0.75
S1	default	0.50	-1.35	1.90	0.80
S1	revised	0.03	-0.07	1.68	0.74

Table 5.4: Default and revised roughness lengths at wind farm masts and consequent changes in error statistics

A major source of systematic error is the parametrisation of roughness length. For example, the grid cell containing S1 has a roughness length in WRF of 0.50m, which represents very rough terrain. The operators of the wind farm site suggest that this is too high (Personal communication), and that a roughness length of 0.03m is more appropriate. Figure 5.17 shows the effect of changing the roughness length and scaling the wind speed from WRF from a higher model level ($\approx 100m$) using a neutral logarithmic profile.

The roughness length parameterisation at all six of the masts was reviewed in consultation with the site operators and by examining their location on Ordnance Survey maps. Two major revisions to roughness length were made, at C1 and S1. S1 had been wrongly attributed to forestry (there was some forestry nearby) and C1 had been wrongly attributed to an urban land-use category (there was a small town nearby). Revisions to roughness lengths are listed in Table 5.4, which also shows the revised error statistics. This can only improve systematic errors and will not improve phase errors. In fact there is a slight deterioration observed in the correlation as a result of taking the wind speed from a higher level. This may be a result of ignoring features of the wind profile resolved in the lower levels e.g. nocturnal jets. However, this was deemed to be less important than the significant reduction in model bias.

This confirms findings of Brower et al. [2004], who found the adequately characterising roughness length was one of the major sources of error in mesoscale models, but also demonstrates that it may be possible to improve the performance at particular locations post-hoc, with the use of higher resolution terrain and land-use data.

However, this result should be interpreted with some caution, as an examination of mast profiles reveals. Of the mast data obtained here, S2, S3, and C2 had anemometers at three individual heights which allowed their profiles to be examined; wind profiles above homogeneous terrain in neutral conditions should exhibit the logarithmic profile defined in §2.6.3. Figure 5.18 shows a plot of $ln(z)$ vs $\bar{U}$ for masts S2, S3 and C2. Since there was not enough information

at the masts to correct for atmospheric stability, only observations likely to be from neutral atmospheric conditions were used. The stability parameter ζ from WRF was used to aid the selection, and only daytime wind speeds (10:00 to 16:00) where $|\zeta| < 0.02$ were used to derive the profiles.

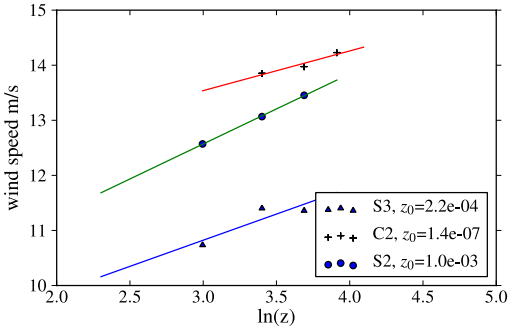

Figure 5.18: Observed vertical profiles at three windfarm masts and fitted logarithmic profiles. Only daytime wind speeds where $|\zeta| < 0.02$ are used in the averaging

Very low wind shear is seen at all masts: S3 actually shows lower wind speed at 40m than 30m. Plotting a least-squares line of best fit allows roughness length to be estimated, albeit with considerable uncertainty [Schaudt, 1998, Wieringa, 1993]. From the line of best fit:

$$\bar{U} = A \cdot ln(z) + B \tag{5.6}$$

z_0 can be estimated at $\bar{U} = 0$. This approach gives roughness lengths (shown on the legend) many orders of magnitude smaller than would be expected based on the prevailing land-use. Even S2, which shows the closest agreement to a logarithmic profile has $z_0 = 0.001$m which is the roughness typically associated with a flat sea surface, considerably lower than expected from the actual land use.

The conclusion is that the observations themselves do not exhibit a surface layer logarithmic profile. This could be due to orographic effects, upwind roughness-length changes, instrumentation error, or flow distortion around the instruments. It suggests that attempts to improve predictions at individual sites would require more detailed modelling, and highlights the danger of using simple scaling laws to downscale from higher levels. It would be interesting to perform some microscale simulations driven by the 3km WRF outputs, but for a national-wide assessment, it was not thought necessary to pursue this approach.

Month	obs mean	wrf mean	obs std	wrf std	B	RMSD	R^2
1	9.89	8.92	4.52	3.82	-0.97	2.33	0.78
2	8.71	7.74	4.19	3.57	-0.97	2.39	0.73
3	8.26	7.15	4.06	3.36	-1.11	2.28	0.76
4	6.98	5.89	3.54	2.96	-1.09	2.05	0.76
5	6.91	5.75	3.44	2.82	-1.16	2.07	0.75
6	6.02	4.91	3.00	2.43	-1.11	2.02	0.69
7	6.41	5.29	3.19	2.60	-1.12	2.05	0.71
8	6.62	5.55	3.08	2.59	-1.07	1.99	0.70
9	7.38	6.31	3.43	3.00	-1.06	1.96	0.77
10	8.69	7.61	3.86	3.33	-1.08	2.09	0.78
11	9.49	8.35	4.15	3.51	-1.14	2.25	0.78
12	9.35	8.29	4.23	3.52	-1.06	2.25	0.78

Table 5.5: Offshore error statistics by month of the year. The performance drops slightly in summer.

5.8.3 Coastal influence

The sharp roughness and temperature gradients at the coast pose fundamental challenges for mesoscale models, as discussed in §2.6.5. PBL schemes are based on assumptions of horizontal homogeneity which do not hold at the coast. Conditions may be strongly stable or unstable as air advects across the temperature boundary, while the change in roughness length leads to the formation of an internal boundary layer. In some cases the influence of land can be seen tens of kilometres offshore [Barthelmie, 1999].

To explore the effect of nearby land, R^2 was plotted as a function of direction sector for each of the in-situ offshore observations, shown in Figure 5.19. The locations of the in-situ observations and their relation to the coast is shown in Figure 4.5. The influence of land does seem to be visible at Aberporth and Pembroke buoys, which are closest to land. At Aberporth, which has land to the east and southeast, R^2 is markedly worse for offshore winds. Similarly at Pembroke, which has land to the northeast, R^2 is lower for offshore winds. However, K5 and K7 also appear to show a directional influence on R^2, despite being relatively far from land, so no firm conclusions can be drawn from this.

5.8.4 Season

Figure 5.20 shows bias by months of the year, and Table 5.5 summarises the offshore statistics by season. There is a reasonably clear indiction that performance is worse in the summer months.

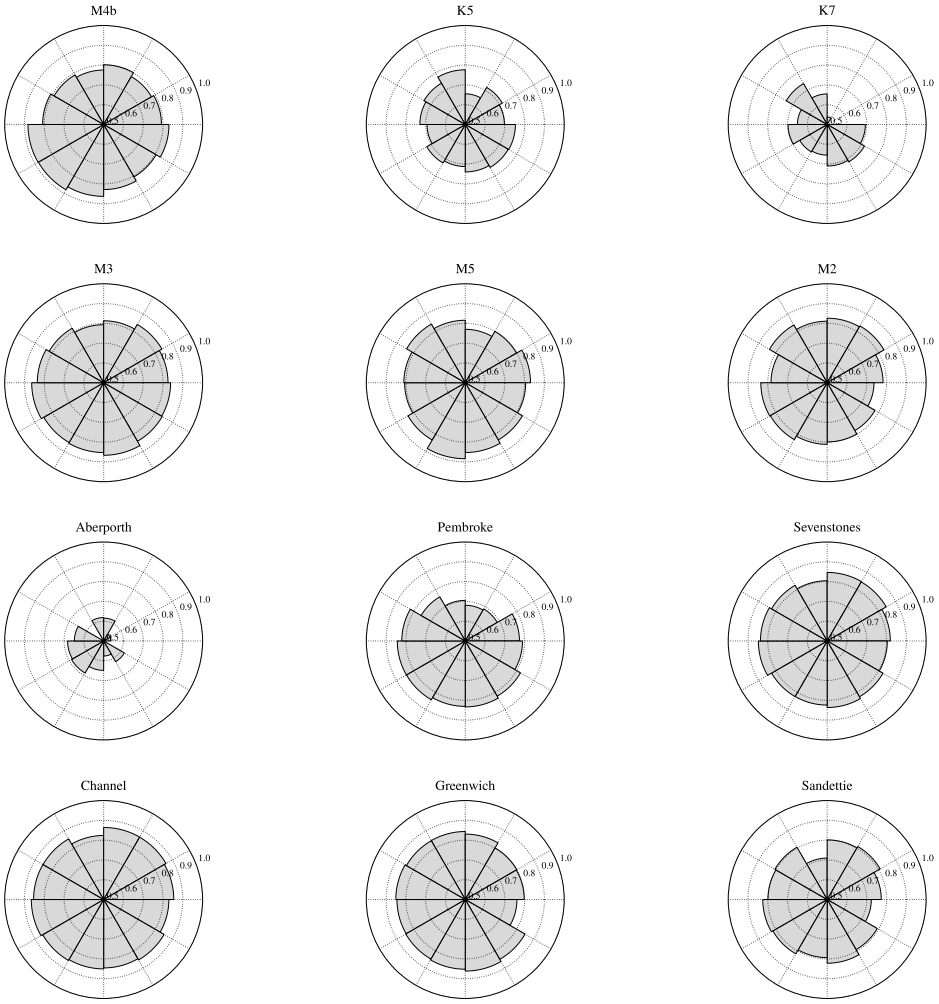

Figure 5.19: R^2 by wind direction for offshore observations. Direction determined by observations. See Figure 4.5 for locations

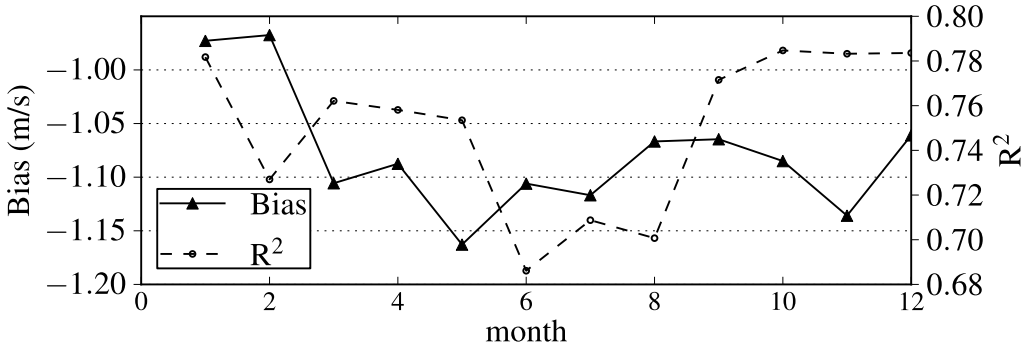

Figure 5.20: B and R^2 by month of the year for offshore observations

5.8.5 Sea surface temperature

While investigating the seasonal effect on performance, it was discovered that SST was not updated in the inner domain during the simulation. Instead, SST was taken at the start of the month and then remained constant. This was despite the fact that the option to update SST had been specified, and was eventually traced to an error in the WRF documentation, a problem which has since been encountered in another study [Bukovsky and Karoly, 2009].

Figure 5.21 shows observed and modelled monthly SST and average air temperature at two sites, Aberporth buoy and the M3 buoy. Observed sea temperature is taken through the hull of the buoy, and the true SST may be slightly cooler due to the cool skin effect. Air temperature is measured at 3m above sea level. Two metre temperature (T2) and SST are taken from WRF directly.

WRF has a too-cold sea in the months where the sea is heating up, and a too-warm sea in the months when the sea is cooling down. The magnitude of this bias is largest in June and November when the observed SST is changing most rapidly.

Of more importance for stability is the air-sea temperature difference. WRF matches the observed air temperatures closely, but predicts a larger difference between air and sea temperature than observed in June, October and November, although in all cases the temperature difference is in the same direction. In June the impact would likely be the prediction of more stable conditions than observed, with reduced convective mixing of momentum and a generally reduced wind speed within the stable layer. In October the impact would be the converse, unstable conditions and generally increased surface winds.

Since the discrepancy in SST will increase throughout the month simulation, bias was plotted as a function of day of the month, Figure 5.22, to show whether bias grows throughout a simulation. No discernible trend is clear, and the SST issue is explored in further detail in the following section which examines error by stability class.

5.8.6 Stability

A challenge for mesoscale models is determining near surface wind speeds in conditions which strongly depart from neutral stability. In addition, since SST was not correctly updated, there may be larger deviations from neutral than observed. Misdiagnosed stability would lead to a

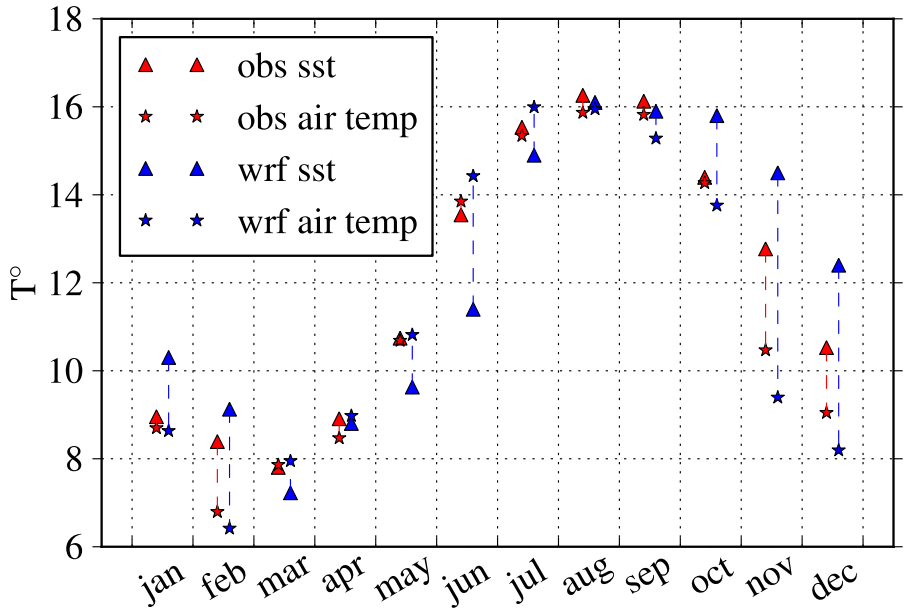

(a) Aperporth

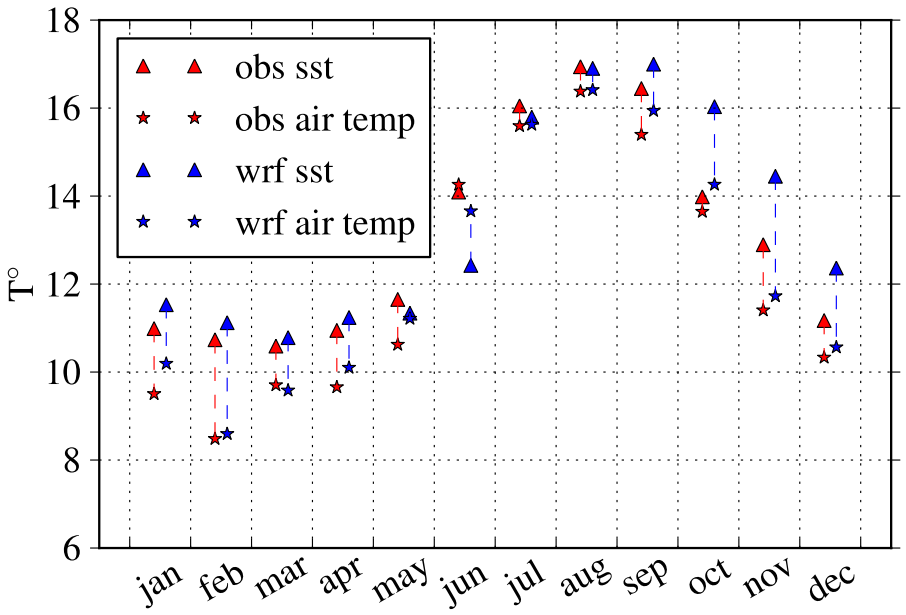

(b) M3

Figure 5.21: Average monthly air temperature (*) and sea surface temperature (Δ). Within each month, buoy observations are on the left (in red) and model simulations on the right (in blue). The largest discrepancy between model and observations occurs in June and November when the rate of change of SST is highest

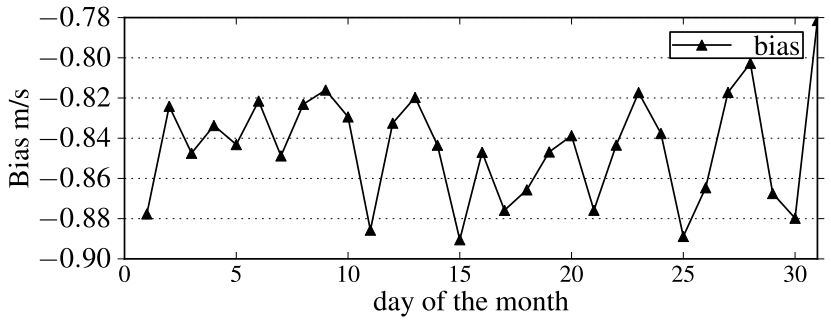

Figure 5.22: Bias by day of the month

Stability class	frequency %	obs mean ms^{-1}	wrf mean ms^{-1}	obs std ms^{-1}	wrf std ms^{-1}	B ms^{-1}	RMSD %	R^2 ms^{-1}
very stable	32	6.29	5.33	3.04	2.49	-0.96	2.06	0.64
stable	11	9.50	8.47	3.48	2.74	-1.03	2.24	0.68
neutral	33	10.64	9.48	3.97	3.16	-1.16	2.47	0.70
unstable	10	7.30	6.05	2.86	1.92	-1.25	2.24	0.58
very unstable	15	4.72	3.59	2.38	1.63	-1.13	2.03	0.50

Table 5.6: Error statistics at offshore in-situ observations by WRF stability class. Stability class is determined by the value of ζ from WRF.

bias in the surface flux u_*, and hence a bias in the surface winds. In order to explore this, statistics by stability class were computed according to the values of ζ and the classification in §2.3. Table 5.6 shows the frequency of stability classes diagnosed by WRF across all offshore in-situ observations. Neutral conditions predominate, though very stable conditions are almost as common. The frequency of stability classes is similar to those found by Barthelmie [1999]. The error statistics within the stable class are similar to the errors in neutral conditions. Very unstable conditions also quite frequently diagnosed, and R^2 is markedly lower for very unstable conditions. This could reflect a mis-diagnosis of unstable conditions caused by the SST problem. In particular, the fact that WRF is diagnosing unstable conditions when the observed average wind speed is over 7ms^{-1}suggests this may be the case. However, it could also reflect the difficulty inherent in predicting wind speeds when the synoptic forcing is not so strong, or greater error in the observations seen in relatively low wind speeds.

The main finding is that the low bias seen offshore is seen in every stability class, which rules out misdiagnosed stability class as a cause.

5.9 Comparison with satellite data

The comparison with in-situ observations strongly suggests a low wind speed bias offshore. Offshore wind speeds are now compared to QuickSCAT and ASCAT wind speeds, as described in §4.4.8. QuickSCAT winds are used for the period 2000-2009, and ASCAT thereafter. These are referred to collectively here as 'satellite winds'.

Daily average satellite wind speeds were interpolated onto the higher resolution WRF grid using bi-linear interpolation. More complex interpolation methods e.g. bi-cubic can lead to problems near the coast by extending the influence of land further offshore.

Figure 5.23 shows a comparison of average wind speeds over the whole period, from 2000 to 2010 inclusive. Although the broad geographic pattern is similar, WRF wind speeds are consistently lower than satellite winds. For example, off the northwest of Scotland, satellite winds show an average of 9.5ms^{-1}, while WRF only shows 8.5ms^{-1}.

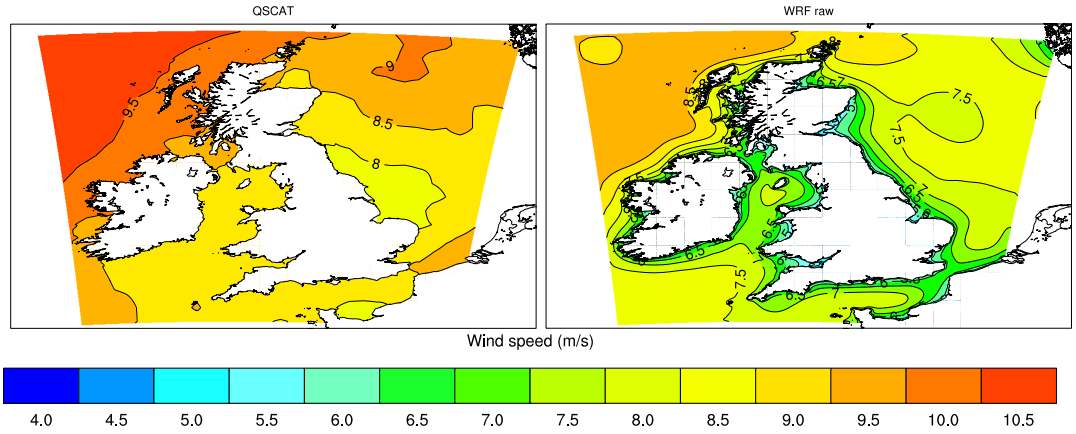

Figure 5.23: Average satellite (left) and WRF winds (right) at 10m amsl

Also of note are some unusual features in the WRF wind field. There is a noticeable low wind speed centre in the North Sea, and another smaller low wind speed centre near the northwest corner of the domain. Figure 5.24 shows these anomalous areas correspond to the location of the oil platforms in the North Sea, and the K5 buoy. Wind speeds from all of these sources are assimilated by the GFS model and other global models. Since they are in areas of relatively sparse of observations, a single observation will have a significant effect on the model solution.

Since analysis nudging was used throughout this study, any bias in the global model could manifest itself in the mesoscale model. It was not feasible to obtain the full GFS dataset for the period in question due to storage constraints, but it is hypothesised that a similar area will

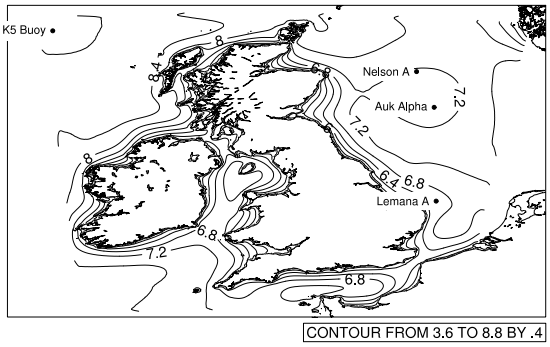

Figure 5.24: Influence of observations on WRF wind speed. The two areas of unusually low wind speed correspond to locations of in-situ observations in an otherwise sparse area. It is hypothesised that these observations are degrading the global and the mesoscale model.

appear in the GFS wind speeds. Indeed, a similar feature is visible in the wind speed maps of the DTI Marine Atlas, which noted "one unexpected feature to the north-west of Scotland" [DTI, 2004], which appears to coincide with the K5 buoy.

This is an important result in itself, as it highlights potential improvements in forecast models from relatively simple changes. In particular, wind speed measurements from oil platforms, which have long been known to be problematic due to the influence of the platform, should either be improved, excluded, or at least given a higher uncertainty in data assimilation programs, so that they are not overly weighted over satellite observations.

As a further illustration of the systematic nature of the bias, plots of average monthly wind speed are shown in Figure 5.25 for January and May 2001, which are typical of a high wind speed and low wind speed month in the period studied. In January, the shape of the wind two wind fields are in broad agreement. However, 10m speeds from WRF are still systematically lower than QuickSCAT across much of the domain, with the highest wind speed off the north-west of Scotland reaching 11ms^{-1}in WRF compared to 13ms^{-1}from satellite observations. A similar low bias is seen in the North Sea. The fact that these biases are seen in the open ocean shows it is not simply coastal effect. In May, the two wind fields show similar geographic features, particularly in the North Sea. However, QuickSCAT data shows higher wind speeds off the northwest of the domain, with wind speeds around 6 or 7 ms^{-1}compared to 4 or 5 ms^{-1}in WRF.

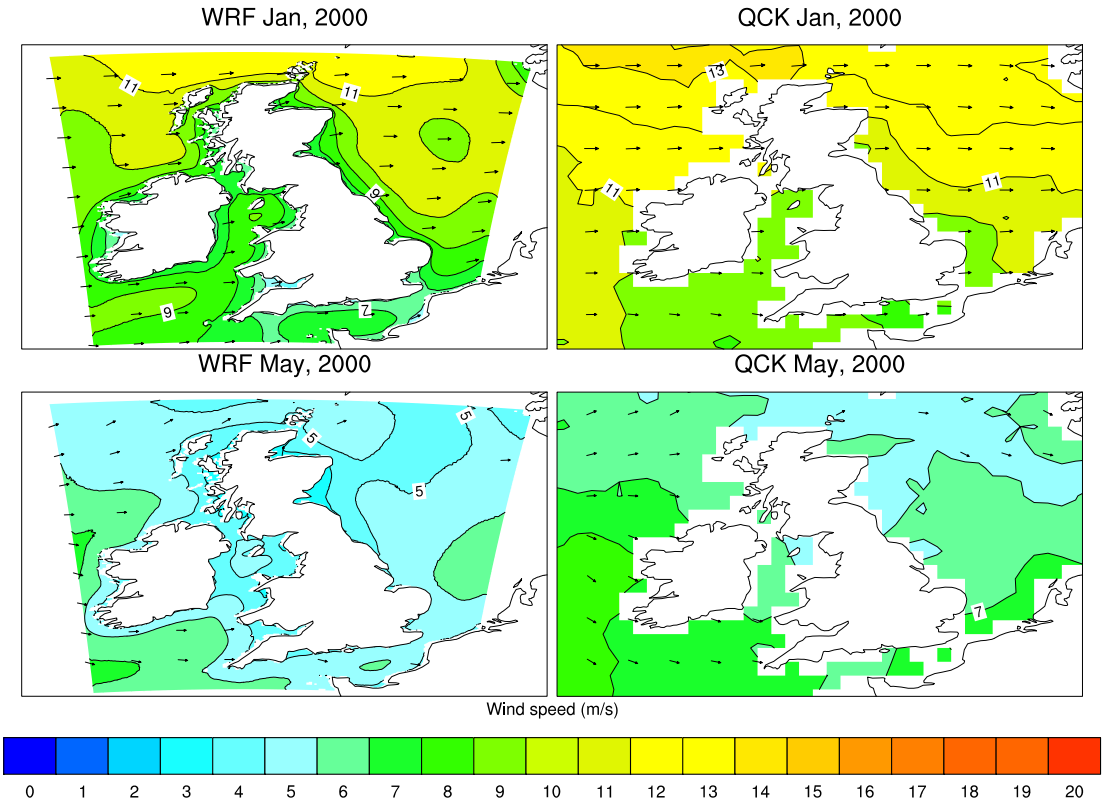

Figure 5.25: Comparison of WRF (left) and QuickSCAT (right) wind vectors for January and May 2000. In January, WRF wind speeds reach a maximum of around 11 ms^{-1}off the northwest of Scotland, while QuickSCAT winds show a maximum of 13ms^{-1}. In May, wind speeds in the open sea in the northwest are significantly lower the QSCAT winds.

5.10 Comparison with other models

5.10.1 Marine Atlas

The Marine Atlas was developed by the DTI to provide data on the renewable resource available offshore. Offshore wind speeds in the Marine Energy Atlas are derived from archived output from the Met Office UM. The main dataset uses just over three years (1st June 2000 - 30th September 2003) of archived output UK Waters configuration, at approximately 11km resolution [DTI, 2004], driven by the global configuration of the UM. In the Marine Atlas, model winds were converted to 10m from the lowest pressure level (approximately 19.5m amsl), using a simple scaling factor of 0.94 [DTI, 2004].

Wind speeds from the Marine Atlas are available as an ArcGIS shapefile, at approximately 12km resolution. For comparison with WRF, wind speeds over the same period were averaged onto the lower resolution Marine Atlas grid, and subtracted from the speed. Figure 5.26 shows the difference in 100m wind speed - comparisons at 10m and 80m showed a similar picture. It can be seen that WRF wind speeds are universally lower offshore by around $1ms^{-1}$, with larger discrepancy of up to $2.5ms^{-1}$in semi-enclosed coastal areas. In the open ocean, the geographic agreement is very good, with both showing very similar spatial variation in wind speeds.

It is worth noting that verification against in-situ observations performed for the Marine Atlas showed errors in the region of 10-15% and as high as 30% at one site [DTI, 2004]. Table 5.7 shows comparisons for those buoys and lightships which overlap between studies. There is a slight difference in the observed figures, suggesting there may be a difference in the quality control used between studies. Bias has been expressed as a percentage since that is quoted in the Marine Atlas. The magnitude of the errors is comparable, however wind speeds from WRF are consistently low, while the Marine Atlas errors vary depending on location. Given the uncertainties involved, it is not desireable to correct one model on the basis of another model. Also, since it only presents monthly averages, and is only derived from three-years of data, the Marine Atlas it is not suitable for correcting the WRF output.

5.10.2 GFS

Finally, the raw output of the GFS was extracted and compared to WRF output and in-situ observations, to investigate whether this might be the source of the low bias. Storage and time

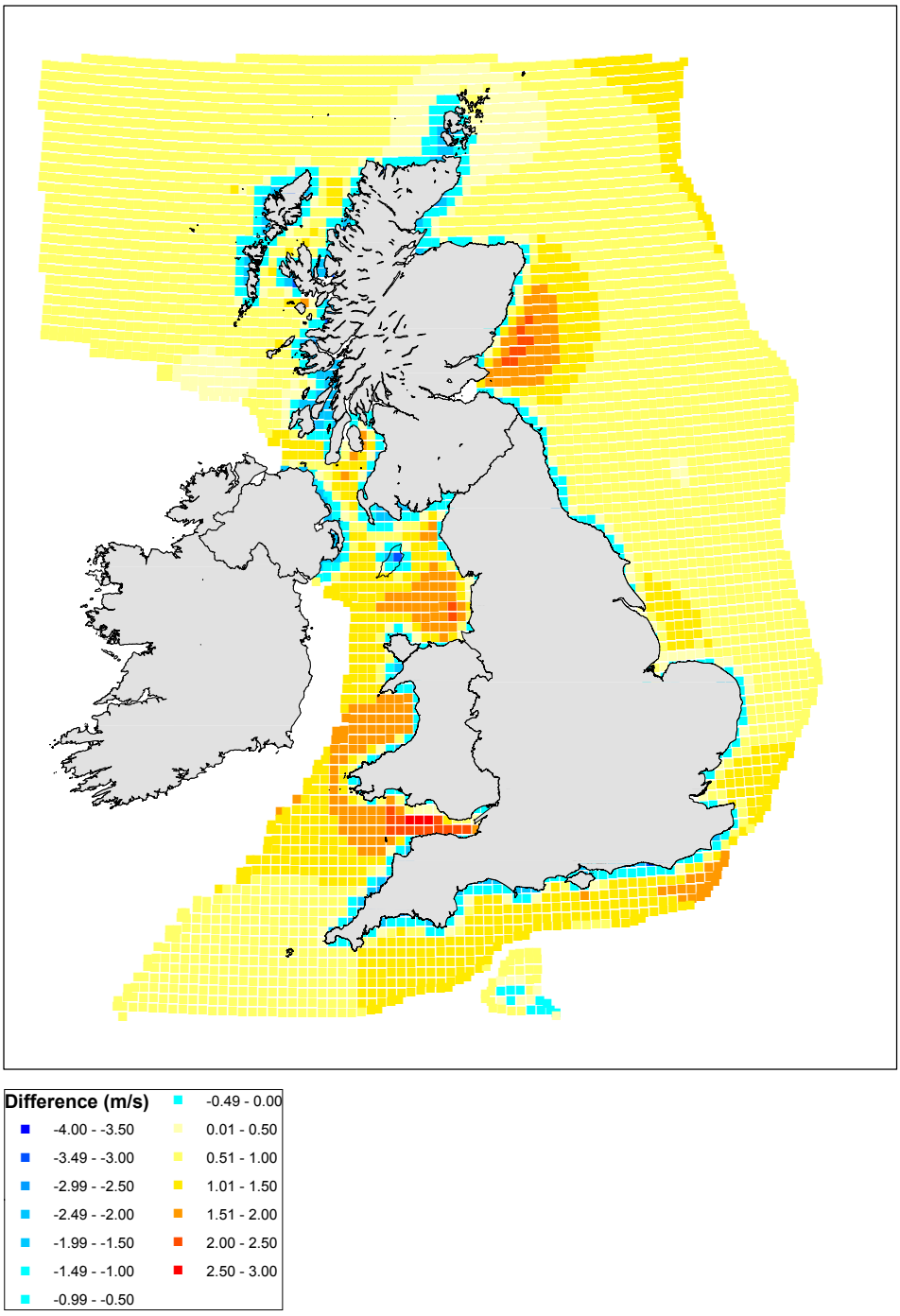

Figure 5.26: Comparison with the DTI Marine Atlas. Difference is computed as [Marine Atlas] - [WRF]

Station	Type	Marine Atlas			This study		
		Model ms^{-1}	Observed ms^{-1}	Bias %	Model ms^{-1}	Observed ms^{-1}	Bias %
K5	Buoy	9.33	7.99	17	7.70	7.95	-3.2
Aberporth	Buoy	7.24	5.60	29	5.24	6.19	-15.3
Sevenstones	Lightship	8.19	8.61	-5	7.64	8.62	-11.4
Greenwhich	Lightship	7.98	8.43	-5	7.01	8.63	-18.7

Table 5.7: Comparison with DTI Marine Atlas validation. The Marine Atlas was derived from three years of output from the UK Waters configuration Met Office Unified Model, and verified against in-situ observations.

constraints prevented the full global reanalysis being downloaded, so a limited comparison across one month was performed. Figure 5.27 compares monthly average GFS 10m wind with WRF 10m wind and in-situ observations for an exposed and coastal buoy. At the exposed location of K5, the agreement between the three sources is reasonably close. As noted, if the observations at K5 are low, this will constrain the GFS model and subsequently WRF.

At a less exposed buoy, such as M2 buoy in the Irish Sea, the GFS winds have a significant low bias compared to the observations. This is very likely due to the lower spatial resolution and coarser land-sea boundary in the GFS 1°data. Figure 5.28 shows the landmask at this resolution, together with the locations of the in-situ observations. Many of observations, particularly on the west coast, fall into land cells. In these cells the GFS wind is biased low compared to offshore observations. Analysis nudging in these regions will tend to act as a sink of momentum.

5.11 Discussion

None of the investigations conclusively reveal the source of the offshore low wind speed bias in WRF. Whatever the reason, this type of bias is common - if not universal - in mesoscale models [Hart et al., 2004, Mass, 2003]. As Hart et al. [2004] states:

> "considerable improvement is needed to existing models to accurately simulate local boundary layer structure and evolution. As a result, current models exhibit systematic biases that limit their application toward detailed point-specific forecasting "

From the investigations here, the most likely cause appears to be a combination of bias inherited from the GFS model through the use of analysis nudging. Part of the bias in the GFS model

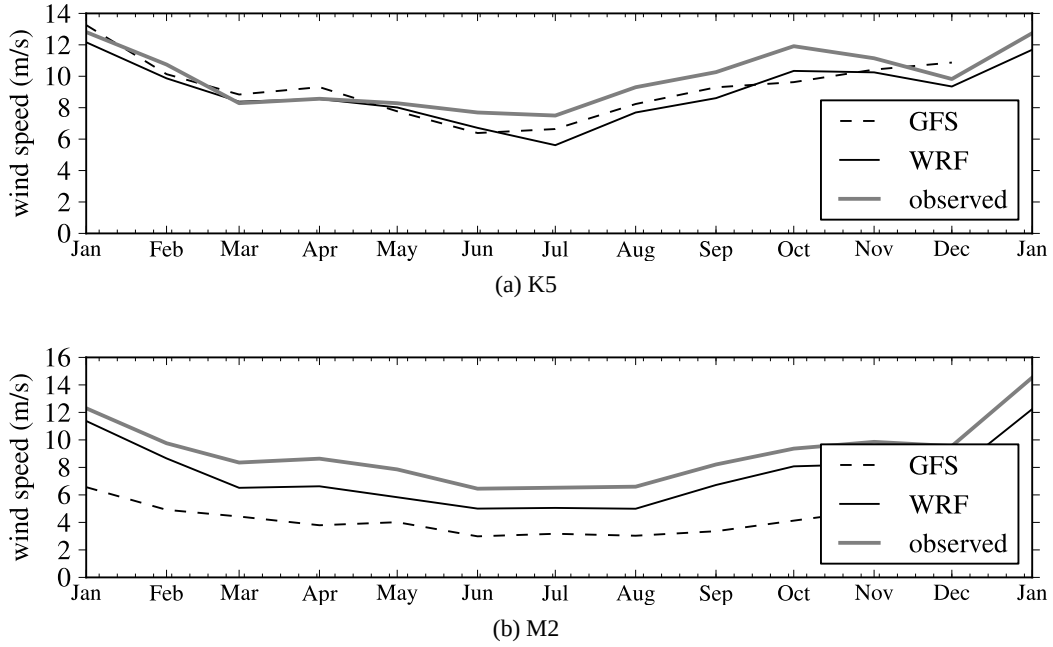

(a) K5

(b) M2

Figure 5.27: Average monthly winds for 2005 from GFS, WRF and in-situ observations. GFS agrees closely with in-situ observations for exposed locations like K5, but is biased low for in-situ observations close to the coast which may fall into land points.

may be due to assimilation of problematic observations at oil platforms and the K5 buoy. Part of the bias towards the coast might be explained by the coarse landmask at 1°resolution.

Another reason for the low bias may be related to the resolution of the global model. Recent studies have found both NCEP and ECWMF reanalysis surface winds to be biased low [Fangohr et al., 2008, Reistad et al., 2011, Thomas et al., 2008]. For example, Reistad et al. [2011] found ERA-40 10m wind to be biased low by about -0.86ms^{-1}, while Kolstad [2008] found NCEP reanalysis surface winds to be significantly (8%) lower than QuickSCAT over the Nordic seas, both in open water but particularly so near the coast.

One explanation of this low bias is an underestimation of peak winds associated with depressions [Cardone et al., 1999, Chelton et al., 2006, Swail and Cox, 2000]. For example, Chelton et al. [2006] found both NCEP and ECMWF models underestimated the intensity, and over-estimated the spatial scale and smoothness of extra-tropical cyclones. This would explain the underestimation of peak wind speeds found here.

As detailed in Chapter 4, the decision to use analysis nudging was to remove a *high* bias seen at onshore met stations. However, recent work [Mass and Ovens, 2011] suggests that this onshore

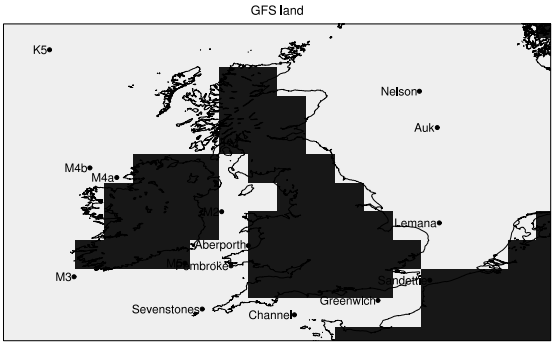

Figure 5.28: GFS landmask at 1°resolution

high bias is due to the neglect of sub-grid scale orographic drag, a problem which will be corrected in future implementations of WRF. It is probable that analysis nudging provides a sink for momentum which should be removed through this mechanism. The use of analysis nudging may remove some of the advantage of a higher resolution model. That said, the overall error statistics and wind speed distributions are very good. Nudging terms are very small, designed not to overwhelm the physical processes being simulated.

In most applications, a small bias may be acceptable, but given the sensitivity of power output to wind speeds, a difference in an average wind between 6.5ms^{-1}and 7.5ms^{-1}could be the difference between a project being commercially viable or not. For this reason it was decided this offshore bias needed to be corrected, and this is the subject of the next chapter.

5.12 Chapter summary

In this chapter, the simulation process used to derive an eleven year reanalysis at 3km resolution was described. Extensive verification against observations was performed, and it was shown that the reanalysis recreates average wind speed distributions, and the spatial and temporal variation in wind speeds across the whole of the British Isles, both onshore and offshore. Hourly, diurnal, seasonal and spatial patterns are all realistic.

Onshore, performance compared to met stations is very good, apart from a few met stations in very complex terrain. Limited comparisons to wind farm masts shows good performance, and these are independent sites whose observations have not been assimilated into the driving model. Systematic errors seen at some wind farm masts were found to be due to incorrect roughness lengths, and could be removed once better information was available. Peak wind

speeds are not represented well.

Offshore, the wind speeds patterns are captured well, but a systematic low bias of around 1-2 $ms^{-1}$is a concern, particularly for coastal observations. The impact of wind direction and atmospheric stability were explored as potential causes, but no conclusive factor emerged which might offer a simple explanation. It was found that anomalous geographic features, not supported by the satellite record, could be traced to the assimilation of observations from platforms and buoys. It is proposed that further investigation of these has the potential to improve the quality of global forecasts models.

The following chapter details a simple correction scheme to remove the low bias seen offshore.

Chapter 6
Offshore Bias Correction

6.1 Introduction

The previous chapter has shown that the model wind speeds compare very well to observed spatial and temporal patterns, although a systematic low bias exists offshore, which was deemed to require further action. This chapter presents a simple correction for the bias based on a complete satellite record over the corresponding period. Consistent with the previous chapter, the term 'satellite wind' is used to collectively refer to QuickSCAT and ASCAT derived wind speeds, described in §4.4.8.

6.2 Background

Post-processing of model output to remove bias has long been applied in weather forecasting [Klein and Glahn, 1974], and is still regarded as a necessary step [Giebel, 2010].

The most common family of approaches are known as Model Output Statistics (MOS) see e.g. [Giebel et al., 2003, Klein and Glahn, 1974, Nielsen et al., 2007, Termonia and Deckmyn, 2007, Vannitsem and Nicolis, 2008]. The general technique is to develop statistical relations between variables of the NWP model, the predictors, and the desired output, the predictand [AMS, 2000]. The predictand may be an error-corrected version of a variable already in the NWP model, or it may be new diagnostic variable, for example the mass of ice on wind turbine blades. A wide variety of techniques can be used to determine the statistical relationship such as simple linear regression, multiple linear regression, Bayesian models, and neural networks; Gel and Raftery [2004] give a good review.

Most error-correction methods are local, restricted to grid points where previous observations are available. It is more difficult to generalise to grid points away from observations. Gel and Raftery [2004] developed a gridded approach by first relating model bias to spatial and temporal variables, such as the latitude or day of the year. This relationship may then be applied to any

grid point, regardless of whether observations exist for that point or not. However, this approach still requires enough observation sites to adequately sample the spatial variables used in the regression. Given the small number of in-situ offshore observations, this kind of approach was not thought applicable.

The satellite scatterometer winds described in §4.4.8 offer the only obvious approach for correcting bias across the whole offshore domain. As already noted, satellite winds are thought to be under-utilised by global models and provide more detail and smaller biases compared to raw GFS output [Chelton et al., 2006]. However, the main limitation of these is their daily time resolution.

The desire was to develop an offshore bias correction which would preserve the temporal and spatial resolution of WRF output. In addition, it was desireable to keep the method transparent, so that the original model data could easily be recovered. The correction had to be derived from the daily satellite data, but be applicable to the hourly WRF data. Finally, a correction had to be derived from, and applied to, each 3km offshore cell over the full eleven-year period.

There are many methods for post-processing, in particular methods based on the Kalman-Filter (KF) can have very dramatic results [Crochet, 2004, Delle Monache et al., 2011, 2008, Libonati et al., 2008, Louka et al., 2008]. Such an approach is adaptive: bias at time t partly determines the bias at time $t + 1$, which allows correction of non-stationary errors such as seasonal effects.

However, it was not thought feasible to apply this methodology across the whole reanalysis dataset. Working with the raw data files is slow, each day of simulated wind speed is stored in a single file, and the whole dataset is too large to fit in the memory of a single machine. Implementing a KF per grid cell would require repeatedly reading through the dataset at each point in the domain, applying a KF to calculate the correction to the daily wind speed, and then applying this to the hourly wind speeds and writing the updated values to a new file. Storage and time constraints meant this was not possible, although it will make an interesting area of further work.

In any case, many simple bias correction schemes have been shown to be very effective [Hamill et al., 2008]. It has been shown in Chapter 5 that the bias is reasonably stationary in time, in which case a linear regression will minimise the RMSD between satellite speeds and model data. Hamill [2010] advocates using the simplest possible effective approach, noting that very often simple techniques are as effective as more complex ones. For these reasons a bias

correction based on linear regression is used here; this has the large advantage of being simple, transparent, and only requires the additional storage of gradient and intercept terms.

6.3 Processing satellite data

Background information about satellite scatterometer winds, and the sources used is given in Chapter 4. Satellite winds are interpolated from the rectilinear latitude-longitude global grid onto the higher resolution curvilinear WRF grid using bi-linear interpolation. This simple interpolation scheme minimises some of the problems associated with interpolation near the coast.

The EQNW from the satellite data is used directly: the aim is to create a simple correction derived directly from the satellite data, without requiring additional estimates of surface fluxes themselves introduce further uncertainties. At the level of monthly averages, the difference between EQNW and real winds is small [Kara, 2008], and the EQNW was found to be unbiased with respect to in-situ observations, §6.4.

The time resolution of the gridded satellite winds is daily. For QuickSCAT this is a direct average of two overhead passes of the satellite, while for ASCAT these two overhead passes are averaged with the aid of NWP model output to determine a true daily average. However, the months where both are available shows the two datasets to be in close agreement, e.g. Figure 6.1.

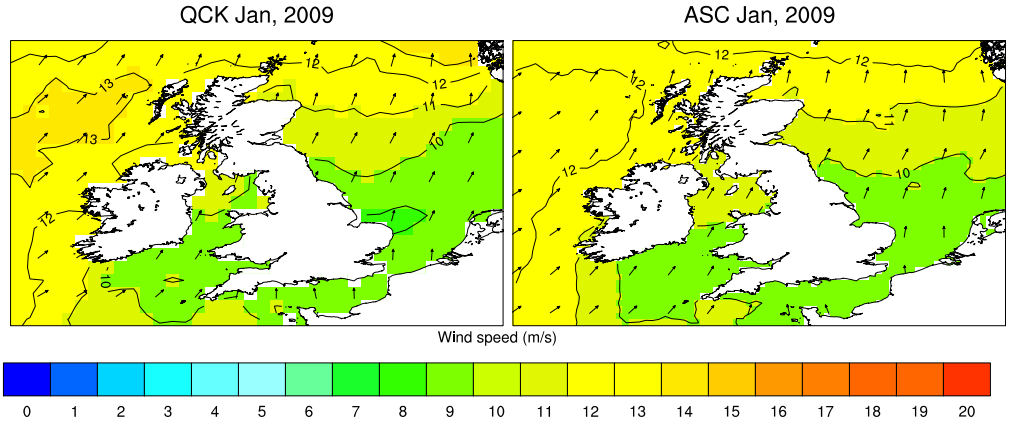

Figure 6.1: Comparison of QuickSCAT and ASCAT winds, January 2009

6.4 Verification of satellite data

In Chapter 5 it was shown that the magnitude of the offshore bias is around 1.0-1.5ms^{-1}. This is comparable in magnitude to the estimated error in scatterometer winds, thought to be 1.5 ms^{-1}[Winterfeldt et al., 2010]. Therefore it is first necessary to compare satellite observations to in-situ observations, to assess whether the satellite winds are indeed less biased than uncorrected WRF output.

Satellite wind speeds are extracted at the locations of all in-situ offshore observations. In-situ observations are converted from the anemometer height to a height of 10m using a neutral logarithmic profile; the adjustment due to height is small as buoy anemometers are at 4m height, and lightships anemometers at 19m.

Figure 6.2 shows daily average wind speeds from all three sources at Channel Lightship. Bias is much lower in the satellite winds (0.08ms^{-1}) than WRF (-0.9ms^{-1}). ASCAT also shows less bias than WRF, although over a much shorter period. However, WRF speeds have much higher correlation, 0.95 compared to 0.88. This is due to the higher temporal resolution of WRF data which enables a much better estimation of the daily average than two passes of a satellite. It shows that WRF captures the temporal patterns very well, and shows that the model wind speed will add significant detail to the daily satellite speed, once systematic bias is removed.

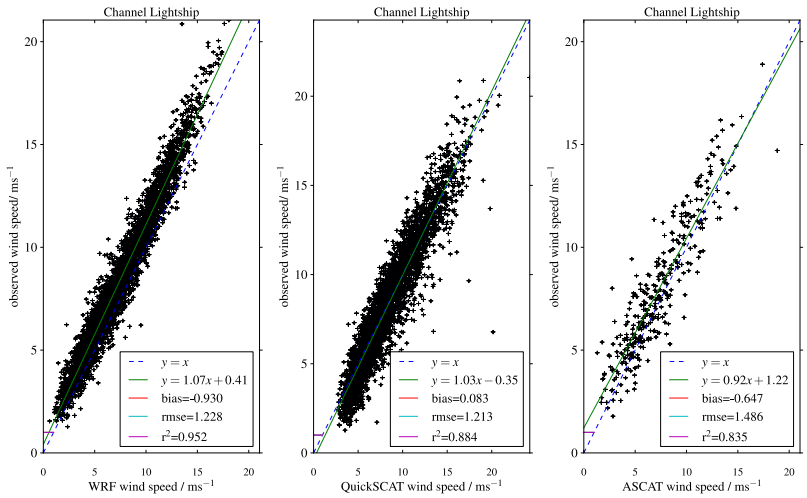

Figure 6.2: Daily average WRF, QuickSCAT and ASCAT data compared to in-situ observations at Channel lightship. WRF data covers the period 2000-2010, QuickSCAT 2000-2009 and ASCAT 2009-2010

Name	Mean (ms^{-1})			B (ms^{-1})		RMSD (ms^{-1})		R^2	
	obs	wrf	sat	wrf	sat	wrf	sat	wrf	sat
Sevenstones lightship	8.40	7.46	8.35	-0.95	-0.06	1.49	1.36	0.90	0.86
Channel lightship	8.27	7.39	8.35	-0.87	0.08	1.29	1.21	0.93	0.88
Sandettie lightship	8.08	6.17	8.52	-1.90	0.44	2.25	1.56	0.88	0.81
Greenwich lightship	8.25	6.72	8.15	-1.50	-0.07	1.85	1.27	0.92	0.88
Aberporth buoy	6.53	5.73	8.07	-0.80	1.54	1.92	2.46	0.69	0.68
Pembroke buoy	7.33	6.56	8.25	-0.77	0.92	1.39	1.81	0.88	0.79
M2	8.70	6.76	8.08	-1.74	-0.52	2.02	1.23	0.90	0.90
M3	8.84	7.53	8.92	-1.22	0.13	1.55	1.17	0.91	0.89
M4a	8.56	7.50	9.21	-1.10	0.73	1.62	1.71	0.88	0.83
M4b	9.35	8.63	9.55	-1.29	-0.17	1.58	1.19	0.94	0.90
M5	8.67	7.12	8.27	-1.50	-0.47	1.88	1.19	0.88	0.89
K5	8.67	8.50	9.84	-0.11	1.29	1.70	2.41	0.79	0.73
K7	8.49	8.52	9.29	0.05	0.87	1.92	2.08	0.73	0.76

Table 6.1: Comparison of daily averaged 10m wind speed between observed, WRF and satellite wind speeds. Satellite wind speeds are taken from QuickSCAT until October 2009, and ASCAT thereafter.

Table 6.1 compares error statistics between WRF and satellite speeds at all available offshore in-situ observations. Satellite data is predominantly less biased than WRF, particularly at lightships and Irish buoys. The satellite winds are much closer to the observed means at all in-situ observations with the exception of Aberporth, Pembroke, K5 and K7, where satellite wind speeds are higher than observed.

Aberporth and Pembroke are very close to the coast, 13km and 7km respectively. Here satellite wind speeds may be contaminated by land, or by errors introduced by interpolation near the coast. Newer versions of the QuickSCAT winds have been released which account for land contamination and are valid much closer to the coast [Vanhoff et al., 2011]. However, these are not yet available for the UK[1].

There are also discrepancies at buoys K5 and K7, where satellite wind speeds are higher than observed. These buoys are very exposed and are not near any significant land masses, so land contamination of the satellite speeds is not the cause. Both K5 and K7 suffer long periods of missing data, particularly over the winter. Before 2008, both buoys had cup anemometers which would often fail or degrade within six-months [Turton and Pethica, 2010]. Salt ingress into anemometer bearings causes the anemometer to slow over time, and is difficult to detect (Turton, personal communication). In 2008, both were serviced and upgraded to dual cup and sonic anemometers [Turton and Pethica, 2010] and since then the match with QuickSCAT data

[1] see http://podaac.jpl.nasa.gov/node/142

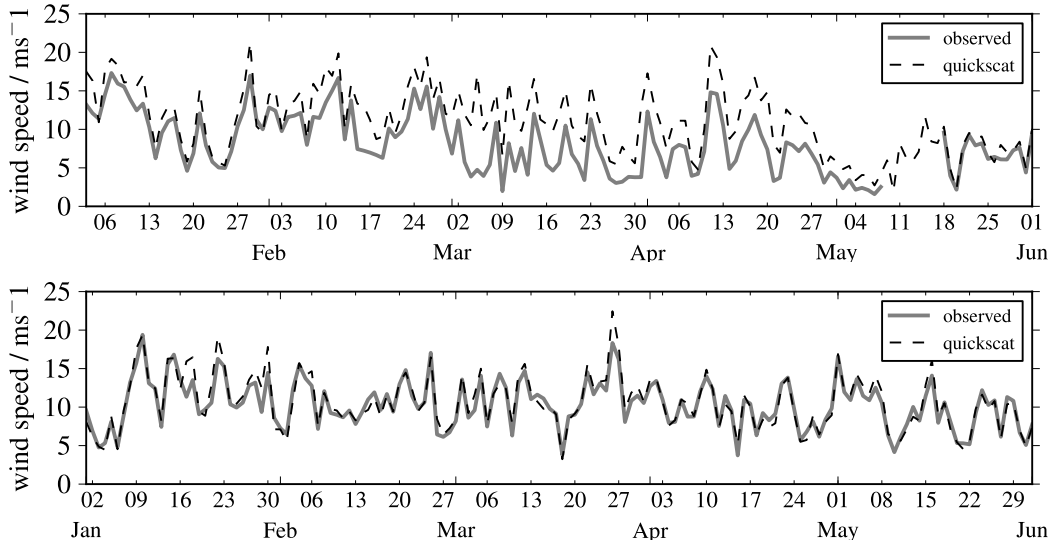

Figure 6.3: Data quality at exposed buoys. Daily averaged QuickSCAT and observed wind speeds at buoy K5. Top plot shows comparison for first 6 months of 2000, where QuickSCAT speeds are significantly higher than observed. The lower plot shows the same comparison for the first six months of 2009 after the anemometer was upgraded. It is concluded that the high bias seen in QuickSCAT winds at K5 and K7 is actually due to problems with the buoy anemometers before 2008.

is considerably closer, shown in Figure 6.3.

It is concluded that that the bias at bias at K5 and K7 is a problem with the anemometers before 2008, and the satellite wind speeds are a more accurate indicator of the long term wind speeds. In fact poor-quality buoy data was the main reason for the anemometer upgrade [Turton and Pethica, 2010]. This further supports the hypothesis developed in the previous chapter, that areas of anomalously low wind speed relate to poor quality observations assimilated into global models.

One concern is that, since satellite wind speeds have been spatially averaged to a 0.5° grid, any correction derived from them may lose geographic detail. Figure 6.4 shows a comparison of average satellite, WRF wind speeds and in situ observations for a region close to the coast. The satellite wind speeds show a fairly universal average of around 8 ms^{-1}, while WRF speeds show much more spatial variation and a greater influence of land. However, the in-situ observations themselves suggest little variation in average wind speeds, and agree much more closely with the satellite speeds. The satellite winds show a average 8.0-8.5ms^{-1}, while WRF shows the highest wind speed in the area only 7.5ms^{-1}. In-situ observations are centered around 8.5ms^{-1},

with only Aberporth and Pembroke buoy showing significantly lower wind speeds from the rest. This suggests that although WRF captures the reduction in wind speed very close to the coast, it generally under-estimates the wind speeds elsewhere, and over-estimates the influence of land relatively far from the coast.

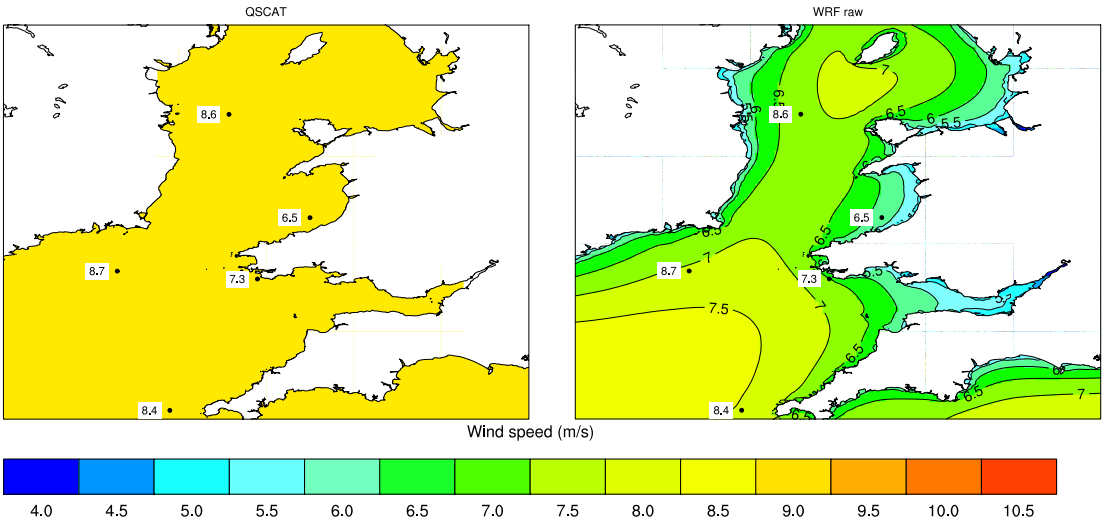

Figure 6.4: Average 10m wind speed from satellite data (left), and average 10m wind speed from WRF (right). Average wind speeds from in situ observations are shown as labels on a white background. WRF shows much more spatial variation than the lower-resolution gridded data, although this variation is not confirmed by the in-situ observations.

6.5 Bias correction method

Two bias correction methods based on linear regression were tried. A linear regression was computed at each WRF grid cell between an 11-year time series of daily average WRF and satellite wind. That is, the coefficients m_i and c_i were calculated for each grid cell i:

$$\overline{U}_i^{\text{sat}} = m_i \overline{U}_i^{\text{wrf}} + c_i \tag{6.1}$$

where $\bar{U}_i^{\text{sat}}$ is the daily average 10m satellite wind, and $\bar{U}_i^{\text{wrf}}$ is the daily average 10m model wind in each grid cell. The advantage of this approach is, if the bias is stationary, this method will return the optimum linear solution. The disadvantage is that, since it contains an intercept term, it will shift wind speed distributions as well as scaling them. Given that the bias is most obvious at higher wind speeds, this may over-correct at low wind speeds.

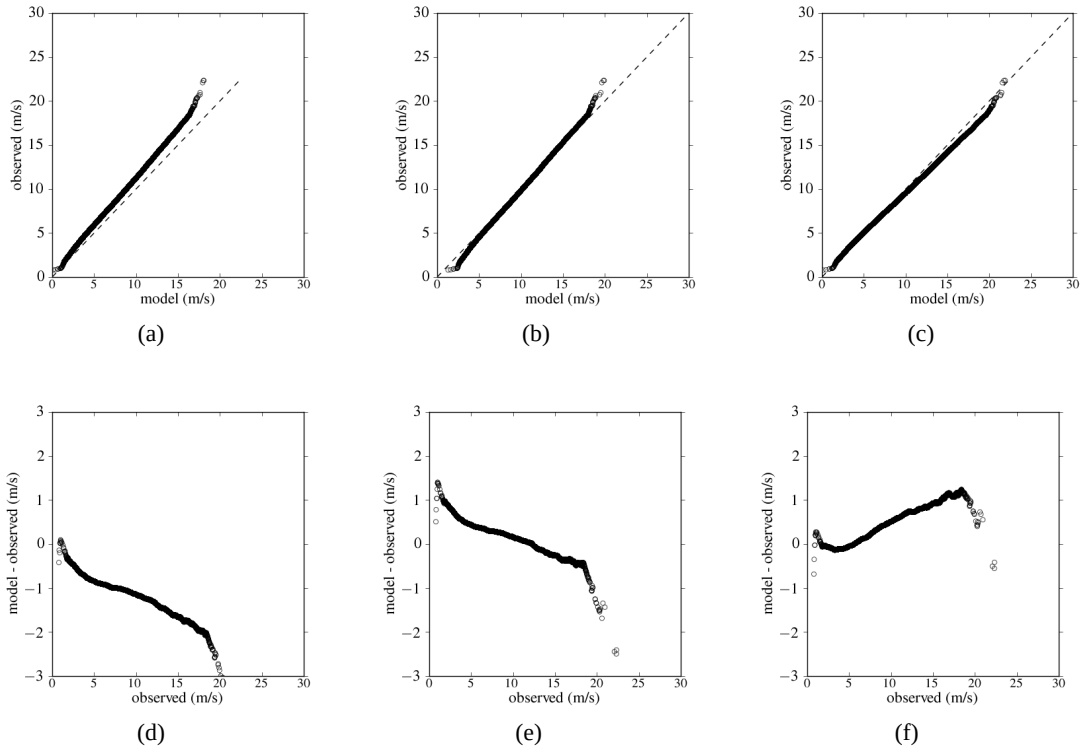

Figure 6.5: Comparison of bias correction methods. Hourly average wind speed across all offshore in-situ observations. (a) uncorrected WRF wind speeds (b) bias corrected WRF wind speeds using linear regression, (c) bias corrected WRF wind speeds using only multiplicative scaling. Plots (d), (e) and (f) show residuals against observed wind speeds for the corresponding plot above.

Therefore a second approach was tested where the intercept, c_i, was constrained to be zero, and only a multiplicative correction remains. Eq 6.1 becomes simply:

$$\overline{U}_i^{sat} = m_i \overline{U}_i^{wrf} \tag{6.2}$$

and the gradient, m_i, is simply the ratio of average satellite wind speeds to model wind speeds. In theory, the more general Eq. 6.1 should find this solution if it is indeed the best fit. However, large errors at higher wind speeds can have a large impact on the intercept term.

Figure 6.5 shows QQ plots against offshore in-situ observations for uncorrected and bias corrected wind speeds using both methods. From the top row of Figure 6.5 it can be seen that both bias correction methods do well at correcting the bias, but the linear regression method is marginally better throughout a larger range of wind speeds. From the bottom row of Figure 6.5,

it can be seen that the first bias correction method tends to over-compensate at low wind speeds, probably due to the intercept term. In contrast, the second method tends to over-correct at higher wind speeds, due to the larger size of the multiplicative term.

Figure 6.6 shows the geographic distribution of the least squares gradient (a) and intercept (b), and also the value of the gradient when only multiplicative scaling is used (c). The intercept terms in Figure 6.5 (b) appear quite large, with values of up to 2 ms^{-1}. However, they are difficult to interpret alone, since they may offset to some extent by a gradient of < 1. Figure 6.5 (c), which can be interpreted alone, shows but the corrections tend to be between 1.0 to 1.2 for the open sea, and between 1.2 to 1.2 for coastal areas. It can also bee seen that the largest corrections, which occur in the Irish Sea and the English Channel, correlate very closely with areas of wind speed bias seen in comparison with the Marine Atlas, Figure 5.26. This gives further support to the notion that the orrections are physically realistic. However, they should be interpreted with caution, as current satellite datasets cannot be relied on close to the coast. It could be that the satellite 'correction' is actually a reflection of poor quality near to the coast, and this approach should be revisited once higher resolution coastal datasets become available for the UK.

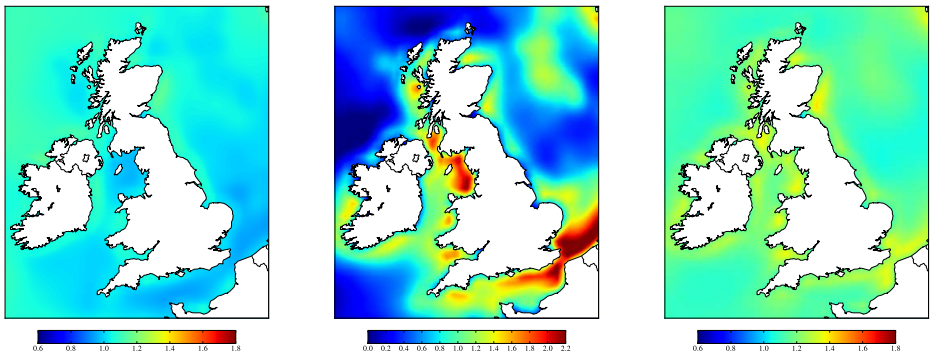

(a) gradient (b) intercept (c) multiplicative scale

Figure 6.6: Bias correction gradient (a), intercept (b), and scale factor alone (c) from linear regression between 11 years of satellite and WRF wind speed

Finally, it should me noted that, although the regression is developed between daily average speeds, the correction is assumed to be applicable to hourly wind speeds. This is a reasonable assumption since it is a linear operation, and therefore can be applied to the hourly components and have the same transformation on the daily averages. It is also assumed that the same correction applies at hub-height. This is supported by the vertical profiles investigated in §5.7,

which show systematic displacement to the wind profile throughout the height range.

6.6 Results

Figure 6.7 shows the model winds corrected by the linear regression and the satellite wind speeds. As intended, the adjustment brings the model data into much closer agreement with satellite wind speeds. In particular it removes the anomalous features associated with observations at oil platforms and buoys. Figure 6.7 also shows a detail close to the coast, also showing averages from in-situ observations. The bias corrected wind speeds agree more closely with the in-situ observations. Much of the spurious geographic variation has been removed, yet the model winds still show a realistic decrease close to the coast, in agreement with in-situ observations.

Table 6.2 summarises revised error statistics at in-situ observations. There is a dramatic improvement in B at all sites, apart from K5 and K7, which are disccussed in § 6.4. There is also an improvement in RMSD at all sites apart from K5 and K7. Importantly, R^2 remains the same at all sites, confirming that the simple linear correction has not altered the temporal patterns. The transformed QQ plots against all offshore observations have already been presented as Figure 6.5. The bias correction brings the distributions in to much better agreement. Once transformed, there is a slight positive bias against in-situ observations; however, this mainly results from the lower than expected speeds at buoys K5 and K7, as discussed previously.

Finally, Figure 6.8 shows the error distribution in the average hourly windspeed against in situ observations both before and after the satellite correction is applied. The bias correction shifts the error distribution, with the new errors reasonably normally distributed about the mean $B = 0.26$ ms^{-1}. Again, this small positive bias mainly relates to the K5 and K7 buoys. Estimating confidence intervals on B directly from the sample quantiles gives ± 0.91, ± 1.20, and ± 1.50 for the 80%, 90% and 95% confidence intervals respectively.

Taken together, these statistics give a very strong verification of the dataset, showing it to be essentially unbiased and give a realistic representation of the spatial and temporal variations in wind speed seen over the eleven year period.

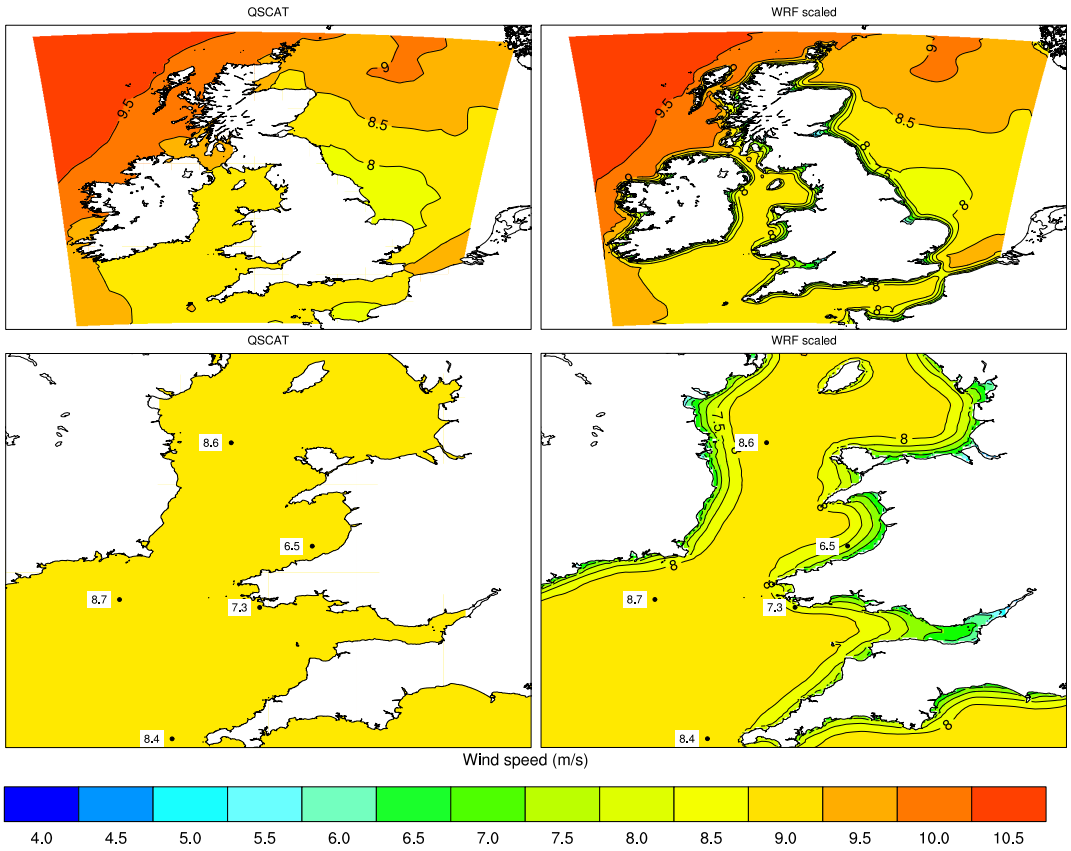

Figure 6.7: Average satellite wind speeds at 10m (left) and bias-corrected WRF winds at 10m (right). Bottom plot shows a detail closer to the coast, with average speeds from in-situ observations shown as labels on a white background.

6.7 Chapter summary

This chapter addresses a low wind speed bias in offshore simulated wind speeds, which would have been of sufficient magnitude to affect conclusions. A complete record of daily average wind speed from satellite records was established. Comparison with in-situ observations showed the satellite wind speeds to be essentially unbiased, and also revealed a potential low wind-speed problem at an exposed UK Met Office buoy before 2007. Satellite winds were then used to derive a simple bias correction, and two bias correction methods were tried based on linear regression. This resulting correction was applied to the hourly wind speeds, which significantly improves the representation of wind-speed distributions, and brought the geographic pattern into much closer agreement with observed patterns.

The bias-corrected dataset represents a major output of the work. It is of use to researchers, wind farm developers, grid operators, policy makers and others. It is used in future chapters

Name	Mean (ms^{-1})			B (ms^{-1})		RMSD (ms^{-1})		R^2	
	obs	raw	sca	raw	sca	raw	sca	raw	sca
Aberporth Buoy	6.19	5.25	6.78	-0.95	0.59	2.24	2.14	0.62	0.62
Channel Lightship	8.57	7.59	8.57	-0.98	0.00	1.92	1.69	0.85	0.85
Greenwich Lightship	8.63	7.02	8.49	-1.61	-0.14	2.4	1.81	0.84	0.84
K5 Buoy	7.95	7.70	9.03	-0.25	1.08	2.03	2.32	0.73	0.73
K7	7.82	7.69	8.51	-0.13	0.69	2.27	2.42	0.65	0.65
M2	7.84	6.29	7.77	-1.55	-0.07	2.18	1.54	0.81	0.81
M3	8.04	6.90	8.17	-1.14	0.12	1.76	1.37	0.84	0.84
M4a	7.88	6.83	8.54	-1.05	0.66	1.87	1.68	0.82	0.82
M4b	8.32	7.16	7.89	-1.16	-0.43	1.86	1.53	0.84	0.84
M5	7.83	6.44	7.68	-1.40	-0.15	1.97	1.39	0.84	0.84
Pembroke Buoy	6.80	5.96	7.23	-0.85	0.43	1.75	1.59	0.80	0.80
Sandettie Lightship	8.34	6.41	8.21	-1.93	-0.12	2.74	2.00	0.80	0.80
Sevenstones lightship	8.62	7.64	8.60	-0.98	-0.02	2.06	1.82	0.82	0.82

Table 6.2: Error statistics calculated for hourly WRF wind speeds against in-situ observations. Table shows in-situ observations (obs), original WRF winds (raw), and bias corrected WRF wind speeds (sca).

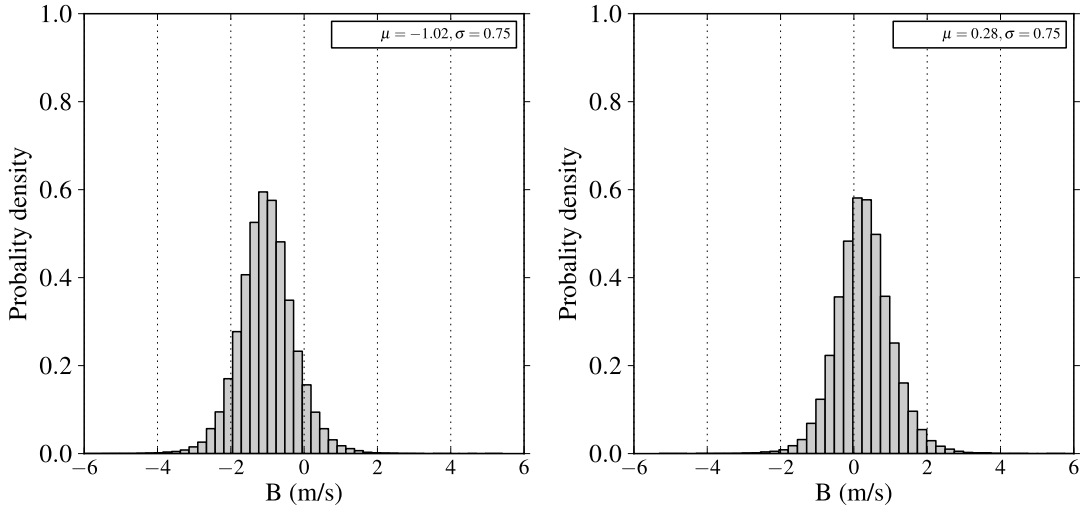

(a) Uncorrected

(b) Bias corrected

Figure 6.8: Distribution of error before and after correction against satellite wind speeds.

to examine the geographic and temporal patterns in power output from current and future wind farms.

Chapter 7
Conversion to power

7.1 Introduction

The previous chapters have described the creation and validation of an 11-year wind speed dataset across the British Isles. This has been shown to capture very well the spatial and temporal variations in wind speed over this period. Onshore, the wind speeds showed very little systematic bias, although the performance depended on the terrain complexity; offshore, a systematic low bias was corrected using eleven years of satellite scatterometer derived wind speeds.

This chapter now examines how this dataset may be used to estimate the outputs from current onshore and offshore wind farms, and validates the approach against published data. This provides support for the analysis chapters which follow later.

7.2 Power curves

7.2.1 Single turbines

The amount of electrical power which can be generated by a wind turbine is proportional to the total kinetic power available [Burton et al., 2011]:

$$P = C_p \frac{1}{2} \rho A U^3 \tag{7.1}$$

where P is power, ρ the air density, A the rotor swept area, U the incident wind speed, and the coefficient of proportionality, C_p, is known as the power coefficient. However the response of a turbine is not simple - C_p is not constant - so the actual relation between wind speed and power generated is not a straightforward cubic relationship, and is usually summarised by a *power curve*. It is useful to define power curves in terms of the normalised power, or *load*

factor (LF):

$$LF = \frac{P}{P_{max}} \tag{7.2}$$

where P is the instantaneous power, and P_{max} is the maximum rated power of the turbine. A typical power curve is shown in Figure 7.1. It is characterised by:

1. a cut-in speed: the speed at which the turbine begins to generate;
2. a rated speed: the speed at which the the turbine reaches maximum output; and
3. a cut-out speed: the speed at which the turbine is shut down to prevent damage.

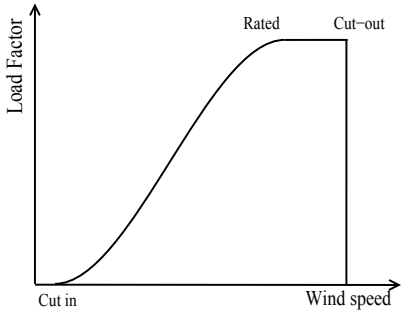

Figure 7.1: Schematic of a typical turbine power curve

The primary use of power curves is to allow developers to predict the energy yield of a site once the wind speed distribution is known. Power curves are determined by field measurements according to strict standards [IEC, 2009], and are usually determined using the *method of bins*, where power is bin-averaged power over 0.5 or 1ms^{-1} bins [Burton et al., 2011].

The reason for using the method of bins is that the raw data typically shows large scatter related to, for example, turbulent variations in wind speed and the dynamic response of the turbine [Gottschall and Peinke, 2008, Kaiser et al., 2007]. The IEC standards define, as far as possible, site characteristics for the testing of turbines. The actual performance of the turbine may be significantly different when deployed in different conditions. In particular, turbulence intensity at the site will have a large effect on the power curve.

The power curve gives the *average* power output of a turbine within each wind speed bin, and a time series of power output created from a power curve gives the *most likely* output given those wind speeds. In the long-term it should match the observed average, but it will not recreate the large scatter seen in real observations.

7.2.2 Wind farms

Estimating the aggregate output from a wind farm is more complex than simply scaling up from a single turbine. The output is influence by a number of factors, mainly:

- variation in wind speed and turbulence across the site;
- wake losses;
- technical availability;
- storm control actions; and
- electrical losses within the wind farm.

Also, it should be noted that observations of whole-farm power curves show greater scatter than single-turbine cases. Figure 7.2 shows the amount of scatter typical in field measurements [Wan et al., 2010]. For a given wind speed, there is clearly a wide-range of observed power outputs, and a number of different regimes can be noted, possibly corresponding to wind direction. The ramp down region at high wind speeds can also be seen.

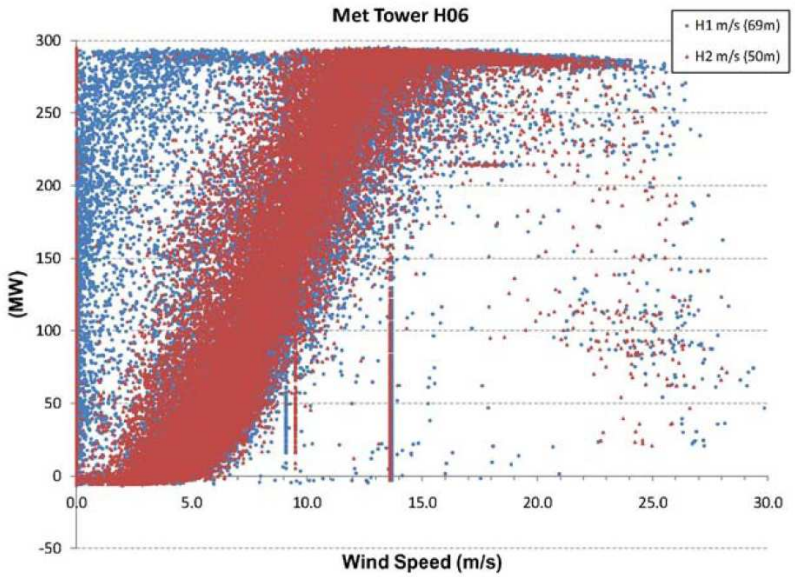

Figure 7.2: An example of the experimental scatter seen in measurements of power curves at operational wind farms. From Wan et al. [2010]. Wind speed as measured at a nearby met mast is on the x-axis, and power output of the whole farm on the y-axis.

Technical Availability

Technical availability of onshore turbines has been well studied and is known to be very high. Harman et al. [2008] reviewed a technical database relating to 14GW of installed capacity and found availability to be 97%; this is typical of the level now guaranteed by manufacturers.

Offshore technology is much less mature and the sites developed so far have been relatively close to shore. Further offshore, access for repair becomes more limited by weather windows. Rather than assume a single number for technical availability, it is studied separately later in the analysis as a sensitivity parameter. Furthermore, the effect of technical availability on load factor is not straightforward. Many studies assume, for example, that a reduction in technical availability of 10% will reduce output by 10%. While this may be a valid assumption for thermal generators, for wind generators it also matters *when* it occurs. If a turbine is unavailable in the winter, it will have a larger reduction in output than if it were unavailable in the summer. This is studied as a sensitivity parameter in Chapter 8.

Electrical losses

Resitive losses in cables, transformers and other balance of plant equipment cause a small loss of energy production, which are of the order of 2% of annual energy production [Manwell et al., 2002a].

Storm control

All wind turbines take action to prevent damage in very high winds. Most large modern turbines are pitch-controlled and in very high winds, typically above 25ms^{-1}, the blades are fully pitched to stop production. Depending on the control strategy, this may be a fairly sudden change to zero output, or a more gradual ramp-down, known as soft storm control. To reduce fatigue loading associated with repeated shut-down events, some form of hysteresis is often implemented where the turbine is not re-started until the wind speed reduces below a particular level.

Wake losses

The most significant losses for a wind farm, as opposed to a single turbine, are wake losses. The energy extracted by a turbine generates a speed deficit downstream, until entrainment of momentum from above causes the wind speed to recover [Burton et al., 2011]. Wake losses are thought to be lower in more complex terrain where turbulence intensity is higher. The effect of wake losses on average energy production for onshore farms is usually found to be in the range 4-12% [Manwell et al., 2002b]. In the cross-wind direction, wake losses can be as high as 40%, and wind farms are generally laid out to minimise wake losses in the prevailing wind direction, although landscape and planning factors may affect the layout.

Most offshore turbines are not radically different from current large onshore turbines, and the power curves have a similar form. However, much less data is available on the aggregate performance of offshore farms. Wakes are generally thought to be more significant, since they persist for longer due to the lower turbulence intensity offshore. However, real world data is lacking, and in particular the effect of atmospheric stability on wake effects is not understood [España et al., 2012]. Most studies predict wake losses of the order of 10-15% [Barthelmie et al., 2007, Mclean and Hassan, 2008]. However, most studies are based on existing wind farms relatively close to shore. Although wake effects are thought to be more significant, for future offshore wind farms, larger losses at lower wind speeds may be compensated by the longer time spent at higher wind speeds, above the steepest part of the power curve.

7.3 Accounting for losses

There are three general ways to account for these losses. The first is to use a single turbine power curve - ignoring the losses - and then scale the final result down by a constant factor. Assuming constant array losses of around 10% is typical [Burton et al., 2011]. An advantage of this approach is it is very simple to apply and transparent. Further, the loss factor can be chosen so that the outputs match long-term published averages. The drawback is that wake losses are not distributed realistically across the wind speed range: using this approach the output of a wind farm never reaches 100%.

The second approach is to use an aggregate power curve, whose shape accounts for losses. The advantage of this approach is that it is relatively simple to apply, yet it distributes wake losses

more realistically through the range of wind speeds, and can also account for the smoothing of wind speeds seen across the whole farm. The drawbacks are that it may be impossible to adequately characterise the farm by a single curve, as wakes losses vary considerably with wind direction [Manwell et al., 2002b]. In addition it may be difficult to make the curve generic and applicable to multiple farms.

The third approach is to try to account for losses separately based on physical considerations, for example, using a CFD model to determine wake losses by wind speed and direction e.g. [Barthelmie et al., 2007, Costa et al., 2006, Li et al., 2011]. However, the physical effects are complex and difficult to predict, and this approach introduces another uncertainty on top of any underlying uncertainties in the wind speed.

The second approach, an aggregate power curve, is used here as it gives a good trade-off between complexity and realism. The third approach of modelling each effect individually using more complex models was not attempted, as it is infeasible to apply this across several hundred wind farms. In any case, when estimating the power from future farms there are many other uncertainties which are as, if not more, significant, such as changes in the future wind speeds, assumptions about the number, size and height of turbines, and assumptions about the layout of wind farms, and assumptions about the technical availability of offshore turbines.

7.3.1 Aggregate power curves

A number of approaches have been taken to produce aggregate power curves, based on theoretical arguments e.g. [Kaiser et al., 2007, Nørgaard, 2004], measured data e.g. [Hayes et al., 2010, Tindal et al., 2008, Wan et al., 2010], or engineering experience and judgements e.g. [Mclean and Hassan, 2008].

All the approaches cited above point to a similar modification to the shape of the curve, shown in Figure 7.3. Power output at low wind speeds may be very slightly higher than expected, as some turbines will be experiencing higher than average wind speeds. As speed increases, the first row of turbines will reach rated power, but turbines in the wakes behind will not. Maximum output is not reached until the average wind speed is sufficiently high that turbines in the back row are at rated wind speed. Finally, the farm output may begin to decline before the cut-out speed is reached, due to wind speed variations across the site and turbulent gusts causing control actions to be taken at individual turbines. The behaviour in the region approaching cut-out speed is not

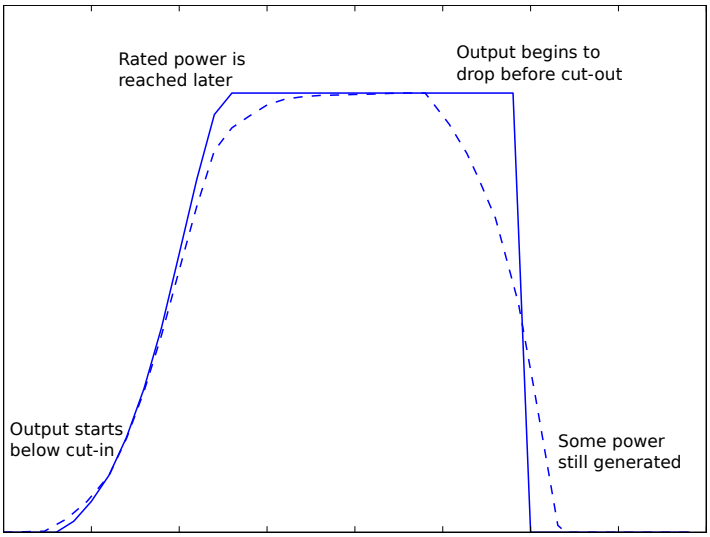

Figure 7.3: Shape of an aggregate power curve (dashed) in relation to a single-turbine curve (solid).

well documented, partly due to the infrequent occurrence of very high winds, but also due to differences in the control strategies between different turbines and site operators. Due to the infrequent occurrence, the behaviour in this region is less important for energy production.

Given the shape outlined in Figure 7.3, a generalised aggregate power curve may be characterised by:

- cut-in speed: the speed at which the farm begins to produce power;
- rated speed: the speed at which the farm reaches rated power;
- ramp-down speed: the speed above which the power begins to decreases;
- cut-out: the speed above which the farm produces no power;
- f_{up}: a function describing the ramp up; and
- f_{down}: a function describing the ramp down.

Hayes et al. [2010] used wind speeds measured at individual nacelles (corrected to represent the free-stream flow) to derive aggregate power curves for two wind farms. Although the

two sites studied had different terrain and geography, the aggregate power curves showed similar features, with significantly reduced power output (compared to a single-turbine curve) in the range 9-15ms^{-1}. They proposed a simple per-unit adjustment based on wind speed, to transform a turbine curve into an aggregate curve. These adjustments are given in Appendix B, Table B.3.

The adjustments defined by Hayes et al. [2010] are derived from measurements at farms with 3MW turbines with fairly standard characteristics: a cut-in speed of 4ms^{-1}and a rated speed of 12ms^{-1}. This is representative of many large turbines, although some very small or very large turbines differ. In order to generalise these per-unit adjustments to all turbines, they were re-defined in terms of a normalised variable I, where

$$I = \frac{U - \text{cut-in}}{\text{cut-out} - \text{cut-in}} \tag{7.3}$$

so they could be applied to any power curve. The interval value is also given in Table B.3. Adjustments at high wind speeds close to cut-out were not published in [Hayes et al., 2010] due to the small number of observations, but the authors confirmed that the output was seen to reduce as the average speed approached the cut-out speed (Hayes, personal communication).

With the adjustments applied, the resulting power curve, Figure 7.4, is shallower than a normal turbine power curve, and can be very well approximated by a logistic function:

$$LF = \frac{1}{1 + e^{-\frac{(U-a)}{b}}} \tag{7.4}$$

where U is the wind speed and a and b are parameters relating to the centre and width of the curve. This has the advantage of being easy to apply, requiring only two parameters, and does not fluctuate or overshoot like higher-order fitted polynomials.

Figure 7.5 shows an example time series using single-turbine power curve and an aggregate curve based on the per-unit adjustments described. The adjusted curve appears to give a realistic estimate of wake losses in the correct wind speed region. Table 7.1 shows the estimated reduction in energy yield using this approach at a high-wind and low-wind site. Energy reductions are of the order 10% to 13%, which agrees with the range of estimates found in the literature. Moreover, energy losses are more realistically distributed across the range of

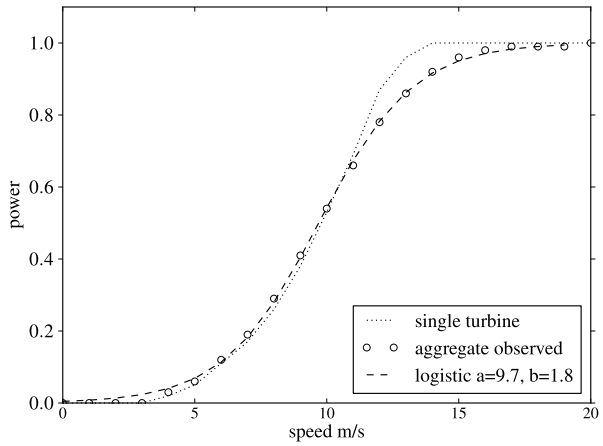

Figure 7.4: Single turbine power curve, measured aggregate power curve from Hayes et al. [2010], and a two-parameter sigmoid approximation to it.

wind speeds, with the highest losses in moderate wind speeds around the steepest part of the power curve. This approach is therefore thought to be realistic for both onshore and offshore sites.

	Weibull parameters		Energy yield		Difference
	k	c	Turbine	Aggregate	
		ms^{-1}	MWh	MWh	%
high wind	2.15	10.56	178	160	-10
low wind	1.88	8.55	130	113	-13

Table 7.1: Reduction in energy yield due to wake losses when modelled with an aggregate power curve compared to a single-turbine curve.

7.3.2 Approach taken

Based on the discussion above, the following approach was taken to define aggregate wind farm curves. Manufacturer's power-curves for a large number of existing turbines ranging from 500kW up to 5MW were taken from WAsP [Troen et al., 2008], and the cut-in speed, rated-speed and cut-out speeds were obtained. Per-unit adjustment of Hayes et al. [2010] were applied to transform the turbine shape into an aggregate shape which reflects array losses. Two-parameter logistic functions (Eq.7.4) were then fitted to the ramp-up region.

In the absence of detailed information, the power curves were made to ramp down from 1 to 0 linearly across the interval [cut-out $-0.5 ms^{-1}$, cut-out $+0.5 ms^{-1}$]. That is, a relatively sharp

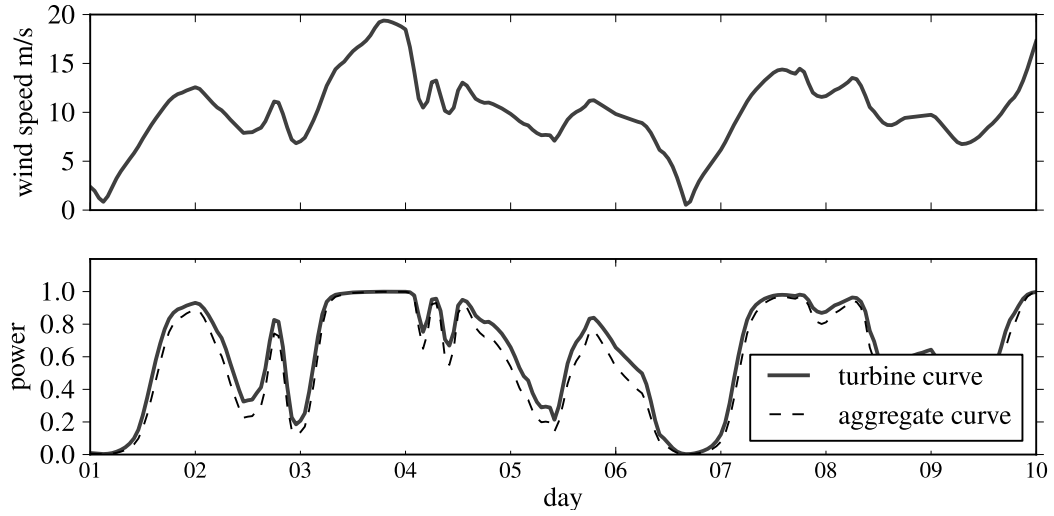

Figure 7.5: Example time series of wind speed (top) and corresponding power output (bottom) using a single-turbine curve, and an aggregate power curve. Wake losses are highest in wind speeds around 5-15ms^{-1}.

cut-off at the nominal cut-out speed was assumed. Electrical losses were assumed fixed at 2%. No account is made technical availability was made at this stage, this is analysed separately as a sensitivity parameter.

Existing wind farms were matched to the turbine power curve using information in the UK Wind Energy Database [Renewable UK, 2011]. This contains the make, model and size of turbine at all operational or under-construction wind farms. Offshore wind farms not yet under construction were assumed to have turbines similar to a REPower 5MW turbine, which is representative of the types of turbine which may be installed at Round 3 sites [Mclean and Hassan, 2008]. The main difference of this power curve is a cut-out at 30ms^{-1}, rather than 25ms^{-1}.

The resulting procedure for predicting the output from each wind farm is best illustrated by an example. To predict the power from a wind farm with ten 3.6MW turbines the following steps are followed:

1. the manufacturer's power curve is selected for the closest available turbine;
2. the curve is transformed by applying adjustments over the ramp-up region;
3. a two-parameter logistic function is then fitted to the ramp-up region;

4. a linear ramp-down about the turbine cut-out speed is assumed;
5. wind speeds are applied to this power curve to give an aggregate LF; and
6. the LF is scaled up by the total installed capacity (10$\times$ 3.6 MW) of the wind farm to give the total power output.

7.4 Comparison to published data

7.4.1 Data sources

Detailed data on the outputs of existing wind farms is not readily available, as data owned by wind farm operators is regarded as commercially sensitive. The main publicly available sources of data are summarised in Table 7.2.

Data source	Aggregation	Time resolution	Comments
BM Reports	Individual wind farms	Half-hourly	Transmission connected only Frequent missing data Quality sometimes questionable
ROC Register	Individual wind farms	Monthly	Comprehensive coverage Early offshore data unreliable
Capital grants reports	Individual wind farms	Monthly	Only offshore Limited time coverage Has technical availability

Table 7.2: Data sources on wind farm outputs

BM reports

The New Electricity Trading Arrangements (NETA) mandate that certain information must be provided to support the balancing mechanism used by the National Grid use to ensure power flows into and out of the transmission grid remain balanced. This data is currently provided by Elexon [2011]. Information is provided in real-time on the output of individual generator units connected to the transmission grid, and some data is also archived. However, archived data is only available from 2010 onwards, and only data from transmission connected wind is available. Hourly output is given to the nearest MWh. Large periods of missing (zero) data is also common in the archives. Table 7.3 summarised the wind farms for which reliable hourly wind data was available.

Name	Region	Capacity (MW)
Black Law	South Lanarkshire	97
Farr Windfarm	Highland	92
Hadyard Hill, Barr	South Ayrshire	130
Kilbraur	Highland	48
Millennium	Highland	40
Toddleburn	Scottish Borders	28
Whitelee	East Renfrewshire	322

Table 7.3: Onshore wind farms with hourly production data from BM Reports.

ROC Register

The primary mechanism in the UK for subsidising wind power are Renewable Obligation Certificates (ROCs). Since April 2002, all UK electricity suppliers have been obliged to obtain a proportion of their energy from renewable sources. This is achieved by issuing ROCs to renewable generators, from whom suppliers can buy these certificates to fulfil their obligation. One ROC is earned per MWh of electricity generated for onshore wind, and 2 ROCs per MWh for offshore wind.

The ROC register is a comprehensive record of the number of ROCs issued to each generator each month, and therefore allows the calculation of monthly load factors at each wind farm. At the time of downloading, the ROC register had data up to the end of February 2010. It was found to be unreliable for offshore wind before 2009, as many of the generators had ROCs aggregated into a whole year e.g. 2007-2008, rather than by month. Data compiled in the capital grants reports was found to be a better source for offshore farms for most of the period.

The ROC register does not contain the coordinates of renewable generators, only the name and the region. The coordinates of wind farms are available in UKWED. However, the only link between these two sources is the name of the wind farm, which is not standard and varies between the two. Alternative names and different spellings are common, for example “Red House Wind Farm” appears in the ROC register while “Gedney Marsh (Red House)” appears in UKWED.

The two datasets were linked using the following algorithm. The names were converted to lower case and common nouns were removed: farm, hill, moor, etc. This ensured the remaining tokens were mainly related to the place name. A fuzzy matching algorithm based on trigrams[1] was applied to create a similarity score (from 0 to 1) between each possible pair of names. Each

[1] http://www.postgresql.org/docs/current/static/pgtrgm.html

name in the ROC register was then matched to the name in UKWED with the highest similarity score, with any matches with a similarity score below 0.3 excluded as unreliable. Finally, the resulting matching was examined manually and a few remaining false or inconclusive matches were excluded.

There are 301 operational onshore wind generators in the ROC register, and 307 in UKWED. Applying the matching algorithm identified 192 definitive matches. Of those, 107 were operational before 1st January 2007, so had at least three years of data; these are used for verification.

Capital grants reports

Offshore wind farms which received UK Government support under the capital grants programme [DTI, 2003] were required to submit annual performance reports for the first few years of operation. This includes monthly load factors, monthly wind speed, and monthly technical availability, and is the only source of offshore data with these figures. Unfortunately it only covers a few farms for a relatively short period, summarised in Table 7.4. Tavner et al. [2010] gives a good summary of the data available in the individual reports.

Windfarm name	Period available
Barrow	Jul 2006 - Jun 2007
Scroby Sands	Jan 2001 - Dec 2007
Kentish Flats	Jun 2006 - Dec 2007
North Hoyle	Jul 2001 - Jun 2007

Table 7.4: Operational offshore wind farms with available capital grants reports.

7.4.2 Onshore

Hourly

Comparison of hourly time series for individual wind farms, Figure 7.6 (a,b), shows a fairly large amount of scatter, typical of that seen when deriving a power curve (see §7.2.2). However, the overall trend is still quite strong. When hourly time series are averaged across multiple farms, the match is much stronger. Figure 7.7 shows the average hourly load factor computed across the seven farms with hourly data available listed in Table 7.3. However, the simulated time series are smoother than the observed time series, and there are periods of low load factors which are not captured. This could be due technical outages, planned turbine maintenance,

changes in wind direction causing additional losses, curtailment due to insufficient network capacity or other factors not modelled.

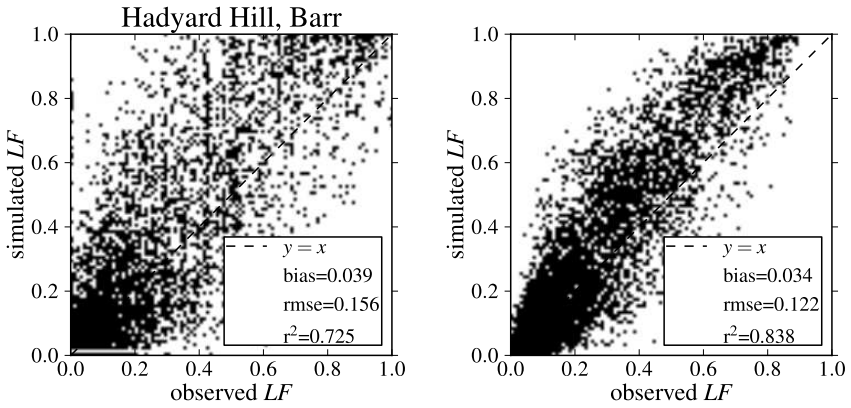

(a) Single farm (b) Average

Figure 7.6: Comparison of hourly load factors at a single transmission connected wind farm, and across seven transmission connected wind farms

The conclusion from the hourly comparison is that the simulated load factors capture the main features of the observed load factors, but shows a large degree of scatter, demonstrating there are many other determining factors than just the wind speeds and average power curve. However, averaging over seven wind farms shows a much stronger relationship, and the hourly output is very well correlated. There is a slight high bias overall against these seven wind farms, $B = 0.03$, but this is before technical availability has been accounted for. Given that technical availability is around 97% for onshore turbines, this suggests the results are unbiased overall.

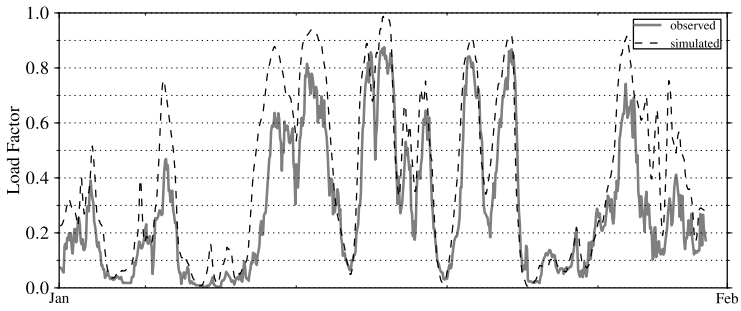

Figure 7.7: Time series of average hourly load factors in January 2010 across the seven wind farms listed in Table 7.3

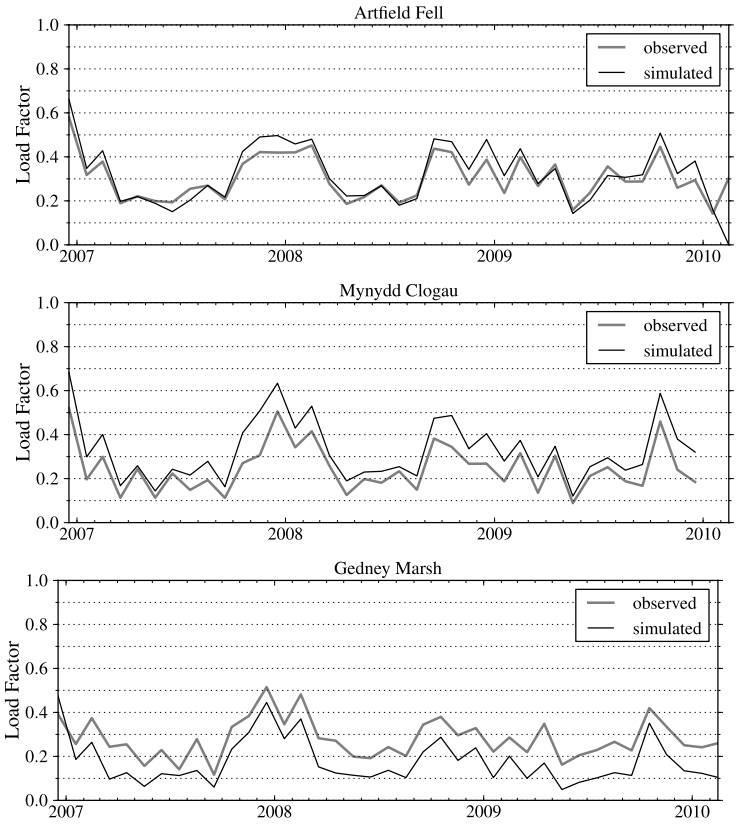

Figure 7.8: The good, the bad, and the ugly: examples of the monthly match at individual wind farms

Monthly

The farms with hourly data are all large, transmission connected wind farms in Scotland. Most of the onshore wind in the UK consists of smaller, distribution connected farms, more widely distributed across the country. The only source of data for distribution connected wind is monthly data from the ROC register.

Figure 7.8 shows the match against three individual farms in the ROC register, distributed around the country. The examples have been chosen to be representative of a good, reasonable, and poor match. There are some systematic differences at individual wind farms as would be expected since the terrain at 3km resolution will not adequately capture all sites.

Figure 7.9 shows the average load factor across 107 farms matched in the ROC register. The match is reasonably good. Again, there is a slight over-prediction, with $B = 0.03$, but this is before adjusting for technical availability.

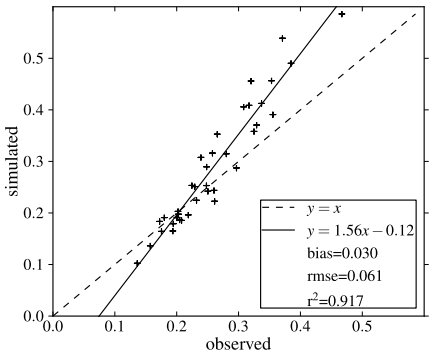

Figure 7.9: Comparison of simulated and observed average monthly load factor over 107 wind farms in the ROC register for the period 2007-2010.

The conclusion from the comparison of monthly values is that patterns are captured very well, simulated load factors may show systematic errors at individual wind farms, but when averaged across a number of sites the agreement is very good, and unbiased once a reduction has been made for technical availability.

7.4.3 Offshore

Hourly

No hourly data for offshore farms was available, therefore verification could only be done at done at a monthly level.

Monthly

Offshore wind farms in the UK have been operational since North Hoyle began generating in 2003, but it is only since 2005 that three or more farms have been operational. Load factors for operational farms are taken from the capital grants reports before 2009, and the ROC register thereafter. Technical availability is available in the capital grant reports, and observed outputs have been adjusted to 100% technical availibility

Figure 7.11 (a-c) shows monthly time series plots for three operational wind farms around the UK coast. The load factor derived from raw WRF speeds and bias-corrected speeds as described in Chapter 6 are shown. It can be seen that load factors derived from the bias-corrected wind speed are in closer agreement, and where there is a discrepancy, it is present in both

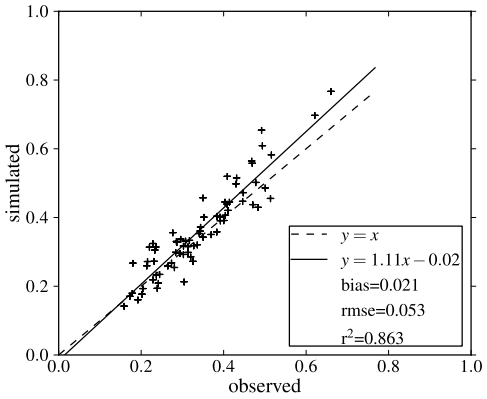

Figure 7.10: Observed and simulated monthly load factors averaged across all operational offshore wind farms.

the corrected and uncorrected wind speeds i.e. it is a not a result of applying the correction. Figure 7.11 shows agreement at all offshore wind farms.

The conclusion from the comparison with offshore farms is that the simulated load factors show a good match with published figures, both in terms of their average values and monthly variation. Although no direct hourly comprisons could be performed, this still gives strong evidence that the simulated hourly output will be realistic.

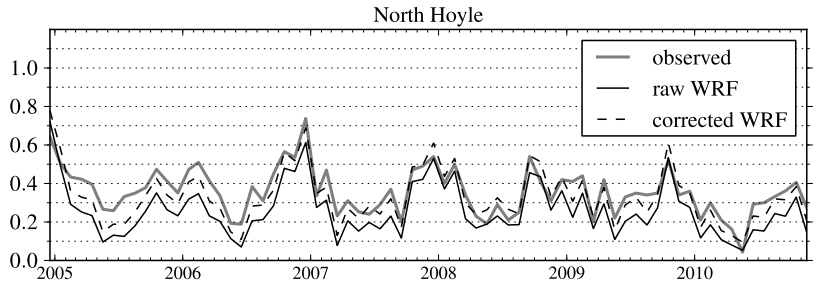

(a)

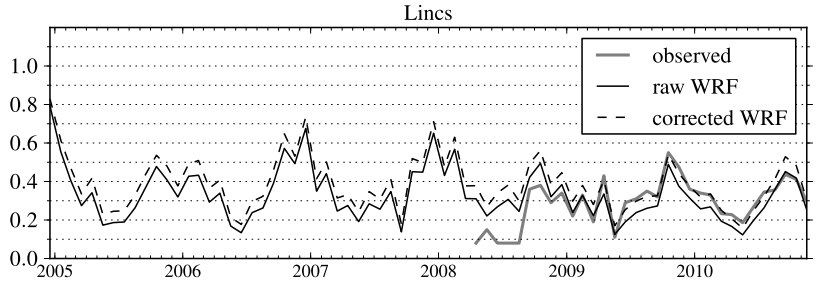

(b)

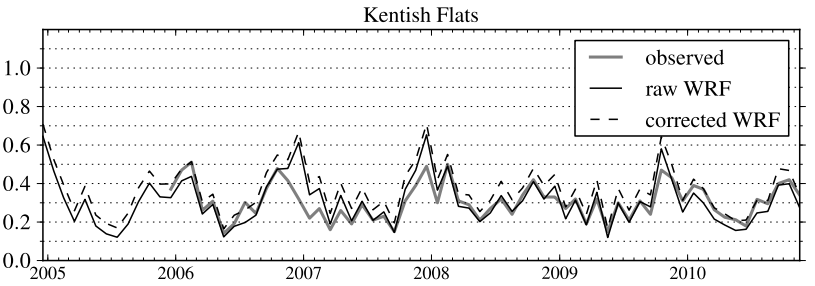

(c)

Figure 7.11: Example of the match at three offshore wind farms

7.5 Chapter summary

Factors affecting the simulation of power output from single turbines and whole wind farms were discussed, and background material on wake and other losses was summarised. The large amount of scatter seen in empirical measurements of power curves was noted, highlighting the inherent difficulties of predicting power-output time series using a power curve. Nonetheless, an aggregate power-curve approach was developed and applied to wind speed data from WRF to simulate power outputs from existing wind farms. Numerous published sources of wind farm data were collated to allow the validation of hourly and monthly time series at existing onshore wind farms, and monthly time series at offshore wind farms.

At individual onshore wind farms, there was a large amount of scatter between the simulated and observed hourly values, though the time series captured the phase and variability of major features very well. When averaged over several large transmission connected wind farms, the scatter was much reduced and the match improved substantially, $R^2 = 0.84$. There was a slight positive bias, $B = 0.03$, which is desireable since no account has yet been made for technical availability.

Comparsion to monthly load factors calculated from the ROC register, showed some systematic bias at individual farms, though this tended to get averaged out across a large number (107) of transmission and distribution connected wind farms. A similar small positive bias, $B = 0.03$ seen in the hourly comparisons, which again is desireable since this was before accounting for technical availability.

Offshore, the agreement between monthly load factors was found to be very good, and the satellite bias-correction derived in the previous chapter was found to work well. Comparison of average monthly load factors over all currently operational onshore wind farms showed good agreement, $R^2 = 0.86$, and a similar positive bias seen at onshore sites, $B = 0.02$, before accounting for technical availability.

This chapter provides valuable evidence that the hourly wind speed data from WRF can be used to create realistic hourly load factors for existing onshore and offshore wind farms. Chapter 5 has already shown that wind speeds are captured well over the whole of the British Isles and surrounding waters. On that basis, it can be assumed that load factors derived at the locations of future wind farms are also realistic and representative. The remaining chapters the expected power production from a future wind fleet and the implications of this.

Chapter 8
Analysis

8.1 Introduction

Previous chapters have described the creation and validation of a high-resolution wind speed dataset spanning a period of eleven years. It has been shown that the dataset captures the variability of wind speeds very well across a variety of spatial and temporal scales. The wind speeds have been shown to match observed averages onshore across a very large number of met stations and onshore masts. Offshore, the wind speeds have been bias-corrected using wind speeds derived from satellite scatterometer measurements. The corrected speeds match observed average values, and the spatial and temporal patterns very well.

It has also been shown that this dataset can be used to model the output of existing onshore and offshore wind farms, and that the patterns of power production are realistic. On this basis, it is proposed that this dataset can be used to provide information and insight about the spatial and temporal patterns of power generation from future wind fleets. Although eleven years is not long enough to be considered a true climatology, it is long enough to capture an extensive range of weather types, and capture a large amount of inter-annual variability, including an extremely calm winter by historic standards.

A large advantage of this dataset is that it represents a true historic time-series, so can be matched to other time-series, such as historic electricity demand. Often studies looking at the wind resources use statistical downscaling to produce an average climatology, which cannot be linked to specific time periods.

This chapter presents an analysis of likely patterns of power and energy production from future wind farms, with a focus on offshore generation. The approach adopted here is to use relatively simple techniques and clear assumptions to demonstrate what can be achieved with the dataset. By making the dataset publicly available, it is hoped these, and other key research questions can be explored in more detail, and that the results are reproducible.

This chapter is divided into three sections: first, some background is reviewed regarding the

possible size and extent of the UK's future offshore wind fleet; second, the analysis approach is presented; finally, the results of the analysis are presented and discussed.

The basic assumption which underpins this analysis is that the last eleven years of wind speed are broadly representative of the expected future wind climate. Although it is known that the climate is changing, the British Isles will continue to be governed by similar mid-latitude synoptic systems seen today, perhaps with a shift in frequencies of weather types and the position of storm tracks. Analysing the impacts of climate change are outside the scope of this work, but are discussed in § 9.4. Also, by providing a link between different weather episodes and patterns of energy production and demand, this dataset could provide a baseline for future climate change studies.

8.2 Background

8.2.1 Growth of wind

Under the European Renewable Energy Directive, the UK has a target to supply 15% of primary energy demand from renewables by 2020. The electricity sector is expected to make the largest contribution, with renewable generation contributing over 30% of electricity generated in the lead scenario [UK Government, 2009].

Wind has seen rapid and sustained growth in the UK over the past decade, and is widely expected to contribute the most to the UK's renewable energy targets. The UK currently has around 4GW of operational onshore wind and around 1.5GW offshore [Renewable UK, 2011]. It is expected that much of the growth in renewables will come from offshore wind generation [PWC, 2010, Toke, 2011]. The Crown Estate has already leased sites which could be developed to around 40GW of installed offshore capacity in a relatively short timescale. These sites have been leased in a series of three rounds, Round 1, Round 2, and Round 3, plus an additional Scottish Exclusivity (SE) round.

Most build-rate projections for the growth of wind energy in the UK are based explicitly on the 2020 renewable energy targets. Various growth projections have been made by industry bodies, with different motivations or purposes, for example to highlight the potential economic value of wind generation for the UK [The Offshore Valuation Group, 2011], to identify the size of the supply chain needed to support growth [Renwewable UK, 2010], or to highlight the number of

jobs which might be supported [Esteban et al., 2011].

However, it is increasingly recognised that the build-rates in these projections are optimistic. For example, a recent report [Crown Estate, 2010] estimated that to develop the 32GW of offshore wind identified in the Round 3 zones according to the developers' stated timetables would require the manufacture and installation of around 1500 turbines per year in the period 2017-2019. Given that installation at many Round 3 sites would not be possible for much of the winter, this would mean installation of tens of turbines per day during admissible weather windows. As well as the obvious practical difficulties, the report concluded such high installation rates could lead to an unwelcome increase in cost.

This highlights the difficulty associated with predicting the future growth rate, and the difficulty with tying an analysis to a particular time-based scenario. A common approach is to develop a number of parallel scenarios, e.g. low growth, high growth etc. However, for this analysis, the key question is not *when* a wind farm gets built, but *where*, and how that changes the overall geographic distribution of capacity. The locations of wind farms will determine how their outputs correlate to one another, and the distribution of capacity between regions will determine how much geographic smoothing is achieved and the likely size of the power flows between regions.

Similarly, it may be diffcult to predict the exact installed capacity at specified points in the future. However, much of the analysis does not depend on the absolute capacities installed, but depends on the relative distribution of capacity between regions. Therefore, for this analysis, rather than invent several time-based scenarios describing the growth of wind out to 2020 or 2030, an approach is taken which highlights how the geographic distribution will change in several stages as more onshore and offshore wind is developed. These are described by a series of 'snapshots' defined in §8.3.

8.2.2 Location of future wind

Onshore

Onshore wind is relatively widespread across the whole UK, although it is concentrated in those areas of high wind resource with good access to the transmission or distribution grid. When assessing the locations of future wind, it would be possible to allocate new wind to 'optimal' sites based on average wind speed and proximity to the grid, with certain areas excluded due to

Status	Num sites > 1MW	Capacity (GW)
Operational	231	3.6
Under construction	36	1.3
Consented	155	3.6
Submitted to planning	202	6.0
Total	668	15.1

Table 8.1: Set of all onshore wind farm locations used in analysis

environmental or planing constraints; this was the approach taken by e.g. Boehme et al. [2006].

However, this approach is somewhat idealistic, as it assumes optimal sites are developed first. In reality, many other factors such as landowner cooperation and the expectation of planning consent, play a very important role; these criteria are difficult, if not impossible, to specify in an automated way. In addition, future development will also come from the extension or re-powering of existing sites with larger turbines.

For the analysis presented here, the exact locations of individual wind farms is not critical provided they are geographically distributed in way broadly representative of the future. For that purpose, the set of locations already developed or earmarked for development is likely to be a reasonable representation of the future.

The Renewable UK 'Wind Energy Database' [Renewable UK, 2011], referred to hereafter as UKWED, has over 700 sites listed as developed or submitted to planning. The number and capacity of wind farms under different categories at the time of downloading are given in Table 8.1. Sites below 1MW are excluded from the analysis as these make a minimal contribution overall, but increase the computational demand of the analysis. The UKWED has information on the make, model and turbine size of all existing operational farms, which allows the output to be assessed using a power curve tailored to each site, as described in Chapter 7.

Although many of the sites submitted to planning will not be approved for development, they are still likely to be geographically representative of the spread of sites which will get developed. The total set of 668 onshore locations which were used in the analysis is shown in Figure 8.1.

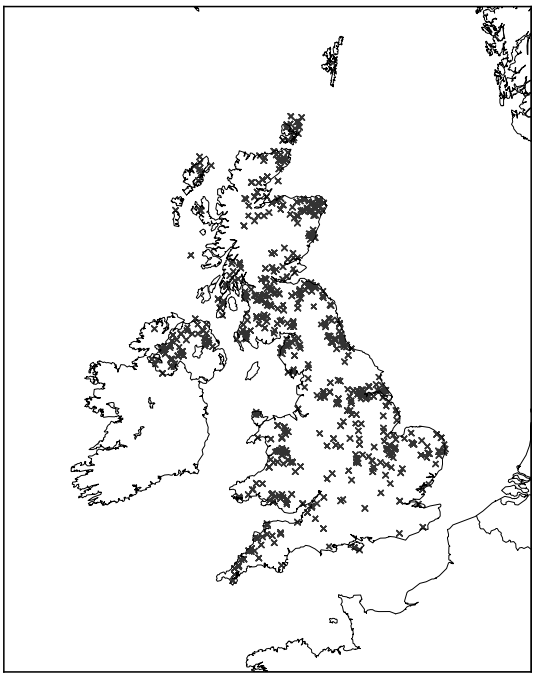

Figure 8.1: Location of all onshore wind farms used in the analysis

Offshore

Determining the locations of future offshore wind farms is easier, as the Crown Estate have leased specific areas of the seabed for offshore wind development. This has been done in three main rounds: Round 1, Round 2 and Round 3, plus one additional 'Scottish Exclusivity' (SE) round. The rounds are designed to allow incremental development of offshore wind, beginning with small shallow-water sites relatively close to shore, before moving to larger and more distant sites. The sites are summarised in Table 8.2 and the locations are shown Figure 8.2.

It is not expected that all of the Round 3 zones will be developed up to the maximum permissible capacity under the lease agreements. To do so would lead to 46 GW of offshore wind capacity, which when combined with onshore wind capacity, would be comparable to UK's current peak demand of around 60GW. In a connection study by National Grid [2008] provided indicative connection capacities for the Round 3 zones, which totalled 25GW compared to 32GW under maximum leases, this is also indicated in Table 8.2.

Since Round 1 and Round 2 zones are relatively small, wind speeds were extracted from the dataset at a single point at the centre of these zones. For Round 3 sites, wind speeds were extracted at the centre point, plus four points at the 'corners' as defined by the maximum and

Round	Num. sites	Max capacity[a]	Indicative capacity[b]	Comments
Round 1	12	1.2	1.2	Most operational
Round 2	17	7.8	7.8	Some operational, most planning or construction
Round 3	9	32	25	Early design and planning stages
Scottish Exclusivity	7	5.5	5.5	Very early design and planning stages
Total	45	46.5	39.5	

[a] maximum available under the Crown Estate lease
[b] indicative capacity assumed by National Grid [2008]

Table 8.2: Summary of Crown Estate leasing rounds

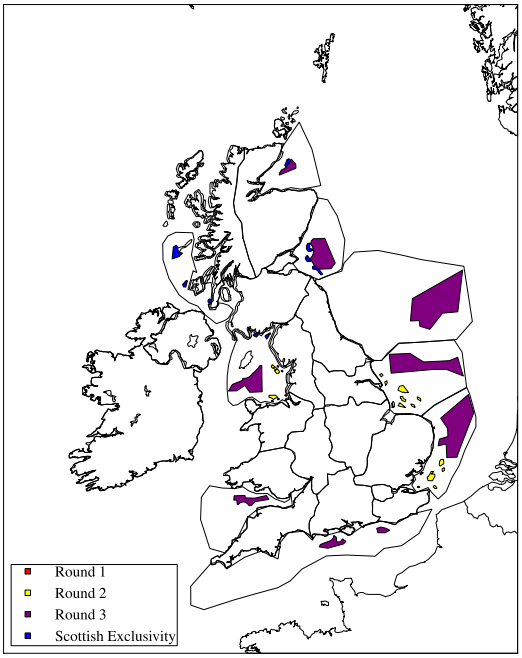

Figure 8.2: Location of Crown Estate leasing rounds

minimum latitude and longitude.

8.2.3 Regional aggregation

It is useful to aggregate the output from individual wind farms into regions to present results at a meaningful level. To do this, a set of regional boundaries were created. Onshore regions were based on the Distribution Network Operator (DNO) boundaries [National Grid, 2011]. Offshore regions were based mainly on the named sea areas around Britain (for example as used for the shipping forecast [UKMO, 2011]) with additional aggregation where appropriate. The regions used for aggregation are shown in Figure 8.3, with a key in Table 8.3.

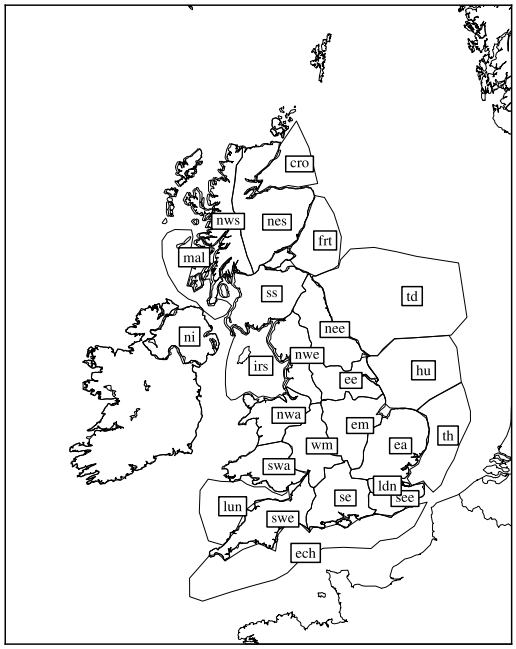

Figure 8.3: Regions used in analysis

Onshore		Offshore	
Code	Name	Code	Name
swe	South West England	ech	English Channel
see	South East England	lun	Lundy
se	South England	th	Thames
ldn	London	hu	Humber
swa	South Wales	irs	Irish Sea
ea	East Anglia	td	Tyne and Dogger
wm	West Midlands	mal	Malin
em	East Midlands	frt	Forth
nwa	North Wales	cro	Cromarty
ee	East England		
nwe	North West England		
ni	Northern Ireland		
nee	North East England		
ss	South Scotland		
nes	North East Scotland		
nws	North West Scotland		

Table 8.3: Region codes and names

8.2.4 Demand

A key question for wind energy integration is how the temporal pattern of wind generation matches current electricity demand e.g. [Boehme et al., 2006, Oswald et al., 2008, Sinden, 2007], so a time-series of electricity demand is necessary to examine these questions in more detail.

Electricity demand in the UK grew steadily up to the year 2000, but has declined slightly since [DECC, 2010]. It is difficult to assess likely demand in 2020 and beyond, since there are many influential factors, such as changes in the economic climate, changes in the cost of fossil fuels, changes in the electricity pricing structure made possible by smart metering, changes in the price structure due to the larger penetration of renewables, and changes in technology and behaviour such as the adoption of electric vehicles.

Central projections [DECC, 2011c] are for demand to decline in the near-term as energy efficiency improves, and to begin to rise slowly after 2020 as electricity begins to make up a larger share of transport. In some scenarios electric vehicles lead to a doubling of demand by 2050 [DECC, 2011a]. However, the projected changes in demand up to 2030 are relatively small, and for the purposes of this analysis, historic demand over the period 2000 to 2010 is used without modification. The major benefit of this approach is it preserves all links between weather and electricity demand.

Historic, aggregated, half-hourly demand data going back to April 2001 is available from National Grid [2011]. The GB 'IO14_DEM' dataset is used here since it is based on operational generation metering and includes station load, but excludes interconnector exports and pumped storage pumping. Figure 8.4 shows the average winter and summer diurnal demand pattern over the study period.

8.2.5 Conventional generation

The conventional generation fleet will not remain fixed: many of the UK's nuclear and coal stations are due to be decomissioned, and there is considerable uncertainty regarding the future generation mix [Ofgem, 2010]. Current and previous UK Government policy indicates support for new nuclear stations, provided they are not directly subsidised [BERR, 2008, DECC, 2011a]. Eight existing sites have been earmarked for potential development, with an indicative timetable which sees new generators on-line by 2017. However, there remains considerable

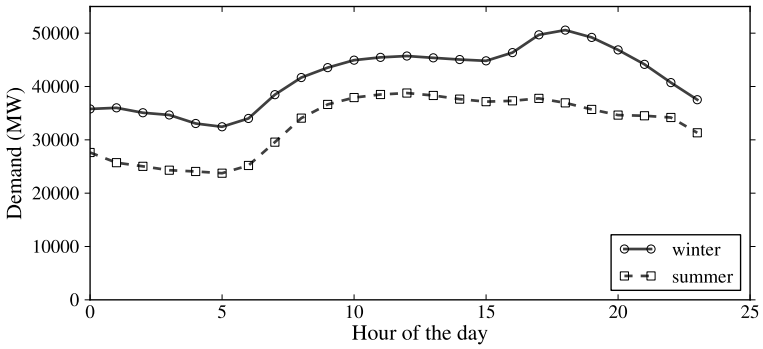

Figure 8.4: Average hourly electricity demand

uncertainty as to when, or whether, these will be delivered by the market [Ofgem, 2010].

The integration of large amounts of wind will put very different requirements on conventional generation. For example there may be more requirement for generators which can respond relatively quickly to provide short to medium-term reserve. However, in the near term wind will continue to be installed against a relatively fixed conventional fleet, and it is useful to take the existing fleet as a baseline against which to analyse how much wind generation might be integrated before large-scale changes would be needed.

The output from the existing conventional fleet is used for part of the analysis. Hourly output by fuel type is available via the Balancing Mechanism Reporting System [Elexon, 2011]. At the time of this analysis data was only available for the period 2009-2010. Figure 8.5 shows conventional generation by fuel type over the period, with only the major fuel types shown for clarity.

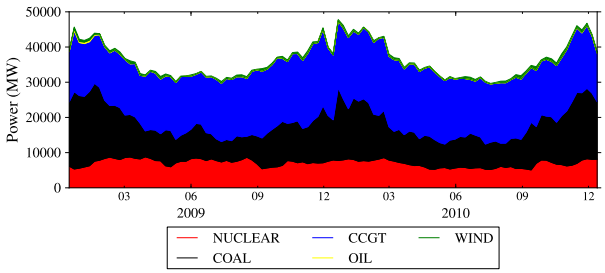

Figure 8.5: Production by major categories of conventional generation. Weekly averages over period 2009-2010

8.3 Analysis approach

The previous sections have described additional datasets used to support this analysis. This section now defines some notation and definitions before the results are presented.

8.3.1 Notations and definitions

Throughout the analysis, variables range over a set of locations and a set of time periods. A single location is an individual wind farm, and a single time period is one hour. A subscript is used to restrict variables to particular time periods, while a superscript restricts variables to particular locations. A lower-case superscript or subscript denotes a single time period or location, while an uppercase superscript or subscript denotes a subset of times or locations, such as a geographic region or particular season. Where a subscript or superscript is omitted, the variables ranges across the whole set. That is, for the wind speed U:

$$U_i^j \text{ : wind speed in period } i, \text{ location } j$$

$$U_i \text{ : set of wind speeds in period } i \text{ across all locations}$$

$$U_i^R \text{ : set of wind speeds in period } i \text{ for all locations in region } R$$

$$U_T^j \text{ : set of wind speeds across period } T \text{ at location } j$$

$$U_T^R \text{ : set of wind speeds across period } T \text{ for locations in } R$$

$$\overline{U^R}_i = \frac{1}{|R|}\sum_{j \in R}(U_i^j) \text{ : average wind speed in period } i \text{ across all locations in } R$$

$$max(U_T^j) = \max_{i \in T}(U_i^j) \text{ : maximum wind speed at location } j \text{ across period } T$$

The following variables are defined:

Rated Capacity, C^j, of wind farm j is the maximum output when all turbines are operating at full capacity

Power Generated, PG_i^j, of a wind farm j, is the average power output in the one hour period i

Power Demanded, PD_i, is the average electrical power demand in the one hour period i.

Energy Generated, EG, is defined as the total energy produced by collection of wind farms,

assuming sufficient load and network capcity exists. If expressed in the units of $[\text{Power}] \cdot h$, i.e. kWh, it is given by:

$$EG_T^R = \sum_{i \in T} \sum_{j \in R} PG_i^j \tag{8.1}$$

Load Factor, LF, over a set of wind farms and a time period is the energy generated over the period, divided by the total which would have been generated if the wind farms had operated at rated capacity for the whole period:

$$LF_T^R = \frac{EG_T^R}{|T| \cdot \sum_{j \in R} C^j} \tag{8.2}$$

When averaging the load factor over multiple wind farms, this definition ensures LF is properly weighted by the rated capacity of each individual wind farm, to ensure that larger wind farms contribute more to the result.

Energy Demanded, ED_T, is total amount of energy used over a period. If expressed in units of $[\text{Power}] \cdot$ hours, i.e. MWh, it is given by:

$$ED_T = \sum_{i \in T} PD_i \tag{8.3}$$

Net demand, ND, is the simply difference between energy generated and energy demanded, and may be negative:

$$ND_T = \sum_{i \in T} (PG_i - PD_i) \tag{8.4}$$

Residual Demand, RD_T, is the difference between energy demanded and energy generated, or zero if generation exceeds demand:

$$RD_T = \sum_{i \in T} max(0, PG_i - PD_i) \tag{8.5}$$

Excess Generation, XG_T is the difference between energy generated and energy demanded where generation exceeds demand:

$$XG_T = \sum_{i \in T} max(0, PD_i - PG_i) \tag{8.6}$$

Energy Contributed, EC, is the energy generated excluding any excess generation:

$$EC_T = \sum_{i \in T} min(PG_i, PD_i) \tag{8.7}$$

it is useful to express the energy contributed as percentage of the energy demanded:

$$\% \text{ contribution} = 100 \cdot \frac{EC}{ED} \tag{8.8}$$

The terms used are illustrated schematically in Figure 8.6. The definitions of EC and ED assume that neither demand nor generation can be shifted in time: wind generation only contributes if sufficient demand exists in each hour. As such, it is a slightly more pessimistic metric than other measures, such as the total energy generated by wind divided by the total energy demanded. However, it is also the most defensible since it contains no implicit assumptions about the viability of large-scale storage, or the extent to which electricity demand can be shifted through behavioural change. These two aspects could be examined in detail with this dataset, but are outside the scope of the current work. It represents the contribution wind energy would make if the demand pattern remained completely unchanged.

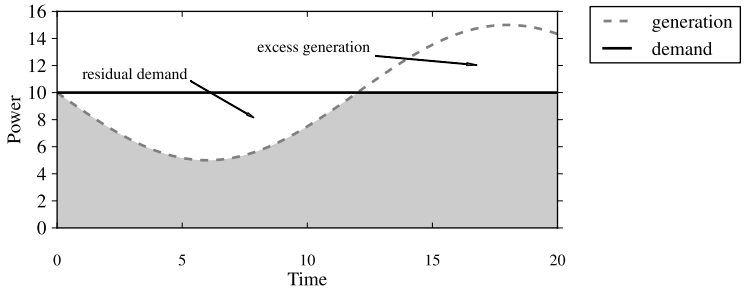

Figure 8.6: Illustration of terms used. Demand is shown constant for clarity. ED is the area under the demand curve. EG is the area under the generation curve. EC is the shaded area. XG and RD are annotated

8.3.2 Analysis snapshots

Following the discussion in §8.2 a number of analysis 'snapshots' are defined. Each snapshot represents a certain geographic distribution of wind generation which may be achieved at some point in the future, broadly based on the consecutive development of the offshore rounds. Analysis snapshots are summarised in Table 8.4 and Figure 8.7.

Snapshot A is representative of the current situation, with most wind onshore and a small amount offshore in Round 1 and Round 2 sites. Snapshot B represents the development of all the Round 2 sites, coupled with the steady growth in onshore wind. Snapshot C represents the development of all of the Round 3 sites, apart from the largest and most distant site, Dogger Bank. Snapshot D represents the development of all Round 3 sites including Dogger Bank. Finally Snapshot E also also includes the Scottish Exclusivity sites. Thus, each snapshot shows a greater proportion of wind capacity offshore, and a progressive shift to sites further from the coast. In absolute terms, there is a relatively large leap between Snapshot B and C - this is to highlight changes which will occur when the balance of wind capacity shifts conclusively offshore.

Under each snapshot, each individual wind farm j is assigned a nominal rated capacity C^j. This results in a total nominal capacity for each snapshot, $\boldsymbol{C} = \sum_j C^j$, which is given in the second column of Table 8.4, and is shown graphically in Figure 8.7. Although each snapshot has a total nominal installed capacity, it is more useful to see a snapshot as describing a geographic distribution of wind farms and their relative sizes. The main purpose of the nominal capacities assigned to each wind farm is to determine a weighted average load factor across any level of geographic aggregation by Eq. 8.2. This enables a range of installed capacities to be analysed for each snapshot.

This implicitly assumes that increasing or decreasing the total installed capacity has no impact on the load factors at individual farms, i.e. that capacity can be added without any diminishing returns due to increased intra or inter-park losses. Given the large space available in offshore zones, this is a reasonable first approximation, although it may not hold if the analysis were extended to very large installed capacities.

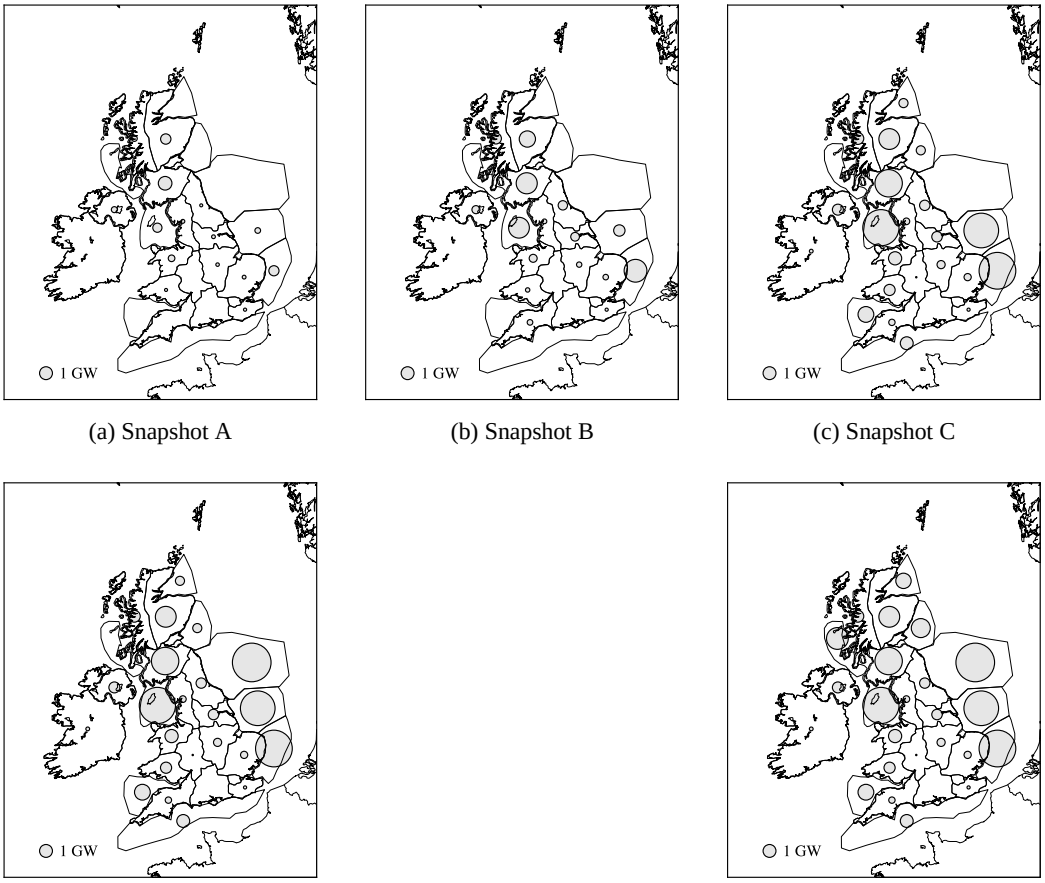

(a) Snapshot A (b) Snapshot B (c) Snapshot C

(d) Snapshot D (e) Snapshot E

Figure 8.7: Nominal capacities installled in each region and the relative distribution under each analysis snapshot

	Nominal Installed Capacity	Distribution (%)				
Snapshot	GW	Onshore	Round 1	Round 2	Round 3	SE
A	4	69	22	9	-	-
B	14	53	9	38	-	-
C	40	33	3	23	41	-
D	49	27	2	19	52	-
E	54	24	2	17	47	10

Table 8.4: Analysis snapshots

8.4 Analysis Results

In this section the analysis results are presented, beginning with average statistics describing the wind speeds, wind speed distributions, load factors and potential contribution of wind energy to energy demand. Then, spatio-temporal patterns of variability are examined and some of the implications are explored.

8.4.1 Average conditions

Wind speeds

Wind conditions have been discussed in Chapters 5 and 6. Average wind conditions but are included again here here since they are integral to the analysis. Figure 8.8 shows average wind speed at 80m above the surface across the period 2000 to 2010 inclusive, after bias correction against satellite wind speeds. As has been previously discussed, these final results agree closely with in-situ observations, and with the output of other modelling studies. Detailed resource maps showing power density and average wind speed by month of the year are included as Appendix A.

Onshore at a national level the major visible patterns relate to terrain height and coastal exposure, with high-level terrain and western coasts having highest wind speeds, and the lowest wind speeds in central England and urban areas. Offshore, the highest wind speeds are seen off the western seaboard, particularly off the northwest coast of Scotland. Over the areas likely to be developed for wind energy, the average wind speeds are reasonably uniform, between 8-10ms^{-1}, decreasing closer to the coast. Of note are regions of slightly higher wind speed either side of the Dover straight, which may be related to the Dover jet [Capon, 2003] and warrant further investigation.

Average wind conditions only reveal one part of the picture, and until now there has been no publicly released assessment of the wind speed *distributions* at the future offshore wind sites in the UK. Table 8.5 provides mean wind speed and Weibull parameters for each individual offshore site in the UK. In addition, the probability that the wind speed is below 5, 10, 15, 20, and 25 ms^{-1} is included in the table.

The range of average wind speeds and Weibull parameters is shown in Figure 8.9. Round 1 sites show the lowest wind speeds, and also the most variation between sites. This is likely

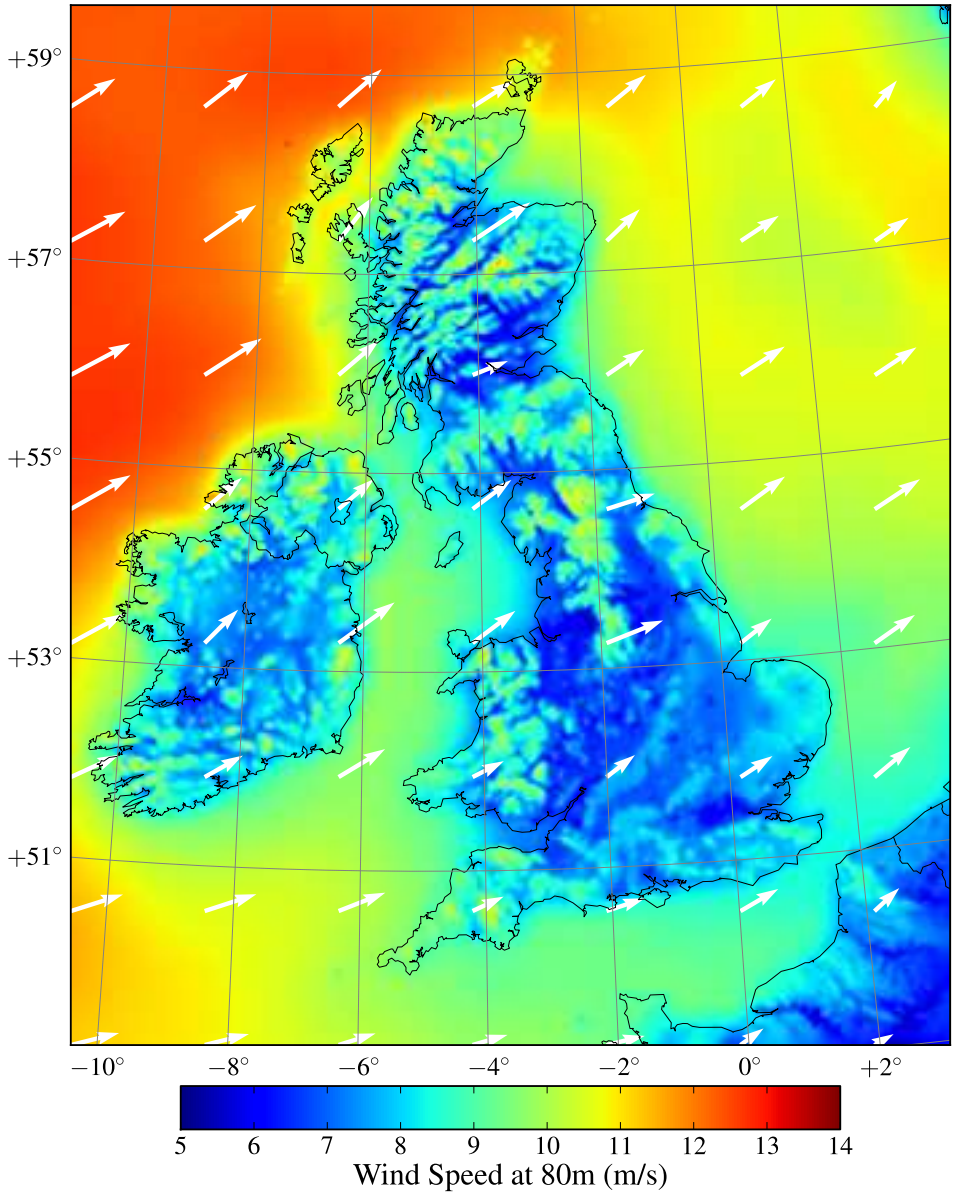

Figure 8.8: Average wind speed at 80m above surface.

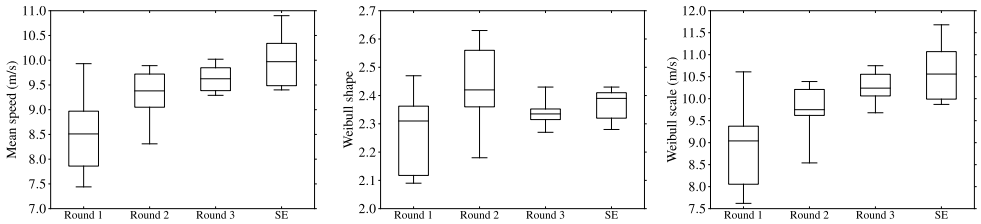

(a) (b) (c)

Figure 8.9: Mean wind speeds and Weibull distributions at offshore wind sites. The whiskers are drawn to the full range of the data

due to the proximity to the coast where the wind speed is sensitive to the distance to the shore and to the onshore topography. The relatively high maximum for Round 1 is from the Beatrice demonstration project: a turbine which was placed on an oil platform off the coast of northeast Scotland.

Round 2 sites also show quite a spread in Weibull parameters, reflecting the range of distances to the shore. The highest shape parameter, 2.63, is associated with the London Array, which shows the wind speeds are more dispersed about the mean. This may be due to differing wind regimes with wind direction: from some directions winds will have blown over very rough urban areas, but from other directions will have had a clean fetch from the North Sea or through the English Channel. It also may relate speed up of wind speeds in the approach to the Dover Straight known to occur in northerly and easterly winds during stable conditions [Capon, 2003]. This warrants further investigation but is outside the scope of this immediate work.

Round 3 sites show a relatively tight distribution of mean wind speeds and Weibull parameters reflecting the more homogeneous wind speeds at this distance from the coast. Scottish Exclusivity sites show a large spread, due to the fact that one site is in an coastal estuary, while another is off the exposed northwest coast.

Load factors

Figure 8.10 shows the distribution of hourly load factors for all onshore, Round 1, Round 2, Round 3 and SE rounds. These are shown before any reductions have been made to account for technical availability. The average load factor for onshore wind is 28%, which agrees well with published figure between 2006-2010 of 26% [DECC, 2010], a particularly good match

Round	Name	Mean	Weibull		$P(U_i^j < x)$ (%)				
		ms^{-1}	k	c ms^{-1}	5	10	15	20	25
1	Barrow	8.95	2.33	9.25	15	65	93	99	99.95
1	Beatrice	9.93	2.45	10.61	12	53	88	99	99.90
1	Burbo Bank	7.44	2.09	7.62	28	78	97	100	99.98
1	Gunfleet Sands I	9.05	2.47	9.50	14	63	94	100	99.98
1	Kentish Flats	8.69	2.31	9.22	17	66	94	100	99.98
1	Lynn & Inner Dowsing	8.33	2.31	8.86	19	69	96	100	99.99
1	North Hoyle	7.86	2.12	8.08	24	74	96	100	99.98
1	Ormonde	9.03	2.35	9.37	15	63	92	99	99.94
1	Rhyl Flats	7.86	2.11	8.06	25	74	95	100	99.98
1	Robin Rigg	7.92	2.10	8.04	25	74	95	99	99.97
1	Scroby Sands	8.71	2.40	9.39	17	65	95	100	99.99
1	Teesside	7.59	2.13	7.99	25	77	97	100	99.99
2	Docking Shoal	9.10	2.37	9.63	15	62	92	99	99.98
2	Dudgeon	9.39	2.43	9.97	13	59	91	99	99.98
2	Greater Gabbard - Galloper	9.89	2.61	10.39	10	54	90	99	99.97
2	Greater Gabbard - Inner	9.81	2.56	10.34	10	55	90	99	99.96
2	Gunfleet Sands II	9.05	2.47	9.50	14	63	94	100	99.98
2	Gwynt y Mor	8.31	2.18	8.54	21	70	94	99	99.98
2	Humber Gateway	9.00	2.33	9.62	16	62	93	99	99.99
2	Lincs	8.57	2.33	9.11	18	67	95	100	99.99
2	London Array	9.86	2.63	10.32	9	54	90	99	99.97
2	London Array I	9.83	2.63	10.29	9	55	90	99	99.97
2	London Array II	9.83	2.63	10.29	9	55	90	99	99.97
2	Race Bank	9.45	2.44	9.99	13	58	91	99	99.98
2	Sheringham Shoal	9.05	2.36	9.62	15	62	93	99	99.98
2	Solway Firth	8.42	2.23	8.57	19	70	94	99	99.97
2	Thanet	9.72	2.61	10.21	10	55	91	99	99.97
2	Triton Knoll	9.41	2.41	10.01	13	58	91	99	99.98
2	Walney I	9.37	2.41	9.75	13	60	91	99	99.94
2	Walney II	9.42	2.42	9.83	12	59	91	99	99.94
2	West Duddon	9.38	2.42	9.74	12	60	91	99	99.94
2	Westernmost Rough	8.98	2.32	9.65	16	62	93	99	99.98
2	West of Duddon Sands	9.35	2.42	9.68	13	61	91	99	99.93
3	Bristol Channel	9.31	2.32	9.68	14	60	91	99	99.94
3	Dogger Bank	9.83	2.30	10.60	14	54	87	98	99.93
3	Firth of Forth	9.90	2.33	10.54	13	54	88	98	99.86
3	Hastings	9.29	2.35	9.80	14	60	91	99	99.95
3	Hornsea	9.41	2.27	10.15	15	58	90	99	99.98
3	Irish Sea	9.69	2.34	10.30	13	56	89	99	99.94
3	Moray Firth	10.02	2.43	10.75	12	52	88	99	99.89
3	Norfolk	9.56	2.36	10.18	13	57	90	99	99.96
3	West Isle of Wight	9.63	2.40	10.20	13	57	89	99	99.95
SE	Argyll Array	10.90	2.40	11.68	10	46	81	96	99.62
SE	Beatrice	9.97	2.42	10.74	12	53	88	99	99.90
SE	Forth Array	9.44	2.31	9.99	14	58	90	99	99.90
SE	Inch Cape	9.40	2.28	9.87	15	59	90	99	99.83
SE	Islay	10.67	2.43	11.40	10	47	83	97	99.69
SE	Kintyre	10.01	2.39	10.56	12	53	87	98	99.83
SE	Neart na Gaoithe	9.53	2.33	9.99	13	58	90	99	99.85

Table 8.5: Wind speed distributions at offshore sites

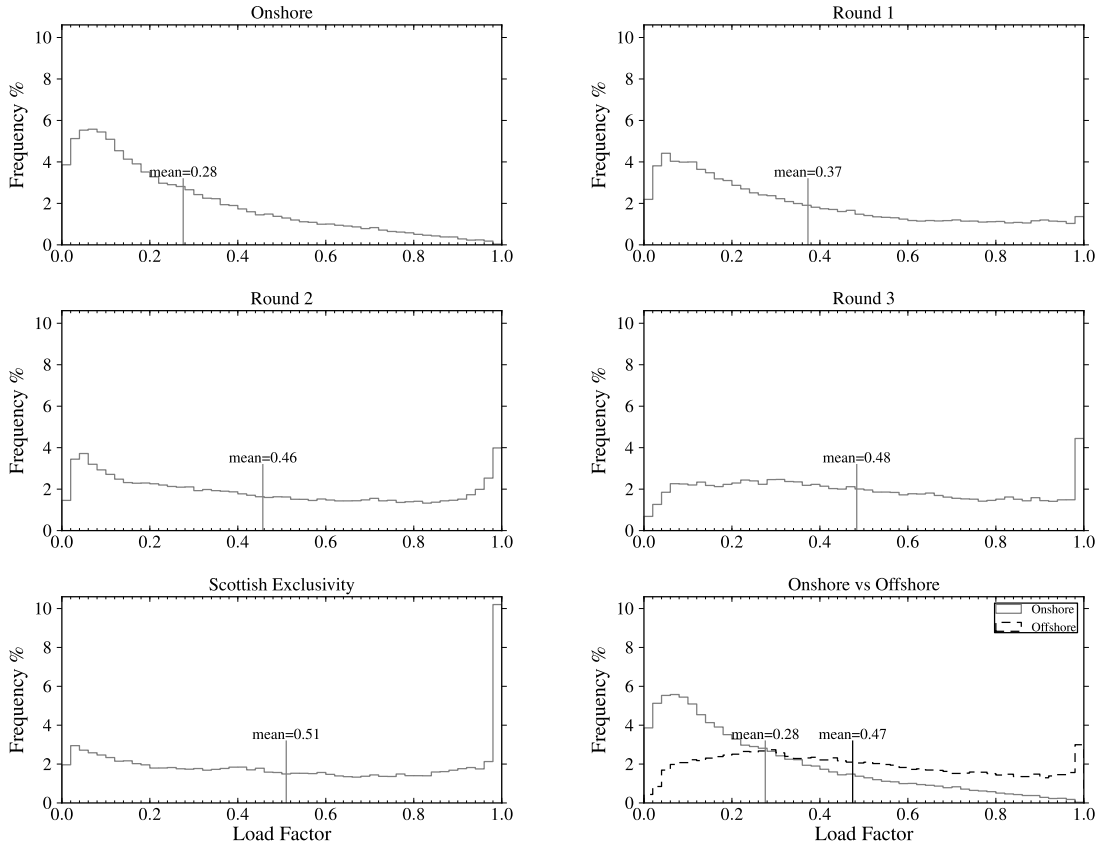

Figure 8.10: Distribution of aggregate LF for onshore, Round 1, Round 2, Round 3 and SE zones

considering technical availability for onshore is around 98% [Harman et al., 2008].

The predicted values for offshore load factors are considerably higher: 37%, 46%, 48% and 51% at Round 1, 2, 3, and SE sites respectively. Again, it should be stressed that this is before any reductions due to technical availibility. These figures agree with other assessments based on more limited wind speed data, for example, Garrad Hassan [2003] predicted load factors of 47.5% for sites with an average wind speed of 9.5ms^{-1}. The shape of the distributions is also changed, with a progressive shift to the right, with offshore wind speeds being higher and more consistent.

Finally, load factor distributions are presented by analysis snapshot in Figure 8.11. This shows how the load factor will change as the distribution of capacity progressively shifts offshore. This starts from an average of 34% for Snapshot A, rising to 42 % for Snapshot E.

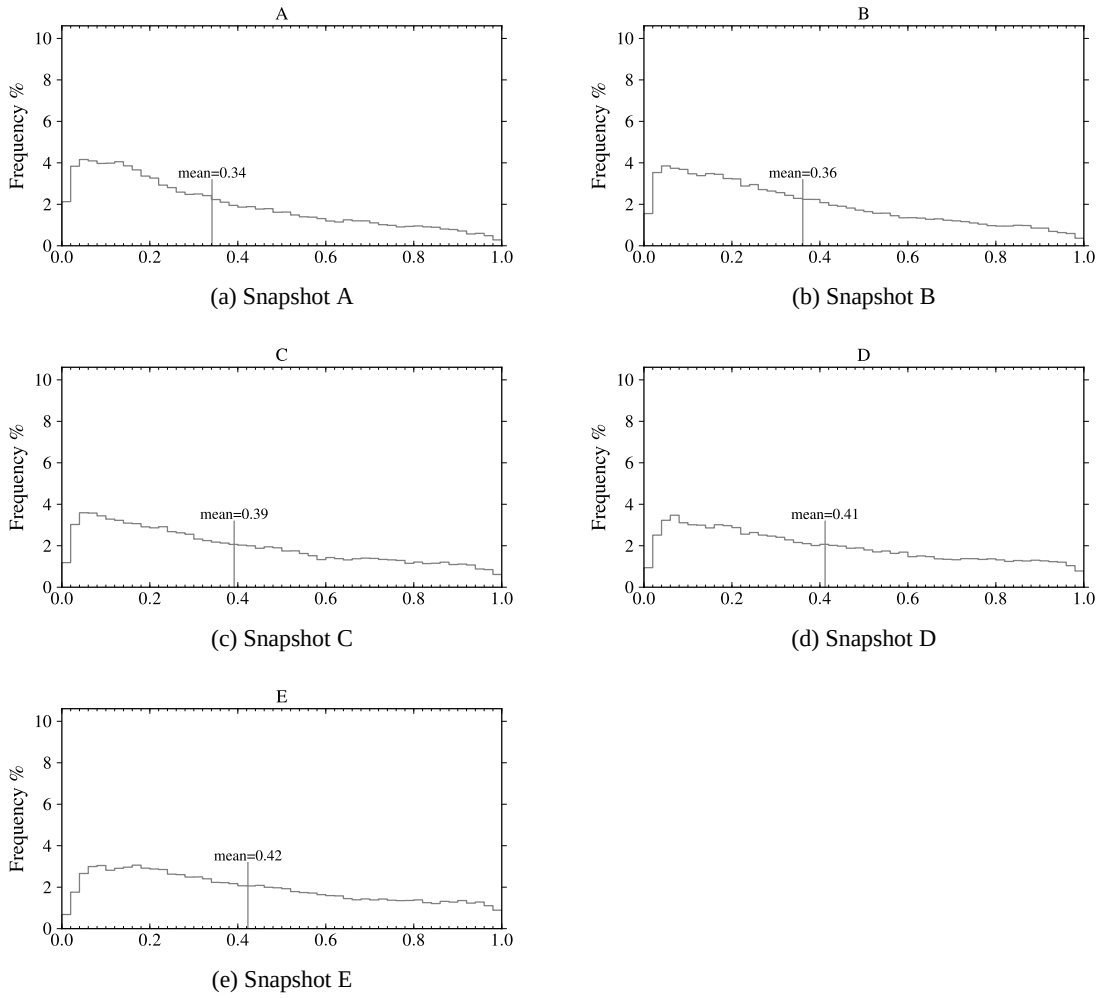

(a) Snapshot A

(b) Snapshot B

(c) Snapshot C

(d) Snapshot D

(e) Snapshot E

Figure 8.11: Distribution of load factors by analysis snapshot

Sensitivity analysis

So far, load factors have been presented without any sensitivities. There are a number of sensitivities which will effect the prediction of load factors from future wind farms, these include:

1. errors in the simulated wind speed over the period;
2. assumptions about wake losses experienced at future wind farms; and
3. assumptions about technical availability.

Curtailment losses due to network constraints are not examined here. To do so adequately would require a reasonably sophisticated model of the network, as well as a range of assumptions or scenarios about the future electricity network; this is outside the scope of this work.

To assess the sensitivity to the simulated wind speed, an estimate of the wind speed error is taken from comparison against in-situ observations, that is from Figure 5.8 for onshore and Figure 6.8 for offshore. To simplify the sensitivity analysis, a single bound of ± 1.2 ms^{-1}was used to encompass the 90% confidence interval for both offshore and onshore wind speeds.

So far, array losses have been applied as described in §7.3.1. Wake losses depend on wind speed, but amount to around a 10% reduction in energy yield (Table 7.1). To assess the sensitivity to wake losses, the analysis was repeated without any wake losses, and with double the adjustments made in the base case. Figure 8.12 shows these factors applied to a particular power curve. Using the same test wind speeds as Table 7.1, the reduction in energy yield using doubled wake losses is around 20%.

The difficulty of estimating technical availability for offshore sites is discussed in §7.2.2. In most studies technical availability is usually assumed to be constant throughout the year e.g. [Boehme et al., 2006, Poyry, 2008]. However, for offshore sites, technical availability may be more sensitive to season, since higher winds and fewer weather windows may reduce technical availability disproportionately in autumn and winter, which would disproportionately affect energy production.

To examine whether this is significant, the impact of a seasonal variation in technical availability is assessed on the load factors of Round 3 farms. This is shown in Table 8.6: it can be seen

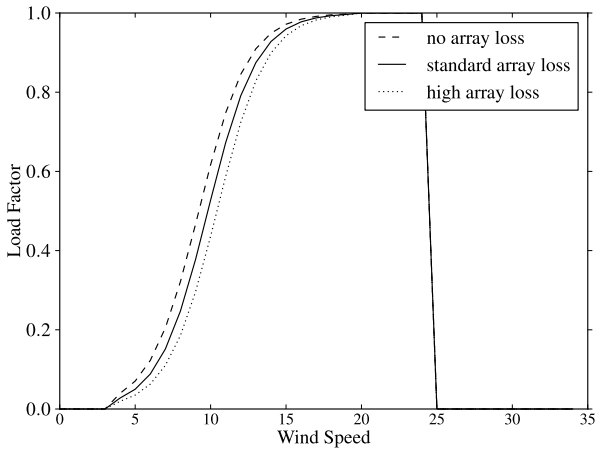

Figure 8.12: Power curves used to study sensitivity to array losses

Technical Availability %		Load Factor %
Spring - Summer	Autumn - Winter	
100	100	48.3
90	90	43.5
95	85	43.1
80	80	38.7
85	75	38.2

Table 8.6: Impact of seasonality on average load factor at Round 3 sites

that the impact of seasonal imbalances in technical availability is minor and is not pursued further. Assuming a constant reduction due to technical availability seems reasonable. For the sensitivity analysis, technical availability was assessed at 80%, 90% and 100%.

Figure 8.13 shows the sensitivities used, and the impact on average load factors at onshore and offshore wind farms. As would be expected, load factors are very sensitive to changes in wind speed. A change in the wind speed of 1.3ms^{-1}changes the load factor by an absolute value of 0.10. Sensitivity to the shape of the aggregate power curve is also very significant. Doubling the array loss factors changes the load factors by an absolute value of 0.05. This highlights the importance of properly understanding array losses, and illustrates the need to develop aggregate power curves based on real offshore data, rather than to make simple assumptions such as fixed array losses. It also highlights the important role that proper layout will play, particularly at more remote Round 3 sites which are larger and where the aesthetic constraints on layout may be more relaxed, allowing for layouts which explicitly aim to reduce array losses. Finally, technical availability is also a significant sensitivity highlighting the need for ongoing

Sensitivity	lower	mid	upper
Wind speed	-1.3ms^{-1}	no change	+ 1.3ms^{-1}
Array loss	doubled ($\approx 20\%$)	baseline($\approx 10\%$)	none
Technical availability	80%	90%	100%

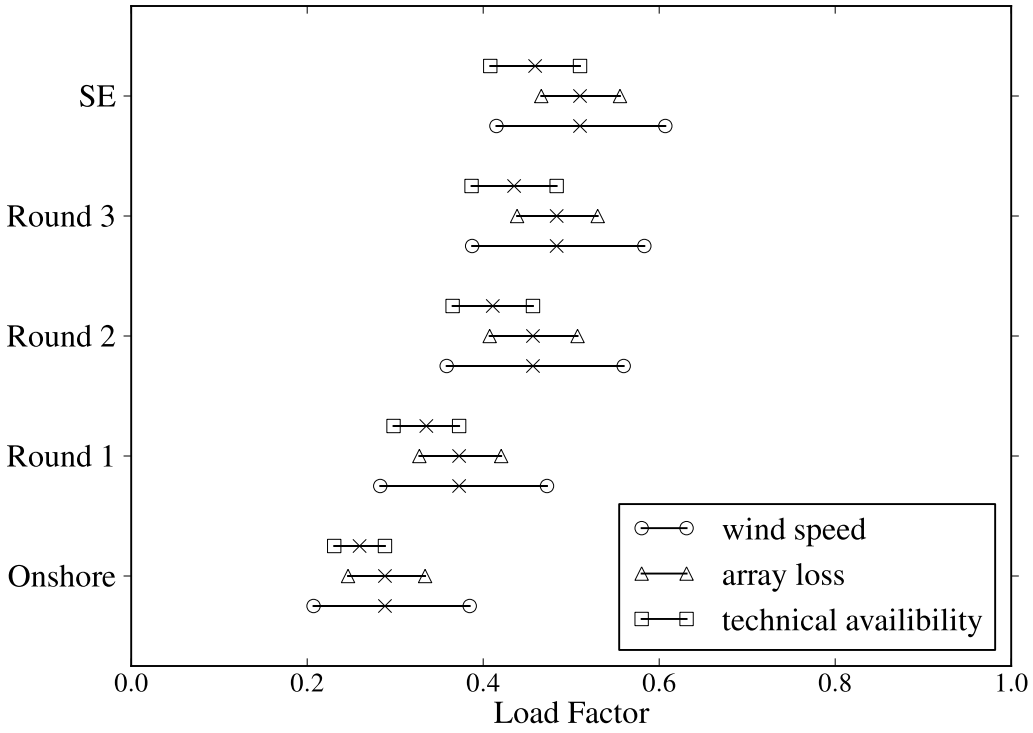

Figure 8.13: Sensitivity of average load factor to wind speed, array losses, and technical availability. Mid value is indicated by the ‘x’.

monitoring and cataloguing of real data.

This section shows conclusively that the load factors from offshore wind farms will be significantly higher than onshore sites, even if low technical availability and high array losses are assumed. The main purpose is to highlight the relative importance of different sensitivities. The high sensitivity to wind speed is shown, and some attempt to put confidence bounds on this is made. Sensitivities to other assumptions are shown, but these are not combined with the wind speed into a single 'uncertainty' as they are simply different assumptions, not empirical estimates of the likely error. Without more data, it is impossible to know whether, for example, a value of technical availability of 80% corresponds to a 90%, 95% or 99% confidence bound on the true value, and it would be misleading to combine them.

For the following sections, the central case from the sensitivity analysis is used, that is, wind speed is not perturbed, technical availability is assumed to be 90%, and baseline array loss factors are used, so that array losses amount to around 10%.

Average energy contribution

This section now examines the overall contribution wind generation could make to meeting existing electricity demand under each analysis snapshot. Energy match is calculated hour-by-hour, but presented at a monthly-level, which smooths out daily and hourly variations. In later sections, hourly variations are shown, and two week-long periods representing the highest and lowest generation are shown.

Figure 8.14 shows the results from the analysis, presented as monthly averages for clarity; a week of maximum and minimum output is shown later. Lines are also drawn corresponding to the energy which would be generated by a constant power output of 10 and 20 GW. This is to give a visual guide as to where the output of any inflexible future baseload generation may be, for example if existing nuclear plants are renewed or new nuclear plants developed.

In Snapshot A, which is representative of the current situation with an installed capacity of 4GW, the wind contribution is 3.6%. This agrees very closely with current figures [DECC, 2011b, p29], which show that wind contributed 2.8% to electricity supply in 2010, or 3.7% when adjusted to average long-term wind conditions [DECC, 2010]. (The wind contribution in Snapshot A for 2010 is 2.9%). The seasonal pattern is very evident, with wind contributing more in the winter. However, at this relatively low penetration there is no significant change in

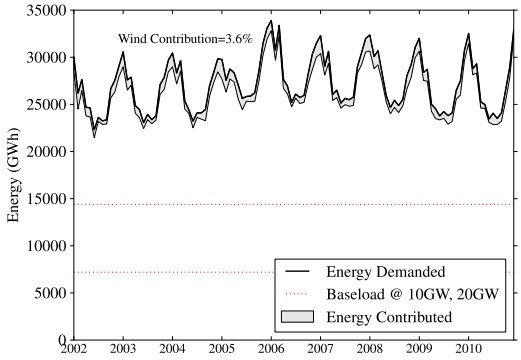

(a) Snapshot A

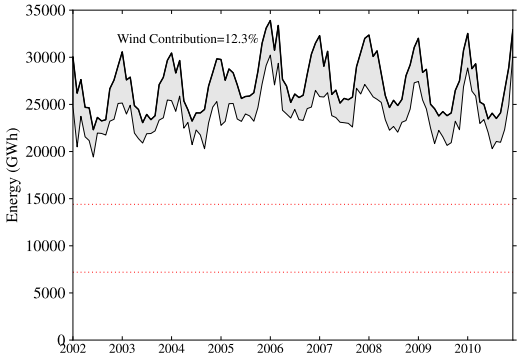

(b) Snapshot B

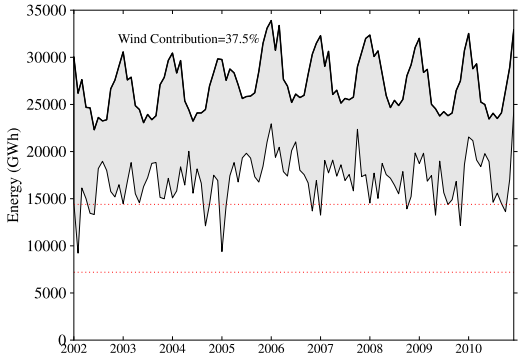

(c) Snapshot C

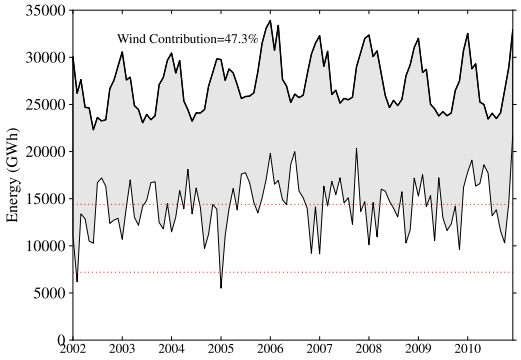

(d) Snapshot D

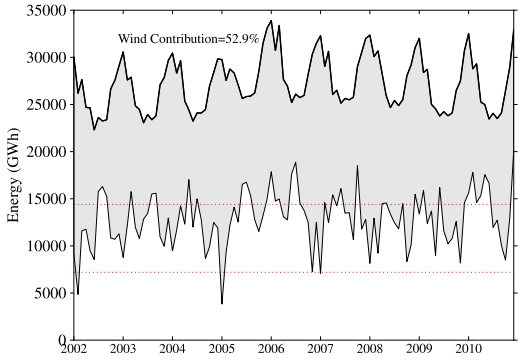

(e) Snapshot E

Figure 8.14: ED, EC and RD by year and month. ED is the top line, EC is the grey shaded area below, and RD is white area below. The energy which would be generated by a constant power output of 10 and 20GW are shown as the two ‘baseline’ lines

the underlying shape of residual demand.

In Snapshot B, which represents a total installed capacity of 14GW, the wind contribution is 12.3%. If electricity generation from other renewable sources such as hydro, biomass, wave and tidal remained at today's levels of around 4.6% of electricity demand [DECC, 2011b], then under this snapshot the UK would produce 17% of electricity from renewable sources. This is significantly higher than today, but still considerably short of the 30% target for 2020. This indicates that developing Round 2 sites alone will not enable the UK to reach its current targets. The seasonal pattern in Snapshot B is evident, with much more energy production in the winter when demand is highest. At a monthly level the residual demand is considerably smoother than the total demand, i.e., wind generation reduces the seasonal range of demand. However, monthly averaging masks a large amount of variation, which is analysed in later sections. In Snapshot B, at monthly average level, the residual demand does not approach the baseload lines at 10GW or 20GW. This shows that the system will still need thermal generation whose primary function will be to supply energy to meet demand, not only to provide reserve or auxiliary functions.

Snapshot C represents a considerably leap in terms of capacity, with 40GW of installed wind. The wind contribution is much higher, 37.5% of energy demand. In this snapshot, wind alone would allow the UK to meet its 2020 renewable energy targets, assuming the network can accomodate this. On a monthly average level, residual demand is little over the baseload line at 20GW. This indicates that if there were an increase of nuclear or other inflexible plant to this level, there would be relatively little energy remaining, on a monthly average level, to be served by other thermal generation. This suggests that the revenue for such generators would have to be found by exploiting much higher electricity price differentials, or from payments for providing other auxilliary services to support the network.

Snapshot D shows a further increase in capacity to 49GW, with wind contribution of 47.2%. Monthly average residual demand approaches the baseload generation line at 10GW, suggesting any inflexible baseload generation above this level may lead to significant curtailment, export, or storage. Snapshot E shows a further increase, with capacity of 54GW giving a wind contribution of 53%, with several winter months where the monthly production meets, or exceeds, the baseload line at 10GW. This suggests that, if inflexible baseload of 10GW were installed in this scenario, significant export or curtailment of wind may occur.

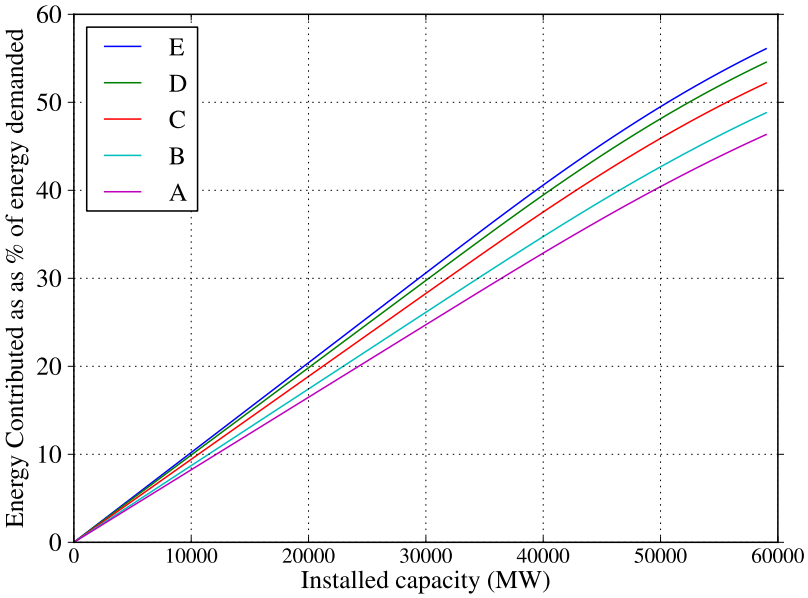

Figure 8.15: Wind contribution as function of snapshot and installed capacity

As described in §8.3.2, the snapshots can be viewed as a describing a geographic distribution of capacity, and can be scaled up or down to reflect different installed capacities. Figure 8.15 shows the wind contribution as percentage of demand, allocating increasing capacity to each snapshot while maintaining the same relative distribution. Figure 8.15 clearly shows the benefit in energy terms of developing offshore sites, with the snapshots with large amounts of offshore wind producing significantly more energy for the same level of installed capacity. It can be seen that to meet targets of 30% of electricity from wind generation alone would require between 30-36GW of installed capacity, depending on the geographic distribution.

In Figure 8.15, the gradients eventually begin to level out at higher wind penetrations, due to the increasing number of hours where wind generation would exceed total demand, with any excess generation discounted as defined in Eq. 8.7. This is shown in Figure 8.16 for Snapshots B, C and D. Net demand is shown (which can be negative), rather than residual demand (which is defined to be positive), to show how much energy might be available for export, storage, or be spilled. In Snapshot B, the distribution of net demand is shifted but not radically changed. In Snapshot C, net demand is considerably reduced, and is negative around 2% of the time and less than 20GW 40% of the time. In Snapshot D, net demand is negative around 18% of the time, and less than 20GW 60% of the time. However, there is only a small reduction in peak demand: even in Snapshot D peak demand is is still around 57GW, compared with 60GW.

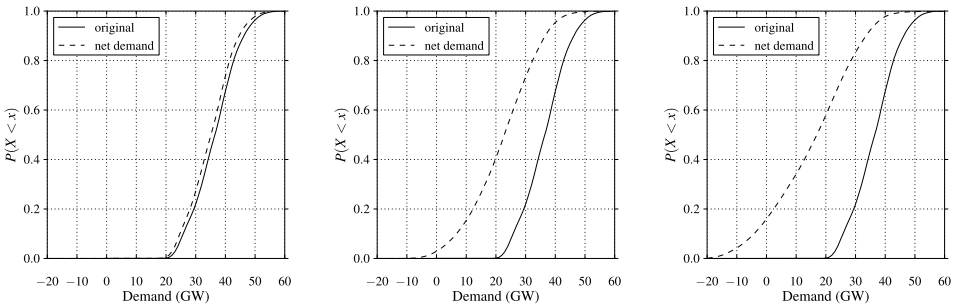

(a) Snapshot B (b) Snapshot C (c) Snapshot D

Figure 8.16: CDF of net demand for three analysis snapshots

Maximum and minimum week

> "It was the best of times, it was the worst of times..."
>
> Charles Dickens, *A Tale of Two Cities.*

So far, the energy contributed has been presented as monthly averages, which masks a large amount of variability. As an illustration of this, two week-long periods with the lowest and highest average load factor are selected, to illustrate the 'best' and 'worst' weeks in terms of energy production.

The week with the lowest aggregate load factor over the period studied was the 7-days beginning 17th May 2010. This was a week which saw a high pressure building from the 17th, and only weakening after the 23rd, with daytime temperatures reaching a record for May of 27°, but nightime temperatures falling to just a few degrees[Brugge, 2011]. The synoptic situation on 20th May is shown in Figure 8.17 (a), which shows high pressure extending from the south of the UK into Norway.

The week with the highest aggregate load factor over the period studied was the 7-days beginning 3rd January 2005. This week saw the UK in a strong westerly flow, with a succession of depressions crossing from the Atlantic [Brugge, 2011]. The synoptic situation on 6th January is shown in Figure 8.17 (b), which shows two deep areas of low pressure to the north of the UK, and a large area of high pressure over southern Europe.

Figure 8.18 shows energy contributed over both periods for each snapshot. Demand is relatively

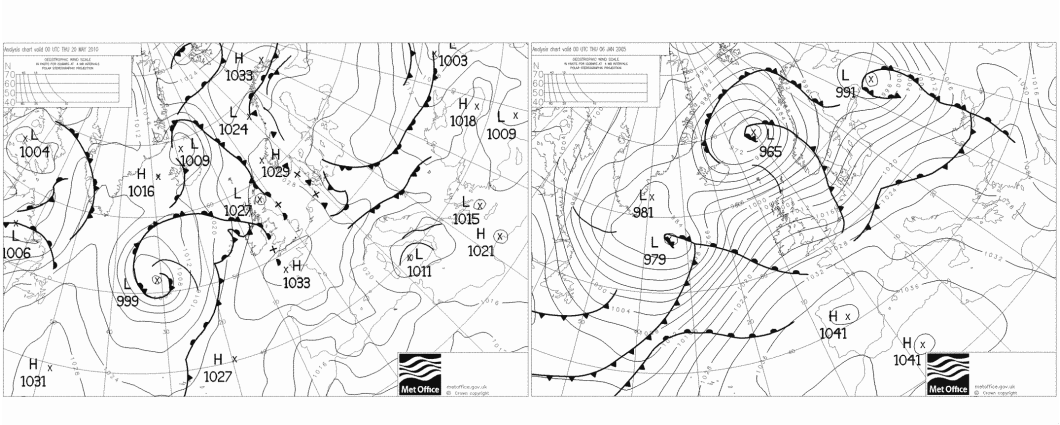

(a) 2010-05-20 00z (b) 2005-01-06 00z

Figure 8.17: Synoptic situations causing the lowest (a) and highest (b) weekly average load factors over whole period.

low in the week in May 2010, with a peak of around 40GW, and relatively high in January 2005, with a peak at 50GW. Of most interest are the snapshots with high penetrations of wind, as the contrast between the two periods are more evident. In Snapshot D, the wind contribution during the 'worst' week is around 6%, with a two-day period in the middle with very little wind contribution at all. In contrast, the contribution during the 'best' week is 95%, with several days where wind meets 100% of electricity demand.

This analysis is important since it illustrates the radically different nature of the system with high penetrations of wind, and the challenges associated with dealing with different extremes. It will be shown in the following sections that the geographic distribution of wind provides a very much smoother resource than single points, but the aggregate output is still very variable, and any system has to be able to deal with periods where very little energy is generated, as well as times where wind could provide all the current demand and more. It should be stressed that wind generation is shown against current demand patterns *as an illustration only*. The conventional generation and demand backdrop may be very different by the time such penetrations of wind are reached. The periods have been selected as the two extremes; analysis in the following sections looks at how often similar periods occur.

It is worth noting that both synoptic systems shown in Figure 8.17 indicate that much of northern Europe would experience similar wind conditions. Although this should be confirmed from observations or other model output, the lack of any significant pressure gradient in Figure 8.17 (a), and the strong westerly flow in Figure 8.17 (b) suggest that in both cases that

the UK, Denmark, Germany and southern Norway and Sweden would experience co-incident low or high wind speeds. This confirms findings of Poyry [2011], which found that wind speed variability across Northen Europe would not simply average out. How often the positions of different synoptic systems cause this to occur across the whole of northern Europe would be interesting further work, and could be examined in broad terms from a global reanalysis dataset.

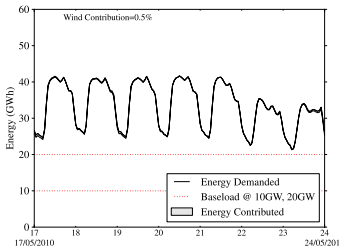

(a) Snapshot A - low

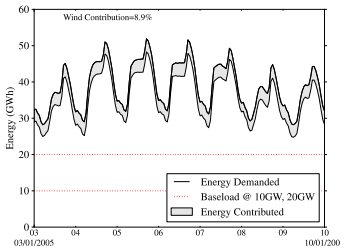

(b) Snapshot A - high

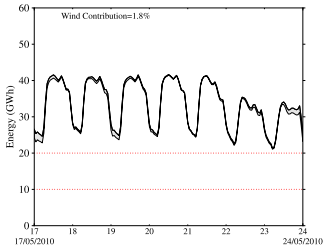

(c) Snapshot B - low

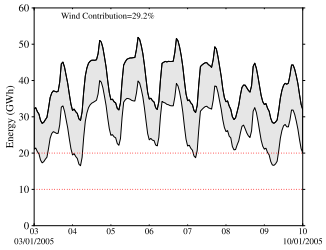

(d) Snapshot B - high

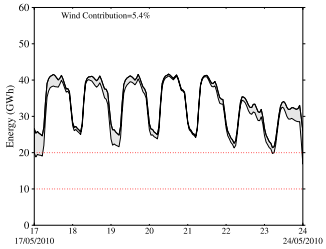

(e) Snapshot C - low

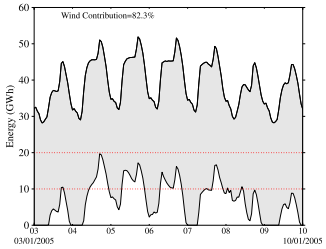

(f) Snapshot C - high

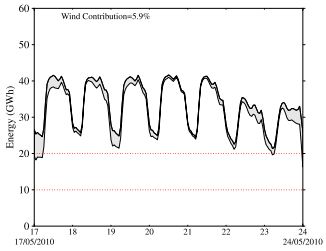

(g) Snapshot D - low

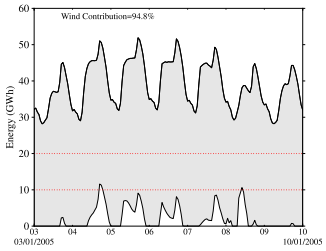

(h) Snapshot D - high

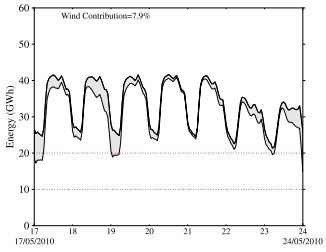

(i) Snapshot E - low

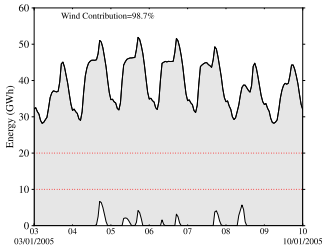

(j) Snapshot E - high

Figure 8.18: Energy production by snapshot for the highest and lowest wind speed week

8.4.2 Spatio-temporal variability

As illustrated by the two extreme cases presented above, the spatio-temporal variability of wind speeds are of crucial importance to the energy system. How wind speeds vary in time, and the the number of co-incident calm periods will determine how much energy must be supplied by alternatives, be that conventional generation, energy storage, imports from other countries, or other sources of renewables.

The following sections examine spatial and temporal patterns seen in wind speeds and in the subsequent outputs from wind farms. Diurnal, seasonal, and annual patterns are examined, before cross correlation between regions, calm periods and ramp events are looked at in more detail.

Diurnal

It was shown in Chapter 5, Figure 5.12, that WRF captured the diurnal variation at typical turbine hub heights relatively well, and that the amplitude of variation was much less than seen at met stations at 10m agl. WRF also showed a small but distinct diurnal pattern at coastal in-situ observations, stronger than the pattern seen in observations.

Figure 8.19 shows whether these wind speed patterns translate into noticeable diurnal patterns in load factor for onshore and offshore sites. For onshore farms, there is a diurnal variation in LF of around 0.02, with a minimum around 0900, and a broad plateau from midday onwards. The pattern is much less distinct than the diurnal pattern in wind speeds seen at 10m met stations [Sinden, 2007], and suggests that prediction of diurnal variations based on met station observations will significantly over-estimate the diurnal variation in load factor.

This relatively low diurnal variation can be explained in part by typical hub height of 80m, at which height diurnal variations in wind speed will be significantly less. From Figure 5.12 showed that the observed and simulated diurnal variaton from mean wind speed was around 0.8ms^{-1}at met masts. However, only one of the masts was at 80m agl, the rest were at 30-40m agl. So the diurnal variation at turbine hub-height would be expected to be less than 0.8ms^{-1}. In addition, diurnal variation will only effect power outputs when it occurs against a background wind speed over the steepest part of the power curve. Outside of this range, diurnal variations will not translate into variations in power output. This small diurnal variation is also seen in studies of Nordic countries [Holttinen, 2005].

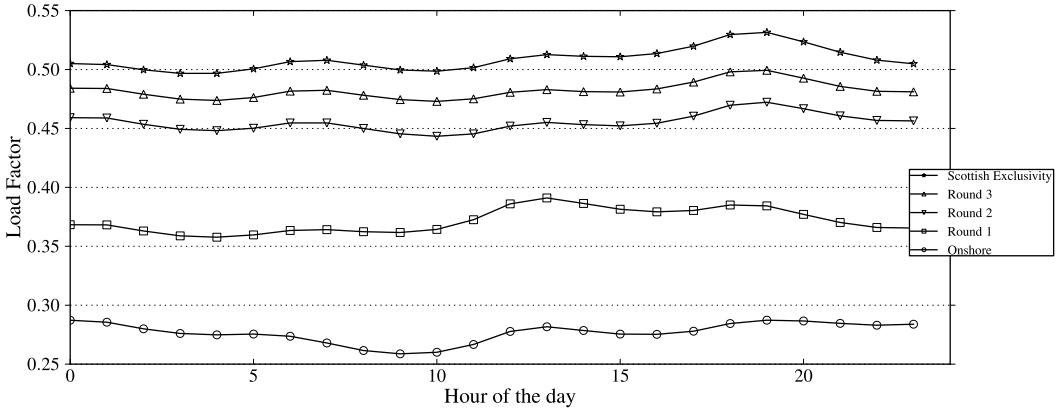

Figure 8.19: Average LF by hour

For Round 1 sites, which are near the coast, there are two weak peaks at 1200 and 1900, which might indicate the influence of a sea-breeze circulation. All the other rounds, which are further from the coast, show a peak at 1900. It is not immediately clear what is causing this peak, and it would be interesting to explore the flow patterns in more detail, perhaps splitting the analysis into onshore and offshore flow e.g. [Lapworth, 2005], and looking at the potential contribution of LLJs. However, this is beyond the scope of current work. Suffice to say, there are indications of diurnal patterns in load factor even at offshore sites, although the magnitude of these are relatively small when compared to typical inter-hourly changes, and are far less important than the variations due to changing synoptic situations.

Seasonal

Seasonal patterns are very pronounced: Figure 8.20 shows the average load factor for each month of the year over the whole period. Load factors are roughly twice as high in winter as summer. This result is well known, and agrees with the findings of e.g. Sinden [2007] who found monthly capacity values ranged from about 40% in the winter to about 20% in the summer. This analysis extends that result by showing the seasonal patterns of offshore load factors follow the same pattern.

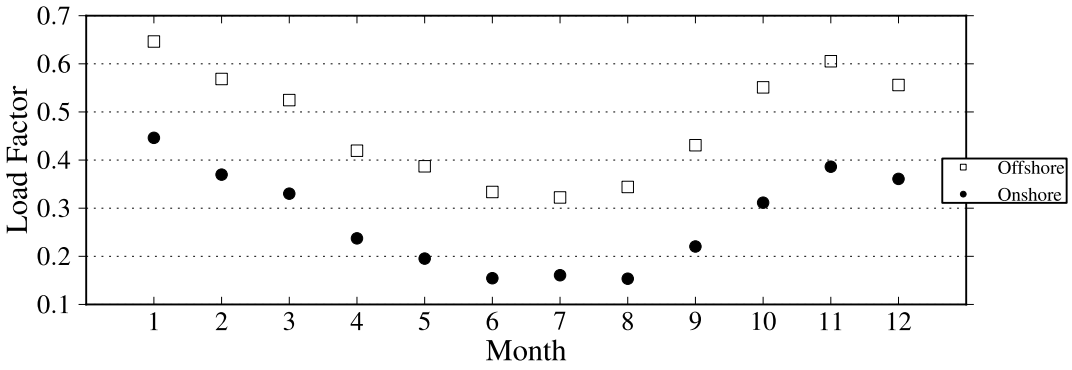

Figure 8.20: Average LF by month

Inter-annual

Figure 8.21 show the inter-annual variation in load factor over the whole period. The variation between most years is within a 5% band (i.e. an absolute change in load factor of 0.05). However in 2010, load factors were exceptionally low, around 20% for onshore sites compared with an average of 28%. The low load factors in 2010 were associated with a strongly negative NAO and persistent blocking high pattern, forcing the jet stream and storm tracks much further south.

This highlights the dangers of assessing wind resource against a short climatology. If the dataset produced in this study had been only ten years, it would have missed the pattern in 2010. It also demonstrates the great benefit that seasonal forecasting could bring [Brayshaw et al., 2011], as being able to predict years of exceptionally low winds would allow contingency plans to be put in place. Although seasonal forecasting has improved considerably in recent decades, overall skill remains fairly moderate [Smith et al., 2011].

Cross-correlation

Of importance for wind energy is the degree of correlation between wind speeds in different areas, since this will determine the extent to which the overall output is smoothed. This section examines this first in the raw wind speeds, then in regional load factors. The extent to which geographic smoothing removes absolute calms and ramp events is examined in a later section.

Wind speed correlation is known to decrease with distance [Hogrefe et al., 2001, Sinden, 2007].

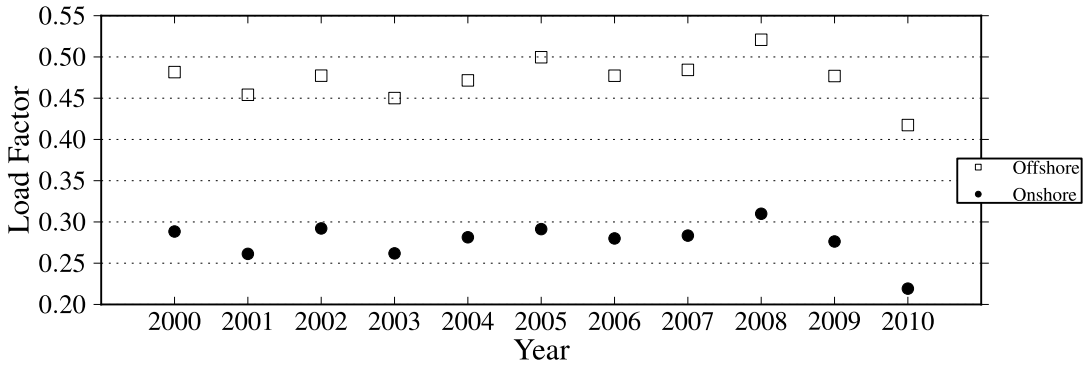

Figure 8.21: Average LF by year

However, this was based on discrete observation at points, rather than a continuous field. By computing the correlation coefficient, R, between wind speeds at each point in the domain against a reference point, (x_{ref}, y_{ref}), the variation of R with distance can be seen. This is shown in Figure 8.22, computed from a reference point in the centre of the domain (a), and a reference point in the upper-left corner of the domain (b). In both cases the correlation can be seen to fall rapidly with distance. The influence of complex terrain can also be seen to reduce the correlation. It is also clear that reduction with distance is not symmetric, and the gradient is steepest in the west-east direction.

Figure 8.22 (c) shows the variation of R with distance. The northwest corner is used as a reference since, of the four corners, it is most representative of the entry points of depressions and is likely to lead any wind speed changes. The correlation can be seen to decrease with distance in both directions, falling to around 0.8 at 200km, and 0.4 at 600km. This broadly agrees with Sinden [2007], who found that the correlation in power output (rather than wind speed) decreases from around 0.8 at 50km down to 0.4 at 400km, and 0.1 at 800km. This analysis confirms that the trend continues offshore. Furthermore it also shows the decrease is not symmetric, but is more rapid in the west-east plane, particularly at distances greater than 200km, showing that wind speeds are correlated over longer distances in the north-south direction. These values are also in line with Hogrefe et al. [2001], who found the correlation decreased to around 0.1 at 800m, when considering the synoptic component of wind speed time-series.

Figure 8.22 shows the maximum rate of change of R is along a south-east bearing. Wind farms

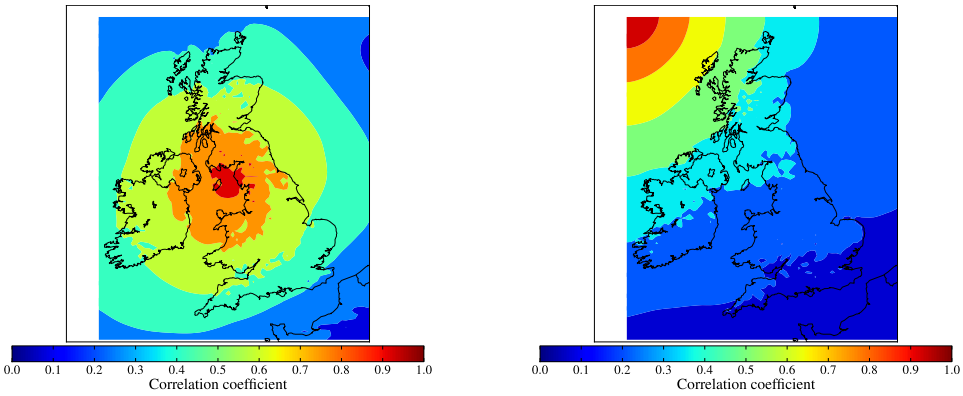

(a) (b)

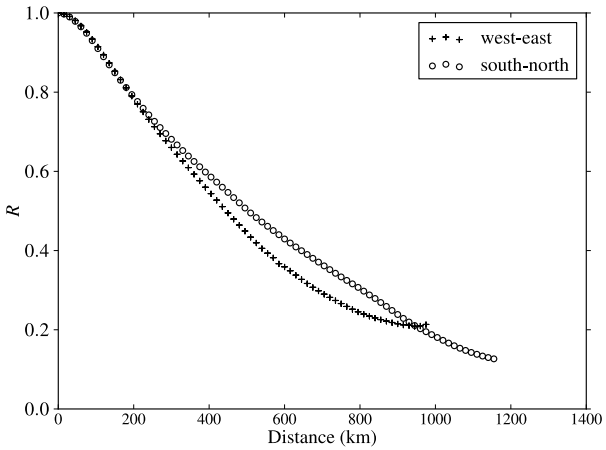

(c)

Figure 8.22: Geographic correlation using (a) $(nx/2, ny/2)$ and (b) $(0, ny)$ as a reference. (c) shows two cross-sections through (b)

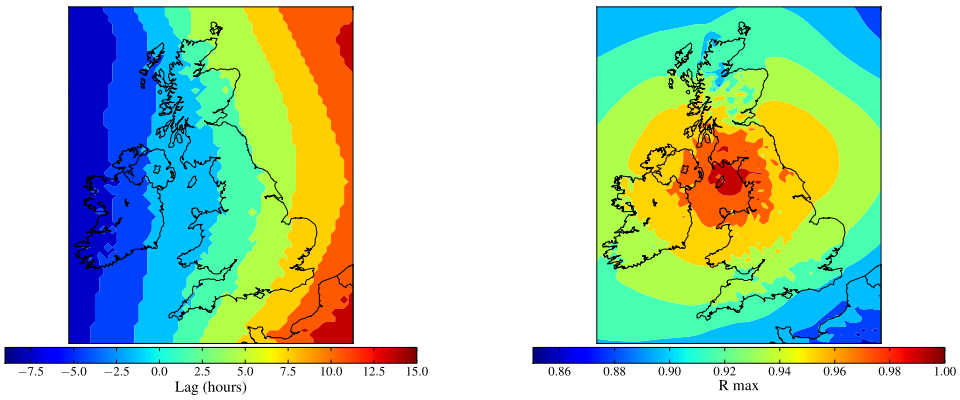

(a) (b)

Figure 8.23: Geographic cross correlation of wind speed against centre of the domain (a) shows the lag in hours of the maximum value of R, (b) shows the value of R at that lag.

separated along this diagonal will tend to be less correlated: wind farms in the Irish Sea will be relatively uncorrelated with wind farms in the Thames region. This highlights a flaw in the analysis by Oswald et al. [2008], who looked at correlations using sites which were largely aligned North-South.

However, this is based on instantaneous hourly values. It is unsurprising that instantaneous correlation decreases rapidly with distance, since wind speeds are governed by synoptic systems which themselves move across the country with a timescale of several hours to days. To examine this in more detail, the cross-correlation is recomputed at a lag of $\pm n$, where n is an integer number of hours.

Figure 8.23 shows (a) the lag at the maximum value of R, and (b) the value of R at that lag. The west-east pattern is very clear showing a lag of around 17-hours across the whole domain. This highlights the eastward-propagating nature of mid-latitude depressions which are the main driver of wind speeds in the UK. By plotting a cross section through this, Figure 8.24, a clear linear relationship is found. The reason for three or four points occurring on the same level is due the timestep of one-hour, meaning only integer lags can be used.

Taking the speed as the inverse of the gradient, a phase speed of around 56 km/h (15.5ms^{-1}) is found, i.e. the average speed at which wind-speed changes propagate across the country. Such a clear pattern highlights the dominant driver of wind speed changes: mid-latitude depressions from the Atlantic progressing eastward over the country on a timescale of days. Figure 8.23 (b) shows that correlation remains high across large distances when the temporal lag is taken into

account, with R above 0.9 for most of the domain.

On a large-scale this is inherently positive for wind energy integration, as it highlights the forecastability of wind speed changes on timescales suitable for bringing conventional plant online to provide reserve. It also is positive for the integration of wind energy over larger geographic domains. From Figure 8.23 it can be reasonably assumed that there is a lag of the order of around 0.5-1 day between the UK and other northern European countries such as Germany or Denmark.

The phase speed is somewhat higher than the 8-10 ms^{-1}typically estimated for synoptic scale features [Canziani and Legnani, 2003]. However, it is still much less than the mean flow speed of the jet stream, and therefore is still consistent with being driven by synoptic scale Rossby waves [Gerber and Vallis, 2009]. TO examine this in more detail, it would be preferable to partition weather types according to large scale synoptic organisation, e.g. using GWL types, and calculate the phase speed under each classification. Much more detailed studies have been done along these line [Hoskins and Ambrizzi, 1993, Yang and Hoskins, 1996], and this type of study is more suited to a global model.

An analysis on similar lines has been done in relation to photochemical pollutants over the Eastern United States [Sistla et al., 1998], where phase shift was calculated by the time of occurrence of maximum ozone concentration.

Finally, load factors at wind farm sites are examined to see how the power outputs relate to one another. This is computed at discrete sites, rather than continuously over the domain. Figure 8.25 shows the cross-correlation between average regional load factor, $\overline{LF^R}_i$, between all offshore regions, taking the Irish Sea region as reference. Only offshore regions are shown for clarity, as these geographically encompass all of the onshore regions. Load factor is less correlated than raw wind speed over the same distance, as expected since the non-linear power curve amplifies small changes. Nevertheless, the same spatio-temporal pattern remains with the average lag between Irish Sea and Tyne-Dogger being around 7-hours.

These results are useful for the design and operation of future networks, as they provide a simple way of relating the outputs of wind farms to one another, and could be used as the basis of statistical forecast models.

This analysis could be taken further, by performing a spectral decomposition the time series,

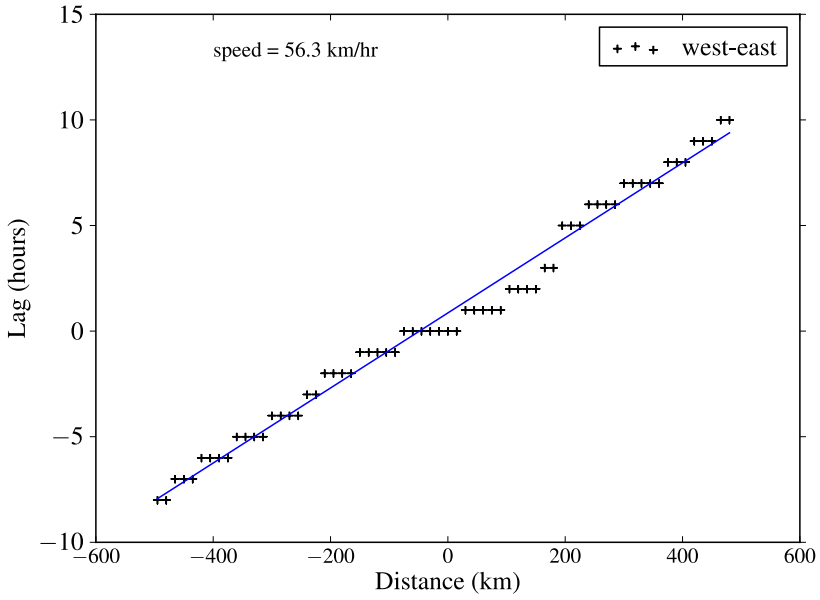

Figure 8.24: Lag with west-east distance from centre of the domain. The best-fit line gives an average phase speed of 56km/hr, or 16 ms^{-1}

e.g. [Hogrefe et al., 2001], which can provide insight beyond traditional time-series bases analyses and verification statistics. However, this is left as further work.

Calms

Meteorologically, calms are usually defined as wind speeds less than 1 knot, or 0.5ms^{-1}. However the typical cut-in speed of a turbine is 3-4ms^{-1}and most turbines generate very little power below 5ms^{-1}, so here a 'calm' is defined as anything under 5ms^{-1}. This would include anything classified as a gentle breeze or less on the Beaufort scale.

When assessing a calm across a set of locations, there is a significant difference between using the average wind speed and the maximum wind speed within a region, that is:

$$P\left[max(U_i^R) < x\right] \leq P\left[\overline{U_i^R} < x\right] \tag{8.9}$$

since it is possible for the average wind speed to be low, while still being high at a number component sites. Here an *absolute calm* is used to mean that the maximum wind speed at all locations is less than 5ms^{-1}, and no individual wind farm is generating:

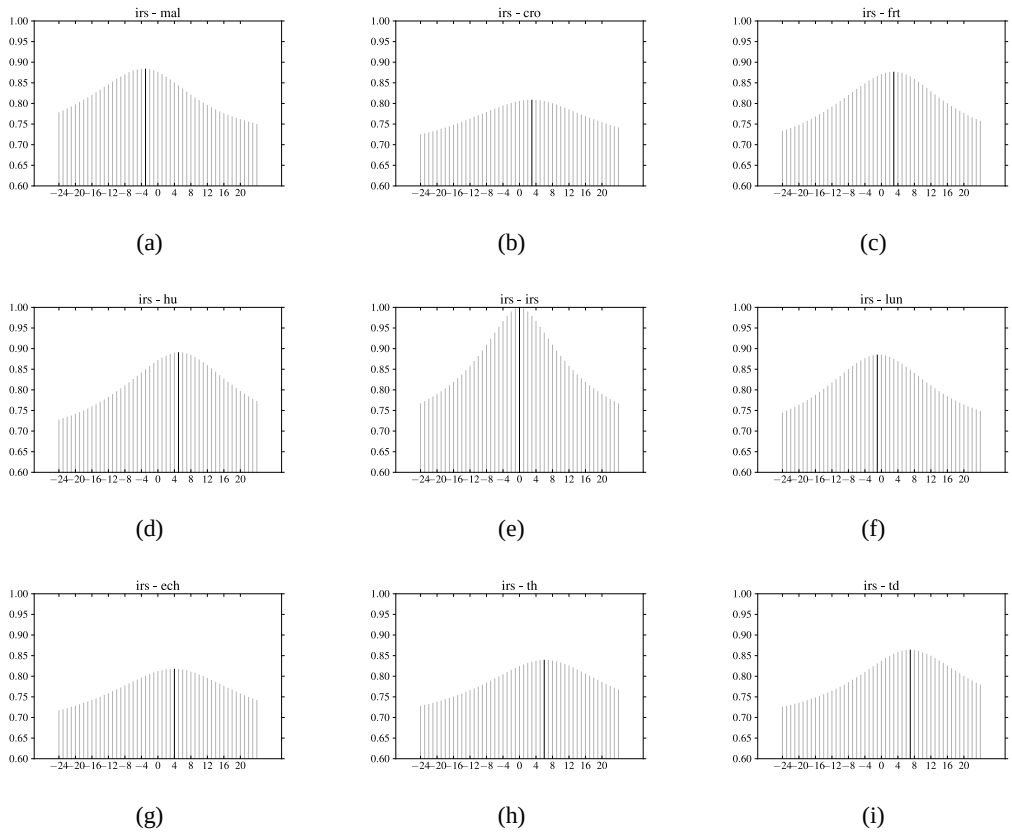

Figure 8.25: Cross correlation of hourly wind speeds between offshore regions, with Irish Sea as the reference region

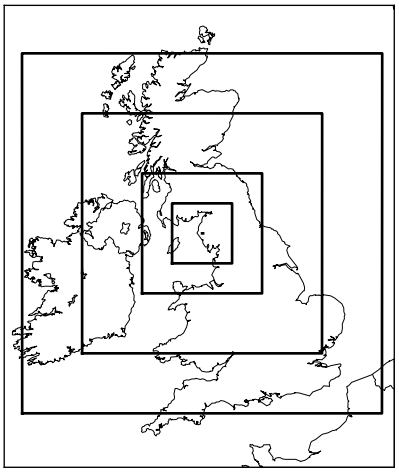

Figure 8.26: Schematic showing the progressive enlargement of geographic subdomains used to calculate the extent of calm conditions

$$P(\text{absolute calm}) = P(max(U_i^R) < 5) \tag{8.10}$$

The geographic extent of calms is assessed using a square sub-domain centred at $(nx/2, ny/2)$, which is progressively enlarged around each edge by a single cell: a few stages in the process are shown in Figure 8.26. At each step the probability of an absolute calm within the sub-domain is calculated from the full eleven-year dataset. The probability of an aboslute calm versus the length length of one side of the domain in shown in Figure 8.27. In a single 3km cell, the probability of a calm hour is around 25%, which agrees with previous analyses [Sinden, 2007]. As the domain is expanded, the chance of a total calm across the region drops very rapidly. For a domain of size 100×100 km, the probability of an absolute calm is only around 5%, and beyond 400×400 km, an absolute calm did not occur in dataset.

This is a steeper drop than that reported by Sinden [2007]; however the analysis here uses a continuous domain which extends offshore, rather than discrete onshore met stations. This shows that widespread absolute calms are incredibly rare when the continuous wind field is analysed. In short, the wind is always blowing somewhere. However it would be misleading to use this continuous analysis to predict the probability of zero power production, since it includes locations such as mountain tops, where there may well be winds above 5ms^{-1}, but no wind farms there. What matters more for wind energy is whether the wind is blowing at wind

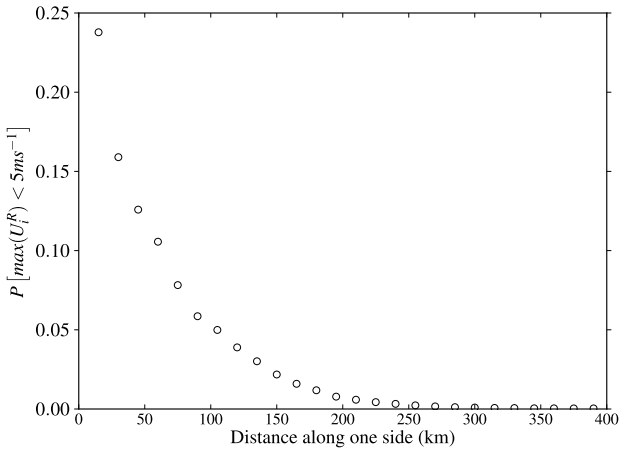

Figure 8.27: Probability of maximum wind speed less than 5ms^{-1}as a function of the width of a square sub-domain centred within the model domain

farms.

The probability of calms at individual offshore wind farms has already been given in Table 8.5, and is around 20%. However, there will also be smoothing between wind farms within a region and between regions. Also, the use of 5ms^{-1}as a cut-off for calms is somewhat arbitrary. It is much more informative to analyse the Cumulative Distribution Function (CDF) over the fulll range of wind speeds aggregated across regions.

To show this, the distribution of $max(U_i^R)$ was calculated for all geographic regions, Figure 8.28. The very thin lines show the CDF for individual geographic regions, while the thick lines show the CDF across all onshore or offshore regions. The probability of an absolute calm within a single offshore region ranges between 5% in Thames to to 14% in Lundy, while the probability of an absolute calm across individual onshore regions ranges from 4% in Northwest Scotland to 51% in London (the next highest outside of London is 27% in the West Midlands). The effect of geographic smoothing is very clear. The probability of an absolute calm across all onshore or offshore regions is far lower than any individual region. In fact, an absolute calm across all onshore regions, or all offshore regions, did not occur in the full eleven year dataset (96360 hours).

On this evidence can be reasonably concluded that the probability of an absolute calm across the entire country is less than once in eleven years, $p < 1 \times 10^5$. However, to accurately assess the probability of such an extreme event, at the very tail of the distribution, would require a

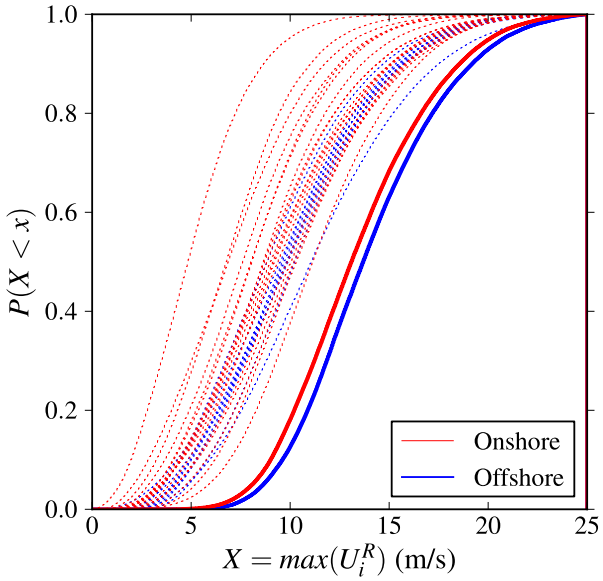

Figure 8.28: CDF for maximum wind speed within a region, $\max(U_i^R)$. The thin dotted lines represent individual geographic regions; the thick lines are aggregated over all onshore and offshore regions.

longer timeseries. It is evident though, that absolute calm periods are very rare indeed.

Although absolute calms are very rare, they are only part of the picture. Windfarms still produce relatively low output at speeds below 8ms^{-1}. Rather than analyse wind speed, it is more relevant to look at the CDF of aggregate load factor; this is shown in Figure 8.29. As expected from the analysis of wind speeds, the probability of zero output across the whole onshore or offshore fleet is zero, at least over these eleven years. There is always a wind farm somewhere producing power.

However, the lines in Figure 8.29 rise relatively steeply from zero. The probability that the aggregate load factor is less than 10% is about 0.3 onshore and 0.1 for the offshore fleet. The most striking feature is the marked difference between onshore and offshore sites in this low-output region. This shows that when average wind speeds are around the steepest part of the power curve, the higher wind speeds offshore translate into a very large benefit in terms of power output.

For a fully diversified offshore fleet, the CDF is quite close to a linear relationship, reflecting the relatively uniform distribution of load factors for offshore sites in Figure 8.10. This provides a

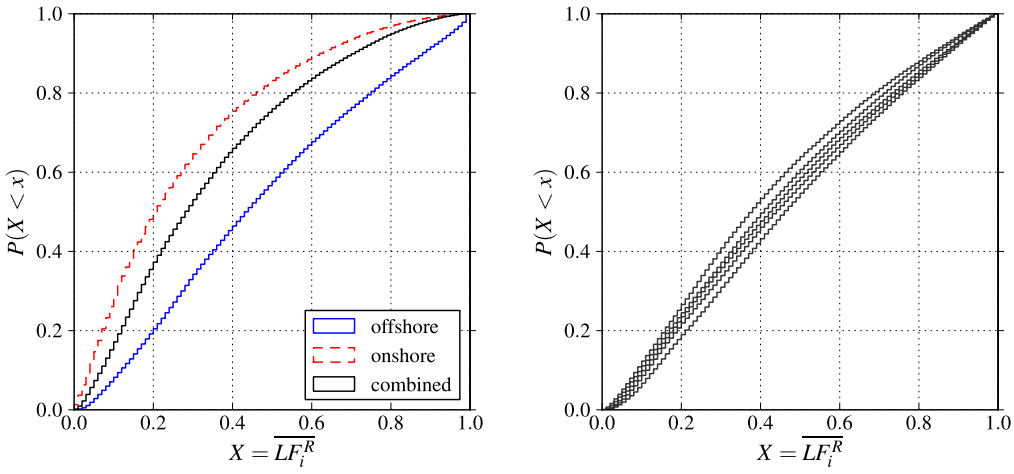

(a) (b)

Figure 8.29: CDF of average load factors. (a) shows average aggregated over onshore and offshore farms. (b) shows average by analysis snapshot: the lines are too close to differentiate by colour or symbols, but Snapshot A is the top line through to Snapshot E at the bottom

convenient rule-of-thumb for assessing the output of offshore wind.

Finally, CDF of aggregate load factor is presented by analysis snapshots A to E in Figure 8.29 (b). The lines are much closer together since they show a progressive shift from onshore generation offshore. The largest difference is in the middle part of the range. For example, the probability of aggregate load factor of less than 0.4 is around 0.55 in Snapshot A and around 0.4 in Snapshot E.

This analysis has shown that absolute calms are very rare - there will almost always be a wind farm generating power somewhere. It has also shown that having wind farms offshore gives considerable benefit in terms of more consistent output and additional geographic smoothing. It has also shown the importance of looking beyond a binary classification of ‘calm’ or ’not calm’, as this reveals only part of the picture. It is much more instructive to look the aggregate production or load factor, and how this is distributed. While zero production is rare, relatively low production is not so rare, even when aggregated across all onshore and offshore wind farms, and clearly the system must be designed around this.

Low output

The previous section has shown that hour-long periods of low output do occur, even when aggregated across the country. A key question is how long these periods last for, since this will determine what type of generation may be suitable for providing the balance. Figure 8.30 shows the CDF for the average load factor across all regions, assuming that wind is geographically dispersed as in Snapshot E. Aggregate load factor is calculated over different averaging windows: hourly, weekly, and daily. This gives a quantification of how often sustained periods of low output occur.

From Figure 8.30 it can be seen that the probability of having an aggregate hourly or daily load factor of < 0.10 is around 10%, while the probability of having a aggregate weekly load factor is around 2%. This shows that calm conditions tend not to persist over periods of a week. The most noticeable of Figure 8.30 feature is that the hourly and daily lines are very close. This demonstrates the link between the spatial and temporal scales: when averaged across all geographic regions, hourly variations are smoothed out and the dominant feature is day-to-day changes related to synoptic conditions.

From a system-wide perspective this suggests that wind integration at an aggregate level is not primarily a challenge of providing fast reserve to replace wind 'outages', but is more a question of day-ahead scheduling of conventional plant, storage, or imports. It shows that sufficient generation must be available to routinely cover periods of low output persisting for a day or more, but low outputs persisting for more than a few days are very rare.

Ramp events

Rapid changes in the aggregate power output of a wind farm or collection of a wind farms are termed 'ramp events'. Ramp events are a challenge for the integration of wind power as they may require the output of conventional generation or pumped storage to be adjusted rapidly, and could lead to large and rapid changes in the power flows in the transmission network [Dragoon, 2010, Ela and Kemper, 2009]. If the system cannot accommodate these changes, it could lead to a loss of load or network instabilities [Dragoon, 2010].

There are a number of ways in which ramp events can be defined [Kamath, 2010]. In this analysis, ramp events are characterised by the gradient of the wind speed or load factor over a

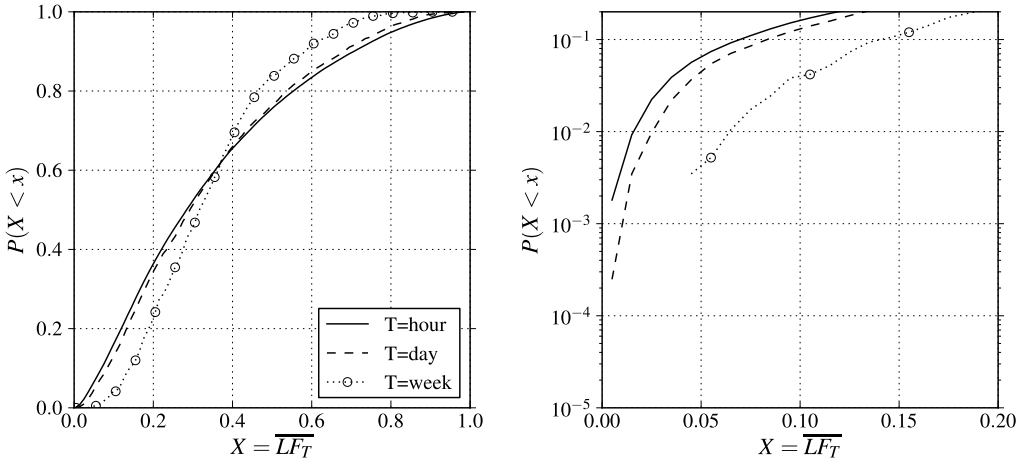

(a) (b)

Figure 8.30: CDF of aggregate load factor over different time widows. (a) shows the the whole CDF while (b) shows the lower tail.

time-window Δt:

$$\frac{\Delta\overline{U^R}}{\Delta t} = \frac{\overline{U^R}_{(t+\Delta t)} - \overline{U^R}_t}{\Delta t} \qquad \frac{\Delta\overline{LF^R}}{\Delta t} = \frac{\overline{LF^R}_{(t+\Delta t)} - \overline{LF^R}_t}{\Delta t} \tag{8.11}$$

Some further notation is introduced: $\Delta\overline{U^R}_{nh}$ is used as shorthand to represent the change over a period of n hours. The units of ΔU are expressed here in ms^{-1}hour^{-1}, rather than ms^{-2}, since the former are more intuitive when discussing ramp events.

As discussed in Chapter 2, since the simulations use Reynold's averaged equations, high frequency turbulent fluctuations on timescales of seconds to minutes are unresolved, and the smallest value of Δt is one hour. In relation to network operation, this means results are relevant to inter-hourly balancing mechanisms, not sub-minute regulation currently provided by the dynamic frequency response of conventional generation.

First, wind speed changes in each 3km cell are analysed, Figure 8.31. An obvious characteristic is that the distribution is zero-centred: the wind changes very little between consecutive 1-hour periods. This result is already well known in weather forecasting - persistence forecasting shows considerable skill over a timescales of a few hours. Hourly wind speed changes range between ± 2.5 ms^{-1}, and the distribution is symmetric showing increases or decreases of the same size are equally likely.

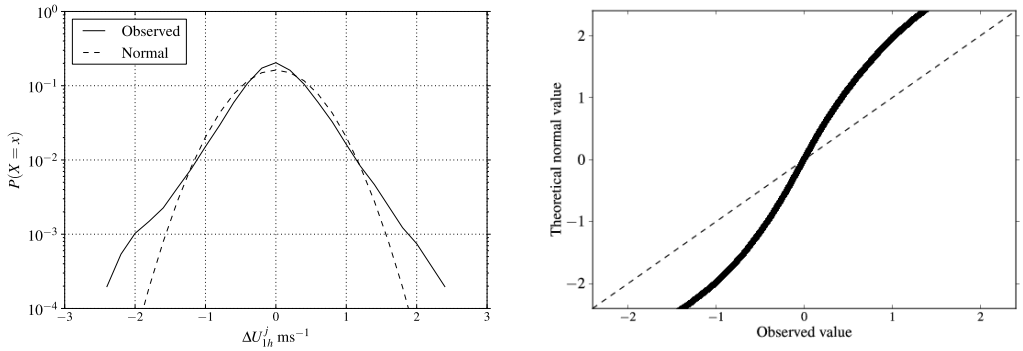

(a) (b)

Figure 8.31: (a) Distribution of hourly wind speed changes within each 3km cell, (b) QQ plot against Normal distribution

The changes are not normally distributed, as evident from the QQ plot, where the distribution is leptokurtic with fatter tails. It suggest something closer to a Levy stationary distribution [Chechkin et al., 2008], which is often found to describe volatile processes which show self-similarity across scales and have 'bursts' of activity, such as some turbulent diffusion processes [Chechkin et al., 2008] and as stock market volatility [Masoliver et al., 2000]. More detailed statistical analysis of the wind speed changes would be interesting, but is left for future work.

As shown in §8.4.2, the wind speed changes show a very clear dominant east-to-west propagation. Therefore ramp events are expected to be smoothed when averaged over larger geographic areas. To examine the relation between $\Delta\overline{U^R}$ and the size of the region R, a number of square subdomains of increasing size were constructed, as shown in Figure 8.26. The distribution of $\Delta\overline{U^R}_{1h}$ for each of these sub-domains, R, is shown in Figure 8.32.

Figure 8.32 shows that ramp events are smoothed considerably when averaged over a wider area. With a domain of width 15 km, the probability of a change in the average wind speed of 1ms^{-1} is around 0.01, or about 88 hours per year. For a domain of width 315 km, the probability of the same event is around 0.005, or 44 hours per year, and for a domain of width 615 km, the probability of the same event is under 0.0001, or 8 hours per year. Moreover, the trend continues as the area is expanded, and the smoothing effect is greater for larger ramps. When averaging over a domain of width 915 km, changes in the hourly wind speed are limited to ± 1.5 ms^{-1}.

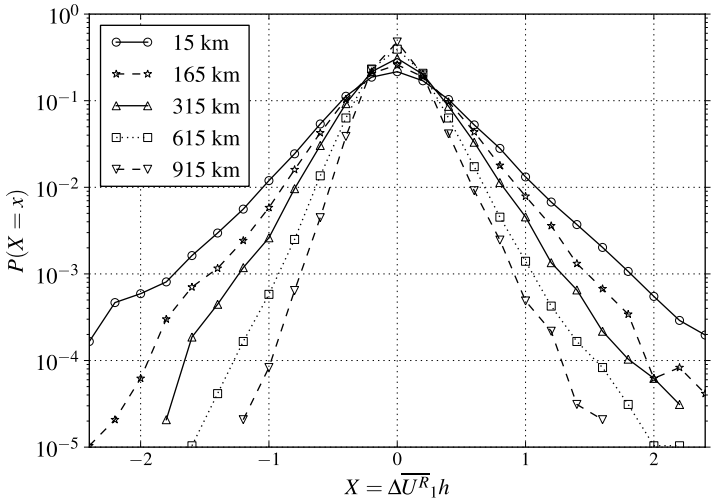

Figure 8.32: Geographic smoothing of wind speed ramps. The distribution of $\Delta\overline{UR}_{1h}$ is shown for a number of sub-domains. The legend shows the length of one side of the domain.

Wind speed changes will have biggest impact when they occur on the steepest part of the power curve. For wind energy, a ramp from an average speed of 2 to 3 ms^{-1} matters very little. Ramp events are now examined in terms of the load factors from wind farms. For this part, it is assumed that wind farms are distributed across all onshore and offsore regions, as per analysis Snapshot E.

Figure 8.33 shows the probability of changes in load factor aggregated over individual geographic regions, and over all regions. Again, the distributions are zero-centred and symmetric. The effect of geographic smoothing is evident and striking: the probability of a load factor change of -0.10 within an individual region ranges between 1×10^{-3} and 5×10^{-3}. When averaged across all regions, the probability is reduced tenfold to 1×10^{-4}.

Also of importance is the duration of a ramp event, since this will determine the total size of the change between the start and finish. Figure 8.34 shows the probability of a ramp event across all regions, calculated over time windows of 1h, 4h, 6h and 12h. Beyond a certain averaging window, there is no clear distinction between a 'ramp-event' and the normal expected changes in output due to the transition between weather patterns.

To compare averaging windows on the same scale, ramp events are expressed by their gradient $\Delta\overline{LF^R}/\Delta t$. In other words gradients seen in the 6-hour averaging window were sustained for 6

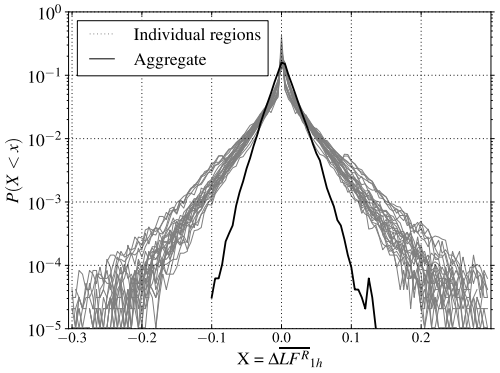

Figure 8.33: Geographic smoothing of ramp events

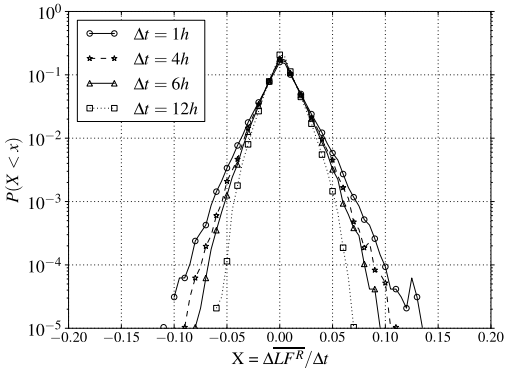

Figure 8.34: Aggregate ramp events by time window Δt

hours and lead to a larger overall change between the start and the end of the event. Figure 8.34 shows that as the averaging window is increased, the probability of a particular ramp gradient is reduced. However, there is relatively little difference between the 1h and 6h lines until gradients of ± 0.05 / hr are reached. This shows that at a country-wide level, ramp events seen over 1 hour tend to persist for 6 hours. This is consistent with changes being driven by transitions between synoptic systems, which take place over timescales of several hours to days, rather than large transient spikes at individual wind farms.

To investigate the distribution of the extreme ramp events in time, the 10 largest hourly ramp events were selected from each of the the 26 geographic regions, and the largest 260 aggregate (across all regions) ramp events were selected. Figure 8.35 (a) shows ramp events in individual regions, and Figure 8.35 (b) shows ramp events across all regions. In Figure 8.35 (a), ramps of ± 1.0 in one hour can be seen, related to high wind speed cut-out and subsequent cut-in in regions with very few wind farms. More common are events of ± 0.3. The largest ramp events

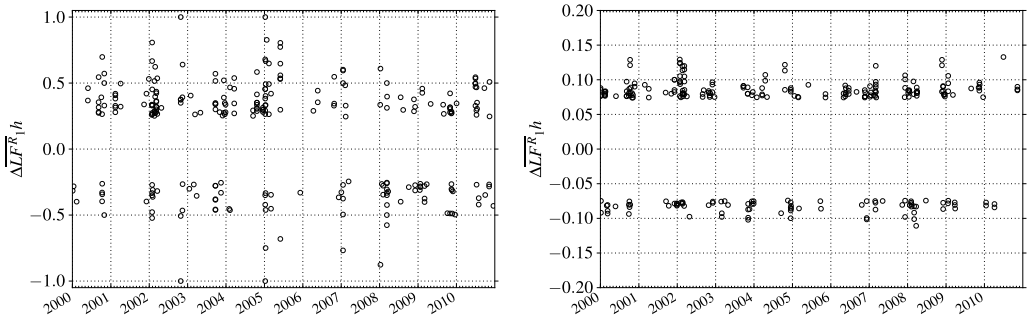

(a) (b)

Figure 8.35: Timing and size of (a) the 10 largest ramp events in 26 individual regions, (b) the 260 largest ramp events aggregated across all regions

tend to be clustered in the winter, although they are by no means exclusive to winter. Ramp events in the aggregate output, range between ± 0.15, demonstrating that geographic smoothing limits overall ramp events to within well-defined bounds. However, even though the aggregate ramp events are much smaller, they are still significant. With 30GW of installed wind capacity, a ramp rate of 0.15 / hour equates to 4.5GW / hour.

This agrees with Wan and Bucaneg [2002], who analysed the real output over the course of one year from two geographically separated sites, and concluded:

> "... despite the stochastic nature of wind power fluctuations, the magnitudes and rates of wind power changes caused by wind speed variations are seldom extreme, nor are they totally random. Their values are bounded in narrow ranges. ... Large swings of wind power do occur, but those infrequent large changes (caused by wind speed changes) are always related to well-defined weather events, most of which can be accurately predicted in advance."

Finally for this part, a preliminary investigation into the largest ramp events occurring in the dataset is made. The largest (simulated) negative ramp occurs in March 2008, and the largest positive ramp occurred at end of June 2010, Figure 8.36. The synoptic picture relating to these are shown in Figure 8.37. In the negative ramp event (top), the UK is in a strong northerly airflow, which is then disrupted as a large area of high pressure edges in from the Atlantic. Figure 8.36 shows the aggregate LF drops from around 0.9 to 0.3 in around 12 hours. The progressive nature of the event can be seen, with individual regions dropping down as the

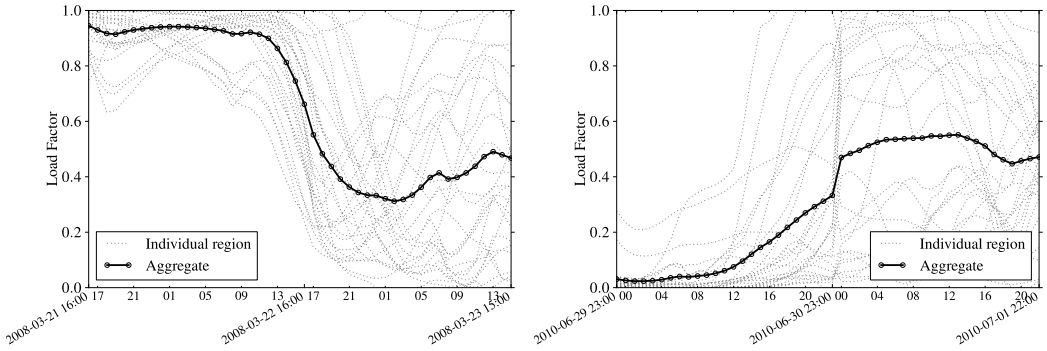

(a) (b)

Figure 8.36: Largest negative and positive ramp events over the entire period

system moves over the country. The largest positive ramp event occurs in June 2010, when a system of weak highs and lows giving way to a fairly deep depression, Figure 8.37 (bottom). Aggregate load factor rises from around 0.1 to 0.5 in 12 hours, with a particularly sharp rise near the end of the period.

From a system operators perspective, what is most important is the change in residual demand, as this is ultimately what determines how much reserve is needed to balance any change in generation. To explore this in more detail, Figure 8.38 compares hourly changes in demand and residual demand, assuming a distribution of wind as in Snapshot D, that is just under 50GW of wind distributed across all the country and through the Round 1, Round 2 and Round 3 offshore zones. The shape of the distribution of changes in demand relate to the diurnal profile. The largest ramps rate is an increase of around 7.5GW / hour seen during the early morning peak. A very striking result is that the largest changes in residual demand with around 50GW of wind on the system are comparable in magnitude to this, with the largest ramp rate around 10 GW/hour. This shows conclusively that, if wind is distributed around the country, and provided network capacity exists, the ramp rates in residual demand will not be significantly larger those managed today. Viewed from a systems perspective, integration of wind is more a question of scheduling and balancing energy on a timescale of several hours, rather than providing fast-acting reserve.

Relation to demand

The expected load factor at periods of high demand is important, as it determines the ability of wind generation to contribute to *generation adequacy*, that is the ability of the whole generation

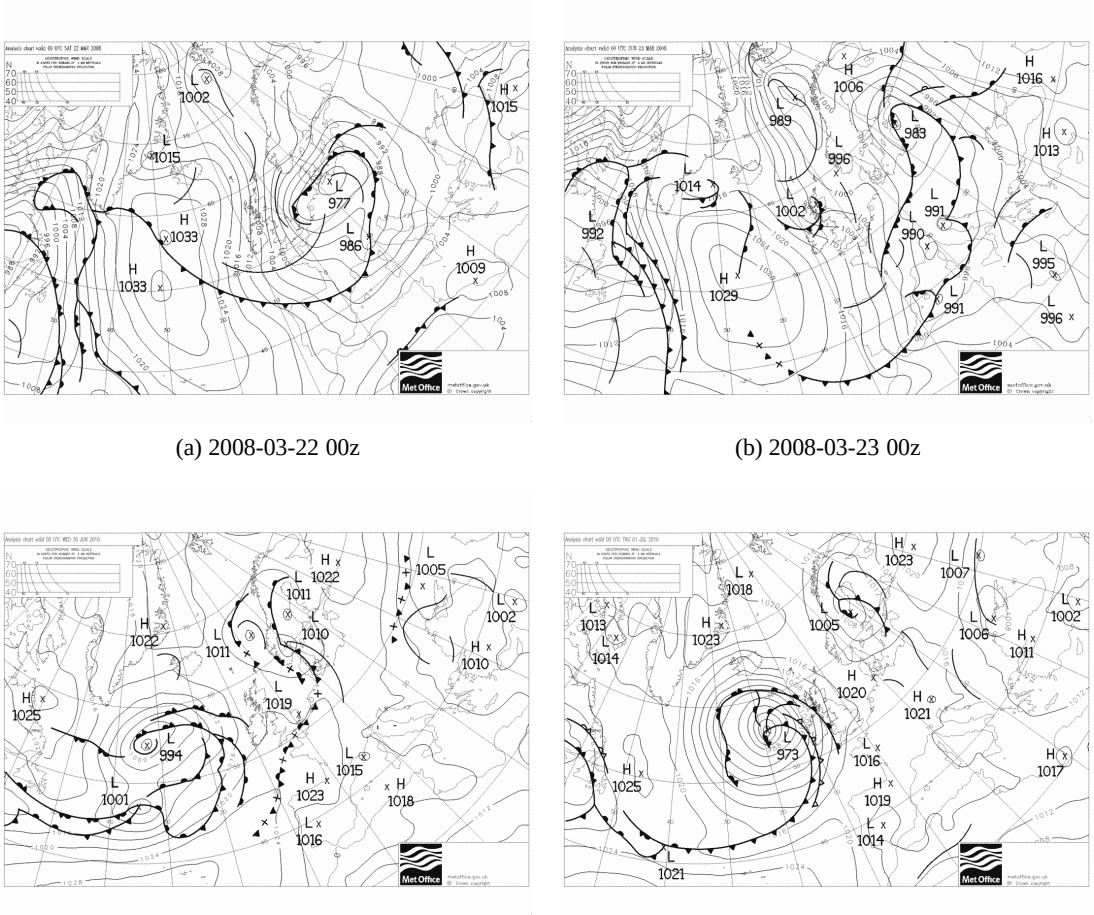

(a) 2008-03-22 00z

(b) 2008-03-23 00z

(c) 2010-06-30 00z

(d) 2010-07-01 00z

Figure 8.37: The synoptic systems causing the largest negative and positive change in aggregate output. Top: a ridge of high pressure pushes into the UK from the west. Bottom: a complex picture of highs and lows give way to depression over the UK. Surface analyses archived at `http://www.wetterzentrale.de/topkarten/tkfaxbraar.htm`, Crown Copywright UK Met Office.

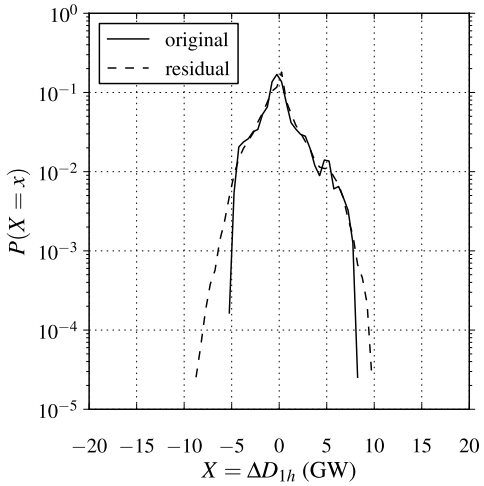

Figure 8.38: Comparison of ramps events in demand and residual demand with 50GW of installed wind capacity.

system to meet demand. Failure to meet demand leads to a *loss of load*, meaning customers are disconnected. Determining the contribution of wind at times of high demand enables the determination of the level of conventional generation required to maintain a desired level of generation adequacy, usually expressed as a loss of load probability.. At times of high demand, less spare conventional capacity is available to meet demand in the case of an outage of a conventional plant. The loss of load expectation is dominated by a small number of these high-demand, high-risk hours, so the behaviour of wind in these hours is of interest. However, very high demand occurs infrequently, so the number of hours included in the calculation of LF falls, and the confidence in the result drops accordingly. The extreme case - the highest absolute demand over the whole period - occurs by definition only once. Although what actually happened in this extreme case is interesting in itself, nothing can be revealed about the distribution of LF.

To estimate the contribution of wind at times of peak demand, an approach following Keane et al. [2011] is taken. Demand is grouped into two-percentile bands, and the aggregate LF within those hours is taken. Figure 8.39 shows the results, with the number of included within each band shown on the right-hand scale. The results confirm a pattern seen onshore by e.g. [Keane et al., 2011, Sinden, 2007], where load factor tends to increase in times of relatively high demand, but declines as the highest demand hours are approached. This is usually attributed to ‘cold snap’, anticyclonic conditions leading to increased demand but relatively little wind, but a more detailed meteorological investigation is given by Brayshaw et al. [2011].

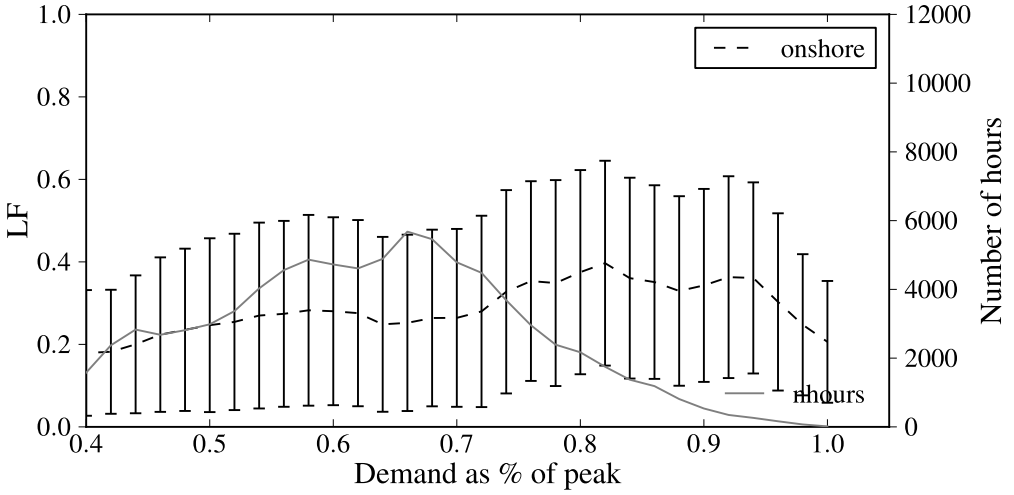

(a) Onshore

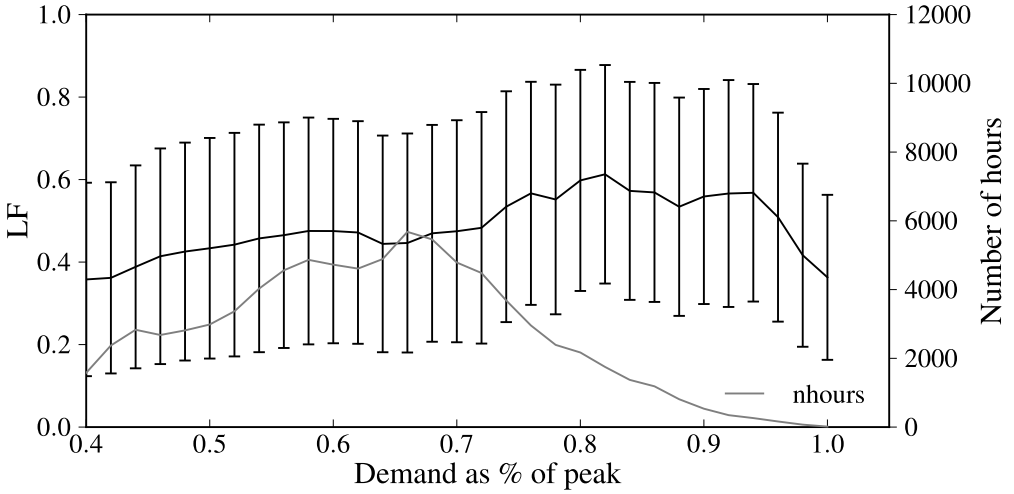

(b) Offshore

Figure 8.39: Average onshore and offshore LF against electricity demand as a % of yearly peak. Error bars show $\pm$ 1 standard deviation. The number of hours within each band is shown on right hand axis

This analysis was pursued to produce the first credible estimate of the *capacity credit* of offshore wind [Hawkins et al., 2011]. Capacity credit is a measure of the level of firm generation which can be relied on to meet demand, and has been previously used for onshore wind [Keane et al., 2011].

However, capacity credit was developed with thermal generators in mind, where the probability of a not being available to contribute to peak demand is dominated by the probability of unplanned outages. Each generator is an independent unit, with a (generally small) probability of an outage in each period. This can be modelled with a binomial distribution, and the probabilities can be summed over many independent generators to give the aggregate distribution. The resulting distribution approaches a Normal distribution, with a high confidence of being relatively close to the mean value, and a very small probability of being at one extreme.

With wind generation, the probability that generation may not be available to meet demand is dominated by natural variation of wind speed, not technical outages. Furthermore, wind farms are not independent, and are governed by the same synoptic systems. Although a mean load factor can be calculated at periods of high demand, the variation about the mean is very high. This is evident by the standard deviations shown on Figure 8.39, not shown in previous studies [Keane et al., 2011]. This is further explored in Figure 8.40, which shows the distribution of LF when demand is within 10% of peak. Although the mean is LF is 55%, there is a good chance LF will be less than 20%. It becomes difficult, and perhaps misleading, to characterise the load factor at peak entirely by a single statistic, the mean, when the distribution has so much spread. This questions the whole approach of determining capacity credit for wind generation, at least without putting confidence bounds on the figure.

8.5 Chapter summary

This chapter uses the WRF re-analysis to analyse the consequences for wind integration in the UK. The chapter provides some background describing the recent growth of wind and future targets. Existing demand patterns and conventional generation are described to provide context to and support the analysis. An analysis method is presented which is flexible enough to model the future growth of wind without being tied to particular assumptions about the timing or location of individual wind farms.

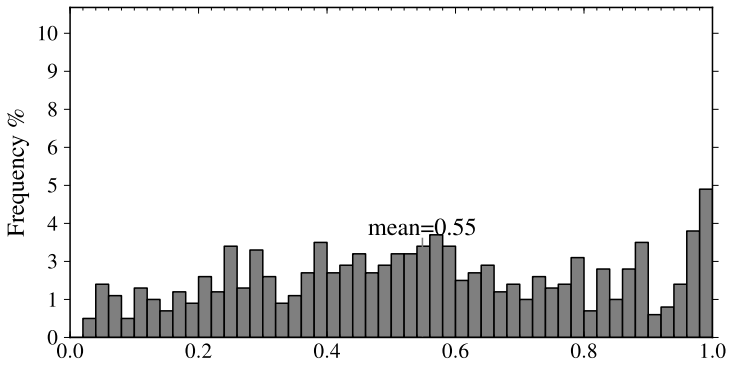

Figure 8.40: LF of offshore wind in hours where demand within 10% of peak

A detailed analysis is then presented, demonstrating the types of question which can be answered using this dataset. The large contribution wind generation can make to satisfying energy demand is shown, and the challenge of integration is highlighted by the selection of highest and lowest production weeks, with an illustration of the synoptic conditions causing this.

Spatial and temporal patterns are then looked at in more detail, including diurnal, seasonal and inter-annual variations in wind speed and load factor. The correlation of wind speeds is shown to decrease rapidly with distance. This traditional analysis is extended to include a temporal axis, showing very clearly the dominant pattern of east-west wind speed changes across the country.

The probability of absolute calms is shown to be very low indeed, although the probability of relatively low aggregate output is not, and distributions of aggregate output are developed for hourly, daily and weekly averaging periods. It is shown that, aggregated across the country, changes happen on a timescale of days rather than hours. Ramp events are examined detail, and probability distributions are developed for various levels of geographic aggregation. It is shown that although large ramp events can occur within a region, when aggregated over all regions, they are constrained within tight bounds.

Finally, the relation of wind output to current patterns electricity demand is shown, and it is confirmed that wind generally has higher than average output in times of relatively high demand, but tails off in the very extreme hours. However the variability of wind, and the challenge of assigning it a capacity credit based on a single value is highlighted. Throughout

the analysis the focus is on deriving probability distributions, to show not just than an event does occur, but *how often* it occurs which is essential for the future design of networks.

Chapter 9
Discussion and conclusion

9.1 Introduction

Providing a safe, secure and clean future energy supply is perhaps one of the most important scientific, political and economic tasks facing society today. The potential to harness renewable energy sources on a large scale offers an immense benefit to society, and also presents an immense challenge.

In the UK, wind energy has enormous potential. In the introduction to this work, it argued that a key step to exploring and overcoming the challenge of renewable integration is a detailed understanding of the physical resource: both the average conditions which determine how much energy is available, and also the spatial and temporal variability which govern when and where it is available. Yet despite the importance of this issue, research, and policy making based on it, is frequently hampered by a lack of reliable, accessible, and freely available data. It is hypothesis that meteorological modelling can provide more insight into some of the key challenges, and a major motivation for this work is to make available a high-quality dataset which can be used to help explore and address some of these challenges. In Chapter 1, requirements were specified that such a dataset must:

- be a realistic representation of the average onshore and offshore wind conditions;
- capture spatial and temporal variability across a range of scales; and
- be physically based, so that relations between wind speed, temperature and other meteorological variables are preserved.

This concluding chapter confirms these objectives have been met, and takes key results from the analysis of Chapter 8 to draw conclusions regarding the integration of large amounts of wind energy into the UK grid. First, a brief chapter summary is given; second, key conclusions are outlined and discussed; finally, the limitations of the approach and options for futher work are discussed.

9.2 Thesis summary

Chapter 1 presents the background and context to this work, sets out the aims and objectives, describes the contribution to knowledge, and provides a summary of the chapters.

Chapter 2 provides some theoretical background and context to the modelling work. A brief 'Cook's tour' of the atmosphere and atmospheric modelling is given. The scales of the atmosphere are discussed and the existence of a spectral gap separating turbulent scales from longer scales is highlighted. Planetary boundary layer processes and the challenges they present to atmospheric models are described.

Chapter 3 provides a review of alternative mesoscale models and concludes that a number of models provide similar sophisticated capabilities, with the main differences being in their ease of use, accessibility, and community support. A modern, open-source, and well-supported mesoscale model, WRF, is chosen for the rest of the work. The main features and options available in WRF are then summarised.

Chapter 4 reviews the sources of observations available for model verification from both in-situ and remote sources. A week-long case study is used to compare different model configurations, in an attempt to limit some of the systematic errors which can occur using poorly chosen options. Significant improvement of error statistics is seen over the baseline case, and a model configuration is chosen to use in the full reanalysis.

Chapter 5 describes the main simulation phase, in which an eleven-year reanalysis over the UK and surrounding waters at 3km resolution is performed. The wind speed outputs are compared to an extensive set of observations. Against onshore met stations, modelled wind speeds are shown to capture observed distributions very well ($B = 0.15$ ms^{-1}, $RMSD = 2.03$ ms^{-1}), although with some large systematic errors seen at some stations in complex terrain. Against offshore observations, a significant low bias of ($B = -1.05$ms^{-1}) is found against buoys and lightships, as well as against wind speeds derived from satellite scatterometers. The effect of various influences on model performance are explored, including terrain complexity, stability and the influence of the coast. It is concluded that it is most likely the low bias offshore is inherited from the global model, due to the lower spatial resolution causing the spatial smoothing of depressions and subsequent under-prediction of peak winds, as well as the assimilation of poorer quality observations at platforms and buoys.

Chapter 6 presents a simple method for removing model bias offshore by linear regression against daily average wind speeds from the QuickSCAT and ASCAT satellites. The satellite datasets are first compared to in-situ observations, and found to be significantly less biased than raw model output. This comparison also confirms that some remote buoys appear to have instrument problems across some of the period studied. The bias-corrected model speeds have significantly improved error statistics, with the bias much reduced ($B = 0.26\text{ms}^{-1} RMSD = 1.88\text{ms}^{-1}$).

Chapter 7 then develops a process for converting wind speeds into the power outputs from wind farms based on a power curve which matches the size and type of the turbine expected to be in use. A method of accounting for wake losses is developed and tested which distributes losses over a range of wind speeds, rather than apply a constant reduction. Sources of published data on wind farm outputs are reviewed, simulated outputs are then compared to published figures for existing farms and shown to be realistic on hourly and monthly timescales.

Chapter 8 presents a detailed analysis of the wind speed dataset and the implications for wind energy integration. Supporting material regarding the projected future growth of wind, existing electricity demand, and conventional generation is presented. An analysis method is then developed which is flexible enough to model the future growth of wind without being tied to particular assumptions about the timing or location of individual windfarms. Results of the analysis are then presented, demonstrating the types of question which can be answered using this dataset. The large contribution that wind generation can make to satisfying electricity demand is shown, and the challenge of integration is quantified by showing the spatial and temporal variability at a number of scales. Throughout the analysis the focus is on deriving probability distributions, to show not just than a certain event occurs, but *how often* it occurs which is essential for the future design of networks.

In the analysis described above, results were presented 'as is' avoiding subjective judgements on the implications for wind energy. In this concluding chapter, some of the key results from the analysis are interpreted as to their implications for the large scale integration of wind energy.

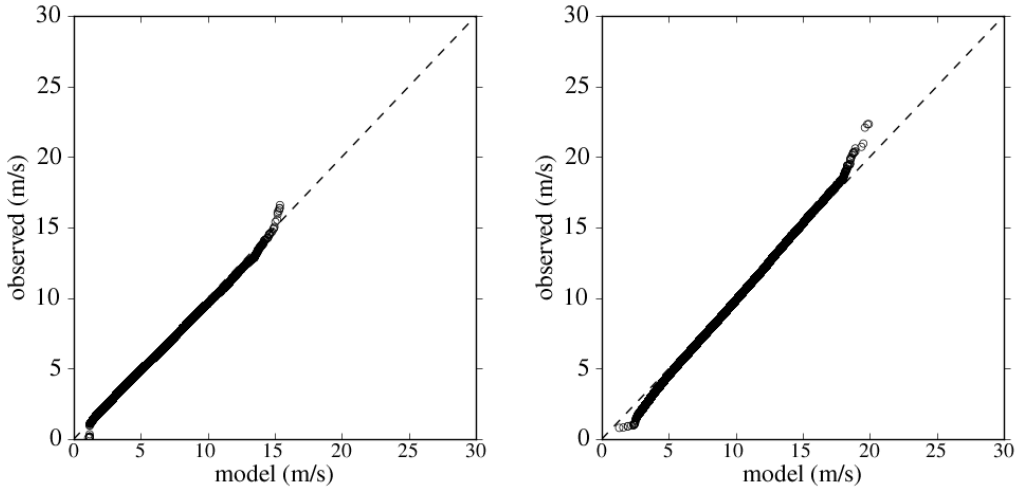

(a) onshore (b) offshore

Figure 9.1: Final QQ plots of observed and modelled hourly mean wind speed against all onshore and offshore in-situ observations

9.3 Conclusions

9.3.1 Wind speed dataset

The main output from the work is a high-resolution reanalysis dataset of wind speeds and other meteorological variables which is an accurate and realistic representation of the recent (2000-2010) wind climate over the whole of the British Isles and surrounding waters. The final error statistics against all available in-situ observations are shown in Table 9.1, and QQ plots of observed and simulated average wind speeds, Figure 9.1 show that this objective has been achieved.

However, the limitations of the dataset have been honestly presented. In particular it is shown that large systematic biases may exists at individual locations, particularly in complex terrain, and it would not be advised to use wind speeds for single point predictions in complex terrain, without accounting for local terrain, or at least correlating with a short set of observations.

category	n	B ms^{-1}	RMSD ms^{-1}	R^2
onshore	237	0.15	2.03	0.64
offshore	19	0.27	1.88	0.71

Table 9.1: Summary of error statistics against all in-situ observations

The fact that such a dataset did not publicly exist previously is somewhat remarkable. Advances in meteorology have long been driven by cooperation and the open and free sharing of data across institutions and national borders for the public good. The commercial aspects of wind energy have not encouraged a similar approach, and it is hoped that, by making this dataset publicly and easily accessible, it will greatly support further research in a scientific tradition of open data sharing.

9.3.2 Wind energy integration

Energy potential

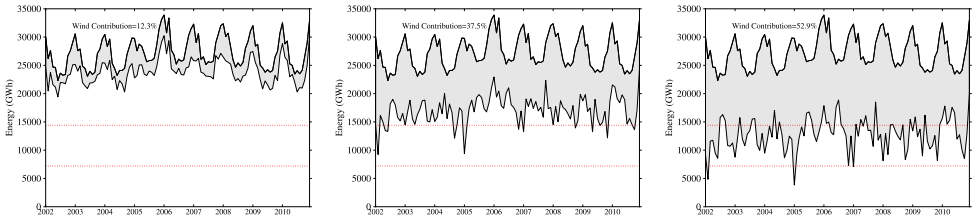

(a) Snapshot B - 14GW (b) Snapshot C - 40GW (c) Snapshot E - 54GW

Figure 9.2: Summary of wind energy's contribution to meeting existing demand. Top line is electricity demand, shaded area is wind contribution, and the remaining area is residual demand.

A major contribution is a detailed quantification of the contribution that wind generation, and particularly offshore wind generation, can make to current electricity demand. Figure 9.2 shows three snapshots, illustrating the fundamental change which would occur in the electricity system with the large scale development of wind.

Figure 9.3 shows that 25% of electricity demand could be met by wind with the installation of around 25-30GW of capacity, depending on its geographic distribution. Even if no increase in other renewable sources are envisaged, and they continue to contribute the 5% they supply today [DECC, 2010], this will allow the UK to generate 30% of electricity demand from renewables, consistent with EU targets for 2020. Whether this level of capacity can be achieved in less than 8 years depends a great deal on the level of political and economic support. Furthermore, the analysis shows that 50% of current electricity demand could be met with 50GW of capacity, provided it is distributed around all of the offshore zones.

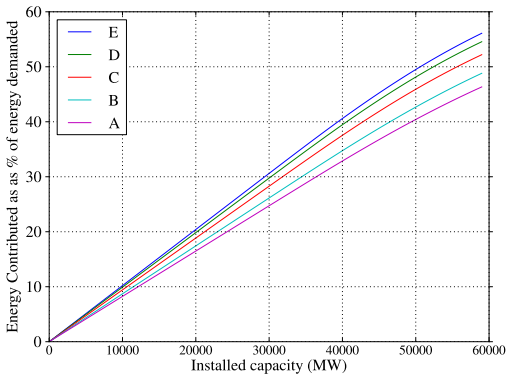

Figure 9.3: Contribution of wind energy to demand by installed capacity under different geographic distributions of wind.

Variability

There has been a long, often heated, debate as to whether the variability of wind generation is a 'show stopper'. On one side, it is argued that the integration across a large area [Milborrow, 2000, Sinden, 2007] aids the integration of wind power and allows the challenges to become manageable. On the other side of the debate [Oswald et al., 2008, Sharman et al., 2011] there are claims that the variability of wind means it is either impossible, or undesirable, to use it is an energy source. The somewhat entrenched positions in this debate were summarised by Gross and Heptonstall [2008]: "East is east, and west is west, and never the twain shall meet". This work brings a large amount of quantitative evidence to this debate.

A major conclusion of this study is that geographic distribution considerably smooths the output from a wind fleet, limiting the rate of change in the aggregate output to within well defined bounds. Geographic smoothing removes mesoscale and sub-mesoscale fluctuations, leaving only the changes associated with more slowly varying synoptic-scale processes on a timescale of several hours to days. The cross-correlation in an east-to-west direction is highlighted, and the characteristic speed of synoptic systems over the country is determined as 56 km / hr.

It is shown conclusively in Figure 9.4 that although wind generation changes the pattern of demand substantially, the ramp rates seen in residual demand with 50GW of wind capacity are comparable to the ramp rates seen, and managed, in diurnal demand patterns today. This contradicts those [Oswald et al., 2008, Sharman et al., 2011], who argues that large amounts of wind will cause larger and more frequent power swings, with negative implications for conventional plant lifetimes and efficiency.

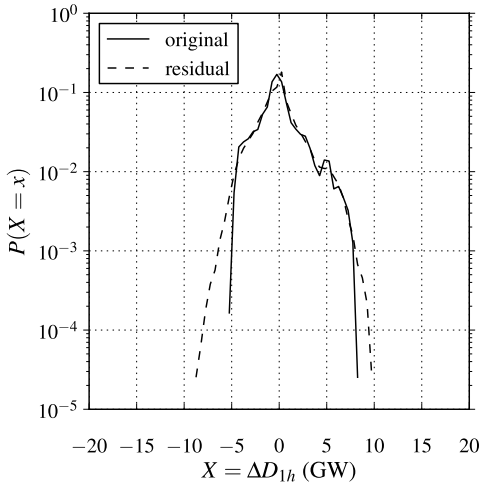

Figure 9.4: Comparison of inter-hourly ramp events in demand and residual demand with 49 GW of wind capacity

On the other hand, it is shown that the variability associated with synoptic scale processes still remains, and the argument used most frequently against wind, that periods of low aggregate wind output and high demand occur, is confirmed and quantified. In these situations, it is clear that conventional generation or significant imports from other countries must be relied on. The findings of Sinden [2007] are confirmed, that periods of absolute calm across the whole wind fleet are exceptionally rare, but it is also shown that times when the entire wind fleet is producing relatively little are not unusual. Even with wind distributed around all offshore sites, the output will be expected to be less than 10% of the maximum for 10% of the time.

However, the claim that conventional generation must be 'on standby' [Sharman et al., 2011] as spinning reserve, and therefore burning fossil fuels, is not supported, since the ramp rates in residual demand are comparable to ramp rates in demand today. 'Warm' units burn fossil fuels in order to provide fast reserve within 20 minutes [Pearmine et al., 2006]. Wind speed ramps governed by synoptic scales are forecastable on a timescales much longer than this, and suitable for scheduling conventional plant in much the same way as is done today.

It is also shown that with an increasing penetration of wind, the residual demand is decreased substantially. This means a much lower utilisation of existing or new conventional plants, requiring these generators to exploit much larger price differentials between windy and calm days, as well as revenue from auxiliary services, to make an economic return.

With an increasing penetration of wind, not only does residual demand decrease, but frequently

becomes negative. With 49 GW of wind on the system, assuming current demand patterms, net demand would be expected to be negative just under 20% of the time, and would be less than 10 GW around 35% of the time.

Traditionally, this might be thought of as energy which, if it could not be stored or exported, is somehow 'wasted' and therefore represents an inefficiency and an argument against wind. However, since the variable cost, the fuel, of wind is free, this is not necessarily an inefficiency. At the very least this energy can be spilled without consequence. Moreover, it represents the potential for wind generation to play a much more active part in the balancing of supply and demand. Modern wind turbines can modulate their output very rapidly through blade feathering, and therefore represent a source of balancing reserve [Ramtharan et al., 2007]. Since it has been shown that times of low residual demand, and hence low spot-price, will be common, it may be more beneficial to operate wind turbines below full capacity and provide balancing reserve to the system. This would also allow better integration with inflexible baseload generation such as nuclear. However, ensuring market incentives are structured in such a way to achieve this is essential. In particular, the current system of compensating wind generators for 'lost' production if they face network or other constraints, would become highly inefficient at high penetrations of wind and would increase the overall cost.

The main conclusion from this work is that many of the perceived challenges of wind integration come from a failure to distinguish between variable and unpredictable. The technical challenges, from a system wide perspective, become tractable provided wind generation can be accurately forecast on a timescales of hours to days ahead, and forecasting is increasingly playing a key role in energy systems [Dobschinski et al., 2007, Foley et al., 2012, Giebel and Kariniotakis, 2003, Lei et al., 2009].

This is not to suggest there are not many other challenges. An ever-present assumption in this work is an ideal electricity network, effortlessly transporting and smoothing generation over any level of geographic aggregation. There are a whole host of questions regarding network capacity, frequency regulation, voltage support, and system stability which are beyond the scope of this work. Significant research, development and investment is being made to try and equip future networks to handle variable generation, and it is hoped this work may contribute to this process.

9.4 Limitations

There are a number of limitations inherent in using any atmospheric model to recreate historic weather patterns, as there are always simplifications and semi-empirical formulations used to represent complex turbulent processes, and the observational record is only a sample of continuous field. In particular in this work, turbulent scales are not explicitly resolved so the dataset can not be used to study variability on very short timescales. Additionally peak wind speeds were not well reproduced and so the impact of high-wind cut-outs is not explored in detail. However these limitations are common to many similar approaches, and are not specific to this work.

There are a number of more specific limitations to this study. Practical constraints limited the time which could be spent configuring WRF. A high bias seen onshore, likely due to the neglect of sub-grid scale orographic drag, lead to the use of analysis nudging which may have affected the quality of the model output offshore. Additionally, a problem with sea surface temperature remaining constant over one month may have affected the quality of model output in the coastal region.

A major limitation onshore is the resolution of 3km, which cannot capture complex terrain features. Work is ongoing within The University of Edinburgh to try various downscaling approaches such as WAsP and more sophisticated CFD modelling to account for local terrain. Other work is experimenting with neural networks to account for systematic and phase errors in the output.

Another limitation is the length of the period simulated, which at eleven years is too short to claim to be a climatology. One solution would be to extend the simulation further back in time. However, there may be more efficient ways of effectively extending the length, by using existing datasets such as the NCEP/NCAR [Kalnay et al., 1996], or ERA-40 reanalysis [Uppala et al., 2005]. A relatively simple approach would be to correlate average monthly wind speeds between this study and a longer reanalysis. This would give an indication of whether the eleven year period studied here is representative of the longer term climate in terms of the average values and monthly variation captured.

A more sophisticated approach would be to classify the weather episodes within the dataset e.g. using GWL types, and compare the frequency distributions between the shorter and longer reanalysis. This may also help to address another limitation: the assumption that the last eleven

years are representative of the future climate. This assumption might not be justified in the face of human-induced climate change. There are a variety of mechanisms by which climate change could affect UK wind speeds. For example, changes in the frequency of negative NAO episodes, changes in the jet stream position, and changes in storm tracks could have a direct effect [Cradden, 2009]. Similarly, other changes could contribute, for example, changes in frequency of Atlantic hurricanes, which often become extra-tropical storms and reach the UK, may have an effect on the wind climate [Jiang and Perrie, 2007].

However, a recent review [Pryor and Barthelmie, 2010] found that most studies projected relatively small changes in the wind climate of northern Europe, with natural variability a much stronger signal than any human-induced climate change. For example, Cradden [2009] examined output from regional climate models over the UK and found very little change in surface wind speeds. However, even representing current wind climates accurately within a GCM is difficult [Brown et al., 2009, Höglund et al., 2009], and the difference between alternative models is often larger than any climate signal. Analysis of observations have generally found small trends in ocean surface wind speeds of around 0.08 ms^{-1} per decade [Tokinaga and Xie, 2010, Wentz et al., 2007]. Young et al. [2011] found a much higher trend, though the methodology was heavily criticised [Wentz and Ricciardulli, 2011].

The UK Climate Change Impacts Program 2009 (UKCIP09) [Murphy et al., 2009] did not include probabilistic assessments of surface wind speed changes, due to the lack of comparable surface variables between different climate models. Results from an 11-member ensemble of the same model showed wind speed changes between $\pm 10\%$, but the ensemble mean showed little change. More recently, probabilistic projections of UK wind speed have been released [Sexton and Murphy, 2010], again showing generally small changes of $< 0.2ms^{-1}$, with natural climate variability contributing the most to uncertainty. However, some model runs with a better representation of stratospheric processes showed greater changes [Sexton and Murphy, 2010] related to changes in the general circulation.

Although current understanding is incomplete, it seems reasonably clear that climate change signals in surface wind speed are much less clear than surface temperature, and on the basis of current knowledge, changes in the wind speed are likely to be small. It would be interesting to classify the reanalysis dataset presented here into weather types, and explore the impact of changes in frequency of certain weather patterns such as blocking highs, but this is an area for future work.

9.5 Future work

Some areas for future work have been mentioned above, for example the use of an objective weather classification for the use in future climate impact studies. Other work is ongoing at Edinburgh to use the dataset to accurately assess the reserve requirements in systems with high penetrations of wind, as well as other work to estimate the contribution which embedded wind generation already makes to the grid. Such generation is not metered by the system operator, and there is considerable uncertainty over its current contribution.

A major area of future work is to use the dataset to do detailed studies of power flows in potential future networks, assessing what level of network capacity, what level of auxiliary support, and what technologies may allow the integration of wind energy into the grid. Another major area of work is to investigate the impact of large-scale storage and flexible demand. In particular it is hoped that the amount of storage needed to achieve a certain level of 'smoothness' in wind output can be quantified and related to the size of physical schemes such as pumped hydro or compressed air storage. This would allow an assessment as to whether such schemes are technically feasible or not.

The most immediate area for further work is to provide an interface to the model data, which allows public access to average statistics and time series. It is envisaged that this will be a graphical front end o the netCDF files based on Google Maps^{TM} or similar.

Finally, if time and computational resource allows, the reanalysis will be continued to the present, and the existing data may be re-run and improved, for example using better PBL parameterisation schemes, higher resolution land-use datasets, and a better treatment of SST.

9.6 Concluding remarks

In Chapter 1, a hypothesis was proposed that advanced meteorological model could deliver new insight into the UK's wind energy resource, and the potential to integrate this on a large scale. On the basis of the arguments made in this chapter, this hypothesis is accepted. By analysing over a sufficiently long period, the probability distribution of important events have been found, rather than focusing on a single selected short time-period. It has been shown that the integration of large-scale wind energy can provide a large part of current electricity demand, displacing large amounts fossil fuel. It has also been shown that such an energy system will have

to cope with periods of very low output relatively frequently, which may mean conventional generation in the medium term. However, it has been shown that the variability of wind is not an insurmountable challenge, since the flexibility required is not so different from the system operated today.

The integrating wind generation requires an approach akin to the approach adopted by sailors:

> "Therefore we should not try to alter circumstances but to adapt ourselves to them as they really are, just as sailors do. They don't try to change the winds or the sea but ensure that they are always ready to adapt themselves to conditions. In a flat calm they use the oars; with a following breeze they hoist full sail; in a head wind they shorten sail or heave to. Adapt yourself to circumstances in the same way."
>
> Bion of Borysthenes, quoted in [Kindstrand and Blomqvist, 1979].

Appendix A
Maps

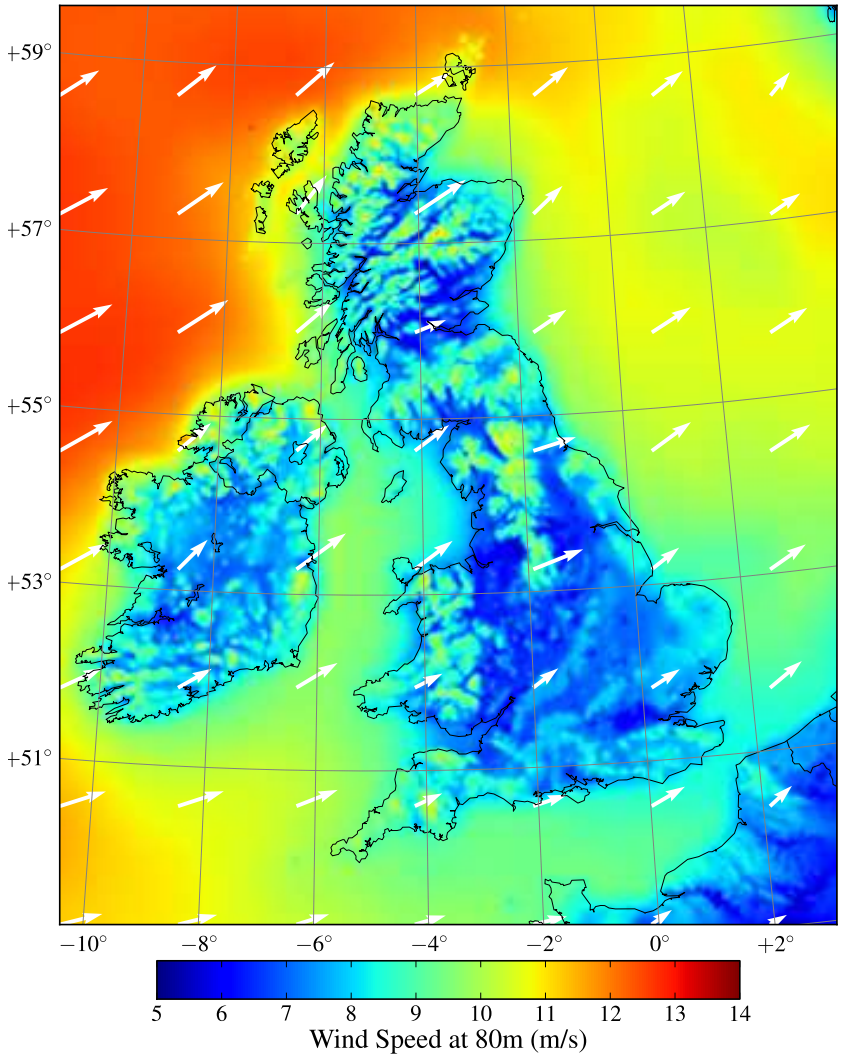

Figure A.1: Average wind speed at 80m agl, 2000-2010

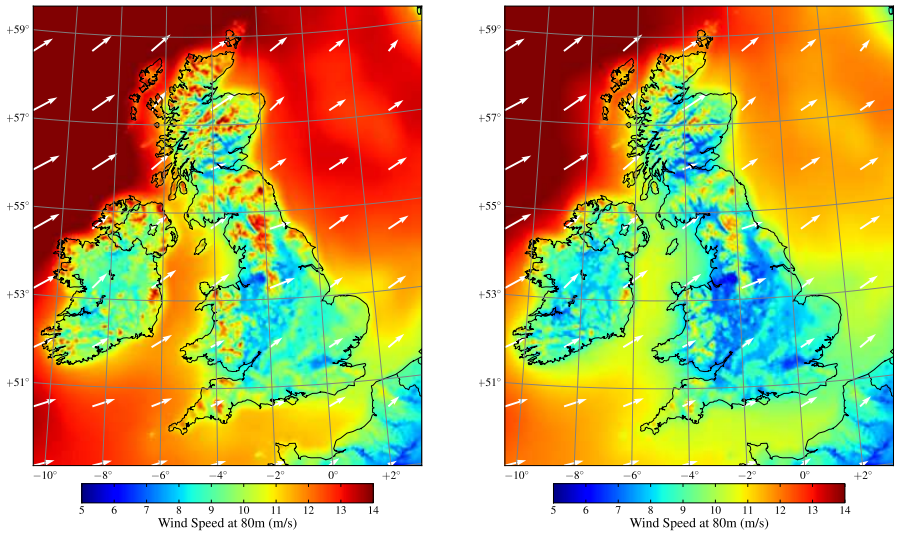

(a) Jan

(b) Feb

(c) Mar

(d) Apr

Figure A.2: Wind speed at 80m agl by month

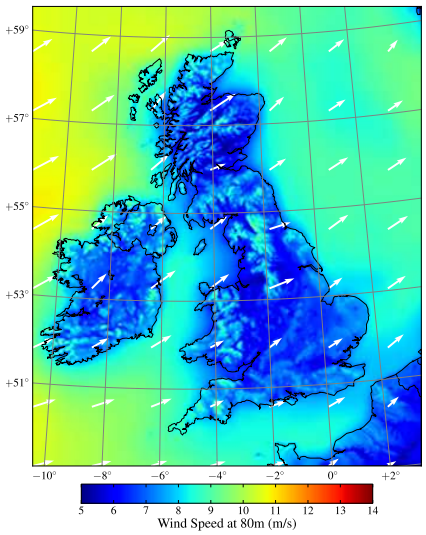

(e) May

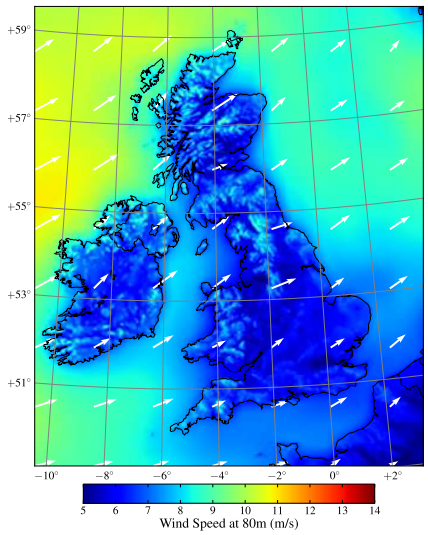

(f) Jun

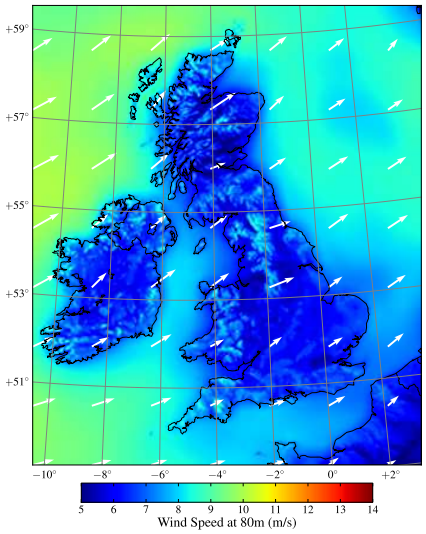

(g) Jul

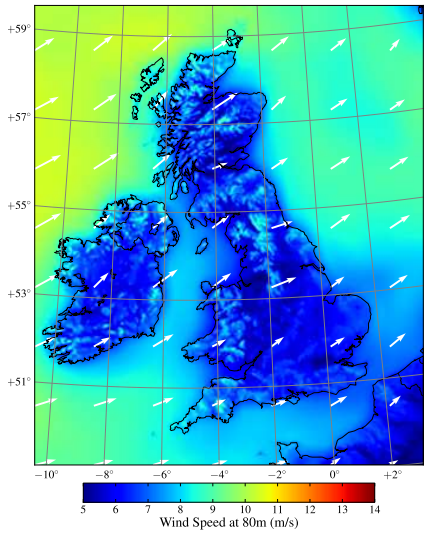

(h) Aug

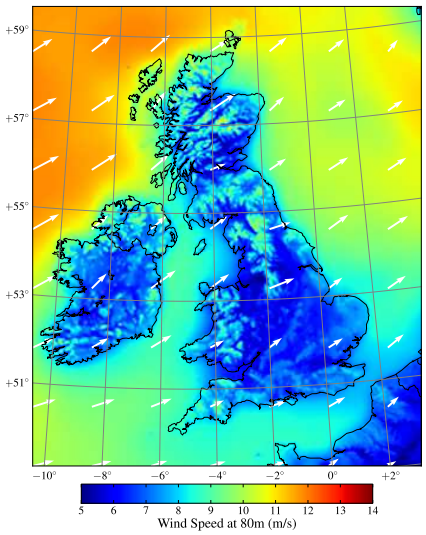

(i) Sep

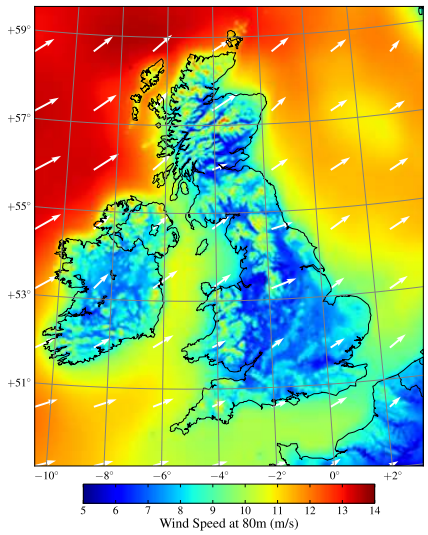

(j) Oct

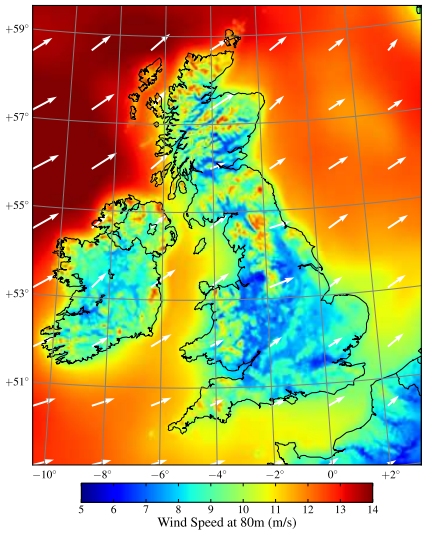

(k) Nov

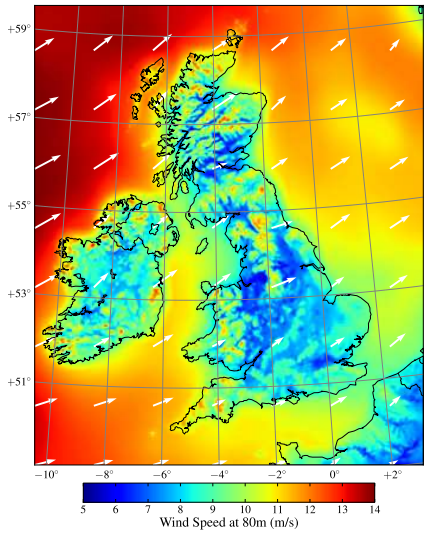

(l) Dec

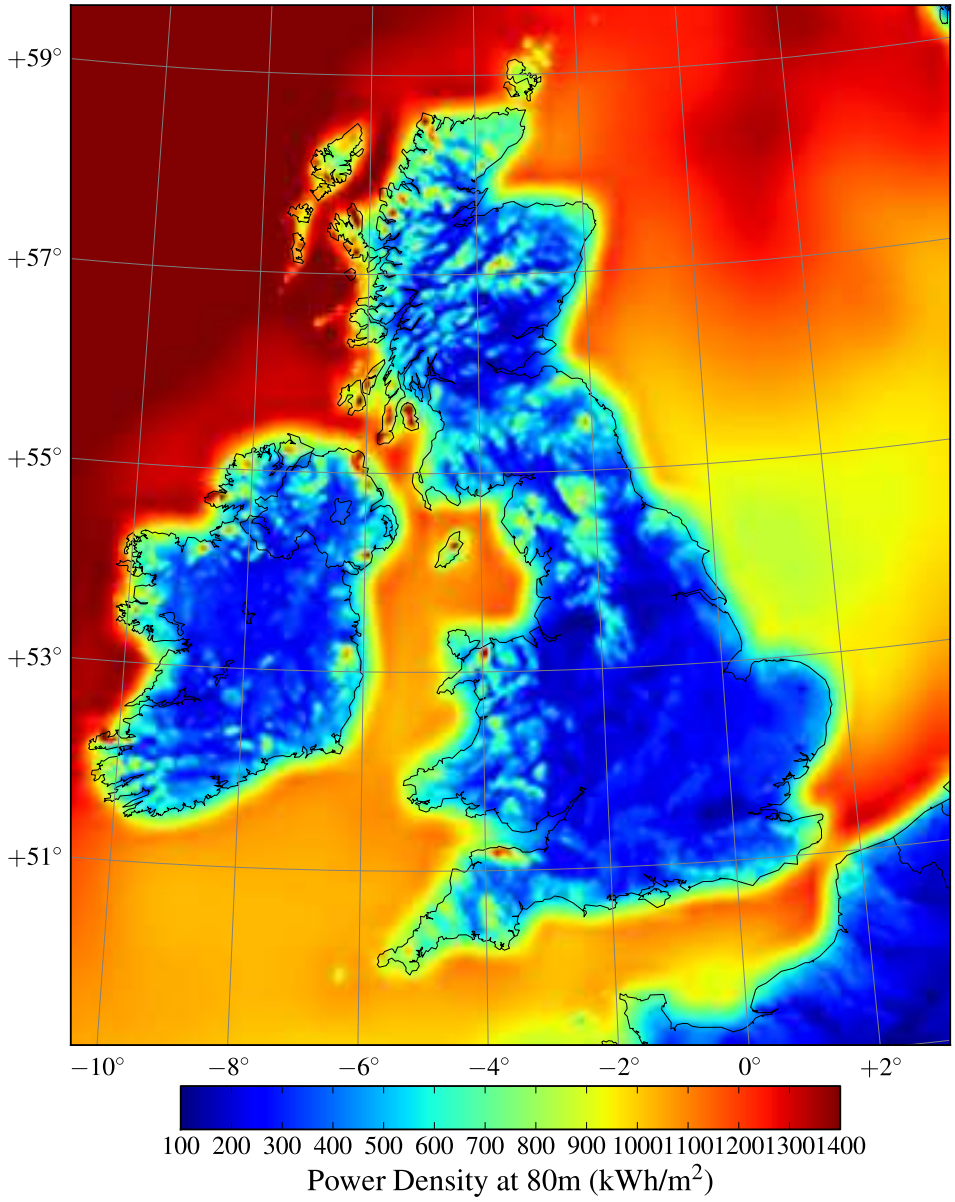

Figure A.1: Average power density at 80m agl, 2000-2010

Appendix B
WRF Options

```
&domains
 time_step                = 135,
 time_step_fract_num      = 0,
 time_step_fract_den      = 1,
 max_dom                  = 3,
 s_we                     = 1,       1,    1,
 e_we                     = 145,   196,  331,
 s_sn                     = 1,       1,    1,
 e_sn                     = 115,    81,  391,
 s_vert                   = 1,       1,    1,
 e_vert                   = 27,     27,   27,
 num_metgrid_levels       = 27,
 num_metgrid_soil_levels  = 2,
 dx                       = 27000, 9000, 3000,
 dy                       = 27000, 9000, 3000,
 grid_id                  = 1,        2,    3,
 parent_id                = 0,        1,    2,
 i_parent_start           = 1,       42,   50,
 j_parent_start           = 1,       28,   20,
 parent_grid_ratio        = 1,        3,    3,
 parent_time_step_ratio   = 1,        3,    3,
 feedback                 = 1,
 smooth_option            = 0,
 eta_levels = 1.0, 0.9950, 0.990,    0.985, 0.960,
     0.93275,   0.908,     0.8547878,0.804364,
     0.7539393, 0.7035151, 0.635023, 0.5527188,
     0.4785737, 0.411915,  0.3521141,0.2985896,
     0.250710,  0.2082415, 0.1704494,0.136992,
     0.1074684, 0.08151028,0.0587756,0.03894893,
     0.02173894,0.0/

&physics
 mp_physics          = 2,     2,     2,
 ra_lw_physics       = 1,     1,     1,
 ra_sw_physics       = 1,     1,     1,
 radt                = 30,    30,    30,
 sf_sfclay_physics   = 2,     2,     2,
 sf_surface_physics  = 2,     2,     2,
 bl_pbl_physics      = 2,     2,     2,
 bldt                = 0,     0,     0,
 sst_update          = 1,
 cu_physics          = 1,     1,     0,
 cudt                = 5,     5,     5,
 isfflx              = 1,
 ifsnow              = 0,
 icloud              = 1,
 surface_input_source  = 1,
 num_soil_layers       = 4,
 num_land_cat        = 20,
 sf_urban_physics    = 0,
 mp_zero_out         = 0,
 maxiens             = 1,
 maxens              = 3,
 maxens2             = 3,
 maxens3             = 16,
 ensdim              = 144,/

&fdda
 grid_fdda             = 1,     1,     1,
 gfdda_inname          = "wrffdda_d<domain>",
 gfdda_end_h           = 8760,   8760,   8760,
 gfdda_interval_m      = 360,   360,   360,
 fgdt                  = 0,     0,     0,
 if_no_pbl_nudging_uv  = 0,     0,     0,
 if_no_pbl_nudging_t   = 0,     0,     0,
 if_no_pbl_nudging_q   = 0,     0,     0,
 if_zfac_uv            = 0,     0,     0,
 k_zfac_uv             = 10,   10,     10,
 if_zfac_t             = 0,     0,     0,
 k_zfac_t              = 10,   10,     10,
 if_zfac_q             = 0,     0,     0,
 k_zfac_q              = 10,   10,     10,
 guv                   = 0.0003,  0.0003, 0.0003,
 gt                    = 0.0003,  0.0003, 0.0003,
 gq                    = 0.0003,  0.0003, 0.0003,
 if_ramping            = 1,
 dtramp_min            = 60.0,
 io_form_gfdda         = 2,/

&dynamics
 w_damping             = 0,
 diff_opt              = 1,
 km_opt                = 4,
 diff_6th_opt          = 0,
 diff_6th_factor       = 0.12,
 damp_opt              = 0,
 base_temp             = 290.
 zdamp                 = 5000.,  5000.,  5000.,
 dampcoef              = 0.01,   0.01,   0.01
 khdif                 = 0,      0,      0,
 kvdif                 = 0,      0,      0,
 non_hydrostatic       = .true., .true., .true.,
 moist_adv_opt         = 1,      1,      1,
 scalar_adv_opt        = 1,      1,      1,
 tke_adv_opt           = 1,      1,      1,/

&bdy_control
 spec_bdy_width        = 5,
 spec_zone             = 1,
 relax_zone            = 4,
 specified             = .true., .false.,.false.,
 nested                = .false., .true., .true.,/

&namelist_quilt
 nio_tasks_per_group = 0,
 nio_groups = 1,/
```

Table B.1: Namelist.input file specifying configuration options

Variable	Description
BN2	brunt-vaisala frequency
COSALPHA	Local cosine of map rotation
HGT	Terrain Height
LANDMASK	land mask (1 for land, 0 for water)
P	perturbation pressure
PB	base state pressure
PBLH	pbl height
PH	perturbation geopotential
PHB	base-state geopotential
PSFC	sfc pressure
Q2	QV at 2 M
QVAPOR	Water vapor mixing ratio
RMOL	1./Monin Ob. Length
SINALPHA	Local sine of map rotation
SST	sea surface temperature
T	perturbation potential temperature (theta-t0)
T2	2m temperature
TH2	2m potential temperature
TKE	turbulence kinetic energy
TKE_MYJ	tke from mellor-yamada-janjic
TSK	surface skin temperature
U	x-wind component
U10	U at 10 M
UST	u* in similarity theory
V	y-wind component
V10	V at 10 M
W	z-wind component
XLAT	latitude, south is negative
XLONG	longitude, west is negative
XTIME	minutes since simulation start
Z0	background roughness length
ZNT	time-varying roughness length

Table B.2: Variables retained in the output from WRF

	Speed U (ms^{-1})	Interval $\frac{U-\text{cut-in}}{\text{cut-in}-\text{cut-out}}$	Adjustment
	1	-	1
	2	-	1
	3	-	1
cut-in	4	0.00	1
	5	0.05	1
	6	0.10	1
	7	0.14	0.99
	8	0.19	0.98
	9	0.24	0.97
	10	0.29	0.95
	11	0.33	0.93
	12	0.38	0.91
	13	0.43	0.91
	14	0.48	0.94
	15	0.52	0.96
	16	0.57	0.98
	17	0.62	0.99
	18	0.67	0.99
	19	0.71	1
	20	0.76	1
	21	0.81	1
	22	0.86	1
	23	0.9	1
	24	0.95	1
cut-out	25	1.00	1

Table B.3: Per-unit adjustments to a turbine power curve with a cut-in speed of 4 $ms^{-1}$and rated speed of 15ms^{-1}

Appendix C
Station verification

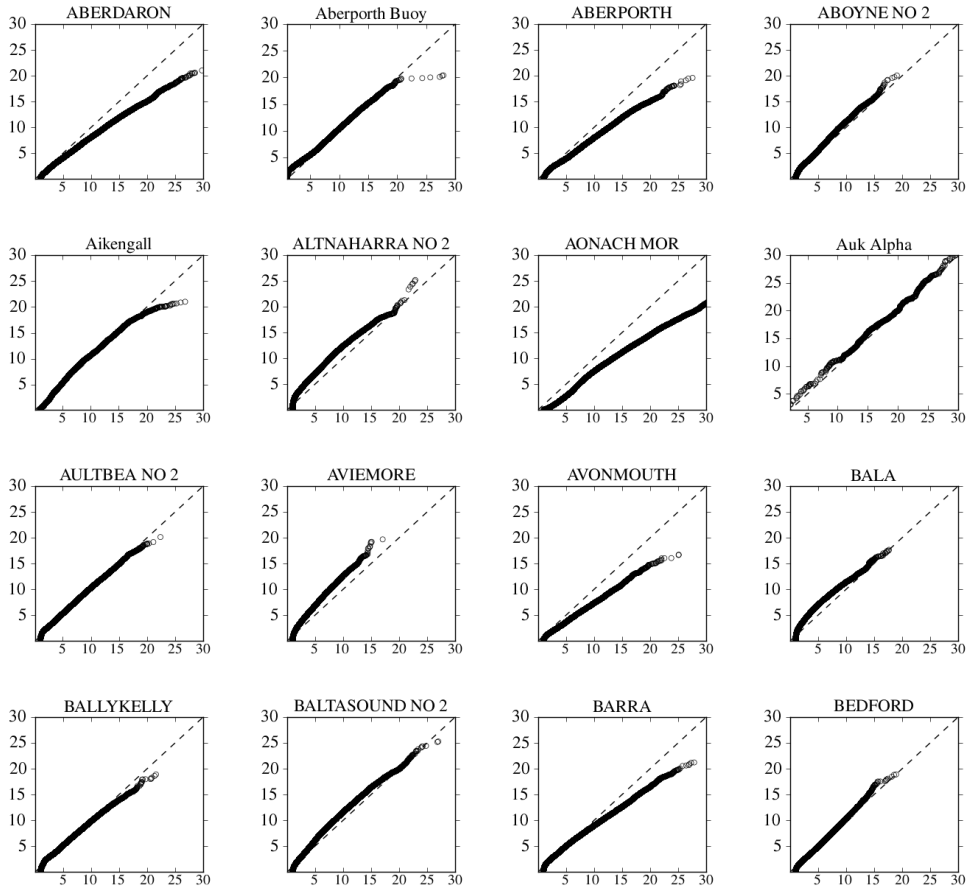

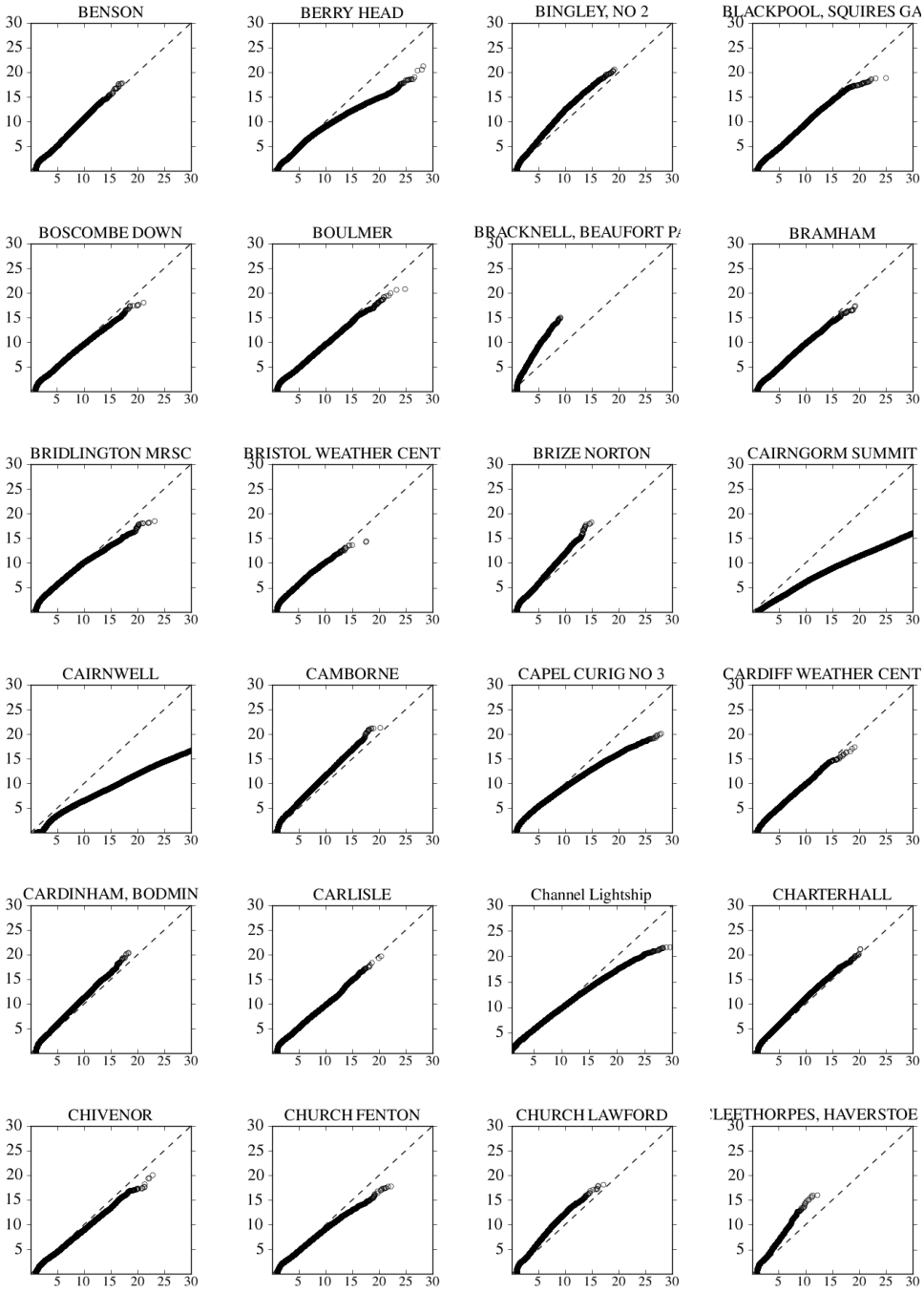
BENSON
BERRY HEAD
BINGLEY, NO 2
BLACKPOOL, SQUIRES GA
BOSCOMBE DOWN
BOULMER
BRACKNELL, BEAUFORT P
BRAMHAM
BRIDLINGTON MRSC
BRISTOL WEATHER CENT
BRIZE NORTON
CAIRNGORM SUMMIT
CAIRNWELL
CAMBORNE
CAPEL CURIG NO 3
CARDIFF WEATHER CENT
CARDINHAM, BODMIN
CARLISLE
Channel Lightship
CHARTERHALL
CHIVENOR
CHURCH FENTON
CHURCH LAWFORD
LEETHORPES, HAVERSTOE
30
25
20
15
10
5
5 10 15 20 25 30

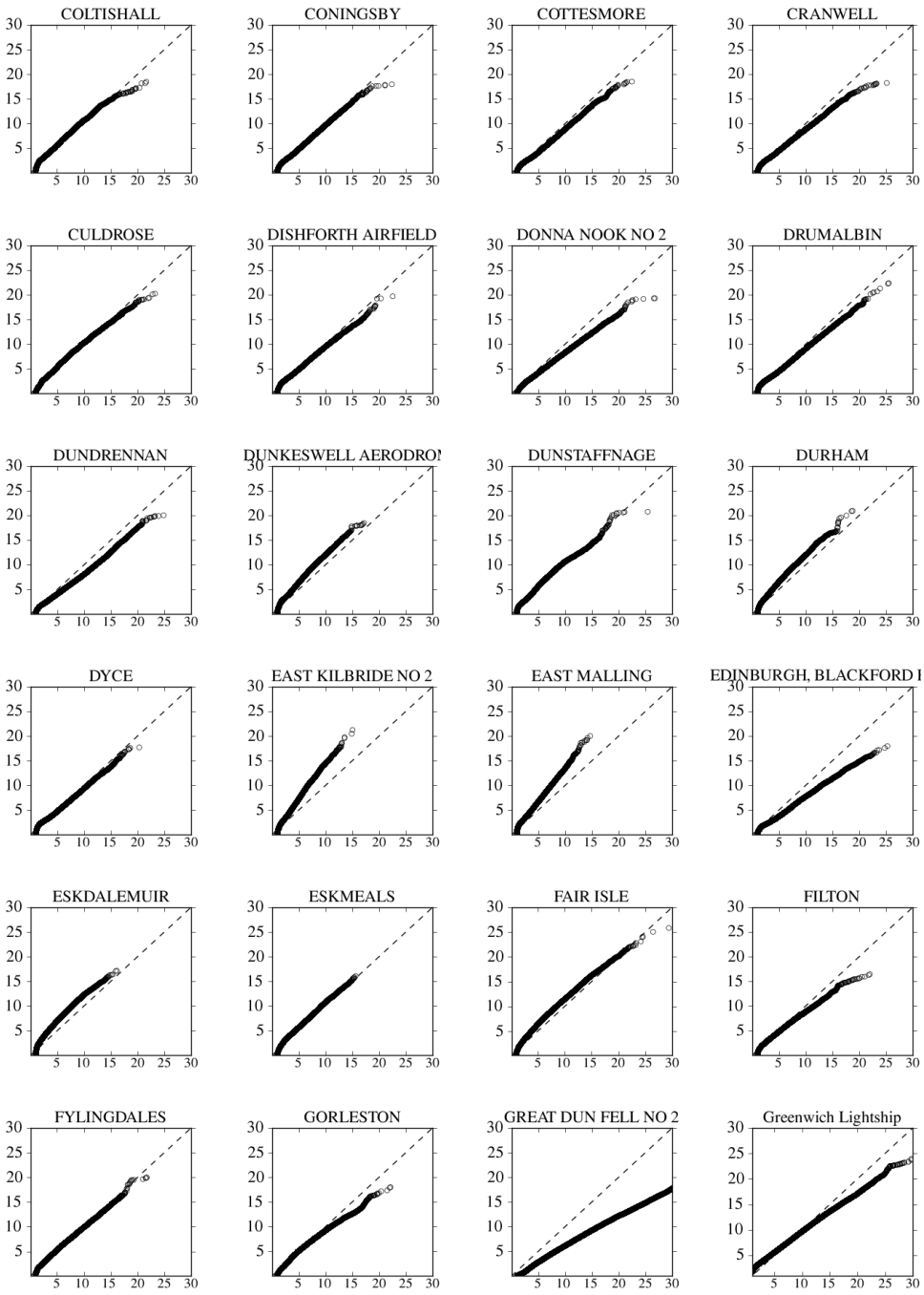
COLTISHALL
CONINGSBY
COTTESMORE
CRANWELL
CULDROSE
DISHFORTH AIRFIELD
DONNA NOOK NO 2
DRUMALBIN
DUNDRENNAN
DUNKESWELL AERODRO
DUNSTAFFNAGE
DURHAM
DYCE
EAST KILBRIDE NO 2
EAST MALLING
EDINBURGH, BLACKFORD I
ESKDALEMUIR
ESKMEALS
FAIR ISLE
FILTON
FYLINGDALES
GORLESTON
GREAT DUN FELL NO 2
Greenwich Lightship

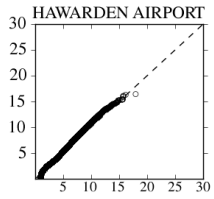
HAWARDEN AIRPORT

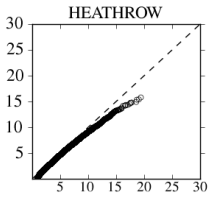
HEATHROW

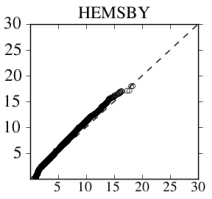
HEMSBY

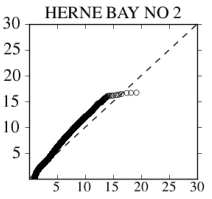
HERNE BAY NO 2

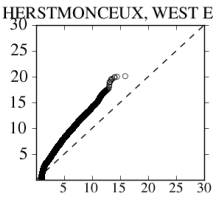
HERSTMONCEUX, WEST E

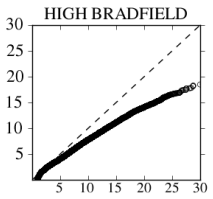
HIGH BRADFIELD

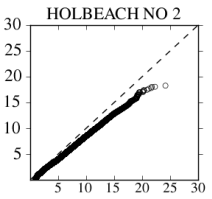
HOLBEACH NO 2

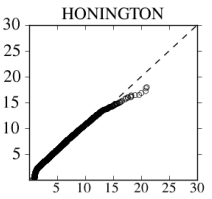
HONINGTON

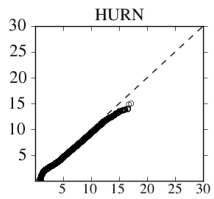
HURN

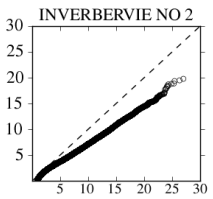
INVERBERVIE NO 2

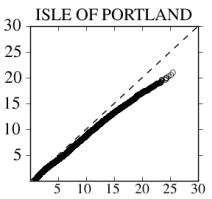
ISLE OF PORTLAND

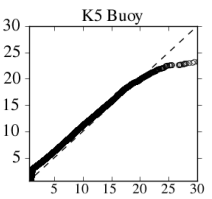
K5 Buoy

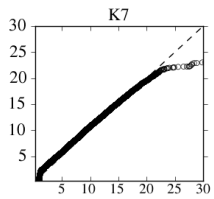
K7

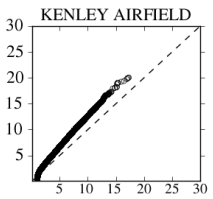
KENLEY AIRFIELD

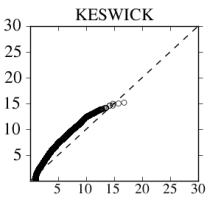
KESWICK

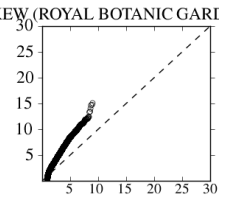
EW (ROYAL BOTANIC GARI

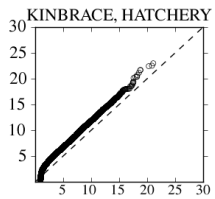
KINBRACE, HATCHERY

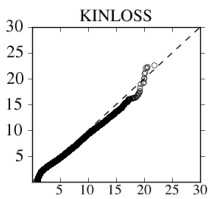
KINLOSS

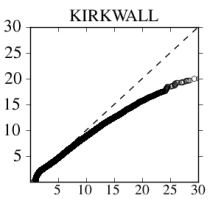
KIRKWALL

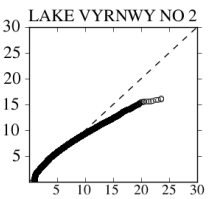
LAKE VYRNWY NO 2

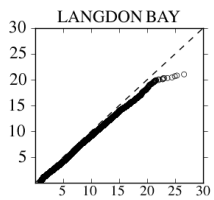
LANGDON BAY

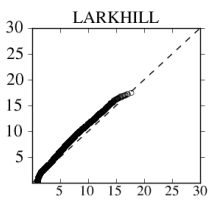
LARKHILL

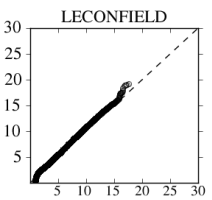
LECONFIELD

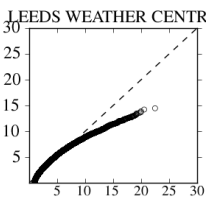
LEEDS WEATHER CENTR

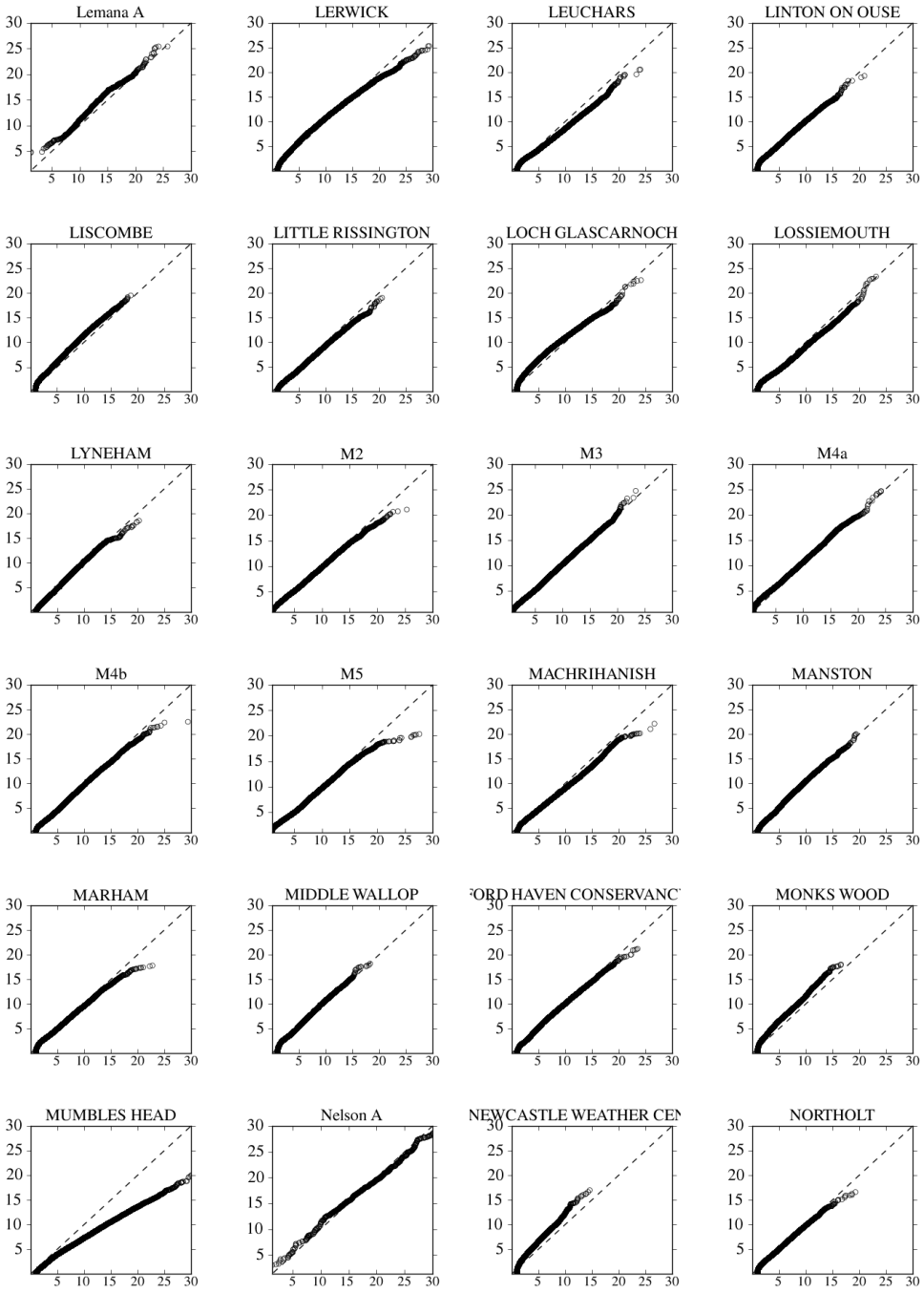
Lemana A
LERWICK
LEUCHARS
LINTON ON OUSE
LISCOMBE
LITTLE RISSINGTON
LOCH GLASCARNOCH
LOSSIEMOUTH
LYNEHAM
M2
M3
M4a
M4b
M5
MACHRIHANISH
MANSTON
MARHAM
MIDDLE WALLOP
ORD HAVEN CONSERVANC
MONKS WOOD
MUMBLES HEAD
Nelson A
NEWCASTLE WEATHER CEN
NORTHOLT

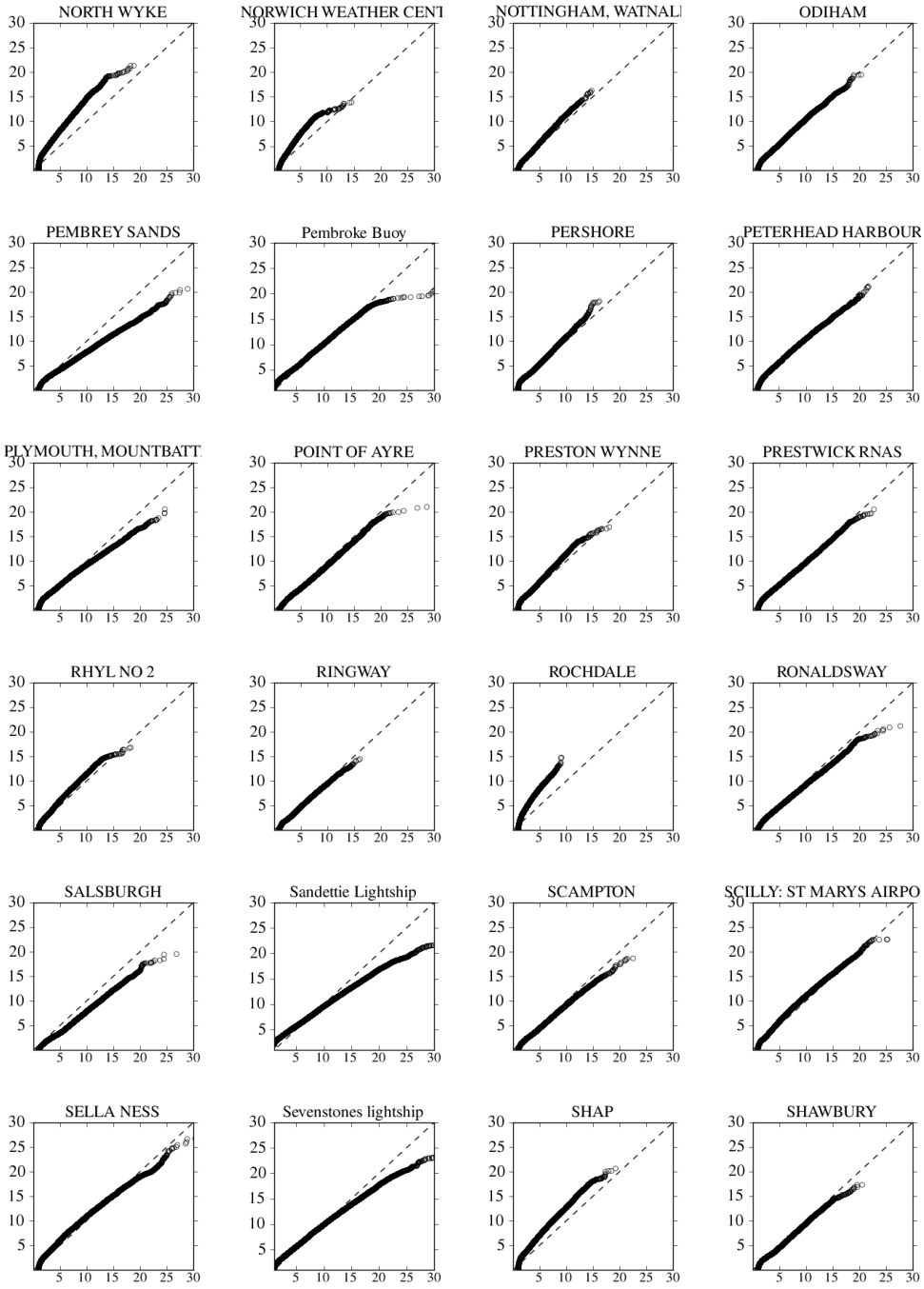
NORTH WYKE
NORWICH WEATHER CENT
NOTTINGHAM, WATNALL
ODIHAM
PEMBREY SANDS
Pembroke Buoy
PERSHORE
PETERHEAD HARBOUR
PLYMOUTH, MOUNTBATT
POINT OF AYRE
PRESTON WYNNE
PRESTWICK RNAS
RHYL NO 2
RINGWAY
ROCHDALE
RONALDSWAY
SALSBURGH
Sandettie Lightship
SCAMPTON
SCILLY: ST MARYS AIRPO
SELLA NESS
Sevenstones lightship
SHAP
SHAWBURY

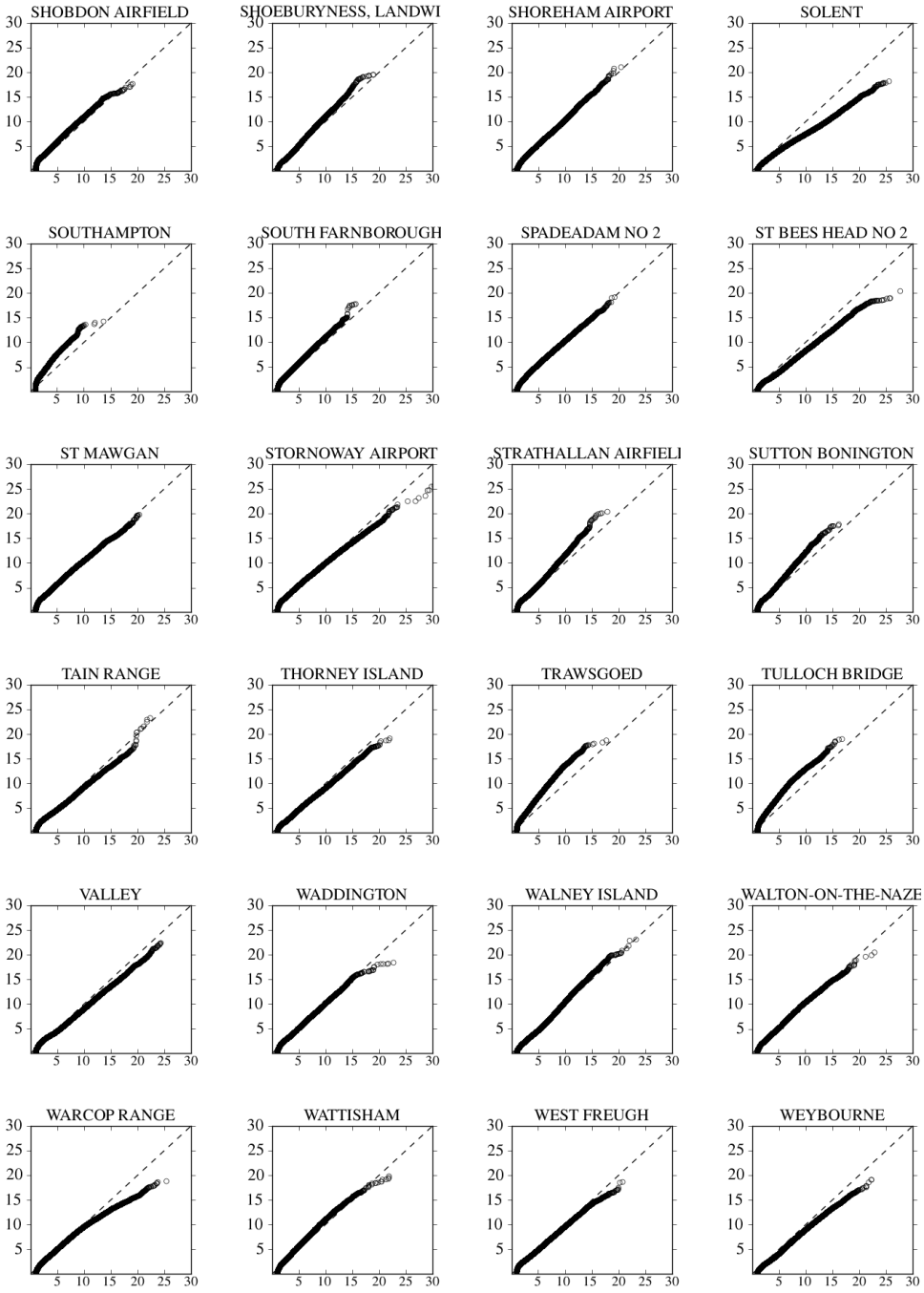
SHOBDON AIRFIELD
SHOEBURYNESS, LANDWI
SHOREHAM AIRPORT
SOLENT
SOUTHAMPTON
SOUTH FARNBOROUGH
SPADEADAM NO 2
ST BEES HEAD NO 2
ST MAWGAN
STORNOWAY AIRPORT
STRATHALLAN AIRFIELI
SUTTON BONINGTON
TAIN RANGE
THORNEY ISLAND
TRAWSGOED
TULLOCH BRIDGE
VALLEY
WADDINGTON
WALNEY ISLAND
WALTON-ON-THE-NAZE
WARCOP RANGE
WATTISHAM
WEST FREUGH
WEYBOURNE

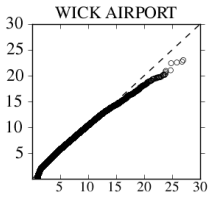
WICK AIRPORT
30
25
20
15
10
5
5 10 15 20 25 30

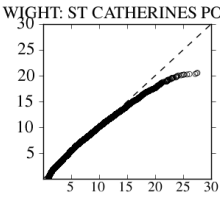
WIGHT: ST CATHERINES PC
30
25
20
15
10
5
5 10 15 20 25 30

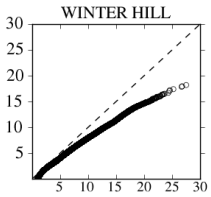
WINTER HILL
30
25
20
15
10
5
5 10 15 20 25 30

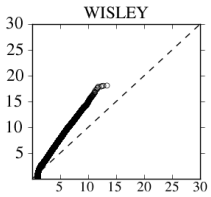
WISLEY
30
25
20
15
10
5
5 10 15 20 25 30

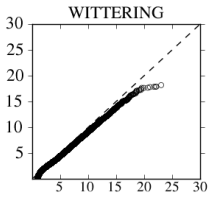
WITTERING
30
25
20
15
10
5
5 10 15 20 25 30

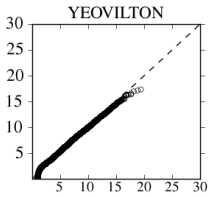
YEOVILTON
30
25
20
15
10
5
5 10 15 20 25 30

References

Adrian, G. (1999). Parallel processing in regional climatology: The parallel version of the Karslruhe Atmospheric Mesoscale Model. *Parallel Computing*, 25(7):777–787.

Adrian, G. and Fiedler, F. (1991). Simulation of unstationary wind and temperature fields over complex terrain and comparison with observations. *Beiträge zur Physik der Atmosphäre*, 64:27–48.

AMS (2000). *Glossary of meteorology*. Allen Press, 2nd (onlin edition. ISBN 9781878220349.

Andreas, E. L., Claffey, K. J., Jordan, R. E., Fairall, C. W., Guest, P. S., Persson, P., and A.A., G. (2006). Evaluations of the von Karman constant in the atmospheric surface layer. *Journal of Fluid Mechanics*, 559:117–149.

Anthes, R. A. and Warner, T. T. (1978). Development of hydrodynamic models suitable for air-pollution and other mesometeorological studies. *Monthly Weather Review*, 106(8):1045–1078.

Ayotte, K. (2008). Computational modelling for wind energy assessment. *Journal of Wind Engineering and Industrial Aerodynamics*, 96(10-11):1571–1590. ISSN 01676105. doi:10.1016/j.jweia.2008.02.002.

Babin, S. and Thompson, D. (2000). Effects of atmospheric boundary layer moisture on friction velocity with implications for SAR imagery. *IEEE Transactions on Geoscience and Remote Sensing*, 38(1):618–621.

BADC (2006). MIDAS Land Surface Stations Data (1853-curent). , British Atmospheric Data Centre.

Barthelmie, R. J. (1999). The effects of atmospheric stability on coastal wind climates. *Meteorological Applications*, 6(1):39–47. ISSN 13504827. doi:10.1017/S1350482799000961.

Barthelmie, R. J. and Pryor, S. C. (2003). Can satellite sampling of offshore wind speeds realistically represent wind speed distributions? *Journal of Applied Meteorology*, 42(1):83–94.

Barthelmie, R. J., Rathmann, O., Frandsen, S. T., Hansen, K. S., Politis, E., Prospathopoulos, J., Rados, K., Cabezón, D., Schlez, W., Phillips, J., Neubert, A., Schepers, J. G., and Pijl, S. P. V. D. (2007). Modelling and measurements of wakes in large wind farms. *Journal of Physics: Conference Series*, 75:012049. ISSN 1742-6596. doi:10.1088/1742-6596/75/1/012049.

Barthelmie, R. J., Sempreviva, A. M., and Pryor, S. C. (2009). Influences of humidity fluxes on offshore wind speed profiles. *Annales Geophysicae*, 28:1043–1052.

Beaucage, P., Glazer, A., Choisnard, J., Yu, W., Bernier, M., Benoit, R., and Lafrance, G. (2007). Wind assessment in a coastal environment using synthetic aperture radar satellite imagery and a numerical weather prediction model. *Canadian Journal of Remote Sensing*, 33(5):368–377. ISSN 1712-7971. doi:10.5589/m07-043.

Beljaars, A. C. M. and Holtslag, A. A. M. (1991). Flux parameterization over land surfaces for atmospheric models. *Journal of Applied Meteorology*, 30(3):327–341. ISSN 0894-8763. doi:10.1175/1520-0450(1991)030⟨0327:FPOLSF⟩2.0.CO;2.

Benoit, R., Binder, P., Schär, C., Chamberland, S., and H (2002). High-performance modelling for the Mesoscale Alpine Programme (MAP) field experiment. *High Performance Computing Systems and Applications*, pp. 301–312.

Benoit, R., Desgagné, M., Pellerin, P., Pellerin, S., Chartier, Y., and Desjardins, S. (1997). The Canadian MC2: A semi-lagrangian, semi-implicit wideband atmospheric model suited for finescale process studies and simulation. *Monthly Weather Review*, 125(10):2382. ISSN 0027-0644. doi:10.1175/1520-0493(1997)125⟨2382:TCMASL⟩2.0.CO;2.

Bentamy, a., Croize-Fillon, D., and Perigaud, C. (2008). Characterization of ASCAT measurements based on buoy and QuikSCAT wind vector observations. *Ocean Science*, 4(4):265–274. ISSN 1812-0792. doi:10.5194/os-4-265-2008.

Bentamy, A. and Fillon, D. C. (2011). Daily ASCAT surface wind fields. , L'Institut Français de Recherche pour l'Exploitation de la Mer.

Berge, E. and Bredesen, R. E. (2007). Combining WAsP with the WRF meso-scale model. Evaluation of wind resource asessment for three Norwegian wind farm areas. , Presentation to WRF users worskhop.

Berge, E., Byrkjedal, O., Ydersbond, Y., Kindler, D., and Kjeller Vindteknikk, A. (2009). Modelling of offshore wind resources. Comparison of a meso-scale model and measurements from FINO 1 and North Sea oil rigs. In *Proceedings of the European Wind Energy Conference*, pp. 1–8.

BERR (2008). Meeting the energy challenge: a white paper on nuclear power. January, Department for Business, Enterprise and Regulatory Reform.

Bianco, L. (2008). Surface layer parameterization in WRF. , Presentation at the ATOC 7500 Mesoscale Modelling Conference.

Bitsuamlak, G., Stathopoulos, T., and Bedard, C. (2004). Numerical evaluation of wind flow over complex terrain: Review. *Journal of Aerospace Engineering*, 17(4):135–145. doi:10.1061/(ASCE)0893-1321(2004)17.

Black, T. L. (1994). The New NMC Mesoscale Eta Model: Description and Forecast Examples. *Weather and Forecasting*, 9(2):265–278. ISSN 0882-8156. doi:10.1175/1520-0434(1994)009⟨0265:TNNMEM⟩2.0.CO;2.

Boehme, T. (2006). *Matching renewable electricity generation with demand in Scotland*. Ph.D. thesis, University of Edinburgh.

Boehme, T., Taylor, J., Wallace, R. A., and Bialek, J. (2006). Matching Renewable Energy Generation With Demand. , Technical Report for the Scottish Executive, Edinburgh.

Boehme, T. and Wallace, R. (2008). Hindcasting hourly wind power across Scotland based on met station data. *Wind Energy*, 11(3):233–244.

Bowen, A. J. and Mortensen, N. G. (1996). Exploring the limitations of WAsP The Wind Atlas and Application Program. In Larsen G C (Ed.), *European Wind Energy Conference*. RisøNational Laboratory, Gotenburg Sweden.

Bowen, A. J. and Mortensen, N. G. (2004). WAsP prediction errors due to site orography. , Risø, Roskilde, Denmark.

Brayshaw, D. J., Troccoli, A., Fordham, R., and Methven, J. (2011). The impact of large scale atmospheric circulation patterns on wind power generation and its potential predictability: A case study over the UK. *Renewable Energy*, 36(8):2087–2096. ISSN 09601481. doi:10.1016/j.renene.2011.01.025.

Brower, M. (2010). Development of eastern regional wind resource and wind plant output datasets. December 2009, Report for the National Renewable Energy Laboratory, New York.

Brower, M., Zack, J., Bailey, B. H., Schwartz, M., and Elliott, D. (2004). Mesoscale modeling as a tool for wind resource assessment and mapping. In *14th Conf. Applied Climatology, Boston, MA*, p. 4.2. AMS, Seattle, Wash.

Brown, R. (1981). On the use of exchange coefficients in modelling turbulent flow. *Boundary-Layer Meteorology*, 20:111–116.

Brown, S., Boorman, P., McDonald, R., and Murphy, J. (2009). Interpretation for use of surface wind speed projections from the 11-member Met Office regional climate model ensemble. , UK Climate Change Impacts Programme.

Brugge, R. (2011). British Isles Weather Diary. , University fof Reading, online weather diary.

Bukovsky, M. S. and Karoly, D. J. (2009). Precipitation Simulations Using WRF as a nested regional climate model. *Journal of Applied Meteorology and Climatology*, 48(10):2152–2159. ISSN 1558-8424. doi:10.1175/2009JAMC2186.1.

Burton, T., Jenkins, N., Sharpe, D., and Bossanyi, E. (2011). *Wind Energy Handbook*. John Wiley and Sons. ISBN 0470699752.

Businger, J. A. (1988). A note on the Businger-Dyer profiles. *Boundary-Layer Meteorology*, 42(1-2):145–151. ISSN 0006-8314. doi:10.1007/BF00119880.

Businger, J. A., Wyngaard, J., Izumi, Y., and Bradley, E. (1971). Flux-profile relationships in the atmospheric surface layer. *Journal of Atmospheric Sciences*, 28:181–189. ISSN 0022-4928.

Butchart, N., Charlton-Perez, A. J., Cionni, I., Hardiman, S. C., Haynes, P. H., Krüger, K., Kushner, P. J., Newman, P. A., Osprey, S. M., Perlwitz, J., Sigmond, M., Wang, L., Akiyoshi, H., Austin, J., Bekki, S., Baumgaertner, A., Braesicke, P., Brühl, C., Chipperfield, M., Dameris, M., Dhomse, S., Eyring, V., Garcia, R., Garny, H., Jöckel, P., Lamarque, J., Marchand, M., Michou, M., Morgenstern, O., Nakamura, T., Pawson, S., Plummer, D.,

Pyle, J., Rozanov, E., Scinocca, J., Shepherd, T. G., Shibata, K., Smale, D., Teyssèdre, H., Tian, W., Waugh, D., and Yamashita, Y. (2011). Multimodel climate and variability of the stratosphere. *Journal of Geophysical Research*, 116(D5):1–21. ISSN 0148-0227. doi:10.1029/2010JD014995.

Canziani, P. O. and Legnani, W. E. (2003). Tropospherictratospheric coupling: Extratropical synoptic systems in the lower stratosphere. *Quarterly Journal of the Royal Meteorological Society*, 129(592):2315–2329. ISSN 1477870X. doi:10.1256/qj.01.109.

Capon, R. A. (2003). Wind speed-up in the Dover Straits with the Met Office New Dynamics Model. *Meteorological Applications*, 10(3):229–237. ISSN 13504827. doi:10.1017/S1350482703003037.

Capps, S. B. and Zender, C. S. (2010). Estimated global ocean wind power potential from QuikSCAT observations, accounting for turbine characteristics and siting. *Journal of Geophysical Research*, 115(D9):1–13. ISSN 0148-0227. doi:10.1029/2009JD012679.

Cardone, V., Cox, A., and Swail, V. (1999). Evaluation of NCEP reanalysis surface marine wind fields for ocean wave hindcasts. In *Proc. WMO Workshop on Advances in Marine Climatology (CLIMAR99)*, pp. 8–15.

Castro, F. A., Palma, J. M. L. M., and Silva Lopes, A. (2003). Simulation of the Askervein flow. Part 1: Reynolds averaged Navier-Stokes equations (k-epsilon turbulence model). *Boundary-Layer Meteorology*, 107:501–530.

Cermak, J., Davenport, A., Plate, E. J., and Viegas, D. (1995). *Wind climate in cities*. Kluwer Academic Publishers. ISBN 0792332024 9780792332022.

Chandrasekar, A., Russell Philbrick, C., Doddridge, B., Clark, R., and Georgopoulos, P. (2003). A comparison study of RAMS simulations with aircraft, wind profiler, lidar, tethered balloon and RASS data over Philadelphia during a 1999 summer episode. *Atmospheric Environment*, 37(35):4973–4984. ISSN 13522310. doi:10.1016/j.atmosenv.2003.08.030.

Chang, T. P. (2010). Performance comparison of six numerical methods in estimating Weibull parameters for wind energy application. *Applied Energy*. ISSN 03062619. doi:10.1016/j.apenergy.2010.06.018.

Charnock, H. (1955). Wind stress on a water surface. *Quarterly Journal of the Royal Meteorological Society*, 81(350):639–640. ISSN 1477870X. doi:10.1002/qj.49708135027.

Chechkin, A., Metzler, R., Klafter, J., and Gonchar, V. (2008). Introduction to the Theory of Lévy Flights. In Rainer, K., Radons, G., and Sokolov, I. M. (Eds.), *Anomalous Transport: Foundations and Applications*, chapter 5. Wiley-VCH Verlag GmbH & Co. KGaA, Weinheim, Germany, 1 edition. ISBN 9783527622979. doi:10.1002/9783527622979.

Chelton, D. B., Freilich, M., Sienkiewicz, J., and Von Ahn, J. (2006). On the use of QuikSCAT scatterometer measurements of surface winds for marine weather prediction. *Monthly weather review*, 134(8):2055–2071. ISSN 0027-0644. doi:10.1175/MWR3179.1.

Chen, F. and Dudhia, J. (2000). Coupling an advanced land durfacehydrology model with the Penn StateNCAR MM5 modeling system. Part I: model implementation and sensitivity. *Monthly Weather Review*, 129:569–585.

Christiansen, M., Koch, W., and Horstmann, J. (2006). Wind resource assessment from C-band SAR. *Remote sensing of Environment*, 105(1):68–81.

Costa, J. C. L. D., Castro, F. A., Palma, J., and Stuart, P. (2006). Computer simulation of atmospheric flows over real forests for wind energy resource evaluation. *Journal of Wind Engineering and Industrial Aerodynamics*, 94(8):603–620.

Cotton, W. R., Pielke, R. A., Walko, R. L., Liston, G. E., Tremback, C. J., Jiang, H., McAnelly, R. L., Harrington, J. Y., Nicholls, M. E., Carrio, G. G., and McFadden, J. P. (2003). RAMS 2001: Current status and future directions. *Meteorology and Atmospheric Physics*, 82(1):5–29.

Cradden, L. (2009). *The Impact of Climate Change on Wind Energy Generation in the UK*. Phd thesis, Edinburgh University.

Crochet, P. (2004). Adaptive Kalman filtering of 2-metre temperature and 10-metre wind-speed forecasts in Iceland. *Meteorological Applications*, 11(2):173–187. ISSN 1350-4827. doi:10.1017/S1350482704001252.

Crown Estate (2010). Towards Round 3 : Building the Offshore Wind Supply Chain.

Davenport, A. G. (1960). Rationale for determining wind design velocities. *American Society of Civil Engineering*, 86:39–68.

Davenport, A. G., Grimmond, C. S. B., Oke, T. R., and Wieringa, J. (2000). Estimating the roughness of cities and sheltered country. In *12th AMS Conf. on Applied Climatology*, pp. 96–99. Asheville.

DECC (2009). The UK renewable energy strategy. , Department for Energy and Climate Change.

DECC (2010). Digest of UK Energy Statistics. , Department for Energy and Climate Change.

DECC (2011a). Planning our electric future: A white paper for secure, affordable and low-carbon electricity. 1, UK Government. doi:10.1161/CIR.0b013e3182456d46.

DECC (2011b). UK Energy in Brief 2011.

DECC (2011c). Updated energy and emissions projections. October, Department for Energy and Climate Change.

Delle Monache, L., Nipen, T., Liu, Y., Roux, G., and Stull, R. (2011). Kalman filter and analog schemes to post-process numerical weather predictions. *Monthly Weather Review*, p. 110318133207035. ISSN 0027-0644. doi:10.1175/2011MWR3653.1.

Delle Monache, L., Wilczak, J., Mckeen, S., Grell, G., Pagowski, M., Peckham, S., Stull, R., Mchenry, J., and Mcqueen, J. (2008). A Kalman-filter bias correction method applied to deterministic, ensemble averaged and probabilistic forecasts of surface ozone. *Tellus B*, 60(2):238–249. ISSN 0280-6509. doi:10.1111/j.1600-0889.2007.00332.x.

Dobschinski, J., Wessel, A., Lange, B., and Bremen, L. V. (2007). Reduction of wind power induced reserve requirements by advanced shortest-term forecasts and prediction intervals. In *Presentation to the Bremen Workshop on Wind Integration*. Bremen.

Donald Ahrens, C. (2008). *Essentials of meteorology: an invitation to the atmosphere*. Cengage Learning. ISBN 0495115584.

Douglas, D. J. F., Gasoriek, D. J. M., Swaffield, P. J., and Jack, L. (2005). *Fluid Mechanics*. Prentice Hall; 5 edition. ISBN 0131292935.

Doyle, J., Jiang, Q., and Chao, Y. (2009). High-resolution real-time modeling of the marine atmospheric boundary layer in support of the AOSN-II field campaign. *Deep Sea Research Part II: Topical*.

Dragoon, K. (2010). *Valuing Wind Generation on Integrated Power Systems*. Elsevier, 1st edition. ISBN 9780815520474. doi:10.1016/B978-0-8155-2047-4.10002-X.

Drennan, W. M., Taylor, P. K., and Yelland, M. J. (2005). Parameterizing the sea surface roughness. *Journal of Physical Oceanography*, 35(5):835–848. ISSN 0022-3670. doi:10.1175/JPO2704.1.

Driesnaar, T. (2011). HIRLAM Newsletter 58. , HIRLAM Technical Newslettters.

DTI (2003). Offshore Wind Capital Grant Scheme. , Department for Trade and Industry.

DTI (2004). Atlas of UK Renewable Marine Renewable Energy Resources: Technical Report.

Dudhia, J. (1989). Numerical study of convection observed during the winter monsoon experiment using a mesoscale two-dimensional model. *Journal of the Atmospheric Sciences*, 46(20):3077–3107. doi:doi:10.1175/1520-0469(1989)046⟨3077:NSOCOD⟩2.0.CO;2.

Dudhia, J. (2010). WRF Physics Options. , Presentation to the WRF user tutorial.

Dutton, J. A. (1976). *The ceaseless wind : an introduction to the theory of atmospheric motion*. McGraw-Hill, New York. ISBN 0070184070.

Dyer, A. J. (1974). A review of flux-profile relationships. *Boundary-Layer Meteorology*, 7(3):363–372. ISSN 0006-8314. doi:10.1007/BF00240838.

Ek, M. B., Mitchell, K. E., Lin, Y., Rogers, E., Grunmann, P., Koren, V., Gayno, G., and Tarpley, J. D. (2003). Implementation of Noah land surface model advances in the National Centers for Environmental Prediction operational mesoscale Eta model. *Journal of Geophysical Research*, 108(D22):1–16. ISSN 0148-0227. doi:10.1029/2002JD003296.

Ela, E. and Kemper, J. (2009). Wind Plant Ramping Behavior. NREL Technical Report. December, National Renewable Energy Laboratory.

Elexon (2011). Balancing Mechanism Reporting System (BMRS) under the The New Electricity Trading Arrangements. , BMRS reporting website.

España, G., Aubrun, S., Loyer, S., and Devinant, P. (2012). Wind tunnel study of the wake meandering downstream of a modelled wind turbine as an effect of large scale turbulent eddies. *Journal of Wind Engineering and Industrial Aerodynamics*, 101:24–33. ISSN 01676105. doi:10.1016/j.jweia.2011.10.011.

Esteban, M., Leary, D., Zhang, Q., Utama, A., Tezuka, T., and Ishihara, K. N. (2011). Job retention in the British offshore sector through greening of the North Sea energy industry. *Energy Policy*, 39(3):1543–1551. ISSN 03014215. doi:10.1016/j.enpol.2010.12.028.

European Environment Agency (2000). CORINE Land Cover 2000 Dataset.

Fangohr, S., Woolf, D. K., Jeffery, C. D., and Robinson, I. S. (2008). Calculating long-term global air-sea flux of carbon dioxide using scatterometer, passive microwave, and model reanalysis wind data. *Journal of Geophysical Research*, 113(C9):1–14. ISSN 0148-0227. doi:10.1029/2005JC003376.

Farr, T. G., Rosen, P. A., Caro, E., Crippen, R., Duren, R., Hensley, S., Kobrick, M., Paller, M., Rodriguez, E., Roth, L., Seal, D., Shaffer, S., Shimada, J., Umland, J., Werner, M., Oskin, M., Burbank, D., and Alsdorf, D. (2007). The shuttle radar topography mission. *Reviews of geophysics*, 45(RG2004):1–33. doi:10.1029/2005RG000183.

Foley, A. M., Leahy, P. G., Marvuglia, A., and McKeogh, E. J. (2012). Current methods and advances in forecasting of wind power generation. *Renewable Energy*, 37(1):1–8. ISSN 09601481. doi:10.1016/j.renene.2011.05.033.

Foreman, R. J. and Emeis, S. (2010). Revisiting the definition of the drag coefficient in the marine atmospheric boundary layer. *Journal of Physical Oceanography*, 40(10):2325–2332. ISSN 0022-3670. doi:10.1175/2010JPO4420.1.

Frank, H. P., Rathmann, O., Mortensen, N. G., and Landberg, L. (2001). The Numerical Wind Atlas: the KAMM/WASP Method.

Frey-Buness, F., Heimann, D., and Sausen, R. (1995). A statistical-dynamical downscaling procedure for global climate simulations. *Theoretical and Applied Climatology*, 50(3-4):117–131. ISSN 0177-798X. doi:10.1007/BF00866111.

Friedl, M. (2002). Global land cover mapping from MODIS: algorithms and early results. *Remote Sensing of Environment*, 83(1-2):287–302. ISSN 00344257. doi:10.1016/S0034-4257(02)00078-0.

Fuentes, U. (1998). Statistisch-dynamische Regionalisierung auf der Basis einer Klassifikation synoptischer Entwicklungen.

Fuentes, U. and Heimann, D. (2000). An improved statistical-dynamical downscaling scheme and its application to the alpine precipitation climatology. *Theoretical and Applied Climatology*, 65(3-4):119–135.

Gallus, W. A. (2000). The impact of step orography on flow in the Eta model: two contrasting examples. *Weather and Forecasting*, 15(5):630–639. ISSN 0882-8156. doi:10.1175/1520-0434(2000)015⟨0630:TIOSOO⟩2.0.CO;2.

Garrad Hassan (2003). Economies of scale , engineering resource and load factors.

Garratt, J. R. and Pielke, R. A. (1989). On the sensitivity of mesoscale models to surface-layer parameterization constants. *Boundary-Layer Meteorology*, 48(4):377–387. ISSN 0006-8314. doi:10.1007/BF00123060.

Gel, Y. and Raftery, A. (2004). Combining global and local grid-based bias correction for mesoscale numerical weather prediction models. In *Proceedings of the 17th Conference on Probaility and Statistics in the Atmospheric Sciences*, number 206 in Probability and Statistics in the Atmospheric Sciences, pp. 1–31. Washington.

Gerber, E. P. and Vallis, G. K. (2009). On the Zonal Structure of the North Atlantic Oscillation and Annular Modes. *Journal of the Atmospheric Sciences*, 66(2):332–352. ISSN 0022-4928. doi:10.1175/2008JAS2682.1.

Giebel, G. (2010). The State-Of-The-Art in Short-Term Prediction of Wind Power: A literature overview. , Riso DTU.

Giebel, G., Badger, J., Louka, P., Kallos, G., Lac, C., Descombes, G., Palomares, A.-M., and Perez, I. M. (2002). Project ANEMOS: Description of NWP, Mesoscale and CFD models. , Project Anemos.

Giebel, G. and Kariniotakis, G. (2003). The state-of-the-art in short-term forecasting of wind power: a literature overview. , Project Anemos.

Giebel, G., Kariniotakis, G., Pinson, P., Siebert, N., and Barthelmie, R. J. (2003). The state of the art in short-term prediction of wind power-from an offshore perspective. , RisøNational Laboratory.

Gilhousen, D. B. (2006). A complete explanation of why moored buoy winds are less than ship winds. *Mariners Weather Log*, 50(1).

Girard, C., Benoit, R., and Desgagné, M. (2005). Finescale Topography and the MC2 Dynamics Kernel. *Monthly Weather Review*, 133(6):1463–1477. ISSN 0027-0644. doi:10.1175/MWR2931.1.

Giri, C., Zhu, Z., and Reed, B. (2005). A comparative analysis of the Global Land Cover 2000 and MODIS land cover data sets. *Remote Sensing of Environment*, 94(1):123–132. ISSN 00344257. doi:10.1016/j.rse.2004.09.005.

Glazer, A. and Yu, W. (2005). Numerical wind energy atlas for Canada. *Geophysical Research Abstracts*, 7(05185).

Golder, D. (1972). Relations among stability parameters in the surface layer. *Boundary-Layer Meteorology*, 3(1):47–58. ISSN 0006-8314. doi:10.1007/BF00769106.

Gottschall, J. and Peinke, J. (2008). How to improve the estimation of power curves for wind turbines. *Environmental Research Letters*, 3(1):015005. ISSN 1748-9326. doi:10.1088/1748-9326/3/1/015005.

Gross, R. and Heptonstall, P. (2008). The costs and impacts of intermittency: An ongoing debate “East is East, and West is West, and never the twain shall meet”. *Energy Policy*, 36(10):4005–4007. ISSN 03014215. doi:10.1016/j.enpol.2008.06.013.

Gryning, S.-E., Batchvarova, E., Brümmer, B., Jørgensen, H., and Larsen, S. (2007). On the extension of the wind profile over homogeneous terrain beyond the surface boundary layer. *Boundary-Layer Meteorology*, 124(2):251–268. ISSN 0006-8314. doi:10.1007/s10546-007-9166-9.

Hamill, T. (2010). Survey of ensemble post-processing techniques. , Technical Report by the NOAA Earth System Research Lab.

Hamill, T. M., Hagedorn, R., and Whitaker, J. S. (2008). Probabilistic forecast calibration using ECMWF and GFS ensemble reforecasts. Part II: precipitation. *Monthly Weather Review*, 136(7):2620–2632. ISSN 0027-0644. doi:10.1175/2007MWR2411.1.

Hamilton, J. (2008). HIRLAM Use of the Hirlam NWP Model at Met Éireann. , Technical Report for Met Éireann.

Harman, K., Walker, R., and Wilkinson, M. (2008). Availability trends observed at operational wind farms. In *European Wind Energy Conference*, April, pp. 1–8.

Hart, K. a., Steenburgh, W. J., Onton, D. J., and Siffert, A. J. (2004). An Evaluation of mesoscale-model-based Model Output Statistics (MOS) during the 2002 Olympic and Paralympic winter games. *Weather and Forecasting*, 19(2):200–218. ISSN 0882-8156. doi:10.1175/1520-0434(2004)019⟨0200:AEOMMO⟩2.0.CO;2.

Hasager, C. B., Frank, H. P., and Furevik, B. R. (2002). On offshore wind energy mapping using satellite SAR. *Canadian Journal of Remote Sensing*, 28(1):80–89.

Hawkins, S., Eager, D., and Harrison, G. (2011). Characterising the reliability of production from future British offshore wind fleets. In *Proceedings of the 1st IET Renewable Power Generation Conference*. IET, Edinburgh.

Hayes, B., Ilie, I., Porpodas, A., and Djokic, S. (2010). Equivalent Power Curve Model of a Wind Farm Based on Field Measurement Data. In *Presentation to Supergen Networks Consortium*, pp. 1–7.

Heimann, D. (1986). Estimation of regional surface layer wind field characteristics using a three-layer mesoscale model. *Beitraege zur Physik der Atmosphaere*, 59:518–537.

Hersbach, H. (2011). Sea surface roughness and drag coefficient as functions of neutral wind speed. *Journal of Physical Oceanography*, 41(1):247–251. ISSN 0022-3670. doi:10.1175/2010JPO4567.1.

Hicks, B. B. (1976). Wind profile relationships from the wangara experiment. *Quarterly Journal of the Royal Meteorological Society*, 102(433):535–551. ISSN 00359009. doi:10.1002/qj.49710243304.

Hisscott, A. (2007). When NWP met climatology: storms over the Isle of Man during January 2005. *Weather*, 62(3):74–77. ISSN 00431656. doi:10.1002/wea.36.

Höglund, A., Meier, H. M., Broman, B., and Kriezi, E. (2009). Validation and correction of regionalised ERA-40 wind fields over the Baltic Sea using the Rossby Centre Atmosphere model . , Swedish Meteorological and Hydrological Institute, Norrkoping.

Hogrefe, C., Rao, S. T., Kasibhatla, P., Kallos, G., Tremback, C. J., Hao, W., Olerud, D., Xiu, A., and Mchenry, J. (2001). Evaluating the performance of regional-scale photochemical modeling systems : Part I - meteorological predictions. *Atmospheric Environment*, 35:4159–4174.

Hogstrom, U. (1988). Non-dimensional wind and temperature profiles in the atmospheric surface layer: A re-evaluation. *Boundary-Layer Meteorology*, 42(1-2):55–78. ISSN 0006-8314. doi:10.1007/BF00119875.

Högström, U., Sahlee, E., Drennan, W., and KK (2008). Momentum fluxes and wind gradients in the marine boundary layer– a multi-platform study. *Boreal Environment*, 6095(December):475–502.

Holton, J. R. (2004). *An introduction to dynamic meteorology*. Academic Press, 4 edition.

Holttinen, H. (2005). Hourly wind power variations in the Nordic countries. *Wind Energy*, 8(2):173–195. ISSN 1095-4244. doi:10.1002/we.144.

Hong, S.-Y., Dudhia, J., and Chen, S.-H. (2004). A revised approach to ice microphysical processes for the bulk parameterization of clouds and precipitation. *Monthly Weather Review*, 132(1):103–120. ISSN 0027-0644. doi:10.1175/1520-0493(2004)132⟨0103:ARATIM⟩2.0.CO;2.

Hong, S.-Y., Noh, Y., and Dudhia, J. (2006). A New Vertical Diffusion Package with an Explicit Treatment of Entrainment Processes. *Monthly Weather Review*, 134:2318–2341.

Hoskins, B. and Ambrizzi, T. (1993). Rossby wave propagation on a realistic longitudinally varying flow. *Journal of the Atmospheric Sciences*, 50(12):1661–1661.

Howard, T. and Clark, P. (2007). Correction and downscaling of NWP wind speed forecasts. *Meteorological Applications*, 14(2):105–116. ISSN 1469-8080. doi:10.1002/met.

Hsu, S. (1992). An overwater stability criterion for the offshore and coastal dispersion model. *Boundary-Layer Meteorology*, 60(4):397–402. ISSN 0006-8314.

Hsu, S., Blanchard, B., and Yan, Z. (2009). Bulk transfer relations for the roughness sublayer. *Boundary-Layer Meteorology*, 134(2):257–267. ISSN 0006-8314. doi:10.1007/s10546-009-9450-y.

Hu, X.-M., Nielsen-Gammon, J. W., and Zhang, F. (2010). Evaluation of three planetary boundary layer schemes in the WRF model. *Journal of Applied Meteorology and Climatology*, 49(9):1831–1844. ISSN 1558-8424. doi:10.1175/2010JAMC2432.1.

IEC (2009). Wind farm power performance testing. , International Electrotechnical Commission.

Ifremer (2002). QuickSCAT scatterometer mean wind field products user manual. February, Ifremer.

Ingleby, B. (2010). Factors affecting ship and buoy data quality: a data assimilation perspective. *Journal of Atmospheric and Oceanic Technology*, 27(9):1476–1489. ISSN 0739-0572. doi:10.1175/2010JTECHA1421.1.

Jackson, P. S. and Hunt, J. C. R. (1975). Turbulent wind flow over a low hill. *Quarterly Journal of the Royal Meteorological Society*, 101(430):929–955.

Janjic, Z. I. (1994). The step-mountain eta coordinate model: Further development of the convection, viscous sublayer and turbulence closure schemes. *Monthly Weather Review*, 122:927–945.

Janjic, Z. I. (1996). The surface layer in the NCEP Eta Model. In *Eleventh Conference on Numerical Weather Prediction*, pp. 354–355. Norfolk, VA.

Janjic, Z. I. (2002). Nonsingular implementation of the Mellor-Yamanda level 2.5 scheme in the NCEP global model. , NCEP Office Note, no 437.

Jiang, J. and Perrie, W. (2007). The Impacts of Climate Change on Autumn North Atlantic Midlatitude Cyclones. *Journal of Climate*, 20(7):1174–1187. ISSN 0894-8755. doi:10.1175/JCLI4058.1.

Jimenez, B. and Tambke, J. (2007). Offshore wind resource assessment with WAsP and MM5: comparative study for the German Bight. *Wind Energy*, 10(2):121–134.

Jin, J., Miller, N. L., and Schlegel, N. (2010). Sensitivity Study of Four Land Surface Schemes in the WRF Model. *Advances in Meteorology*, 2010:1–12. ISSN 1687-9309. doi:10.1155/2010/167436.

Jolliff, J. K., Kindle, J. C., Shulman, I., Penta, B., Friedrichs, M. A., Helber, R., and Arnone, R. A. (2009). Summary diagrams for coupled hydrodynamic-ecosystem model skill assessment. *Journal of Marine Systems*, 76(1-2):64–82. ISSN 09247963. doi:10.1016/j.jmarsys.2008.05.014.

JPL (2010). Cross-Calibrated , Multi-Platform Ocean Surface Wind Velocity Product (MEaSUREs Project). May, Jet Propulsion Laboratory.

Justice, C., Townshend, J., and Vermote, E. (2002). An overview of MODIS Land data processing and product status. *Remote Sensing of Environment*, 83:3 – 15.

Kain, J. S. (2004). The KainFritsch Convective Parameterization: An Update. *Journal of Applied Meteorology*, 43(1):170–181. ISSN 0894-8763. doi:10.1175/1520-0450(2004)043⟨0170:TKCPAU⟩2.0.CO;2.

Kaiser, K., Langreder, W., Hohlen, H., and Højstrup, J. (2007). Turbulence correction for power curves. *Wind Energy*, pp. 159–162.

Kallos, G. (1997). The regional weather forecasting system SKIRON. In *Proceedings of the Symposium on Regional Weather Prediction on Parallel Computer Environments*. Athens.

Kallos, G., Boukas, L., Mimikou, N., and N, M. (1998). The Skiron System: Parallelization of the Eta Model. In *8th ECMWF Workshop: Towards Terra Computing*.

Kallos, G. and Nickovic, S. (2001). A model for prediction of desrt dust cycle in the atmosphere. *Journal of Geophysical Research*, 106(16):113–118.

Kalnay, E., Kanamitsu, M., Kistler, R., Collins, W., Deaven, D., Gandin, L., Iredell, M., Saha, S., White, G., Woollen, J., Zhu, Y., Leetmaa, A., Reynolds, R., Chelliah, M., Ebisuzaki, W., Higgins, W., Janowiak, J., Mo, K. C., Ropelewski, C., Wang, J., Jenne, R., and Joseph, D. (1996). The NCEP/NCAR 40-Year Reanalysis Project. *Bulletin of the American Meteorological Society*, 77(3):437–471.

Kalthoff, N., Bischoff-Gauß, I., Fiedler, F., Thurauf, J., Kohler, M., Fiebig-Wittmaack, M., Novoa, E., Pizarro, C., Castillo, R., Gallardo, L., and Others (2002). Mesoscale wind regimes in Chile at 30 S. *Journal of Applied Meteorology*, 41(9):953–970.

Kamath, C. (2010). Understanding wind ramp events through analysis of historical data. In *IEE PES Transmission and Distribution Conference and Exposition*, pp. 1–6. IEEE, New Orleans.

Kara, A. (2008). Air-sea stability effects on the 10 m winds over the global ocean: Evaluations of air-sea flux algorithms. *Journal of Geophysical Research*, 113(C4):1–14. ISSN 0148-0227. doi:10.1029/2007JC004324.

Keane, A., Milligan, M., Dent, C. J., Hasche, B., D'Annunzio, C., Dragoon, K., Holttinen, H., Samaan, N., Soder, L., and O'Malley, M. (2011). Capacity Value of Wind Power. *IEEE Transactions on Power Systems*, 26(2):564–572. ISSN 0885-8950. doi:10.1109/TPWRS.2010.2062543.

Kim, D.-H., Lee, H.-W., and Lee, S.-H. (2010). Evaluation of wind resource using numerically optimized data in the southwestern Korean Peninsula. *Asia-Pacific Journal of Atmospheric Sciences*, 46(4):393–403. ISSN 1976-7633. doi:10.1007/s13143-010-0021-4.

Kindstrand, J. F. and Blomqvist, J. (1979). *Bion of Borysthenes: a collection of the fragments with introduction and commentary, Volumes 11-13*. Uppsala University, Uppsala. ISBN 9155404863.

Klein, W. H. and Glahn, H. R. (1974). Forecasting Local Weather by Means of Model Output Statistics. *Bulletin of the American Meteorological Society*, 55(10):1217–1227. ISSN 0003-0007. doi:10.1175/1520-0477(1974)055⟨1217:FLWBMO⟩2.0.CO;2.

Klemp, J. B., Dudhia, J., and Hassiotis, a. D. (2008a). An Upper Gravity-Wave Absorbing Layer for NWP Applications. *Monthly Weather Review*, 136(10):3987–4004. ISSN 0027-0644. doi:10.1175/2008MWR2596.1.

Klemp, J. B., Gill, D. O., Barker, D. M., Duda, M. G., Wang, W., and Powers, J. G. (2008b). A Description of the Advanced Research WRF Version 3.

Kok, K., Schreur, B. W., and Vogelezang, D. (2008). Valuing information from mesoscale forecasts. *Meteorological Applications*, 15(1):103–111. ISSN 13504827. doi:10.1002/met.54.

Kolstad, E. W. (2008). A QuikSCAT climatology of ocean surface winds in the Nordic seas: Identification of features and comparison with the NCEP/NCAR reanalysis. *Journal of Geophysical Research*, 113(D11):1–15. ISSN 0148-0227. doi:10.1029/2007JD008918.

Kong, F. (2002). An experimental simulation of a coastal fog-stratus case using COAMPS (tm) model. *Atmospheric research*.

Kristensen, L. (1998). Cup anemometer behavior in turbulent environments. *Journal of Atmospheric and Oceanic Technology*, 15(1969):5–17.

Landberg, L. (1999). Short-term prediction of the power production from wind farms. *Journal of Wind Engineering and Industrial Aerodynamics*, 80(1-2):207–220. ISSN 01676105. doi:10.1016/S0167-6105(98)00192-5.

Lange, B., Højstrup, J., Larsen, S., and Barthelmie, R. J. (2001). A fetch dependent model of sea surface roughness for offshore wind power utilisation. In *Proceeding of the European Wind Energy Conference*, 1, pp. 830–833. Citeseer.

Lange, B., Johnson, H. K., Larsen, S., Højstrup, J., Kofoed-Hansen, H., and Yelland, M. J. (2004). On Detection of a Wave Age Dependency for the Sea Surface Roughness. *Journal of Physical Oceanography*, 34(6):1441–1458. ISSN 0022-3670. doi:10.1175/1520-0485(2004)034⟨1441:ODOAWA⟩2.0.CO;2.

Lapworth, A. (2005). The diurnal variation of the marine surface wind in an offshore flow. *Quarterly Journal of the Royal Meteorological Society*, 131(610):2367–2387. ISSN 00359009. doi:10.1256/qj.04.161.

Large, W. G., Morzel, J., and Crawford, G. B. (1995). Accounting for Surface Wave Distortion of the Marine Wind Profile in Low-Level Ocean Storms Wind Measurements. *Journal of Physical Oceanography*, 25(11):2959–2971. ISSN 0022-3670. doi:10.1175/1520-0485(1995)025⟨2959:AFSWDO⟩2.0.CO;2.

Lazić, L., Pejanović, G., and Živković, M. (2010). Wind forecasts for wind power generation using the Eta model. *Renewable Energy*, 35(6):1236–1243. ISSN 09601481. doi:10.1016/j.renene.2009.10.028.

Legates, D. R. and McCabe, G. J. (1999). Evaluating the use of goodness-of-fit Measures in hydrologic and hydroclimatic model validation. *Water Resources Research*, 35(1):233. ISSN 0043-1397. doi:10.1029/1998WR900018.

Lei, M., Shiyan, L., Chuanwen, J., Hongling, L., and Yan, Z. (2009). A review on the forecasting of wind speed and generated power. *Renewable and Sustainable Energy Reviews*, 13(4):915–920. ISSN 13640321. doi:10.1016/j.rser.2008.02.002.

Lemelin, D., Surry, D., and Davenport, A. (1988). Simple approximations for wind speed-up over hills. *Journal of Wind Engineering and Industrial Aerodynamics*, 28(1-3):117–127. ISSN 01676105. doi:10.1016/0167-6105(88)90108-0.

Li, Y., Paik, K.-J., Xing, T., and Carrica, P. M. (2011). Dynamic overset CFD simulations of wind turbine aerodynamics. *Renewable Energy*, 37(1):298–285. ISSN 09601481. doi:10.1016/j.renene.2011.06.029.

Libonati, R., Trigo, I., and Dacamara, C. (2008). Correction of 2 m-temperature forecasts using Kalman Filtering technique. *Atmospheric Research*, 87(2):183–197. ISSN 01698095. doi:10.1016/j.atmosres.2007.08.006.

Liston, G. E. and Pielke, R. a. (2000). A Climate Version of the Regional Atmospheric Modeling System. *Theoretical and Applied Climatology*, 66(1-2):29–47. ISSN 0177-798X. doi:10.1007/s007040070031.

Liu, H., Olsson, P. Q., Volz, K. P., and Yi, H. (2006). A climatology of mesoscale model simulated low-level wind jets over Cook Inlet and Shelikof Strait, Alaska. *Estuarine, Coastal and Shelf Science*, 70(4):551–566. ISSN 02727714. doi:10.1016/j.ecss.2006.06.011.

Liu, W., Tang, W., (US), J. P. L., Aeronautics, U. S. N., and Administration, S. (1996). *Equivalent neutral wind*. National Aeronautics and Space Administration, Jet Propulsion Laboratory, California Institute of Technology.

Liu, Y., Warner, T., Liu, Y., Vincent, C., Wu, W., Mahoney, B., Swerdlin, S., Parks, K., and Boehnert, J. (2011). Simultaneous nested modeling from the synoptic scale to the LES scale for wind energy applications. *Journal of Wind Engineering and Industrial Aerodynamics*. ISSN 01676105. doi:10.1016/j.jweia.2011.01.013.

Lorenz, E. N. (2006). Reflections on the conception, birth, and childhood of numerical weather prediction. *Annual Review of Earth and Planetary Sciences*, 34:37–45.

Louka, P., Galanis, G., Siebert, N., Karinotakis, G., Katsafados, P., Pytharoulis, I., and Kallos, G. (2008). Improvements in wind speed forecasts for wind power prediction purposes using Kalman filtering. *Journal of Wind Engineering and Industrial Aerodynamics*, 96(12):2348–2362. ISSN 01676105. doi:10.1016/j.jweia.2008.03.013.

Loveland, T., Reed, B., Brown, J., Ohlen, D., Zhu, Z., Yang, L., and Merchant, J. (2000). Development of a global land cover characteristics database and IGBP DISCover from 1 km AVHRR data. *International Journal of Remote Sensing*, 21(6-7):1303–1330.

Lubitz, W. and White, B. (2007). Wind-tunnel and field investigation of the effect of local wind direction on speed-up over hills. *Journal of Wind Engineering and Industrial Aerodynamics*, 95(8):639–661. ISSN 01676105. doi:10.1016/j.jweia.2006.09.001.

Manwell, J. F., McGowan, J., and Rogers, A. (2002a). *Wind energy explained : theory, design and application*. Wiley, Chichester. ISBN 0471499722.

Manwell, J. F., Rogers, A. L., McGowan, J. G., and Bailey, B. H. (2002b). An offshore wind resource assessment study for New England. *Renewable Energy*, 27(2):175–187.

Martin, J. E. (2006). *Mid-latitude atmospheric dynamics: a first course*. Wiley, 1st edition. ISBN 0470864656.

Masoliver, J., Montero, M., and Porra, J. (2000). A dynamical model describing stock market price distributions. *Physica A: Statistical Mechanics and its Applications*, 283(3-4):559–567. ISSN 03784371. doi:10.1016/S0378-4371(00)00117-5.

Mass, C. F. (2003). IFPS and the Future of the National Weather Service. *Weather and Forecasting*, 18(1):75–79. ISSN 0882-8156. doi:10.1175/1520-0434(2003)018⟨0075:IATFOT⟩2.0.CO;2.

Mass, C. F. and Kuo, Y.-H. (1998). Regional Real-Time Numerical Weather Prediction: Current Status and Future Potential. *Bulletin of the American Meteorological Society*, 79(2):253–263.

Mass, C. F. and Ovens, D. (2011). Fixing WRFs High Speed Wind Bias: A New Subgrid Scale Drag Parameterization and the Role of Detailed Verification. In *Presentation to the WRF Users Workshop*.

Mclean, A. J. R. and Hassan, G. (2008). Equivalent Wind Power Curves. Report for the Trade Wind Project. October, Garrad Hassan.

Mellor, G. and Yamada, T. (1982). Development of a turbulence closure model for geophysical fluid problems. *Reviews of geophysics and space physics*, 20(4):851–875.

Mengelkamp, H. T. (1997). Statistical-dynamical downscaling of wind climatologies. *Journal of Wind Engineering and Industrial Aerodynamics*, 67-68:449–457. ISSN 01676105. doi:10.1016/S0167-6105(97)00093-7.

Mesinger, F., JANJIC, Z., and Nickovic, S. (1988). The step-mountain coordinate: Model description and performance for cases of Alpine lee cyclogenesis and for a case of an Appalachian development. *Monthly Weather Review*, 116(7):1493–1518.

Meteo France (2012). Papers in NWP specialised international journals with a reviewing commitee.

Milborrow, D. (2000). The real costs and problems of integrating wind. *Windpower Monthly*, pp. 5–9.

Mlawer, E. J., Taubman, S. J., Brown, P. D., Iacono, M. J., and Clough, S. A. (1997). Radiative transfer for inhomogeneous atmospheres: RRTM, a validated correlated-k model for the longwave. *Journal of Geophysical Research*, 102(D14):16663–16682. ISSN 0148-0227. doi:10.1029/97JD00237.

Monin, A. and Obukhov, A. (1954). Basic laws of turbulent mixing in the surface layer of the atmosphere. *Contrib. Geophys. Inst. Acad. Sci., USSR,(151)*, 24(151):163–187.

Mortensen, N. G., Larsen, S. E., and Troen, I. (1990). Response of neutral boundary layers to change of roughness, boundary layer meteorolog. *Boundary-Layer Meteorology*, 50(1988):205–225.

Murphy, A. (1988). Skill scores based on the mean square error and their relationships to the correlation coefficient. *Mon. Wea. Rev*, 116:2417–2424.

Murphy, J. M., Sexton, D. M. H., Jenkins, G. J., Booth, B. B. B., Brown, C. C., Clark, R. T., Collins, M., Harris, G. R., Kendon, E. J., Betts, R. A., Brown, S. J., Humphrey, K. A., McCarthy, M. P., McDonald, R. E., Stephens, A., Wallace, C., Warren, R., Wilby, R., and Wood, R. A. (2009). *UK Climate Projections Science Report: Climate Change Projections*. December. Meteorological Office Hadley Centre.

National Grid (2008). Round 3 Offshore Wind Farm Connection Study. , National Grid.

National Grid (2011). Distribution Network Operator (DNO) Companies.

NCAR (2008). *WRF ARW Version 3 Modelling System User's Guide*. Nartional Center for Atmospheric Research.

NCAR (2011). Real Time Weather Data.

NCEP (2008). User's Guide for the NMM Core of the Weather Research and Forecast (WRF) Modeling System Version 3.

NCEP (2010). U.S. National Centers for Environmental Prediction, updated daily: NCEP FNL Operational Model Global Tropospheric Analyses, continuing from July 1999. , National Center for Environmental Prediction, Published by the CISL Data Support Section at the National Center for Atmospheric Research, Boulder.

Neumann, K., Herold, M., Hartley, a., and Schmullius, C. (2007). Comparative assessment of CORINE2000 and GLC2000: Spatial analysis of land cover data for Europe. *International Journal of Applied Earth Observation and Geoinformation*, 9(4):425–437. ISSN 03032434. doi:10.1016/j.jag.2007.02.004.

Nielsen, H. A., Pinson, P., Nielsen, T. S., Christiansen, L., Madsen, N. H., Giebel, G., Badger, J., Guo Larsen, X., Ravn, H., Tøfting, J., and Others (2007). Intelligent wind power prediction systems: Final report. Fu 4101, Riso.

Nielsen, M., Astrup, P., Hasager, C., Barthelmie, R. J., and SC (2004). Satellite information for wind energy applications. *RisøNational Laboratory*.

Niewiadomski, M., Leung, D., and Benoit, R. (1999). Simulations of wind field and other meteorological parameters in the complex terrain of Hong Kong using MC2-a mesoscale numerical model. *Journal of Wind Engineering and Industrial Aerodynamics*, 83(1-3):71–82.

Nørgaard, P. (2004). A Model to Simulate the Aggregated Wind Power Time Series for an Area. In *European Wind Energy Conference*, 3.

NRL (2003). COAMPS Version 3 model description. *PU/7500-03-448, Marine*.

Ofgem (2010). Project Discovery - Options for delivering secure and sustainable energy supplies.

Oswald, J., Raine, M., and Ashrafball, H. (2008). Will British weather provide reliable electricity? *Energy Policy*, 36(8):3212–3225. ISSN 03014215. doi:10.1016/j.enpol.2008.04.033.

Paiva, L. M., Bodstein, G. C., and Menezes, W. F. (2009). Numerical simulation of atmospheric boundary layer flow over isolated and vegetated hills using RAMS. *Journal of Wind Engineering and Industrial Aerodynamics*, 97(9-10):439–454. ISSN 01676105. doi:10.1016/j.jweia.2009.07.006.

Panofsky, H. A. and Dutton, J. A. (1984). *Atmospheric Turbulence: Models and Methods for Engineering Applications*, volume p. Wiley. ISBN 0471057142.

Papadopoulos, A., Katsafados, P., Kallos, G., and Nickovic, S. (2001). The Weather Forecasting System for POSEIDON An Overview. *The Global Atmosphere and Ocean System*, 00(0):1–19.

Pasquill, F. (1974). *Atmospheric diffusion: the dispersion of windborne material from industrial* ... Wiley and Sons, New York.

Paulson, C. A. (1970). The Mathematical Representation of Wind Speed and Temperature Profiles in the Unstable Atmospheric Surface Layer. *Journal of Applied Meteorology*, 9(6):857–861. ISSN 0021-8952. doi:10.1175/1520-0450(1970)009⟨0857:TMROWS⟩2.0.CO;2.

Peña, A. and Gryning, S.-E. (2008). Charnock's Roughness Length Model and Non-dimensional Wind Profiles Over the Sea. *Boundary Layer Meteorology*, 128:191–203. ISSN q.

Peña, A., Gryning, S.-E., and Hasager, C. B. (2008). Measurements and Modelling of the Wind Speed Profile in the Marine Atmospheric Boundary Layer. *Boundary-Layer Meteorology*, 129(3):479–495. ISSN 0006-8314. doi:10.1007/s10546-008-9323-9.

Pearmine, R., Song, Y. H., Williams, T. G., and Chebbo, A. (2006). Identification of a loadfrequency characteristic for allocation of spinning reserves on the British electricity grid. *IEE Proceedings Generation Transmission and Distribution*, 153(6):633. ISSN 13502360. doi:10.1049/ip-gtd:20050404.

Pedersen, T. F. (2003). Development of a Classification System for Cup Anemometers - CLASSCUP. April, RisøNational Laboratory.

Petersen, C., Kmit, M., Nielsen, N. W., Amstrup, B., and Huess, V. (2005). Technical Report 05-13 Performance of DMI-HIRLAM-T15 and DMI-HIRLAM-S05 and the storm surge model in winter storms. , Danish Meterorological Institute.

Petersen, E. L., Mortensen, N. G., Landberg, L., Højstrup, J., and Frank, H. P. (1998). Wind power meteorology. Part I: climate and turbulence. *Wind Energy*, 1(1):2–22. ISSN 1095-4244. doi:10.1002/(SICI)1099-1824(199809)1:1⟨2::AID-WE15⟩3.0.CO;2-Y.

Pidwirny, M. and Jones, S. (2010). *Fundamentals of Physical Geography*. PhysicalGeography.net, 2nd edition.

Pilinis, C., Kassomenos, P., and Kallos, G. (1994). Modling of Photochemical Pollution in Athens, Greece. Application of the RAMS-CALGRID Modeling System. *Atmospheric Environment*, 27B(4):353–370.

Pinard, J., Benoit, R., and Yu, W. (2005). A WEST wind climate simulation of the mountainous Yukon. *Atmosphere-ocean*, 43(3):259–281.

Ploski, J. (2007). Implementing the WRF Model on the German Grid. *October*, pp. 1–22.

Potter, C. W., Lew, D., Mccaa, J., Cheng, S., Eichelberger, S., and Grimit, E. (2008). Creating the Dataset for the Western Wind by WIND ENGINEERING and Solar Integration Study. *Wind Engineering*, 32(4).

Poulos, G. S., Bossert, J. E., McKee, T. B., and Pielke, R. a. (2007). The Interaction of Katabatic Flow and Mountain Waves. Part II: Case Study Analysis and Conceptual Model. *Journal of the Atmospheric Sciences*, 64(6):1857–1879. ISSN 0022-4928. doi:10.1175/JAS3926.1.

Poyry (2008). IIMPLICATIONS OF THE UK MEETING ITS GET 2020 RENEWABLE ENERGY TARGET. August, Poyry Energy Consulting.

Poyry (2011). ANALYSING TECHNICAL CONSTRAINTS ON RENEWABLE GENERATION TO 2050: A report to the Committee on Climate Change. March, Poyry Energy Consulting.

Pryor, S. C. and Barthelmie, R. J. (2010). Climate change impacts on wind energy: A review. *Renewable and Sustainable Energy Reviews*, 14(1):430–437. ISSN 13640321. doi:10.1016/j.rser.2009.07.028.

PWC (2010). Meeting the 2020 renewable energy targets : Filling the offshore wind financing gap. , Pricewaterhouse Coopers.

Ramtharan, G., Ekanayake, J. B., and Jenkins, N. (2007). Support for Spinning Reserve from DFIG based wind turbines. *Power*, (August):8 – 11. doi:10.1109/ICIINFS.2007.4579158.

Rantamaki, M., Apohjola, M., Tisler, P., Bremer, P., Kukkonen, J., and Karppinen, a. (2005). Evaluation of two versions of the HIRLAM numerical weather prediction model during an air pollution episode in southern Finland. *Atmospheric Environment*, 39(15):2775–2786. ISSN 13522310. doi:10.1016/j.atmosenv.2004.12.050.

Reistad, M., Breivik, O. y., Haakenstad, H., Aarnes, O. J., Furevik, B. R., and Bidlot, J.-R. (2011). A high-resolution hindcast of wind and waves for the North Sea, the Norwegian Sea, and the Barents Sea. *Journal of Geophysical Research*, 116(C5):1–18. ISSN 0148-0227. doi:10.1029/2010JC006402.

Renewable UK (2011). UK Wind Energy Database (UKWED).

Renwewable UK (2010). UK Offshore Wind : Building an Industry. June, Renewable UK. Report by Douglas Westwood.

RPN (2011). AnemoScope.

Sampe, T. and Xie, S.-P. (2007). Mapping High Sea Winds from Space: A Global Climatology. *Bulletin of the American Meteorological Society*, 88(12):1965–1978. ISSN 0003-0007. doi:10.1175/BAMS-88-12-1965.

Schaudt, K. J. (1998). A New Method for Estimating Roughness Parameters and Evaluating the Quality of Observations. *Journal of Applied Meteorology*, 37(5):470–476. ISSN 0894-8763. doi:10.1175/1520-0450(1998)037⟨0470:ANMFER⟩2.0.CO;2.

Sertel, E. and Robock, A. (2010). Impacts of land cover data quality on regional climate simulations. *International Journal of Climatology*. doi:10.1002/joc.

Sexton, D. and Murphy, J. (2010). Probabilistic projections of wind speed. In *UKCP Users Community Workshop*. Met Office Hadley Centre, Birmingham,.

Sharan, M. (2009). Performance of various similarity functions for nondimensional wind and temperature profiles in the surface layer in stable conditions. *Atmospheric Research*, 94(2):246–253. ISSN 01698095. doi:10.1016/j.atmosres.2009.05.014.

Sharman, H., Leyland, B., and Livermore, M. (2011). Renewable Energy: Vision or Mirage, . , Adam Smith Institute, London.

Shen, B.-W., Atlas, R., Chern, J.-D., Reale, O., Lin, S.-J., Lee, T., and Chang, J. (2006). The 0.125 degree finite-volume general circulation model on the NASA Columbia supercomputer: Preliminary simulations of mesoscale vortices. *Geophysical Research Letters*, 33(5):1–4. ISSN 0094-8276. doi:10.1029/2005GL024594.

Sinden, G. (2007). Characteristics of the UK wind resource: long-term patterns and relationship to electricity demand. *Energy Policy*, 35(1):112–127.

Sistla, G., Hao, W., Ku, J.-y., and Kallos, G. (1998). An Operational Evaluation of Two Regional-Scale Ozone Air Quality Modeling Systems over the Eastern United States. *Bulletin of the American Meteorological Society*, 82:945–964.

Skibin, D. and Businger, J. A. (1985). The vertical extent of the log-linear wind profile under stable stratification. *Atmospheric Environment (1967)*, 19(1):27–30. ISSN 00046981. doi:10.1016/0004-6981(85)90133-7.

Smedman, A., Bergström, H., and Hogstrom, U. L. F. (1996). Low level jets - a decisive factor for offshore wind energy siting in the Baltic Sea. *Wind Engineering*, 23(2):133–142.

Smith, D., Scaife, A., and Kirtman, B. (2011). Migration and Global Environmental Change SR6 : What is the current state of scientific knowledge with regard to seasonal and decadal forecasting ? October, UK Government Office for Science.

Sood, A. and Suselj, K. (2006). High Resolution NWP North Sea Wind Forecasts in the Marine Atmospheric Boundary Layer. *of the European Wind Energy Conference, Athens*, pp. 1–5.

Storm, B. A. (2008). *Modeling of Low-Level Jets over the Great Plains: Implications for Wind Energy*. Phd, Texas Tech University.

Stull, R. B. (1988). *An Introduction to Boundary Layer Meteorology (Atmospheric and Oceanographic Sciences Library)*. Springer. ISBN 9027727694.

Swail, V. R. and Cox, A. T. (2000). On the Use of NCEPNCAR Reanalysis Surface Marine Wind Fields for a Long-Term North Atlantic Wave Hindcast. *Journal of Atmospheric and Oceanic Technology*, 17(4):532–545. ISSN 0739-0572. doi:10.1175/1520-0426(2000)017⟨0532:OTUONN⟩2.0.CO;2.

Tavner, P. J., Long, H., and Feng, Y. (2010). Early experiences with UK round 1 offshore wind farms. *Proceedings of the ICE - Energy*, 163(4):167–181. ISSN 1751-4223. doi:10.1680/ener.2010.163.4.167.

Taylor, K., Diagnosis, L. L. N. L. P. C. M., and Intercomparison (2000). Summarizing multiple aspects of model performance in a single diagram. *Journal of Geophysical Research*, (106):7183–7192.

Termonia, P. and Deckmyn, A. (2007). Model-Inspired Predictors for Model Output Statistics (MOS). *Monthly Weather Review*, 135(10):3496–3505. ISSN 0027-0644. doi:10.1175/MWR3469.1.

The Offshore Valuation Group (2011). The offshore valuation : a a valuation of the UKs offshore renewable energy resource.

Thomas, B. R., Kent, E. C., Swail, V. R., and Berry, D. I. (2008). Trends in ship wind speeds adjusted for observation method and height. *International Journal of Climatology*, 28(6):747–763. ISSN 08998418. doi:10.1002/joc.1570.

Tindal, A., Johnson, C., Leblanc, M., Harman, K., and Rareshide, E. (2008). Site specific adjustments to wind turbine power curves. In *AWEA Windpower Conference Houston*, June, pp. 1–11.

Toke, D. (2011). The UK offshore wind power programme: A sea-change in UK energy policy? *Energy Policy*, 39(2):526–534. ISSN 03014215. doi:10.1016/j.enpol.2010.08.043.

Tokinaga, H. and Xie, S.-p. (2010). Wave and Anemometer-based Sea-surface Wind (WASWind) for Climate Change Analysis. *Journal of Climate*, 24:267–285. ISSN 08948755. doi:10.1175/2010JCLI3789.1.

Tremback, C. J. and Walko, R. L. (2005). RAMS: Regional Atmospheric Modelling System - User's Guide.

Troen, I., Mortensen, N. G., and Petersen, E. (2008). Wasp Wind Atlas Analysis and Application Programme: User's Guide. , Riso National Laboratory.

Turton, J. (2009). E-Surfmar moored buoy technical description E-Surfmar moored buoy systems. , UKMO.

Turton, J. and Pethica, C. (2010). Assessment of a New Anemometry System for the Met Offices Moored Buoy Network. *Journal of Atmospheric and Oceanic Technology*, 27(12):2031–2038. ISSN 0739-0572. doi:10.1175/2010JTECHA1475.1.

UK Government (2009). *The UK Renewable Energy Strategy*. Office of Public Sector Information. ISBN 9780101768627.

UKGOV (2008). Climate Change Act. , UK Government Parliamentary Act, London.

UKMO (2008). The Unified Model.

UKMO (2010). Met Office Surface Data Users Guide. , UK Meteorological Office.

UKMO (2011). Met Office: Shipping forecast and gale warnings.

UKRC (2011). HECToR HECToR Home Page.

Undheim, O. (2005). *The non-linear microscale flow solver 3DWind. Developments and validation*. Ph.D. thesis, Norwegian University of Science and Technology.

University of Athens (2011). RAMS High Resolution Forecast.

Uppala, S. M., KÅ llberg, P. W., Simmons, A. J., Andrae, U., Costa, V. D., Fiorino, B. M., Gibson, J. K., Haseler, J., Hernandez, A., Kelly, G. A., Li, X., Onogi, K., Saarinen, S., Sokka, N., Allan, R. P., Andersson, E., Arpe, K., Balmaseda, M. A., Beljaars, A. C. M., Berg, L. V. D., Bidlot, J., Bormann, N., Caires, S., Chevallier, F., Dethof, A., Dragosavac, M., Fisher, M., Fuentes, M., Hagemann, S., Hólm, E., Hoskins, B. J., Isaksen, L., Janssen, P. A. E. M., Jenne, R., Mcnally, A. P., Mahfouf, J. F., Morcrette, J. J., Rayner, N. A., Saunders, R. W., Simon, P., Sterl, A., Trenberth, K. E., Untch, A., Vasiljevic, D., Viterbo, P., and Woollen, J. (2005). The ERA-40 re-analysis. *Quarterly Journal of the Royal Meteorological Society*, 131(612):2961–3012.

USNRC (1992). *Coastal meteorology: a review of the state of the science*. National Academy Press, Washington DC.

Vanhoff, B., Risien, C., Strub, P., and Foley, D. (2009). A High Resolution Ocean Vector Wind Product for the California Current System from 10 Years of QuikSCAT Scatterometer Data. In *Eastern Pacific Ocean Conference Symposium Abstracts*.

Vanhoff, B., Risien, C., Strub, P., Foley, D., and Chelton, D. B. (2011). A high resolution ocean vector wind product for the California Current System from 10 years of QuikSCAT scatterometer data. In *Eastern Pacific Ocean Conference*.

Vannitsem, S. and Nicolis, C. (2008). Dynamical Properties of Model Output Statistics Forecasts. *Monthly Weather Review*, 136(2):405–419. ISSN 0027-0644. doi:10.1175/2007MWR2104.1.

Vickers, D. and Mahrt, L. (2006). Evaluation of the air-sea bulk formula and sea-surface temperature variability from observations. *Journal of Geophysical Research*, 111(C5):1–14. ISSN 0148-0227. doi:10.1029/2005JC003323.

Vickers, D. and Mahrt, L. (2010). Sea-surface roughness lengths in the midlatitude coastal zone. *Quarterly Journal of the Royal Meteorological Society*, 136(649):1089–1093. ISSN 00359009. doi:10.1002/qj.617.

Vieno, M. (2005). The use of an Atmospheric Chemistry-Transport Model (FRAME) over the UK and the development of its numerical and physical schemes.

Wallcraft, A. J., Kara, A. B., Barron, C. N., Metzger, E. J., Pauley, R. L., and Bourassa, M. A. (2009). Comparisons of monthly mean 10 m wind speeds from satellites and NWP products over the global ocean. *Journal of Geophysical Research*, 114(D16):D16109. ISSN 0148-0227. doi:10.1029/2008JD011696.

Wan, Y.-h. and Bucaneg, D. (2002). Short-Term Power Fluctuations of Large Wind Power Plants. *Journal of Solar Energy Engineering*, 124(4):427. ISSN 01996231. doi:10.1115/1.1507762.

Wan, Y.-h., Ela, E., and Orwig, K. (2010). Development of an Equivalent Wind Plant Power-Curve. In *Proceedings of WindPower 2010*, June. NREL, Dallas, Texas.

Warner, T. T. (2011). *Numerical Weather and Climate Prediction*. Cambridge University Press, 1st edition.

Weber, R. (1999). Remarks on the definition and estimation of friction velocity. *Boundary-Layer Meteorology*.

Wentz, F. J. and Ricciardulli, L. (2011). Comment on "Global trends in wind speed and wave height". *Science (New York, N.Y.)*, 334(6058):905; author reply 905. ISSN 1095-9203. doi:10.1126/science.1210317.

Wentz, F. J., Ricciardulli, L., Hilburn, K., and Mears, C. (2007). How much more rain will global warming bring? *Science*, 317(5835):233–235.

Werth, D. and Garrett, A. (2010). Patterns of Land-Surface Errors and Biases in the Global Forecast System. *Monthly Weather Review*, 139(2004):1569–1582. ISSN 0027-0644. doi:10.1175/2010MWR3423.1.

Wieringa, J. (1993). Representative roughness parameters for homogeneous terrain. *Boundary-Layer Meteorology*, 63(4):323–363. ISSN 0006-8314. doi:10.1007/BF00705357.

Wieringa, J., Davenport, A. G., Grimmond, C. S. B., and Oke, T. R. (2001). New revision of Davenport Roughness Classification. *Proc., 3EACWE, Eindhoven, The Netherlands*.

Winterfeldt, J., Andersson, A., Klepp, C., Bakan, S., and Weisse, R. (2010). Comparison of HOAPS, QuikSCAT, and Buoy Wind Speed in the Eastern North Atlantic and the North Sea. *IEEE Transactions on Geoscience and Remote*, 48(1):338–348. ISSN 0196-2892. doi:10.1109/TGRS.2009.2023982.

Wippermann, F. and Gross, G. (1981). On the construction of orographically influenced wind roses for given distributions of the large-scale wind. *Beitr. Phys. Atmos*, 54:492–501.

WRF (2011). The Weather Research & Forecasting Model Website: Real Time Forecasting.

Yague, C., Viana, S., Maqueda, G., and Redondo, J. M. (2006). Influence of stability on the flux-profile relationships for wind speed , ϕ m , and temperature , ϕ h , for the stable atmospheric boundary layer. *Nonlinear Processes in Geophysics*, 13:185–203.

Yang, G. and Hoskins, B. (1996). Propagation of Rossby waves of nonzero frequency. *Journal of the atmospheric sciences*, 53(16):2365–2378.

Yelland, M. J., Moat, B. I., Pascal, R. W., and Berry, D. I. (2002). CFD Model Estimates of the Airflow Distortion over Research Ships and the Impact on Momentum Flux Measurements. *J. Atmos. Oceanic Technol*, 19:1477–1499.

Yim, S. H. L., Fung, J. C. H., Lau, A. K. H., and Kot, S. C. (2007). Developing a high-resolution wind map for a complex terrain with a coupled MM5/CALMET system. *Journal of Geophysical Research-Atmospheres*, 112(D5):–.

Young, I. R., Zieger, S., and Babanin, A. V. (2011). Global trends in wind speed and wave height. *Science (New York, N.Y.)*, 332(6028):451–5. ISSN 1095-9203. doi:10.1126/science.1197219.

Zhang, D. and Anthes, R. C. (1982). A high-resolution model of the planetary boundary-layer-sensitivity tests and comparisons with SESAME-79 data. *Journal of Applied Meteorology*, 21:1594–1609.

Zhang, K., Mao, H., Civerolo, K., Berman, S., Ku, J., Rao, S., Doddridge, B., Philbrick, C., and Clark, R. (2001). Numerical investigation of boundary-layer evolution and nocturnal low-level jets: Local versus non-local PBL schemes. *Environmental Fluid Mechanics*, 1(2):171–208.